

Université
de Toulouse

THÈSE

En vue de l'obtention du
DOCTORAT DE L'UNIVERSITÉ DE TOULOUSE

Délivré par :
Institut National Polytechnique de Toulouse (INP Toulouse)

Discipline ou spécialité :
Dynamique des fluides

Présentée et soutenue par :
Jérôme DOMBARD

le : jeudi 20 octobre 2011

Titre :
Simulation Numérique Directe des sprays dilués anisothermes
avec le Formalisme Eulérien Mésoscopique
Direct Numerical Simulation of non-isothermal dilute sprays
using the Mesoscopic Eulerian Formalism

Ecole doctorale :
Mécanique, Énergétique, Génie civil et Procédés (MEGeP)

Unité de recherche :
Institut de Mécanique des Fluides de Toulouse (IMFT, UMR 5502)

Directeur(s) de Thèse :
Thierry POINSOT, Directeur de recherche (IMFT), Directeur de thèse
Laurent SELLE, Chargé de Recherche (CNRS), Co-Directeur de thèse

Rapporteurs :
Marc MASSOT, Professeur (Ecole Centrale de Paris)
Alfredo SOLDATI, Professeur (Université d'Udine, Italie)

Membre(s) du jury :
Julien REVEILLON, Professeur (Université de Rouen), Président
Philippe VILLEDIEU, Chercheur (ONERA, Toulouse), Examineur
Olivier SIMONIN, Professeur (Université de Toulouse), Examineur
Anthony ROUX, Ingénieur (Turbomeca), ? W TdW
Stéphane JAY, 5ZSdYé VVdVZVdZVW(18B 7@fi ? W TdW



À Cindy
À André

...
À la mémoire de Bernadette

Résumé

Le contexte général de cette thèse est la Simulation Numérique Directe des écoulements diphasiques dilués anisothermes. Un accent particulier est mis sur la détermination précise de la dispersion des particules et du transfert de chaleur entre la phase porteuse et dispersée. Cette dernière est décrite à l'aide d'une approche Eulérienne aux moments: le Formalisme Eulérien Mésoscopique (FEM) [41, 123], récemment étendu aux écoulements anisothermes [78]. Le principal objectif de ce travail est de déterminer si ce formalisme est capable de prendre en compte de manière précise l'inertie dynamique et thermique des particules dans un écoulement turbulent, et particulièrement dans une configuration avec un gradient moyen. Le code de calcul utilisé est AVBP.

La simulation numérique d'un spray dilué avec une approche Eulerienne soulève des questions supplémentaires sur les méthodes numériques et les modèles employés. Ainsi, les méthodes numériques spécifiques aux écoulements diphasiques implémentées dans AVBP [69, 103, 109] ont été testées et revisitées. L'objectif est de proposer une stratégie numérique précise et robuste qui résiste aux forts gradients de fraction volumique de particule provoqués par la concentration préférentielle [132], tout en limitant la diffusion numérique. Ces stratégies numériques sont comparées sur une série de cas tests de complexité croissante et des diagnostics pertinents sont proposés. Par exemple, les dissipations dues à la physique et au numérique sont extraites des simulations et quantifiées. Le cas test du tourbillon en deux dimensions chargé en particules est suggéré comme une configuration simple pour mettre en évidence l'impact de l'inertie des particules sur leur champ de concentration et pour discriminer les stratégies numériques. Une solution analytique est aussi proposée pour ce cas dans la limite des faibles nombres de Stokes. Finalement, la stratégie numérique qui couple le schéma centré d'ordre élevé TTGC et une technique de stabilisation, aussi appelée viscosité artificielle, est celle qui fournit les meilleurs résultats en terme de précision et de robustesse. Les paramètres de viscosité artificielle (c'est-à-dire les senseurs) doivent néanmoins être bien choisis.

Ensuite, la question des modèles nécessaires pour décrire correctement la dispersion des particules dans une configuration avec un gradient moyen est abordée. Pour ce faire, un des modèles RUM (appelé AXISY-C), proposé par Masi [78] et implémenté dans AVBP par Sierra [120], est validé avec succès dans deux configurations: un jet plan diphasique anisotherme 2D et 3D. Contrairement aux anciens modèles RUM, les principales statistiques de la phase dispersée sont désormais bien prédites au centre et aux bords du jet.

Finalement, l'impact de l'inertie thermique des particules sur leur température est étudié. Les résultats montrent un effet important de cette inertie sur les statistiques mettant en évidence la nécessité pour les approches numériques de prendre en compte ce phénomène. Ainsi, l'extension du FEM aux écoulements anisothermes, c'est-à-dire les flux de chaleur RUM (notés RUM HF), est implémentée dans AVBP. L'impact des RUM HF sur les statistiques de température des

particules est ensuite évalué sur les configurations des jet 2D et 3D. Les champs Eulériens sont comparés à des solutions Lagrangiennes de référence calculées par B. Leveugle au CORIA et par E. Masi à l'IMFT pour les jets 2D et 3D, respectivement. Les résultats montrent que les RUM HF améliorent la prédiction des fluctuations de température mésoscopique, et dans une moindre mesure la température moyenne des particules en fonction de la configuration. Les statistiques Lagrangiennes sont retrouvées lorsque les RUM HF sont pris en compte alors que les résultats sont dégradés dans le cas contraire.

Mots clefs: Ecoulements diphasiques anisothermes, Formalisme Eulérien Mésoscopique, Approche Euler/Euler, Transfert de chaleur, Simulation Numérique Directe

Summary

This work addresses the Direct Numerical Simulation of non-isothermal turbulent flows laden with solid particles in the dilute regime. The focus is set on the accurate prediction of heat transfer between phases and of particles dispersion. The dispersed phase is described by an Eulerian approach: the Mesoscopic Eulerian Formalism [41, 123], recently extended to non-isothermal flows [78]. The main objective of this work is to assess the ability of this formalism to accurately account for both dynamic and thermal inertia of particles in turbulent sheared flows. The CFD code used in this work is AVBP.

The numerical simulation of dilute sprays with an Eulerian approach calls for specific modeling and raises additional numerical issues. First, the numerical methods implemented in AVBP for two-phase flows [69, 103, 109] were tested and revisited. The objective was to propose an accurate and robust numerical strategy that withstands the steep gradients of particle volume fraction due to preferential concentration [132] with a limited numerical diffusion. These numerical strategies have been tested on a series of test cases of increasing complexity and relevant diagnostics were proposed. In particular, the two-dimensional vortex laden with solid particles was suggested as a simple configuration to illustrate the effect of particle inertia on their concentration profile and to test numerical strategies. An analytical solution was also derived in the limit of small inertia. Moreover, dissipations due to numerics and to physical effects were explicitly extracted and quantified. Eventually, the numerical strategy coupling the high-order centered scheme TTGC with a stabilization technique –the so called artificial viscosity– proved to be the most accurate and robust alternative in AVBP if an adequate set-up is used (*i.e.* sensors). Then, the issue of the accurate prediction of particle dispersion in configurations with a mean shear was addressed. One of the RUM model (denoted AXISY-C), proposed by Masi [78] and implemented by Sierra [120], was successfully validated in a two-dimensional and a three-dimensional non-isothermal jet laden with solid particles. Contrary to the former RUM models [63, 103], the main statistics of the dispersed phase were recovered at both the center and the edges of the jet. Finally, the impact of the thermal inertia of particles on their temperature statistics has been investigated. The results showed a strong dependency of these statistics to thermal inertia, pinpointing the necessity of the numerical approaches to account for this phenomenon. Therefore, the extension of the MEF to non isothermal conditions, *i.e.* the RUM heat fluxes, has been implemented in AVBP. The impact of the RUM HF terms on the temperature statistics was evaluated in both configurations of 2D and 3D jets. Eulerian solutions were compared with Lagrangian reference computations carried out by B. Leveugle at CORIA and by E. Masi at IMFT for the 2D and 3D jets, respectively. Results showed a strong positive impact of the RUM HF on the fluctuations of mesoscopic temperature, and to a lesser extent on the mean mesoscopic temperature depending of the configuration. Neglecting the RUM HF leads to erroneous results whereas the Lagrangian statistics are recovered when they are accounted for.

Keywords: Non-isothermal two-phase flows, Mesoscopic Eulerian Formalism, Eulerian-Eulerian approach, Heat transfer, Direct Numerical Simulation

Contents

Nomenclature	1
Introduction	3
I Equations, models and numerical strategies	12
1 A local Eulerian-Eulerian approach for non-isothermal flows	13
1.1 Choice of the approach for the dispersed phase	14
1.2 Lagrangian approach	15
1.2.1 Particle characteristic times	16
1.3 The Mesoscopic Eulerian Formalism - extension to non-isothermal flows	17
1.3.1 Methodology to obtain the MEF set of equations	18
1.3.2 Moments of the mesoscopic variables and governing equation	20
1.3.3 Closure of the equations	22
1.3.4 Final set of equations	25
1.3.5 Existence of a correlated and uncorrelated particle temperature	27
1.3.6 Effect of particle inertia on temperature variances	29
2 Numerical strategies	31
2.1 Specificities of the dispersed phase	32
2.1.1 Compressibility effects	32
2.1.2 Crossing trajectories	33
2.2 Numerical structure of AVBP with the MEF	33
2.2.1 Cell-vertex approach	34
2.2.2 Source terms	36
2.2.3 Convective scheme	36
2.2.4 Temporal advancement	38
2.2.5 Diffusive terms	41
2.3 Artificial viscosity	42
2.3.1 Sensors	43
II Evaluation of the numerical strategies	47
3 Convection of a 1D particle volume fraction crenel	49

3.1	Presentation of the configuration	50
3.1.1	Methodology	51
3.2	How to get rid of spurious oscillations?	52
3.3	How to withstand stiff gradients?	54
3.3.1	Set up of the AV sensor	55
3.3.2	Comparison of the two numerical strategies: PSI scheme and “TTGC+AV”	58
4	Particle-laden vortex	61
4.1	Description of the configuration	62
4.2	Governing equations of the carrier phase	63
4.3	Governing equations of the dispersed phase	63
4.3.1	Normalization procedure	65
4.3.2	Analytical solution when $St \ll 1$	66
4.4	Methodology	66
4.5	Particle-laden vortex simulations at low inertia	67
4.5.1	Comparison of EE and EL results with the analytical solution	67
4.5.2	Effect of the mesh resolution	70
4.6	Vortex laden with inertial particles ($St = 1$)	74
5	Particle-laden decaying Homogeneous Isotropic Turbulence	77
5.1	Brief theoretical background	78
5.2	Description of the test case	81
5.2.1	Initialization procedure	81
5.3	Methodology	84
5.3.1	Previous work with the MEF with this test case	84
5.3.2	Present work: presentation of the test cases	85
5.4	Macroscopic evaluation of numerical strategies	86
5.5	Discrete kinetic energy balance of the dispersed phase	89
5.5.1	Analytical derivation	89
5.5.2	Application of this diagnostic to the test cases	91
5.6	Conclusions	93
III	A posteriori tests of the MEF extended to non-isothermal flows	94
6	Influence of the thermal inertia in dispersed-phase flows - 2D non-isothermal particle-laden jet	95
6.1	Introduction	96
6.2	Description of the solvers and modeling equations	97
6.2.1	Carrier phase flow solvers	98
6.2.2	Eulerian/Lagrangian formulation	98
6.2.3	Eulerian/Eulerian formulation: the Mesoscopic Eulerian Formalism	99
6.3	Configuration and boundary conditions	101
6.3.1	Computational domain	101
6.3.2	Mesh and boundary conditions	102
6.3.3	Turbulence injection	102

6.3.4	Dispersed phase characteristics	103
6.4	Results and analysis	104
6.4.1	Carrier phase	104
6.4.2	Dynamics of the dispersed phase	106
6.4.3	Influence of thermal inertia: analysis of Lagrangian simulations	108
6.4.4	Influence of thermal inertia: validation of the Eulerian simulations	108
6.5	Conclusions	111
6.6	Influence of the RUM model and coupling with the RUM heat fluxes	112
6.6.1	Dynamics of the dispersed phase	112
6.6.2	Temperature statistics of the dispersed phase	119
6.6.3	Additional conclusions	123
7	Evaluation of the MEF extended to non-isothermal flows - 3D non-isothermal particle-laden jet	124
7.1	Configuration	125
7.1.1	Initial conditions	125
7.1.2	Definition of the normalization numbers	127
7.1.3	Numerical setup and methodology	128
7.2	Analysis of the carrier phase	130
7.3	Analysis of the dispersed phase	132
7.3.1	Analysis of the Lagrangian database	132
7.3.2	Mesh convergence of the Eulerian simulations	132
7.3.3	Evaluation of the RUM models	137
7.3.4	Influence of the RUM heat fluxes	143
7.4	Conclusions	145
	Conclusion	149
	A Carrier phase	152
	B Additional transport equations of high-order moments of the dispersed-phase	154
	C Additional results	156

Acknowledgements

Les remerciements sont la dernière pierre à l'édifice que constitue une thèse. Je vais essayer ici de remercier l'ensemble des personnes qui ont participé de près ou de loin à cette aventure. Je risque d'oublier certaines personnes tant elles ont été nombreuses. Merci de ne pas m'en tenir rigueur. Une fois la soutenance passée, je commence à comprendre peu à peu que ce n'est pas une fin, mais seulement le début d'une nouvelle vie, qui sera sans doute plus difficile que ces trois dernières années.

Tout d'abord, je tiens à exprimer ma gratitude et mon profond respect à mes deux directeurs de thèse: Thierry Poinsot, directeur de recherche au CNRS et Laurent Selle, chargé de recherche au CNRS. Votre encadrement a non seulement été irréprochable, mais vous avez su le faire avec toute l'humanité qui vous caractérise. Je ne vous remercierai jamais assez de m'avoir fait confiance et de m'avoir offert des opportunités qui m'ont marqué, comme le Summer Program du CTR. Vous avez su rendre passionnantes et inoubliables ces trois années. Encore une fois merci!

Je remercie aussi mon jury de thèse d'avoir accepté d'en faire partie malgré vos emplois du temps chargés: le président Julien Reveillon, les rapporteurs Marc Massot et Alfredo Soldati, mes examinateurs Philippe Villedieu et Olivier Simonin et les invités Anthony Roux et Stéphane Jay, qui ont fait l'honneur de juger mon travail.

J'ai effectué ma thèse à l'Institut de Mécanique des Fluides de Toulouse au sein du groupe PSC. Cela m'a permis de rencontrer beaucoup de personnes de qualité. Je pense en particulier aux différents thésards et post-docs que j'ai eu le plaisir de rencontrer, les anciens comme les nouveaux, dont certains sont maintenant des amis: Nicolix, Enrica (see you in L.A), Floflo (fait gaffe aux rousses et aux brunes, elles font tourner la tête), Marion L. (ca va le faire!), Renaud A., Roel, JF, Marie-Charlotte, Romain, et tous les autres. Nicolix, merci pour les deux années de thèse à partager ton bureau. Elles ont été un moteur pour mon début de thèse. J'ai aussi une pensée pour ma dernière année avec Adrien le jeune padawan. Je te souhaite le meilleur pour ta fin de thèse (comme le dirait TP: je ne me fais pas de soucis pour toi). Enrica, ma thèse te doit beaucoup, grâce à tes modèles bien sûr, mais aussi à la vulgarisation de ton manuscrit et à tes corrections méticuleuses. Te connaissant maintenant beaucoup mieux, ton entête de thèse tiré de Blade Runner: "I have seen things you people wouldn't believe" a vraiment été bien choisi. Merci aussi aux thésards du bureau des jeun's dans lequel je me suis si souvent réfugié pour décompresser: Marion P. (merci pour les twixs), Nico, Guillaume, Adrien D. et Dani le petit Colombien. Merci aussi aux permanents Pascal Fede (une partie de squash de plus et je te bat-tais), Eric Climent, Olivier Praud, Moïse Marchal et Rudy Bazile ainsi qu'à Florence. J'associe aussi à mes remerciements tout le staff administratif, Catherine, Muriel et Sandrine ainsi que le

service info et le groupe cosinus, particulièrement Annaïg et Hervé (je me souviendrai toujours de ta méthode pour se débarrasser d'un chat en dénudant des fils électriques). Je tiens à exprimer toute ma gratitude à l'atelier pour leur aide pour les différentes réparations de mon kayak.

L'utilisation et le développement dans le code AVBP m'a permis de collaborer avec l'équipe CFD du CERFACS. Un grand merci aux thésards que j'ai eu la chance de côtoyer: Felix (les deux mois au CIEMAT avec toi reste mémorable), Marta, Nico L. (merci pour tes conseils, tips et relecture sur le numérique), ainsi qu'aux seniors Benedicte Cuenot, Laurent Gicquel, Gabriel Staffelbach (un grand merci pour tes nombreux conseils et coups de main pour coder et tout le reste), Eleonore Riber, Olivier Vermorel et Florent Duchaine. Les deux mois en tant qu'ingénieur d'étude au CERFACS m'ont permis de faire de nouvelles rencontres. Merci à tous les thésards Geof, Anthony R., Thomas P. et Jean-Phi et au staff administratif Marie et Michèle pour m'avoir accueilli dans de si bonnes conditions.

Une thèse ne se résume pas qu'au travail et je tiens à remercier chaleureusement mes amis pour leur encouragement et les bons moments passés ensemble pendant ces trois années, Tom, Ious, Grogay, Sam, Sylvie, Chris, Tieno, Ophé, Cumcum, p'tit Sam, Nany et tous les autres. Merci aussi à mon équipe de kayak polo pour les bons moments aux entrainements et en compétition.

Je tiens aussi à remercier mes parents pour leur soutien. Et enfin, last but not least, Cindy avec qui je partage ma vie. Merci pour ton soutien sans faille pendant les deux dernières années et de m'avoir supporté pendant les quatre derniers mois les plus difficiles. Nous avons su surmonter cette épreuve en équipe. L'avenir nous réserve plein de bonnes choses. Je te dédie tout particulièrement ce travail.

Nomenclature

Subscripts

f or ${}_f$	Fluid or carrier phase
p or ${}_p$	Particle or dispersed phase
ac	Acoustic
ref	Reference quantity

Shortcuts

2D	two-dimensional
3D	three-dimensional
AV	Artificial Viscosity
CFD	Computational Fluid Dynamics
CFL	Courant-Friedrichs-Lewy
CM	Colin Martinez (AV sensor)
DNS	Direct Numerical Simulations
EE	Euler/Euler
EE	Eulerian/Eulerian
EL	Euler/Lagrange
EL	Eulerian/Lagrangian
FE	Finite Element
FV	Finite Volume
HF	Heat Flux
HIT	Homogeneous Isotropic Turbulence
LES	Large Eddy Simulations

LHS	Left Hand Side
LW	Lax Wendroff
MEF	Mesosopic Eulerian Formalism
MKE	Mesosopic Kinetic Energy
MMEF	Multi-fluid Mesoscopic Eulerian Formalism
NDF	Number Density Function
PDF	Probability Density Function
PP	Passot-Pouquet
PSI	Positive Streamwise Invariant
PTC	Particle Trajectory Crossing
QMOM	Quadrature Method of Moments
RHS	Right Hand Side
rms	root mean square
RUE	Random Uncorrelated Energy
RUM	Random Uncorrelated Motion
S	Sanjose (AV sensor)
T	Total (AV sensor)
TKE	Turbulent Kinetic Energy
TPF	Two-Phase Flow
TTGC	Two-step Taylor-Galerkin Colin
VKP	von Kármán Pao
VOF	Volume of Fluid

Greek letters

α_p	Particle volume fraction
α	particle-to-fluid heat capacity ratio
$\delta F_{p,i}$	i^{th} component of the RUM heat flux
$\delta \Omega_{p,i}$ and $\delta \Delta_{p,j}$	3^{rd} -order moment accounting for the correlations between the RUM velocity and temperature
$\delta \theta_\theta$	RUM temperature variance
$\delta \Theta_{p,i}$	i^{th} component of the RUM heat flux
$\delta \theta_p$	RUM kinetic energy
$\delta_{i,j}$	Kronecker symbol
δq_θ	conditional-averaged RUM temperature variance
Δt	Time step
η_k	Kolmogorov scale
γ	ratio of the specific heats of the gas at constant pressure and constant volume
Γ_v	vortex strength
λ_f^f	Longitudinal Taylor scale of the fluid
λ_f^g	Transversal Taylor scale of the fluid
λ_f	Thermal conductivity of the fluid
μ_f	dynamic viscosity of the fluid
ν_f	kinematic viscosity of the fluid
ν	CFL number
Ω_j	cell j
ρ	density
τ_θ	Thermal relaxation time of the fluid
$\tau_{fp}^{F\theta}$	mean macroscopic thermal relaxation time

τ_{fp}^F	mean macroscopic dynamic relaxation time
τ_f	Dynamic relaxation time of the fluid
τ_p	Dynamic relaxation time of the particles
θ	width of the initial gradient
$\varepsilon^{(2)}$	2^{nd} -order AV coefficient
$\varepsilon^{(4)}$	4^{th} -order AV coefficient
ε_f	Dissipation rate of the turbulent kinetic energy
ζ_{extr}	AV sensor on the extrema
ζ_{grad}	AV sensor on the gradients
d_p	particle diameter

Non-dimensional numbers

I_{turb}	Turbulence intensity
Re	Reynolds number
Re_K	Reynolds number based on the Kolmogorov scale
Re_p	Particle Reynolds number
Re_t	Fluid turbulent Reynolds number
Re_{ac}	acoustics Reynolds number
St	Dynamic Stokes number
St_θ	Thermal Stokes number
We	Weber number
M	Mach number
Nu	Nusselt number
Pr	Prandtl number

Operators

$\tilde{\cdot}$	mesoscopic quantity
-----------------	---------------------

Roman letters

$D_j^{(2)}$	2^{nd} -order-AV residual at node j
-------------	---

$\mathbf{D}_j^{(4)}$	4 nd -order-AV residual at node j	$C_{p,p}$	Heat capacity at constant pressure of the particles
\mathbf{N}_j	Residual at node j	g_{pp}	Particle concentration function
\mathbf{R}_e	vector of the residual at cell K_e	II_S	Second invariant of $S_{p,ij}$
\mathbf{S}	Vector of the source terms	III_S	Third invariant of $S_{p,ij}$
\mathbf{U}	Vector of the conservative variables	L_f^f	Longitudinal integral length scale of the fluid
\mathbf{u}	Velocity (vector)	L_f^g	Transverse integral length scale of the fluid
\mathbf{x}	Position (vector)	l_e	Most energetic length scale
\mathcal{D}_j	cells around node j	L	Length
\mathcal{H}_f	Fluid realization	n_p	Particle number density
\mathcal{H}_p	Particle realization	P	Pressure
q_θ^2	particle temperature variance	q_f^2	Turbulent kinetic energy of the fluid
\tilde{c}_p	particle sound speed	R_θ^{pp}	two-point spatial correlations of particle temperature
$\underline{\mathbf{D}}_{j,e}$	Distribution matrix of \mathbf{R}_e at node j	R_v	Characteristic radius of a vortex
$\vec{\mathcal{F}}^C$	inviscid flux tensor	$S_{p,ij}$	rate of strain tensor
$\vec{\mathcal{F}}^V$	viscous flux tensor	S	Square root of II_S
\vec{S}_k	normal at the vertex k	T	Temperature
$\tilde{\mathbf{E}}_{p,i}$	i^{th} component of the mesoscopic heat flux	t	Time
B_{max}	maximal threshold (AV sensor)	V_e	Volume associated to the node e
B_{min}	minimal threshold (AV sensor)		
C_D	Drag coefficient		
c	speed of sound		
$C_{p,f}$	Heat capacity at constant pressure of the fluid		

Superscripts
 * or + normalized variable

Introduction

The consumption of fossil fuel in transportation is a major issue for three main reasons: (1) increasing cost of oil, (2) pollutant emissions and (3) impact on global climate through green-house gases [74, 114, 139]. Many countries have adopted stringent regulations in order to reduce emission levels and that of the European commission –the Euro standards– is among the strictest in the world. Consequently, the automotive industry is searching for novel ways to optimize combustion and globally reduce fuel consumption. In most internal combustion engines, fuel is liquid. Because the chemical reactions involved in the combustion process occur in the gaseous state, the detailed understanding of atomization and evaporation processes is instrumental to the improvement of the overall engine. Gaseous combustion is obviously a complex field (see [68, 94, 153] and reference therein) but this complexity is further increased for two-phase flows because of the gas/liquid interface and the coupling between evaporation, turbulent mixing and combustion [100]. For example, combustion regimes (premixed and non-premixed) observed in gaseous combustion become much more complex in two-phase flows where droplets can evaporate anywhere in the flow, leading to numerous combustion regimes [19, 68, 102]. Numerical simulations have become standard tools to investigate these issues. Indeed, because of the short time and length scales associated with two-phase flow combustion, numerical simulations can complement experimental investigations, even if it is still virtually impossible for a simulation to account for all physical phenomena from the injection of the liquid into the engine to the flame. The present work lies in this framework and focuses specifically on the accurate prediction of the droplet dispersion and temperature –which are of paramount importance for their evaporation– using Direct Numerical Simulations (DNS) of dilute sprays in non-isothermal conditions. This work is part of a project granted by the French National Agency denoted SIGLE¹ which aims at improving the numerical methods to simulate sprays in internal combustion engines.

The injection of a liquid jet may be roughly separated in three steps that are function of the liquid volume fraction [44], as shown in Fig. 1. First, close to the injector, the liquid volume fraction is very high and because inertial forces are usually much larger than surface tension, the liquid jet undergoes atomization. Large scale structures of pure liquid may be observed: ligaments, clusters of large droplets, etc. This process is usually referred to as primary break-up. Due to the interaction with the surrounding turbulent carrier phase, these structures may further break up into smaller droplets. Downstream of the dense primary atomization zone, the mass loading and volume fraction of the liquid become sufficiently small to consider that the liquid phase is indeed composed by a large number of small droplets: it is the dilute regime. Moreover, surface tension effects are usually larger than inertial effects in this region, so that

¹from the original French name: Simulations aux Grandes échelles des jets de carburants LiquidEs dans les moteurs à combustion interne.

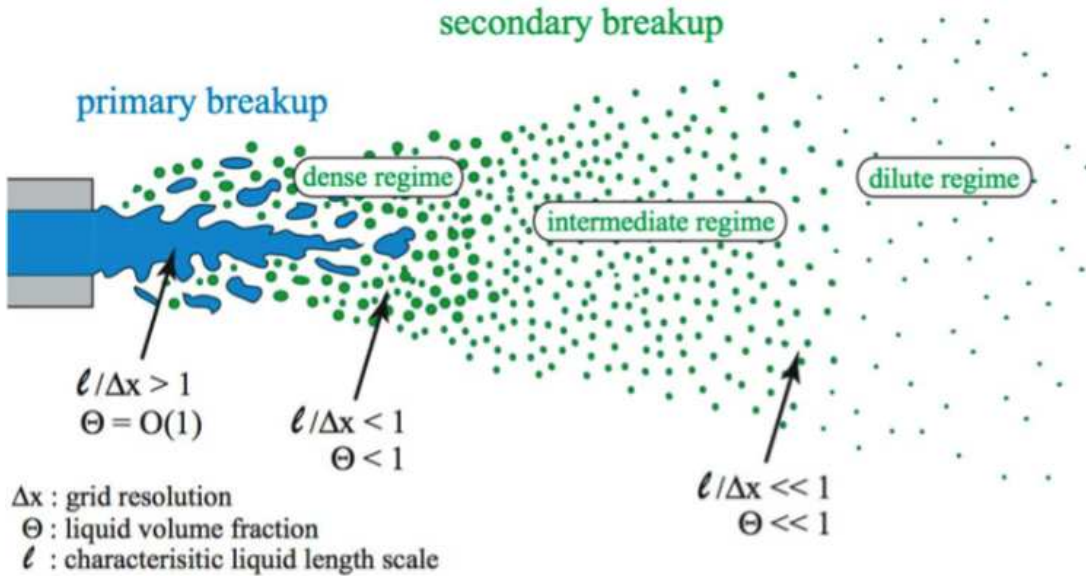


Figure 1: Phenomenology of the atomization of a spray. Excerpted from a presentation of M. Herrmann during the Summer Program of the CTR 2008, Stanford.

droplets are often assumed to be spherical. Since the topology of the liquid phase is drastically different between the dense and the dilute regimes, specific numerical methods are required. First, methods that track the interface of the liquid phase are well adapted for the dense region, such as surface-marker [141], Level-set [29, 49, 136] or Volume-of-Fluid (VOF) [47, 99] methods. These methods can be used to describe the dilute regime, but tracking explicitly the interface of a large number of small spherical droplets would lead to an extreme amount of computational time and seems inadequate. Therefore, the dilute regime may be better described by a Lagrangian description of the individual droplets or parcels [7, 42] or by an Eulerian description of the spray as a continuum field. Because the characteristics of the dilute spray region depend on the details of the atomization processes, the specification of the boundary condition is often crucial for the accuracy of numerical simulations. They can be simply based on first principles, experimental data [128] or numerical simulations [140]. Note that recent advances have been made to simulate the intermediate zone, where a large number of scales are present. These multi-scale methods rely on a coupling between interface tracking methods and Lagrangian description of particles [50, 140]. Nevertheless, the computational cost of such numerical simulations, describing the entire atomization of a jet from the largest to the smallest scale, is extreme, even relying on massively parallel computing. Therefore, realistic industrial configurations of jet injections usually assume that the spray is already atomized and composed of spherical droplets. The present work lies in this last framework and focuses on the numerical simulation of the dilute region.

Because of their inertia, the droplets may not exactly follow the fluid resulting in a phenomenon called preferential concentration [82, 132]: a cloud of particle embedded in a turbulent flow will preferentially collect in low vorticity and high shear regions. The relevant parameter to describe this behavior is the Stokes number (St), defined as the ratio between the particle

response time (τ_p) and a characteristic time of the fluid (τ_f). When τ_f is based on the Kolmogorov scale, the preferential concentration is maximum for $St \sim 1$ [148], pinpointing that this process is controlled by the small-scale structures of the turbulence [9]. This phenomenon leads to the creation of very steep gradients of particle volume fraction. In other words, a droplet may be incompressible but a cloud of droplets behaves as a highly compressible phase. Moreover, it may impact significantly other important processes such as inter-particle collisions [135, 149] or evaporation [100]. An other consequence of the inertia is particle trajectory crossing (PTC). At large St , droplets are weakly influenced by the surrounding carrier phase and have ballistic trajectories that may cross. This process is enhanced by the polydisperse nature of many sprays resulting in a wide range of particle inertia. PTC may result in collisions but the low particle volume fraction of dilute spray usually allows to neglect them.

The Lagrangian tracking of particles naturally describes PTC and particle preferential concentration. Particles are usually assumed as pointwise and one of the main issues for Lagrangian solvers is the correct integration of dispersed/carrier phase quantities at the position of particles. This method is very accurate and is considered as the reference to validate new models or closure terms in other approaches. However, the Lagrangian approach may become cumbersome because its computational cost is roughly proportional to the number of particles in the domain. Though the increasing raw power of the computational clusters is a good point for this approach, its parallelization is not trivial [42] and remains an issue. Contrary to the Lagrangian method, the Eulerian approach [71, 123] treats the dispersed phase as a continuum and represents it through a limited number of variables such as the particle volume fraction, velocity or temperature. The advantage of the Eulerian formulation is that its computational cost does not depend of the number of particles and is also very easy to parallelize through domain decomposition. As far as the computational cost is concerned, the Eulerian approach is thus a good candidate to carry out numerical simulations of industrial configurations. Nevertheless, it usually requires efforts in two fields:

- Modeling: models for Eulerian approaches are difficult to develop, especially for multi-size sprays.
- Numerics: the equations for Eulerian models correspond roughly to the equations of highly compressible gases. They exhibit sharp fronts, shocks and their resolution in a simulation is a problem in itself.

As far as modeling is concerned, the first issue is to build a solid background on which the equations for the liquid phase can be derived: Eulerian equations of the dispersed phase may be obtained by several methods. One may spatially average the dispersed phase over a scale of the order of the Kolmogorov scale [32, 33]. Another method, referred to as Eulerian equilibrium approach, solves the particle volume fraction and derives the particle velocity and temperature from the underlying fluid [37, 38]. Other methods use a probabilistic formulation of the dispersed phase by analogy with the kinetic theory of gases [98, 152]. A number density function (NDF) of the spray is introduced, which satisfies the Williams-Boltzmann equation. The explicit resolution of this equation –referred to as “full spray equation method” in [90]– is impracticable at a reasonable cost due to the large number of variables. An alternative solution –often referred to as “moment approach”– is to write a set of governing equations for selected moments of the spray NDF. In this framework, recent advances have tackled the two aspects of polydispersion and PTC. For example, de Chaisemartin *et al.* [28] extended the multi-fluid method [46, 70],

which consists in discretizing the spray NDF into droplet size intervals, to evaporating sprays. In its simplest form, the multi-fluid approach assumes a mono-kinetic spray NDF conditioned by the droplet size, so that it is unable to account for PTC: singularities arise when particle trajectories cross. Nevertheless, these singularities can be controlled by using adequate numerical schemes [13] –often referred to as kinetic schemes– to preserve the positivity of the particle volume fraction. The inability of the multi-fluid method to account for PTC and its high computational cost when a large number of size intervals is used, motivated the use of high-order moment methods. Following the Quadrature Method of Moments (QMOM) method [76], Kah and collaborators [61, 62] proposed two approaches: the Eulerian Multi Size Moment (EMSM) and the Eulerian Multi Velocity Moment (EMVM), which respectively and successfully address the two issues of spray polydispersion and PTC.

One aspect of two-phase flows has been studied only in a limited way and has significant effects for reacting two phase flows: the heat transfer between phases and the variance of particle temperature. Indeed, the heat transfer between fuel droplets and the surrounding gas may have a strong impact on the local evaporation rate as evaporation is a non-linear phenomenon. The resulting fluctuations of local equivalence ratio are known to have an impact on ignition, flame propagation or even combustion instabilities [66, 75, 88]. An accurate description of heat transfer to the dispersed phase is therefore necessary. And yet, very few studies have directly tackled the issue of particle temperature dispersion, which is mainly due to the lack of experimental data of non-isothermal two-phase flows [155]. Recent experimental techniques –such as rainbow thermometry– seem promising but further improvements are required [144]. An alternative path is to use DNS: a few studies of non-isothermal academic configurations, coupled with lagrangian tracking of particles, have been carried out. Berlemont *et al.* [10] studied the influence of temperature fluctuations on droplet evaporation in isotropic and homogeneous turbulence. They pointed out that temperature fluctuations must be taken into account when turbulent evaporation is considered, since the PDF of particle diameter broadens significantly when temperature fluctuations increase. The mechanism of two-phase heat and turbulent transport by particles was investigated in academic configurations such as decaying isotropic turbulence or homogeneous shear flow with an imposed mean temperature gradient [24, 57, 58, 113, 119, 151]. The impact of various parameters such as the particle dynamical response time τ_p , the Prandtl number, Pr , the Reynolds number, Re and mass-loading ratio, r_{ml} , on the statistics of particle temperature was investigated but the thermal relaxation time that combines all these parameters was not explicitly introduced. As a matter of fact, the notion of thermal inertia [23, 78] –the analog of dynamic inertia for particle dispersion– is still a novel notion.

Consequently, we chose the Mesoscopic Eulerian Formalism (MEF) [41] for its ability to reproduce local and instantaneous behavior of particles embedded in a turbulent flow. This formalism belongs to the family of Eulerian moment approach. It is based on the idea that the Lagrangian particle velocity may be divided into two contributions (*cf.* Fig. 2): (1) an Eulerian particle velocity field which is spatially correlated and shared by all particles and (2) a spatially-uncorrelated component proper to each particle which stems from inertial effects, referred to as the Random Uncorrelated Motion (RUM). The fundamental difference between the MEF and the other moment approaches lies in the statistical operator used to derive the equations for the moments. It is defined as the ensemble average over a large number of particle realizations for only one fluid realization. The ensemble-averaging of the spray NDF leads to additional terms in the set of governing equations related to the RUM: the RUM velocity-stress tensor, which

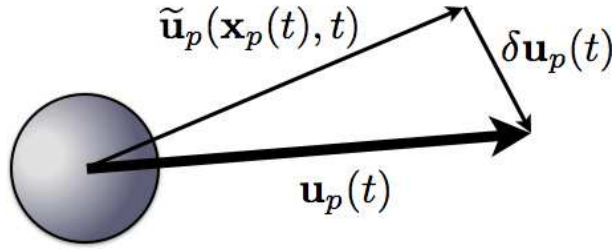


Figure 2: Sketch illustrating the splitting of the Lagrangian particle velocity ($\mathbf{u}_p(t)$) into two contributions: (1) an Eulerian particle velocity field ($\tilde{\mathbf{u}}_p(\mathbf{x}_p(t), t)$) which is spatially correlated and shared by all particles and (2) a spatially-uncorrelated component ($\delta \mathbf{u}_p(t)$) proper to each particle which stems from inertial effects, referred to as Random Uncorrelated Motion.

must be closed. The MEF has been implemented in the CFD code used in this work (AVBP²). Several important advances on the MEF have been achieved in previous studies:

- **Closure of the MEF set of equations.** The closure of the RUM velocity stress tensor is an important issue in the MEF. Simonin *et al.* [123] and Kaufmann [63] suggested a “2+1-equation” approach in which the RUM velocity stress tensor is closed using a viscosity assumption. This approach was *a priori* and *a posteriori* tested in homogeneous and Isotropic turbulence (HIT) [63, 83, 103] and showed a good ability to capture the main statistics of the dispersed phase. However, it failed in configurations with a mean shear [55, 103]. Recently, Masi [78] proposed and *a priori* tested new models for the RUM velocity stress tensor able to cope with mean velocity gradients. The *a posteriori* validation of these models is carried out by Sierra [120].
- **Spray polydispersion.** Vié [145] coupled the Multi-fluid method and the MEF –resulting in the Multi-fluid mesoscopic Eulerian Formalism (MMEF)– to treat evaporating polydispersed sprays. The MMEF inherits of the high computational cost related to the Multi-fluid methods but efficiently tackles the spray polydispersion.
- **Extension of the MEF to non-isothermal flows.** Masi [78] extended the MEF to non-isothermal flows, splitting the particle temperature into two contributions, similarly to the particle velocity. Masi also proposed closure models for the resulting additional term arising in the energy equation, referred to as RUM heat fluxes, and *a priori* tested them with the NTMIX code [14].

However, several issues remain:

- **Numerics.** Because of inertia, particles tend to gather in high shear and low vorticity regions [132], resulting in very steep gradients of particle volume fraction. Since this quantity has to remain positive, specific numerics must be used. Two solutions have been proposed in the context of AVBP: (1) the use of high-order schemes coupled with stabilization techniques [103, 112, 145] and (2) the implementation of more adapted schemes like the PSI scheme [69]. Nevertheless, additional work must be done to characterize and

²<http://pantar.cerfacs.fr/4-26334-The-AVBP-code.php>

refine these numerical strategies. Indeed, they often induce significant numerical diffusion that deteriorates the prediction of particle volume fraction.

- **Modeling of the particle dispersion in mean-sheared configurations.** Most spray injection systems involve a mean gradient of the velocity field. It is thus of paramount importance that the closure of the RUM velocity stress tensor [103, 78] –referred to as “RUM model” in this work– be valid for such configurations. It should be pointed out that heat transfer can not be accurately described if the dynamics of the spray is not properly captured.
- **Modeling of the heat transfer.** The thermal inertia of particles yields an uncorrelated contribution in the heat transfer analog to the RUM for the dynamics. Without proper modeling, this may result in a strong bias in the prediction of mean and fluctuations of particle temperature. This additional contribution is called the *RUM heat flux*.

The objective of the present work is then threefold. First, a robust and accurate numerical strategy must be provided in the context of AVBP that withstands steep particle-volume fraction gradients with a limited numerical diffusion. Then, the issue of the RUM modeling in a configuration with a mean shear will be addressed. One of the new RUM models proposed by Masi [78], and implemented by Sierra [120], will be tested. Once the particle dispersion is sufficiently well described, the final objective of this thesis is the *a posteriori* study of the MEF extended to non-isothermal flows with the implementation of the RUM heat fluxes in AVBP. The objective is to assess the ability of the MEF to accurately account for both dynamic and thermal inertia of particles in turbulent flows with a mean shear.

The manuscript is organized as follows:

- **Part I** presents the general equations, models and numerical strategies used in this work for the numerical simulation of a spray of particles. **Chapter 1** details the derivation of the set of moments with the MEF extended to non isothermal flows. Since several unclosed terms appear in the equations, a few models are proposed and their limitations highlighted. The first chapter ends with a brief description of *a priori* tests carried out by Masi [78]: the existence of an uncorrelated temperature of particles is shown and the impact of the thermal inertia of particle over their temperature variance is studied. Along with a brief presentation of the structure of AVBP, two numerical strategies are proposed in **Chapter 2** to deal with specificities of two-phase flow simulations with an Eulerian approach. A procedure is also suggested to decrease the cost of such approaches. Finally, the various sensors of the stabilization technique –the so-called artificial viscosity (AV)– employed in AVBP are described.
- The numerical strategies proposed in the first part are tested in **Part II** over three academic configurations of increasing complexity (*cf.* Tab. 1). In **Chapter 3**, the one-dimensional convection of a crenel of particle volume-fraction simply illustrates the two issues of numerical instabilities and the transport of steep gradients. It allows a straightforward evaluation of the two numerical strategies. Then, the simulation of a two-dimensional vortex laden with solid particles is performed in **Chapter 4**. This configuration allows to simply illustrate the impact of the dynamic inertia of the particles on their concentration

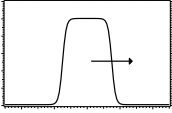


Chap. 3		1D convection of a crenel of particle volume fraction
Chap. 4		2D vortex laden with solid particles
Chap. 5		Homogeneous Isotropic Turbulence laden with solid particles

Table 1: Non-isothermal academic test cases carried out in Part II, summarized by their number of chapter, typical field of particle volume fraction and name

profile and assess the numerical strategies. Moreover, an analytical solution of the particle volume fraction at the center of the vortex is proposed in the limit of small St . The issue of mesh resolution is also addressed with the discrete budget of the particle volume fraction. Finally, the configuration of a particle-laden homogeneous isotropic turbulence (HIT) is carried out in **Chapter 5**. The impact of the convective scheme and AV sensor and the effect of the mesh resolution on the Eulerian simulations are evaluated using two diagnostics: (1) a measurement of preferential concentration and a comparison with Lagrangian results and (2) a discrete balance of the kinetic energy of the dispersed phase. This diagnostic allows to separate explicitly and quantify the dissipations due numerics and due to physics. Part II finally discriminates one numerical strategy that provides both accuracy and robustness.

- **Part III** consists in the *a posteriori* application of the MEF extended to non-isothermal flows, conducted with the numerical strategy defined in the second part. First, the influence of the thermal inertia of the particles is investigated in **Chapter 6** with the two-dimensional configuration of a particle-laden non-isothermal jet (*cf.* Tab. 2). The impact of the RUM model on the dynamics and temperature statistics of the dispersed phase and the coupling with the RUM heat fluxes is investigated for several thermal inertia. Only mesoscopic statistics are compared since uncorrelated variables were not available in this configuration. Eulerian computations are compared to Lagrangian simulations performed by B. Leveugle at CORIA. Finally, the configuration of a three-dimensional non-isothermal jet laden with solid particles is carried out in **Chapter 7**. This last configuration allows a thorough evaluation of the MEF since both mesoscopic and uncorrelated quantities are available. Therefore, the effect of the RUM model and RUM heat fluxes can be investigated with the comparison of high-order moments. In this last configuration, the reference


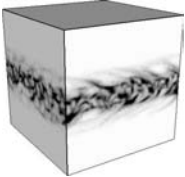
Chap. 6		2D non-isothermal jet laden with solid particles
Chap. 7		3D non-isothermal jet laden with solid particles

Table 2: Non-isothermal application test cases carried out in Part III, summarized by their number of chapter, typical field of particle volume fraction and name

Lagrangian database has been computed by Masi [78] at IMFT.

Note that Part II and Part III may be read independently.

Part I

Equations, models and numerical strategies

Chapter 1

A local Eulerian-Eulerian approach for non-isothermal flows

Contents

1.1	Choice of the approach for the dispersed phase	14
1.2	Lagrangian approach	15
1.2.1	Particle characteristic times	16
1.3	The Mesoscopic Eulerian Formalism - extension to non-isothermal flows	17
1.3.1	Methodology to obtain the MEF set of equations	18
1.3.2	Moments of the mesoscopic variables and governing equation	20
	Definitions	20
	Transport equations	22
1.3.3	Closure of the equations	22
	Momentum equations	22
	RUM models classification	24
	Temperature equation	25
1.3.4	Final set of equations	25
1.3.5	Existence of a correlated and uncorrelated particle temperature	27
1.3.6	Effect of particle inertia on temperature variances	29

The numerical code used in this work is AVBP¹ and has been jointly developed by CERFACS and IFP Energies Nouvelles. The main domain of application has long been the Large Eddy Simulations (LES) of turbulent reacting gaseous flows in complex geometries [11, 116]. However, two-phase flow modeling has been recently considered in several consecutive studies [59, 63, 77, 103, 112, 117, 145]. The present work does not focus on the carrier phase. The reader is referred to the AVBP handbook [15] and to the references cited therein. The governing equations for the fluid are briefly summarized in App. A.

¹<http://pantar.cerfacs.fr/4-26334-The-AVBP-code.php>

This chapter focuses on the description of the dispersed phase. After a brief overview of the existing numerical approaches devoted to the simulation of the dispersed phase in Sec. 1.1, the Mesoscopic Eulerian Formalism [41] is chosen due to its ability to reproduce local and instantaneous features of particles embedded in a turbulent flow. Lagrangian simulations are used in this work as the reference to validate the MEF. The main governing equations are described in Sec. 1.2. Then, the MEF is detailed in Sec. 1.3, with an emphasis on its recent extension to non-isothermal flows [78]. As a first step toward LES, this work considers the transport equations for Direct Numerical Simulations (DNS).

1.1 Choice of the approach for the dispersed phase

The presence of a dispersed phase increases dramatically the complexity of the flow description. While the fluid is generally solved as a continuum with an Eulerian point of view, numerous approaches exist to describe the dispersed phase. None are perfect and they must be considered as complementary. All have their advantages and limitations, depending on the physical characteristics of the configuration. By way of example, Fig. 1.1 presents the range of applicability of these approaches, which is separated in terms of length-scale and timescale, following the work of Elghobashi [34]. This regime map is non exhaustive but illustrates three major key parameters

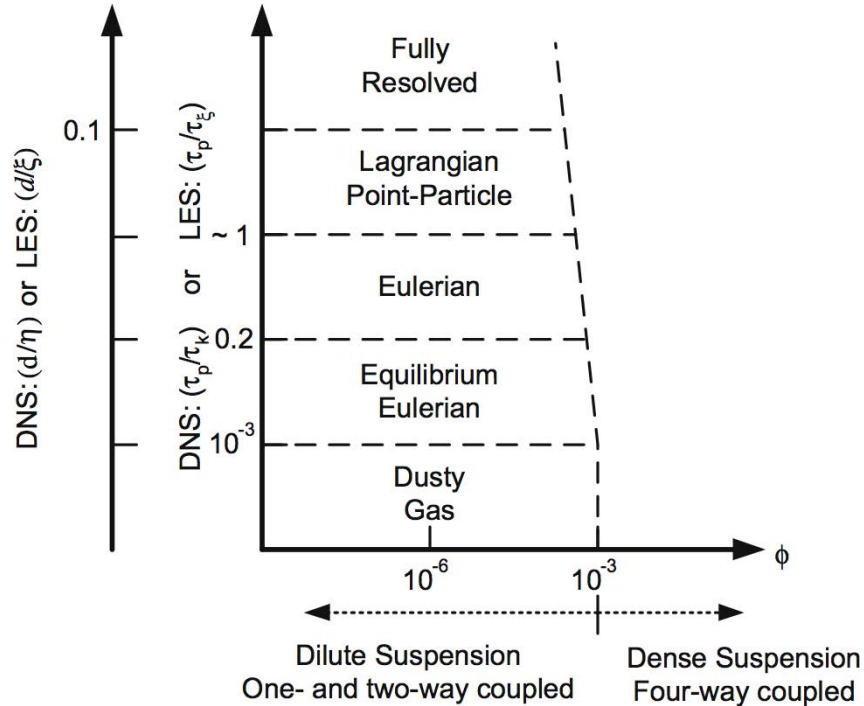


Figure 1.1: Regime map for turbulent particle-laden turbulent flows. Their range of applicability is separated in term of length-scale and timescale. Φ denotes the volume fraction occupied by the dispersed phase, τ_p , τ_k and τ_ξ are the characteristic time of the particles and of the smallest scale of the fluid in DNS and LES, respectively. Excerpted from [8].

in multiphase flows: (1) the particle volume fraction, which determines the coupling between

the carrier and dispersed phase (2) the value of the particle diameters in comparison with the smallest resolved scale and (3) the particle inertia, specified by the time scales of the carrier and dispersed phase. The present work focuses specifically in the point (3), *i.e.* the effect of the particle dynamic and thermal inertia on their statistics. First, the main assumptions relative to the dispersed phase, made in the present work are summarized below:

- H1** - The dispersed phase is diluted (the particle volume fraction $\alpha_p < 0.1\%$) and the fluid volume fraction is $1 - \alpha_p \simeq 1$.
- H2** - Particles are spherical, rigid and non-rotating.
- H3** - Particles are smaller than the smallest turbulent fluid scale.
- H4** - The density ratio between the fluid and the particles is large $\rho_p/\rho_f \gg 1$.
- H5** - There is neither evaporation nor radiative transfer. Only conductive heat transfer is considered.
- H6** - The temperature is uniform inside the particles.
- H7** - The spray is monodisperse.
- H8** - Gravity is negligible.

These assumptions simplify considerably the study of the dispersed phase. For example, **H1** implies that the dispersed phase has no effect on the carrier phase, neither on the momentum nor on the energy equations (*one-way* coupling). Furthermore, we assume that particle-particle interactions are negligible (no collisions). Then, Fig. 1.1 is a good starting point to choose the numerical approach to simulate the dispersed phase.

The dusty gas approach, where particles follow perfectly the fluid, is rejected as it cannot capture important phenomena of particle dispersion such as preferential concentration [132]. The Eulerian Equilibrium approach [37, 39], recently extended to non-isothermal flows [38] would be a good candidate. The major advantage is its low computational cost. Indeed, the particle velocity is expressed as an expansion in terms of the fluid velocity and only the particle number density is transported. The accuracy of this approach was evaluated in forced isotropic turbulence [96] and showed satisfactorily results at small Stokes number regarding the preferential concentration. However, this approach fails for Stokes number - based on the Kolmogorov length scale - close or superior to unity. Then, this approach is not considered in the present work.

An other Eulerian approach, called the Mesoscopic Eulerian Formalism (MEF) extends somewhat the restriction on particle Stokes number [41]. Furthermore, Masi [78] *a priori* investigated the issue of particle thermal inertia in turbulent flows. Thus, the MEF was retained for this work, which can be considered as an *a posteriori* study of this formalism in the context of non-isothermal flows. This formalism is detailed in Sec. 1.3. The Lagrangian approach is briefly described in Sec. 1.2 since it is used as the reference to validate the MEF approach.

1.2 Lagrangian approach

In the Lagrangian framework, particles are tracked individually, integrating the Newton equations of motion and energy. This approach brought some insight on important aspects of turbulent dispersed-phase flows, like the preferential concentration of particles [132, 36], the effect

of turbulence on interphase coupling [148] or turbulence modulation due to the presence of particles [12], among others. This approach is also used to propose closure models for Eulerian formulations [41, 83]. Eulerian quantities are obtained from the Lagrangian simulations by projection on the Eulerian grid. A sufficiently large number of particles is required to provide converged statistics. In their article, Kaufmann *et al.* [65] recommend at least 10 particles and a well-chosen projector to circumvent the intrinsic filtering and statistical error of the projection method. These “true” Eulerian quantities serve as a reference in this work to validate the FEM.

The different forces acting on a single particle (drag, added-mass, history, lift, among others) have been summarized in previous work [41, 63, 103]. As the particle density is much larger than that of the fluid (**H4**), only the drag force acts on the particle motion. Following [81, 43, 4], the governing equations of the motion and temperature of each particles read:

$$\frac{d\mathbf{x}_p}{dt} = \mathbf{u}_p \quad (1.1)$$

$$\frac{d\mathbf{u}_p}{dt} = -\frac{1}{\tau_p}(\mathbf{u}_p - \mathbf{u}_{f@p}) \quad (1.2)$$

$$\frac{dT_p}{dt} = -\frac{1}{\tau_\theta}(T_p - T_{f@p}), \quad (1.3)$$

where \mathbf{x}_p , \mathbf{u}_p and T_p denote the particle position, velocity and temperature, $\mathbf{u}_{f@p}$ and $T_{f@p}$ the undisturbed fluid velocity and temperature at the particle centre location. The dynamic and thermal particle response times, τ_p and τ_θ are defined in Sec. 1.2.1 (*cf.* Eqs. 1.4 and 1.5, respectively).

1.2.1 Particle characteristic times

The general expressions of the microscopic dynamic and thermal relaxation times read:

$$\tau_p = \frac{4\rho_p d_p}{3\rho_f C_D \|\mathbf{u}_p - \mathbf{u}_{f@p}\|} \quad (1.4)$$

$$\tau_\theta = \frac{\text{Pr} \rho_p d_p^2 C_{p,p}}{6\text{Nu} \mu_f C_{p,f}}, \quad (1.5)$$

where d_p and ρ_p stand for the particle diameter and density, ρ_f and μ_f the density and dynamic viscosity of the fluid and $C_{p,p}$ and $C_{p,f}$ denote the particle and fluid heat capacities.

These definitions account for non-linearities of external forces and heat exchange where C_D and Nu are the corrected drag coefficient [115] and corrected Nusselt number [97],

$$C_D = \frac{24}{\text{Re}_p} (1 + 0.15 \text{Re}_p^{2/3}) \quad (1.6)$$

$$\text{Nu} = 2 + 0.55 \text{Re}_p^{1/2} \text{Pr}^{1/3}. \quad (1.7)$$

Both C_D and Nu depend on the particle Reynolds number Re_p , defined as:

$$\text{Re}_p = \frac{d_p \|\mathbf{u}_p - \mathbf{u}_f @ p\|}{\nu_f}, \quad (1.8)$$

where ν_f is the kinematic viscosity of the fluid.

In the Stokes' regime ($\text{Re}_p \ll 1$), the two characteristic times can be simplified as:

$$\tau_p = \frac{\rho_p d_p^2}{18\mu_f} \quad (1.9)$$

$$\tau_\theta = \frac{\text{Pr} \rho_p d_p^2 C_{p,p}}{12\mu_f C_{p,f}} = \frac{3}{2} \text{Pr} \alpha \tau_p, \quad (1.10)$$

where $\alpha = C_{p,p}/C_{p,f}$ is the particle-to-fluid heat capacity ratio. Note that τ_θ depends linearly on τ_p . In other words, the particle dynamic inertia directly impacts the thermal inertia. This issue is tackled in Sec. 1.3.6.

Dynamic inertia of particles is characterized by the dynamic Stokes number², defined as the ratio of the particle and fluid characteristic time:

$$\text{St} = \frac{\tau_p}{\tau_f}. \quad (1.11)$$

The definition of a fluid characteristic time τ_f can be somewhat ambiguous depending on the configuration [5]. In the present work, τ_f will be defined for each configuration. One may then define the thermal Stokes number as

$$\text{St}_\theta = \frac{\tau_\theta}{\tau_f}, \quad (1.12)$$

Here, we assume that the fluid characteristic time of motion and heat exchange are the same [23].

1.3 The Mesoscopic Eulerian Formalism - extension to non-isothermal flows

Large particle inertia is a major issue for Eulerian formalisms. Unity Stokes number defines a threshold from where the Eulerian approaches based on the monokinetic assumption no longer capture the accurate motion of particles. The MEF [41, 121] extends somewhat this limitation. The cornerstone of this formalism is the splitting of the particle velocity in two components (*cf.* Fig. 2): (1) a mesoscopic velocity, shared by all the particles and spatially correlated and (2) an uncorrelated component, called the Random Uncorrelated Motion (RUM) velocity³.

$$u_{p,i}(t) = \tilde{u}_{p,i}(\mathbf{x}_p(t), t) + \delta u_{p,i}(t), \quad (1.13)$$

where $\tilde{u}_{p,i}$ stands for the mesoscopic velocity and $\delta u_{p,i}$ the RUM velocity. From hereafter, mesoscopic and RUM attributes will refer to the correlated and uncorrelated part, respectively

²In the literature, the Stokes number often refers to the dynamic Stokes number. The issue of particle thermal inertia is recent. In this thesis, the ‘‘dynamic’’ attribute will sometimes be dropped when there is no ambiguity with the thermal Stokes number.

³The RUM has been previously denoted the Quasi-Brownian motion [41], due to the random character of the RUM. This denomination is not used in the present work.

denoted by a $\tilde{\cdot}$ and a δ . Note that the definition in Eq. 1.13 is Lagrangian since the particle is followed along its trajectory $\mathbf{x}_p(t)$.

1.3.1 Methodology to obtain the MEF set of equations

Fig. 1.2 presents the different steps to derive the equations for the MEF. It encapsulates the work of Février [40] and Simonin [122] but also includes the recent extension of the MEF to non-isothermal flows by Masi [78]. Actually, this methodology can be applied to any kind of physics (evaporation, combustion, etc..) as it is an analogy of the kinetic theory of non-uniform gases [17, 98]. This section summarizes previous works [69, 78, 103].

1. The first step is the choice of an appropriate refined-grid PDF $W_p^{(k)}$ [98], which depends on the physical properties (*i.e.* phase space) taken into account. In this work, $W_p^{(k)}$ is built from a combination of Dirac functions δ :

$$W_p^{(k)}(\mathbf{x}, \mathbf{c}_p, \xi_p, t) = \delta(\mathbf{x} - \mathbf{x}_p^{(k)})\delta(\mathbf{c}_p - \mathbf{u}_p^{(k)})\delta(\xi_p - T_p^{(k)}). \quad (1.14)$$

The function $W_p^{(k)}$ equals unity if a particle k has its center of mass at position $\mathbf{x}_p = \mathbf{x}$, with a velocity $\mathbf{u}_p = \mathbf{c}_p$ and a temperature $T_p = \xi_p$, and zero otherwise. Conceptually, there are no limitations of the particle properties of the refined-grid PDF. For example, the particle-mass phase space must be considered when evaporation is dealt with [80].

2. The novelty of the MEF is the specific ensemble averaging of $W_p^{(k)}$. For a given fluid realization \mathcal{H}_f , the one-particle conditional PDF $\tilde{f}_p^{(1)}$ is defined as the ensemble average over a large number N_p of particle realizations \mathcal{H}_p , slightly differing in initial conditions:

$$\tilde{f}_p^{(1)}(\mathbf{x}, \mathbf{c}_p, \xi_p, t; \mathcal{H}_f) = \lim_{N_p \rightarrow \infty} \left[\frac{1}{N_p} \sum_{\mathcal{H}_p} \sum_{k=1}^{N_p} W_p^{(k)}(\mathbf{x}, \mathbf{c}_p, \xi_p, t; \mathcal{H}_p | \mathcal{H}_f) \right], \quad (1.15)$$

where N_p is the (fixed) number of particles in any realization. This procedure requires that \mathcal{H}_f was not modified by the particle realizations, fulfilled by the assumption of diluted dispersed phase (**H1**, Sec. 1.1).

3. By analogy with the kinetic theory of non-uniform gases [17, 98], the transport equation of the one-point conditional PDF is obtained with a Boltzmann-like equation:

$$\frac{\partial \tilde{f}_p^{(1)}}{\partial t} + \frac{\partial}{\partial x_j} \left[c_{p,j} \tilde{f}_p^{(1)} \right] = - \frac{\partial}{\partial c_{p,j}} \left[\frac{du_{p,j}}{dt} \tilde{f}_p^{(1)} \right] - \frac{\partial}{\partial \xi_p} \left[\frac{dT_p}{dt} \tilde{f}_p^{(1)} \right] + \left(\frac{\partial \tilde{f}_p^{(1)}}{\partial t} \right)_{coll} \quad (1.16)$$

The first and second term of the RHS stand for the effect of external forces and heat transfer acting on the particle, respectively. The last term accounts for particle interaction (collisions, coalescence, break-up, etc..).

4. The Enskog equation is obtained by multiplying Eq. 1.16 by a test function $\psi(\mathbf{c}_p, \xi_p)$ and then applying a mesoscopic average operator.

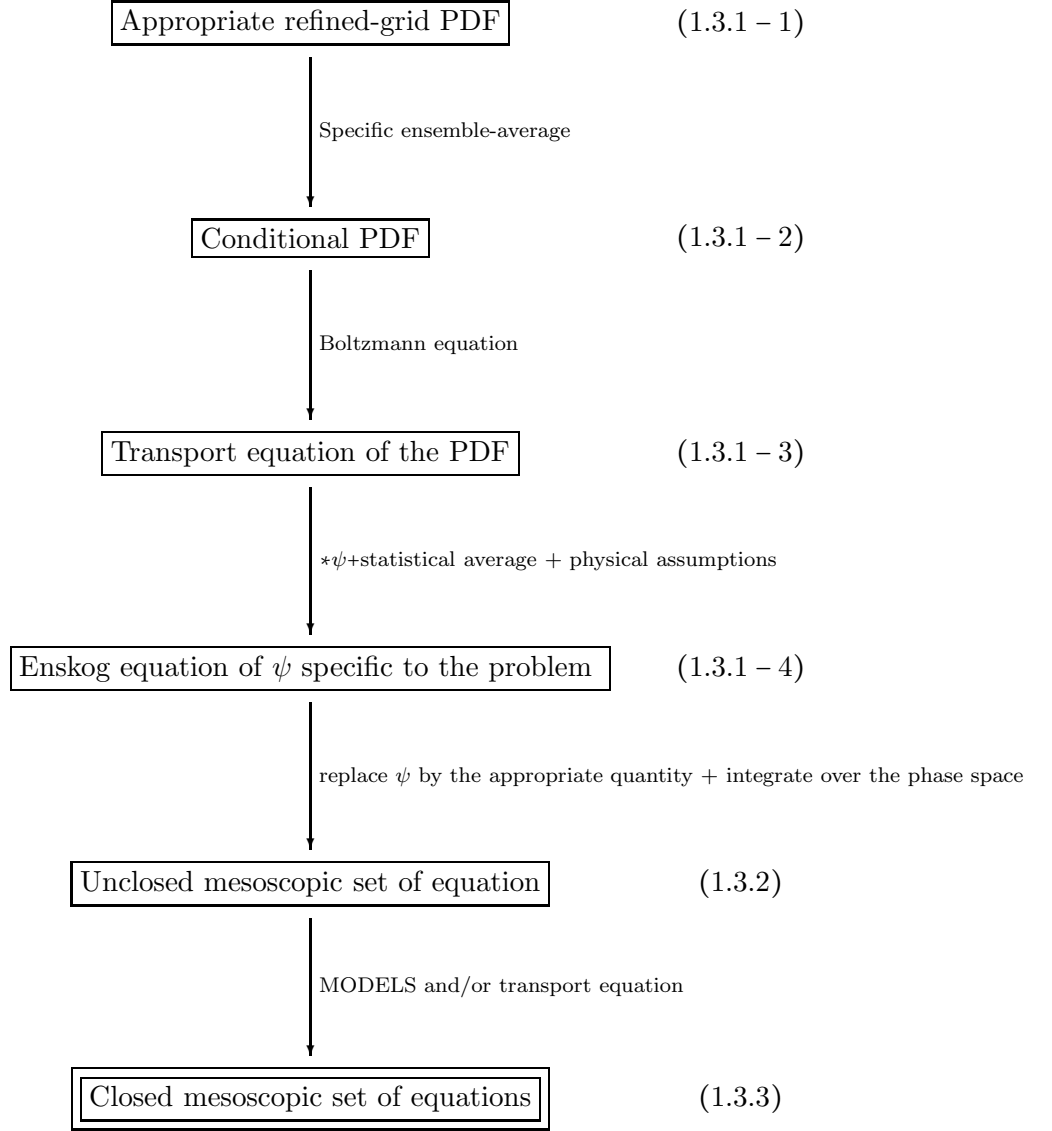


Figure 1.2: General methodology to derive the moment approach using the MEF. Labels at the right correspond to the section number where more details can be found.

The mesoscopic average of any function $\psi(\mathbf{c}_p, \xi_p)$ yields the mesoscopic quantity $\tilde{g}_p(\mathbf{x}, t)$ by integration over the phase space:

$$\tilde{g}_p(\mathbf{x}, t) = \frac{1}{\tilde{n}_p(\mathbf{x}, t)} \int \psi(\mathbf{c}_p, \xi_p) \tilde{f}_p^{(1)}(\mathbf{x}, \mathbf{c}_p, \xi_p, t | \mathcal{H}_f) d\mathbf{c}_p d\xi_p, \quad (1.17)$$

where \tilde{n}_p is the particle number density:

$$\tilde{n}_p = \int \tilde{f}_p^{(1)}(\mathbf{x}, \mathbf{c}_p, \xi_p, t | \mathcal{H}_f) d\mathbf{c}_p d\xi_p. \quad (1.18)$$

The ensemble average operator is hereafter denoted

$$\langle g_p(t) \rangle_c = \tilde{g}_p(\mathbf{x}, t) = \langle g_p(t) | \mathbf{x}_p(t) = \mathbf{x}; \mathcal{H}_f \rangle, \quad (1.19)$$

and represents the ensemble average of $g_p(t)$ over a large number of particle realization for a given fluid realization \mathcal{H}_f .

The uncorrelated component of the quantity $g_p(\mathbf{x}, t)$ is defined as

$$\delta g_p(t) = g_p(t) - \tilde{g}_p(\mathbf{x}(t), t) \quad (1.20)$$

Applying this operator on Eq. 1.16 yields the Enskog equation for a quantity ψ :

$$\frac{\partial}{\partial t} \tilde{n}_p \langle \psi \rangle_c + \frac{\partial}{\partial x_j} \tilde{n}_p \langle u_{p,j} \psi \rangle_c = \tilde{n}_p \left\langle \frac{du_{p,j}}{dt} \frac{\partial \psi}{\partial c_{p,j}} \right\rangle_c + \tilde{n}_p \left\langle \frac{dT_p}{dt} \frac{\partial \psi}{\partial \xi_p} \right\rangle_c + \mathbb{C}(\tilde{n}_p \psi) \quad (1.21)$$

The term $\mathbb{C}(\tilde{n}_p \psi)$ stands for the modification of $\tilde{n}_p \psi$ due to particle collisions. The first two RHS terms are closed using the same hypothesis than with Lagrangian equations in Sec. 1.2. In our work, only the drag force and heat transfer are taken into account. Finally, the Enskog equation under the hypothesis of Sec.1.1 reduces to:

$$\frac{\partial}{\partial t} \tilde{n}_p \langle \psi \rangle_c + \frac{\partial}{\partial x_j} \tilde{n}_p \langle u_{p,j} \psi \rangle_c = -\frac{\tilde{n}_p}{\tilde{\tau}_p} \left\langle (\mathbf{u}_p - \mathbf{u}_{f@p}) \frac{\partial \psi}{\partial c_{p,j}} \right\rangle_c - \frac{\tilde{n}_p}{\tilde{\tau}_\theta} \left\langle (T_p - T_{f@p}) \frac{\partial \psi}{\partial \xi_p} \right\rangle_c, \quad (1.22)$$

where $\tilde{\tau}_p$ and $\tilde{\tau}_\theta$ are the mesoscopic thermal and dynamic relaxation times, accounting for non linearities and external forces.

$$\tilde{\tau}_p = \left\langle \frac{1}{\tau_p} \right\rangle_c^{-1} \quad (1.23)$$

$$\tilde{\tau}_\theta = \left\langle \frac{1}{\tau_\theta} \right\rangle_c^{-1}. \quad (1.24)$$

In this study, most of the simulations are carried out in regime of Stokes where

$$\tilde{\tau}_p \simeq \tau_p \quad (1.25)$$

$$\tilde{\tau}_\theta \simeq \tau_\theta. \quad (1.26)$$

Consequently, the notation τ_p or τ_θ will be often used in the manuscript.

1.3.2 Moments of the mesoscopic variables and governing equation

Definitions

Simonin [122] and Février *et al.* [41] defined the first moments of the PDF, relative to the particle motion:

- The particle number density \tilde{n}_p , already defined in Eq. 1.18.
- The mesoscopic particle velocity:

$$\tilde{u}_{p,j}(\mathbf{x}, t) = \langle u_{p,j}(t) \rangle_c = \frac{1}{\tilde{n}_p} \int c_{p,j} \tilde{f}_p^{(1)}(\mathbf{x}, \mathbf{c}_p, \xi_p, t | \mathcal{H}_f) d\mathbf{c}_p d\xi_p \quad (1.27)$$

- The RUM velocity stress tensor:

$$\delta R_{p,ij}(\mathbf{x}, t) = \langle \delta u_{p,i}(t) \delta u_{p,j}(t) \rangle_c = \frac{1}{\tilde{n}_p} \int [c_{p,i} - \tilde{u}_{p,i}] [c_{p,j} - \tilde{u}_{p,j}] \tilde{f}_p^{(1)}(\mathbf{x}, \mathbf{c}_p, \xi_p, t | \mathcal{H}_f) d\mathbf{c}_p d\xi_p \quad (1.28)$$

- The RUM kinetic energy⁴ is defined as half the trace of $\delta R_{p,ij}$:

$$\delta \theta_p(\mathbf{x}, t) = \frac{1}{2} \delta R_{p,kk} = \frac{1}{2} \langle \delta u_{p,k}(t) \delta u_{p,k}(t) \rangle_c \quad (1.29)$$

- The RUM velocity third order moment:

$$\delta Q_{p,ijk}(\mathbf{x}, t) = \langle \delta u_{p,i}(t) \delta u_{p,j}(t) \delta u_{p,k}(t) \rangle_c \quad (1.30)$$

Masi [78] wrote the moments of the PDF relative to the particle temperature:

- The mesoscopic particle temperature:

$$\tilde{T}_p(\mathbf{x}, t) = \langle T_p(t) \rangle_c = \frac{1}{\tilde{n}_p} \int \xi_p \tilde{f}_p^{(1)}(\mathbf{x}, \mathbf{c}_p, \xi_p, t | \mathcal{H}_f) d\mathbf{c}_p d\xi_p \quad (1.31)$$

- The RUM heat flux:

$$\delta \Theta_{p,i}(\mathbf{x}, t) = \langle \delta u_{p,i}(t) \delta T_p(t) \rangle_c \quad (1.32)$$

- The RUM temperature variance:

$$\delta \theta_\theta(\mathbf{x}, t) = \frac{1}{2} \langle \delta T_p(t) \delta T_p(t) \rangle_c \quad (1.33)$$

- The third order moments accounting for the correlations between the RUM velocity and temperature:

$$\delta \Omega_{p,i}(\mathbf{x}, t) = \langle \delta u_{p,i}(t) \delta T_p(t) \delta T_p(t) \rangle_c \quad (1.34)$$

$$\delta \Delta_{p,ij}(\mathbf{x}, t) = \langle \delta u_{p,i}(t) \delta u_{p,j}(t) \delta T_p(t) \rangle_c \quad (1.35)$$

The transport equations of the mesoscopic moments are obtained by replacing ψ in Eq. 1.22 by the appropriate function and integrating over the phase space. The details of the derivation are not presented and can be found in [122].

⁴Also called Random Uncorrelated Energy (RUE) [63, 103]

Transport equations

The transport equations of the particle number density, momentum, RUM stress tensor, particle mesoscopic temperature and RUM heat fluxes read:

$$\frac{\partial \tilde{n}_p}{\partial t} + \frac{\partial}{\partial x_j} \tilde{n}_p \tilde{u}_{p,i} = 0 \quad (1.36)$$

$$\frac{\partial}{\partial t} \tilde{n}_p \tilde{u}_{p,i} + \frac{\partial}{\partial x_j} \tilde{n}_p \tilde{u}_{p,i} \tilde{u}_{p,j} = -\frac{\tilde{n}_p}{\tilde{\tau}_p} (\tilde{u}_{p,i} - u_{f,i}) - \boxed{\frac{\partial}{\partial x_j} \tilde{n}_p \delta R_{p,ij}} \quad (1.37)$$

$$\begin{aligned} \frac{\partial}{\partial t} \tilde{n}_p \delta R_{p,ij} + \frac{\partial}{\partial x_j} \tilde{n}_p \delta R_{p,ij} \tilde{u}_{p,j} &= -2 \frac{\tilde{n}_p}{\tilde{\tau}_p} \delta R_{p,ij} - \tilde{n}_p \delta R_{p,kj} \frac{\partial \tilde{u}_{p,i}}{\partial x_k} \quad \dots \\ &\dots - \tilde{n}_p \delta R_{p,ik} \frac{\partial \tilde{u}_{p,j}}{\partial x_k} - \frac{\partial}{\partial x_k} \tilde{n}_p \delta Q_{p,ijk} \end{aligned} \quad (1.38)$$

$$\frac{\partial}{\partial t} \tilde{n}_p C_{p,p} \tilde{T}_p + \frac{\partial}{\partial x_j} \tilde{n}_p C_{p,p} \tilde{u}_{p,j} \tilde{T}_p = -\frac{\tilde{n}_p C_{p,p}}{\tilde{\tau}_\theta} (\tilde{T}_p - T_f) - \boxed{\frac{\partial}{\partial x_j} \tilde{n}_p C_{p,p} \delta \Theta_{p,j}} \quad (1.39)$$

$$\begin{aligned} \frac{\partial}{\partial t} \tilde{n}_p C_{p,p} \delta \Theta_{p,i} + \frac{\partial}{\partial x_j} \tilde{n}_p C_{p,p} \tilde{u}_{p,j} \delta \Theta_{p,i} &= -\tilde{n}_p C_{p,p} \left(\frac{1}{\tilde{\tau}_p} + \frac{1}{\tilde{\tau}_\theta} \right) \delta \Theta_{p,i} - \tilde{n}_p C_{p,p} \delta \Theta_{p,j} \frac{\partial \tilde{u}_{p,i}}{\partial x_j} \\ &\quad - \tilde{n}_p C_{p,p} \delta R_{p,ij} \frac{\partial \tilde{T}_p}{\partial x_j} - \frac{\partial}{\partial x_j} \tilde{n}_p C_{p,p} \delta \Delta_{p,ij}, \end{aligned} \quad (1.40)$$

The first terms of the RHS of Eq. 1.37 and Eq. 1.39 represent the inter-phase coupling by drag and heat exchange, respectively. These terms are present in any Eulerian formalism of non-isothermal two-phase flows. The originality of the MEF lies in the presence of second-order terms in Eq. 1.37 and Eq. 1.39, highlighted by boxed frames. They represent the transport of the mesoscopic velocity and temperature by the RUM velocity stress tensor and RUM heat fluxes (RUM-HF), respectively (*cf.* Eqs. 1.38 and 1.40). The novelty of this work is the transport of the particle temperature by the RUM-HF, and most of all its possible impact on particle temperature statistics.

1.3.3 Closure of the equations

The system of equations Eq. 1.36-1.40 is not closed. Every moment of n^{th} -order depends of the $n+1^{th}$ order moment. Then, assumptions must be made to close this set of equations.

Momentum equations

The modeling of the RUM velocity stress tensor has been the center of attention of many consecutive studies since Février proposed the MEF [41]. It can be considered as the major bottleneck of the MEF.

A “2+1-equations” approach was suggested [123, 65] in which the RUM velocity stress tensor is splitted into a deviatoric and a spherical part, accounting for the RUM kinetic energy:

$$\delta R_{p,ij} = \underbrace{\delta R_{p,ij}^*}_{\text{modeled}} + \frac{2}{3} \underbrace{\delta \theta_p}_{\text{solved}} \delta_{ij}, \quad (1.41)$$

where the deviatoric part $\delta R_{p,ij}^*$ is modeled while a transport equation is solved for the RUM kinetic energy. The evolution equation for $\delta\theta_p$ is obtained by taking half the trace of Eq. 1.38:

$$\frac{\partial}{\partial t} \tilde{n}_p \delta\theta_p + \frac{\partial}{\partial x_j} \tilde{n}_p \delta\theta_p \tilde{u}_{p,j} = -2 \frac{\tilde{n}_p}{\tilde{\tau}_p} \delta\theta_p - \tilde{n}_p \delta R_{p,ij} \frac{\partial \tilde{u}_{p,i}}{\partial x_j} - \frac{1}{2} \frac{\partial}{\partial x_j} \delta Q_{p,ij}. \quad (1.42)$$

The spherical and deviatoric parts of $\delta R_{p,ij}$ are analogous to the pressure and viscous contribution in the kinetic theory of gases, respectively.

The last term to model in Eq. 1.42 is the third-order RUM velocity correlation. Kaufmann [63] proposed to model $\delta Q_{p,ij}$ by analogy with the Fick's law for the fluid temperature:

$$\frac{1}{2} \delta Q_{p,ij} = -\kappa_{\text{RUM}} \frac{\partial}{\partial x_j} \delta\theta_p, \quad (1.43)$$

where κ_{RUM} is a diffusive coefficient [121] modeled in analogy with :

$$\kappa_{\text{RUM}} = \frac{10}{27} \tilde{\tau}_p \delta\theta_p. \quad (1.44)$$

The transport equation of the RUM kinetic energy is then closed. Therefore, the remaining modeling effort are for the deviatoric part of the RUM velocity stress tensor $\delta R_{p,ij}^*$. Hereafter, the closure equation of $\delta R_{p,ij}^*$ will be referred as ‘‘RUM model’’

In this work, two RUM models will be used, denoted VISCO and AXISY-C, proposed by [63, 78] and implemented in AVBP by Sierra [120]. The VISCO model is one of those proposed by Simonin *et al.* [123] and Kaufmann *et al.* [65], summarized by Riber [103]. It is a viscosity model where $\delta R_{p,ij}^*$ and the rate of strain tensor $S_{p,ij}^*$ are linearly related by an eddy-viscosity:

$$\delta R_{p,ij}^* = -2\nu_{\text{RUM}} S_{p,ij}^* \quad (1.45)$$

$$S_{p,ij}^* = \frac{1}{2} \left[\frac{\partial \tilde{u}_{p,i}}{\partial x_j} + \frac{\partial \tilde{u}_{p,j}}{\partial x_i} - \frac{2}{3} \frac{\partial \tilde{u}_{p,k}}{\partial x_k} \delta_{ij} \right], \quad (1.46)$$

where the particle uncorrelated viscosity ν_{RUM} uses the particle relaxation time as a typical timescale:

$$\nu_{\text{RUM}} = \frac{\tilde{\tau}_p \delta\theta_p}{3}. \quad (1.47)$$

This model assumes the equilibrium and light anisotropy of $\delta R_{p,ij}$. It was *a priori* [83] and *a posteriori* [63, 103] tested in a particle-laden HIT, providing satisfactory results at moderate Stokes numbers (up to $\text{St}_K \sim 2.2$). However, it failed in mean-sheared turbulent particle-laden configurations [55, 103]. Unfortunately, the majority of industrial applications involve mean-sheared flows. In this form, the RUM model limits the MEF in this type of configuration.

The AXISY-C model has been proposed by Masi [78, 79]. In this model,

$$\delta R_{p,ij}^* = \text{sign}(III_s) \left(\frac{2}{3} \right)^{1/2} 2\delta\theta_p \frac{S_{p,ij}^*}{S}, \quad (1.48)$$

where $S = \sqrt{II_s}$ and III_s are the square root of the second invariant II_s and the third invariant of $S_{p,ij}^*$, respectively. To put it in a nutshell, AXISY-C and VISCO are both viscosity models with a

linear relationship between $\delta R_{p,ij}^*$ and the rate-of-strain tensor. They differ by their characteristic time scale, the assumption made on the structure of $\delta R_{p,ij}^*$ and their ability to reproduce reverse energy exchange between the RUM and mesoscopic motion. Their main characteristics are recalled in Tab. 1.1. The next section summarizes some of the main observations done by Masi,

	VISCO	AXISY-C
Definition	$\delta R_{p,ij}^* = -\frac{2}{3}\tilde{\tau}_p\delta\theta_p S_{p,ij}^*$	$\delta R_{p,ij}^* = \text{sign}(III_s)\left(\frac{2}{3}\right)^{1/2} 2\delta\theta_p \frac{S_{p,ij}^*}{S}$
Time scale	$\tilde{\tau}_p$	S^{-1}
Assumed structure of $\delta R_{p,ij}^*$	Light anisotropy Local equilibrium	Axisymmetry One-component state
Relation between $\delta R_{p,ij}^*$ and $S_{p,ij}^*$	Linear	Linear
Reverse energy exchange	No	Yes

Table 1.1: Main characteristics of VISCO and AXISY-C RUM models

from an *a priori* study [78] of the RUM model in an academic configuration with a mean-shear [143].

RUM models classification

Masi [78] raised three important issues:

1. **The typical timescale used by the RUM models.** One fundamental assumption of VISCO is that the particle motion adjusts quickly to any change due to the local strain. This assumption is broken when the ratio of the particle relaxation time and the mesoscopic-shear timescale is large, $\tilde{\tau}_p \mathcal{S} \gg 1$. Then, the use of $\tilde{\tau}_p$ as the typical timescale, like in VISCO, is controversial. The magnitude of the rate-of-strain tensor, seems more relevant and “inertial-free” than $\tilde{\tau}_p$ for RUM models .
2. **The type of relationship between $\delta R_{p,ij}^*$ and the rate of strain tensor (linear/non-linear).** The study of the structure and alignment of $\delta R_{p,ij}^*$ and $S_{p,ij}^*$ in mean-sheared configuration yields the following conclusions:
 - the tensors $\delta R_{p,ij}^*$ and $S_{p,ij}^*$ behave in axisymmetric contraction and expansion, respectively, independently of the particle inertia. In other words, the RUM agitation develops in one preferred direction while it is damped in the other.
 - $\delta R_{p,ij}^*$ behaves as in one-component limit state.
 - $\delta R_{p,ij}^*$ and $S_{p,ij}^*$ are not aligned.

Thus, the assumption of light anisotropy of $\delta R_{p,ij}^*$ made for VISCO is questionable. Masi proposed a new viscosity-like model based on these observations, which accounts for the axisymmetry and preferred direction of $\delta R_{p,ij}^*$, denoted AXISY. The non-alignment of $\delta R_{p,ij}^*$ and $S_{p,ij}^*$ makes the hypothesis of linear relationship questionable.

3. **The ability to reproduce reverse energy exchange.** One key feature of the MEF is the local exchange of kinetic energy between the mesoscopic and the RUM motion. This exchange occurs in both ways, from mesoscopic to RUM and vice-versa, acting as a dissipation/production term in the equations of mesoscopic and RUM kinetic energy [78]. The ability to reproduce the reverse energy exchange is thus of paramount importance to have good levels of mean dissipation rate. The viscosity-like models VISCO and AXISY showed their inability to reproduce the reverse energy exchange. Masi remarked that the sign of the third invariant of the rate-of-strain tensor, $\text{sign}(III_S)$, could be used to account for this reverse energy exchange. Thus, $\text{sign}(III_S)$ is used as a “correction” for AXISY, denoted “AXISY-C”.

More complex models, like the non-linear models, may be better to account for the non-alignment between $\delta R_{p,ij}^*$ and $S_{p,ij}^*$. However, only VISCO and AXISY-C are used in this work, the focus being on thermal dispersion of the particles. The idea is to have a sufficiently good dynamics of the particles in order to study the impact of the RUM-HF term. Please refer to [78] and [120] for the *a priori* and *a posteriori* study of the non-linear RUM models, respectively.

With this, Eq. 1.37 is closed so the last contribution to model is the RUM-heat fluxes $\delta\Theta_{p,i}$ in Eq. 1.39.

Temperature equation

As a first approach, it was decided to use as little additional modeling as possible for $\delta\Theta_{p,i}$. Consequently, we opted for a resolution of the conservation equations for $\delta\Theta_{p,i}$ derived by Masi [78], Eq. 1.40 is recalled here for the sake of clarity:

$$\begin{aligned} \frac{\partial}{\partial t} \tilde{n}_p C_{p,p} \delta\Theta_{p,i} + \frac{\partial}{\partial x_j} \tilde{n}_p C_{p,p} \tilde{u}_{p,j} \delta\Theta_{p,i} &= -\tilde{n}_p C_{p,p} \left(\frac{1}{\tilde{\tau}_p} + \frac{1}{\tilde{\tau}_\theta} \right) \delta\Theta_{p,i} - \tilde{n}_p C_{p,p} \delta\Theta_{p,j} \frac{\partial \tilde{u}_{p,i}}{\partial x_j} \\ &\quad - \tilde{n}_p C_{p,p} \delta R_{p,ij} \frac{\partial \tilde{T}_p}{\partial x_j} - \frac{\partial}{\partial x_j} \tilde{n}_p C_{p,p} \delta \Delta_{p,ij}. \end{aligned} \quad (1.49)$$

The first RHS term of Eq. 1.49 represents the dissipation of the RUM-HF by particle inertia. The second and third RHS terms represent the production by the mesoscopic velocity and temperature gradients. The fourth term accounts for the diffusion by third-order moments. In the present work, $\delta \Delta_{p,ij}$ is neglected. This last assumption is solely based on pragmatism as we do not yet have models available for this term.

Note that the RUM velocity stress tensor appears in the third RHS term of Eq. 1.49. Thus, the RUM model has an impact on the RUM-HF.

1.3.4 Final set of equations

Therefore, the final set of equations used in this work is:

$$\frac{\partial \tilde{n}_p}{\partial t} + \frac{\partial}{\partial x_j} \tilde{n}_p \tilde{u}_{p,i} = 0 \quad (1.50)$$

$$\begin{aligned} \frac{\partial}{\partial t} \tilde{n}_p \tilde{u}_{p,i} + \frac{\partial}{\partial x_j} \tilde{n}_p \tilde{u}_{p,i} \tilde{u}_{p,j} &= -\frac{\tilde{n}_p}{\tilde{\tau}_p} (\tilde{u}_{p,i} - u_{f,i}) - \frac{\partial}{\partial x_j} \tilde{n}_p \delta R_{p,ij} \\ &\quad - \frac{2}{3} \frac{\partial}{\partial x_i} \tilde{n}_p \delta \theta_p \end{aligned} \quad (1.51)$$

$$\begin{aligned} \frac{\partial}{\partial t} \tilde{n}_p \delta \theta_p + \frac{\partial}{\partial x_j} \tilde{n}_p \delta \theta_p \tilde{u}_{p,j} &= -2 \frac{\tilde{n}_p}{\tilde{\tau}_p} \delta \theta_p - \tilde{n}_p \delta R_{p,ij} \frac{\partial \tilde{u}_{p,i}}{\partial x_j} \\ &\quad - \frac{1}{2} \frac{\partial}{\partial x_j} \delta Q_{p,ij} \end{aligned} \quad (1.52)$$

$$\frac{\partial}{\partial t} \tilde{n}_p C_{p,p} \tilde{T}_p + \frac{\partial}{\partial x_j} \tilde{n}_p C_{p,p} \tilde{u}_{p,j} \tilde{T}_p = -\frac{\tilde{n}_p C_{p,p}}{\tilde{\tau}_\theta} (\tilde{T}_p - T_f) - \frac{\partial}{\partial x_j} \tilde{n}_p C_{p,p} \delta \Theta_{p,j} \quad (1.53)$$

$$\begin{aligned} \frac{\partial}{\partial t} \tilde{n}_p C_{p,p} \delta \Theta_{p,i} + \frac{\partial}{\partial x_j} \tilde{n}_p C_{p,p} \tilde{u}_{p,j} \delta \Theta_{p,i} &= -\tilde{n}_p C_{p,p} \left(\frac{1}{\tilde{\tau}_p} + \frac{1}{\tilde{\tau}_\theta} \right) \delta \Theta_{p,i} - \tilde{n}_p C_{p,p} \delta \Theta_{p,j} \frac{\partial \tilde{u}_{p,i}}{\partial x_j} \\ &\quad - \tilde{n}_p C_{p,p} \delta R_{p,ij} \frac{\partial \tilde{T}_p}{\partial x_j} \end{aligned} \quad (1.54)$$

As for the fluid (*cf.* App. A), this set of equations can be written in compact form

$$\frac{\partial \mathbf{U}_p}{\partial t} + \vec{\nabla} \cdot \vec{\mathcal{F}}(\mathbf{U}_p) = \mathbf{S}_p, \quad (1.55)$$

where $\mathbf{U}_p = (\tilde{n}_p, \tilde{n}_p \tilde{u}_{p,i}, \tilde{n}_p \delta \theta_p, \tilde{n}_p C_{p,p} \tilde{T}_p, \tilde{n}_p C_{p,p} \delta \Theta_{p,i})^T$ is the vector of conservative variables of the dispersed phase. $\vec{\mathcal{F}}$ and \mathbf{S}_p are the flux and source terms vector of the dispersed phase. The flux vector can be decomposed into a convective and a viscous component:

$$\vec{\mathcal{F}}(\mathbf{U}_p) = \vec{\mathcal{F}}_p^C(\mathbf{U}_p) + \vec{\mathcal{F}}_p^V(\mathbf{U}_p, \vec{\nabla} \mathbf{U}_p), \quad (1.56)$$

where $\vec{\mathcal{F}}_p^C$ corresponds to the convective flux (only depends of \mathbf{U}_p) and $\vec{\mathcal{F}}_p^V$ denotes the viscous fluxes (depends also of $\vec{\nabla} \mathbf{U}_p$).

These two flux vectors read

$$\vec{\mathcal{F}}_p^C = \begin{pmatrix} \tilde{n}_p \tilde{u}_{p,i} \\ \tilde{n}_p \tilde{u}_{p,i} \tilde{u}_{p,j} + \frac{2}{3} \tilde{n}_p \delta \theta_p \delta_{ij} \\ \tilde{n}_p \delta \theta_p \tilde{u}_{p,j} \\ \tilde{n}_p C_{p,p} \tilde{T}_p \tilde{u}_{p,j} \\ \tilde{n}_p C_{p,p} \delta \Theta_{p,i} \tilde{u}_{p,j} \end{pmatrix} \quad (1.57)$$

$$\vec{\mathcal{F}}_p^V = \begin{pmatrix} 0 \\ \tilde{n}_p \delta R_{p,ij} \\ \frac{1}{2} \delta Q_{p,ij} \\ \tilde{n}_p C_{p,p} \delta \Theta_{p,j} \\ 0 \end{pmatrix}. \quad (1.58)$$

Moreover, the source terms vector reads

$$\mathbf{S}_p = \begin{pmatrix} 0 \\ -\frac{\tilde{n}_p}{\tilde{\tau}_p}(\tilde{u}_{p,i} - u_{f,i}) \\ -2\frac{\tilde{n}_p}{\tilde{\tau}_p}\delta\theta_p - \tilde{n}_p\delta R_{p,ij}\frac{\partial\tilde{u}_{p,i}}{\partial x_j} \\ -\frac{\tilde{n}_p C_{p,p}}{\tilde{\tau}_\theta}(\tilde{T}_p - T_f) \\ -\tilde{n}_p C_{p,p} \left[\left(\frac{1}{\tilde{\tau}_p} + \frac{1}{\tilde{\tau}_\theta} \right) \delta\Theta_{p,i} + \delta\Theta_{p,j} \frac{\partial\tilde{u}_{p,i}}{\partial x_j} + \delta R_{p,ij} \frac{\partial\tilde{T}_p}{\partial x_j} \right] \end{pmatrix}. \quad (1.59)$$

The previous sections focused on the mathematical description and closure of the dispersed phase governing equations. Sec. 1.3.5 gives some elements on the new concept of correlated and uncorrelated particle temperature.

1.3.5 Existence of a correlated and uncorrelated particle temperature

Following the same methodology than Février [40] for particle velocity, Masi studied the Eulerian two-point correlations of particle temperature in an academic configuration. The configuration is a particle-laden Homogeneous Isotropic Turbulence (HIT) with a constant mean temperature gradient in the normal y -direction [23]. For computational cost concern, the turbulence is frozen after that the stationary state has been reached.

The two-point spatial correlation of particle temperature, obtained from projected mesoscopic fields, reads:

$$R_\theta^{pp} = \frac{\langle \tilde{n}_p(\mathbf{x}, t) \tilde{T}'_p(\mathbf{x}, t) \tilde{n}_p(\mathbf{x} + \mathbf{r}, t) \tilde{T}'_p(\mathbf{x} + \mathbf{r}, t) \rangle}{\langle \tilde{n}_p(\mathbf{x}, t) \tilde{n}_p(\mathbf{x} + \mathbf{r}, t) \rangle}, \quad (1.60)$$

where \tilde{n}_p and \tilde{T}'_p are the mesoscopic number density and temperature fluctuations.

Fig. 1.3 shows the large variation of R_θ^{pp} when the St_θ increases. For very small St_θ , this correlation decreases exponentially and is very close to its fluid counterpart. When the St_θ increases, the ratio $R_\theta^{pp}/2q_\theta^2$ departs from unity when \mathbf{r} tends to zero. That means that two neighboring particles have very different temperature, indicating an uncorrelated component of T_p . Moreover, the continuous shape of R_θ^{pp} , apart from this initial peculiarity, suggests that particles share a common temperature.

That is the reason why Masi proposes to split the particle temperature into two contributions, one in terms of the Eulerian mesoscopic field, spatially correlated and shared by all the particles and a residual contribution, spatially uncorrelated:

$$T_p(t) = \tilde{T}_p(\mathbf{x}_p(t), t) + \delta T_p(t), \quad (1.61)$$

where \tilde{T}_p denotes the mesoscopic temperature and δT_p the RUM temperature⁵. It is the analog of the particle velocity decomposition in mesoscopic and RUM components, Eq. 1.13.

⁵It is called RUM temperature and not Random Uncorrelated Temperature (RUT) because any uncorrelated variable is denoted by the ‘‘RUM’’ prefix.

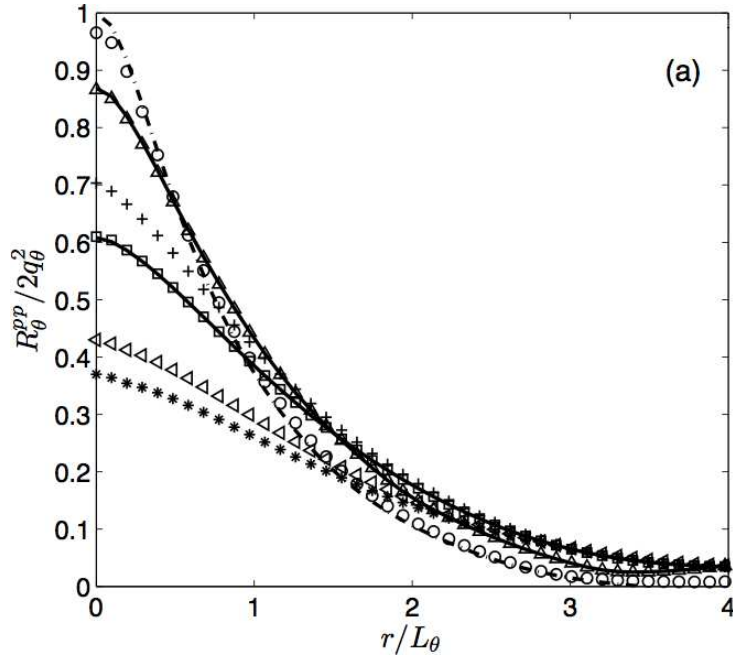


Figure 1.3: Influence of particle thermal inertia on the two-point particle temperature correlations. The dash-dotted line represents the fluid. Symbols: Increasing particle thermal inertia, from \circ : $St_\theta = 0.05$ to $*$: $St_\theta = 4.28$. q_θ^2 stands for the total particle temperature variance, \mathbf{r} for the radial distance between the particles and L_θ for the thermal integral length scale. Excerpted from [78].

As mentioned in Sec. 1.3.1, these quantities are obtained by an ensemble average over a large number of particle realizations for a single fluid realization \mathcal{H}_f . The ensemble-average operator complies with the following properties:

- The ensemble average of the RUM contribution is zero: $\langle \delta T_p | \mathbf{x}_p(t) = \mathbf{x}; \mathcal{H}_f \rangle = 0$.
- The RUM and the mesoscopic contributions are spatially uncorrelated: $\langle \tilde{T}_p \delta T_p | \mathbf{x}_p(t) = \mathbf{x}; \mathcal{H}_f \rangle = 0$.
- The RUM contribution and the fluid are spatially uncorrelated: $\langle T_f \delta T_p | \mathbf{x}_p(t) = \mathbf{x}; \mathcal{H}_f \rangle = 0$.

Using these properties, high-order quantities like the particle temperature variance split into the sum of a mesoscopic and RUM part:

$$q_\theta^2 = \tilde{q}_\theta^2 + \delta q_\theta^2, \quad (1.62)$$

where q_θ^2 , \tilde{q}_θ^2 and δq_θ^2 denote the total, mean mesoscopic and mean RUM particle temperature variance, respectively. These quantities are defined as follows:

$$q_\theta^2(\mathbf{x}, t) = \frac{1}{2} \langle T_p'(\mathbf{x}, t) T_p'(\mathbf{x}, t) | \mathbf{x}_p(t) = \mathbf{x} \rangle \quad (1.63)$$

$$\tilde{q}_\theta^2(\mathbf{x}, t) = \frac{1}{2} \frac{\langle \tilde{n}_p(\mathbf{x}, t) \tilde{T}_p'(\mathbf{x}, t) \tilde{T}_p'(\mathbf{x}, t) \rangle}{\langle \tilde{n}_p(\mathbf{x}, t) \rangle} \quad (1.64)$$

$$\delta q_\theta^2(\mathbf{x}, t) = \frac{\langle \tilde{n}_p(\mathbf{x}, t) \delta \theta_\theta(\mathbf{x}, t) \rangle}{\langle \tilde{n}_p(\mathbf{x}, t) \rangle}. \quad (1.65)$$

Spatial averages can be easily obtained in this academic configuration by a volume average over the computational domain. Therefore, the impact of particle inertia is studied in Sec. 1.3.6 using the mean temperature variances.

1.3.6 Effect of particle inertia on temperature variances

The computation of q_θ^2 and δq_θ^2 gives a macroscopic understanding of how particle inertia impacts the particle temperature. This analysis done by Masi is similar to what has been done by Février to understand the effect of dynamic inertia on particle motion. However, the effect of inertia on temperature is more complex than on motion. Indeed, there are two relaxation times instead of one, τ_p and τ_θ , and they are coupled (Eq. 1.10). The impact of these two degrees of freedom is

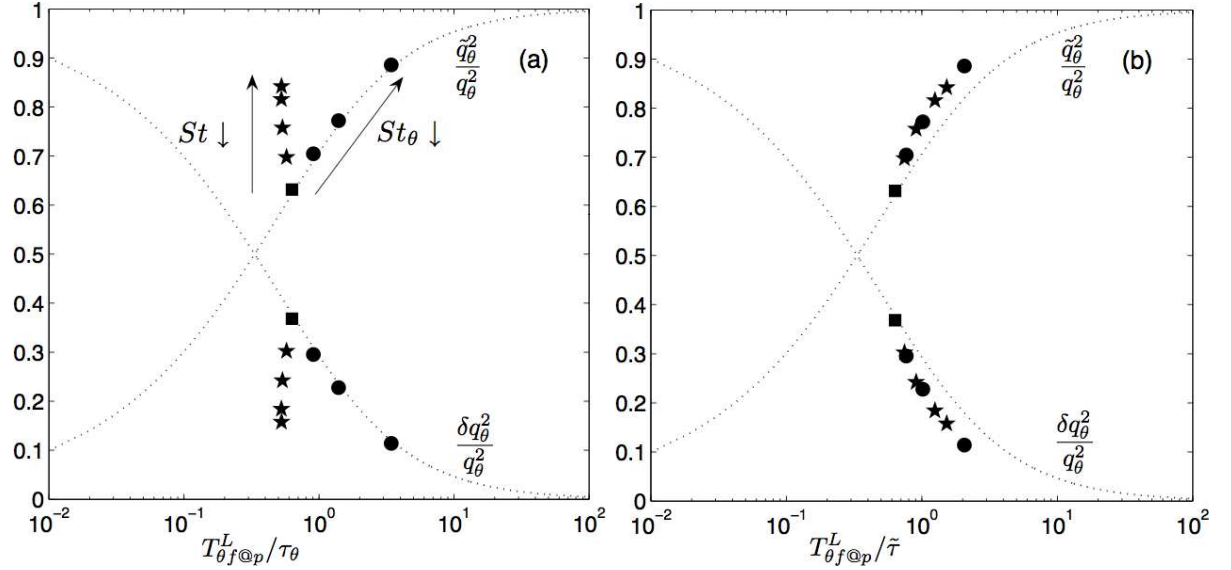


Figure 1.4: Effect of particle inertia on mean mesoscopic and RUM temperature variances as a function of the inverse of the thermal and harmonic Stokes number, $\tilde{St}^{-1} \sim T_{\theta,f@p}^L / \tilde{\tau}$ and $St_\theta^{-1} \sim T_{\theta,f@p}^L / \tau_\theta$. Case A (\bullet): ($St = cst$ and St_θ varies), Case B (\star): (St varies and $St_\theta = cst$), \blacksquare : simulation of reference ($St \sim St_\theta$). From [78].

separately characterized in Fig. 1.4(a):

- Case A: **Effect of St_θ** ($St = cst$). As expected, the mesoscopic contribution increases when St_θ increases (up to 1/3 for $St \sim St_\theta \sim 1.5$). In other words, two neighboring particles have closer temperature when they are “thermally lighter”.

- **Case B: Effect of St** ($St_\theta = cst$). Interestingly, the St has a strong impact on temperature statistics. The mesoscopic contribution increases when St decreases.

Masi [78] concludes that “ [...] the thermal correlation between two particles may increase when the correlation in motion increases. Indeed, a decrease of the dynamic inertia involves a decrease of the separation velocity between two particles which is represented by the RUM velocity. So, two separate particles will stay longer time together leading to an increase of the thermal correlation between them with a maximum corresponding to the correlation between one particle and the fluid.”

Moreover, Masi suggests that the relevant time scale is the harmonic mean between the dynamic and thermal response times $\tilde{\tau} = 2(\tau_p\tau_\theta)/(\tau_p + \tau_\theta)$. Using $\tilde{\tau}$ as the reference timescale, case A and B results flock together, as shown in Fig. 1.4(b).

After a brief summary of the assumptions done in the present work about the dispersed phase, the MEF has been chosen due to its ability to reproduce the local and instantaneous properties of particles embedded in a fully non-homogeneous turbulent flow. The methodology to derive the MEF has been briefly detailed, leading to a first unclosed set of equations. Then, the different models used in the present work have been described, leading to the closed set of equations used in this work. Finally, first *a priori* results performed by Masi [78] on an academic configuration are recalled and point out the necessity to take into account the uncorrelated part of the temperature when particles are thermally inertial. If not, the particle temperature dispersion will be badly predicted as some part of the temperature variance will not be resolved. This justifies the extension of the MEF to non-isothermal flows, where the particle uncorrelated temperature is taken into account (*i.e.* the RUM heat fluxes). In other words, the last RHS term of Eq. 1.39 is implemented in AVBP.

Chapter 2

Numerical strategies

Contents

2.1	Specificities of the dispersed phase	32
2.1.1	Compressibility effects	32
2.1.2	Crossing trajectories	33
2.2	Numerical structure of AVBP with the MEF	33
2.2.1	Cell-vertex approach	34
2.2.2	Source terms	36
2.2.3	Convective scheme	36
2.2.4	Temporal advancement	38
	Characteristic time step of the carrier and dispersed phase	38
	Fast-TPF procedure	39
2.2.5	Diffusive terms	41
2.3	Artificial viscosity	42
2.3.1	Sensors	43
	Sensors based on the extrema	44
	Sensors based on the gradients	45

The objective of this chapter is to present the numerical backbone of AVBP and the numerical methods used in this work. The idea is to understand the pros and cons of these methods in the context of two-phase flow simulations within an Eulerian framework.

AVBP was initially created to simulate stationary external flows of aerodynamics type configurations. Since the mid-nineties, it has been intensively developed for the modeling of unsteady turbulent gaseous flows (reactive and non-reactive) for mainly internal flow configurations in complex geometries (combustion chambers). It is only years later that two-phase flow modeling was tackled with the implementation of the MEF [63, 103] and more recently with a Lagrangian solver [42]. As mentioned in Chap. 1, the dispersed phase is solved thanks to an Eulerian approach in the present work. The carrier and dispersed phase set of equations reduce to the same compact form (Eq. A.4 for the fluid and Eq. 1.55 for the particles), so that the same numerical methods can be used for both phases as a first step. It is what has been done in AVBP, where

most of two-phase flow numerical strategies were adapted from those used for the fluid.

However, the physics of the dispersed and carrier phases is different. The specificities of the dispersed-phase and their implications on the numerical strategies are presented in Sec. 2.1. Then, the different numerical approaches used in AVBP are briefly described in Sec.2.2. For more details, the reader is referred to the AVBP handbook [15] or the work of Lamarque [69]. Finally, a special focus is made on the stabilization procedure of centered schemes in Sec. 2.3, the so-called artificial viscosity (AV), which is the numerical bottleneck of this work.

2.1 Specificities of the dispersed phase

2.1.1 Compressibility effects

As mentioned in Chap. 1, particles in a turbulent flow tend to preferentially accumulate in low-vorticity and high-shear regions [132]. This preferential concentration is maximal around unity Stokes number when the characteristic time scale of the fluid is based on the smallest scale of the turbulence. The Stokes number based on the Kolmogorov scale is denoted St_K . Physical features of the dispersed phase can be partially explained by the study of a simplified set of the MEF equations. Kaufmann [63] considers a one-dimensional, monodisperse case without source terms nor coupling (no drag force) and without uncorrelated temperature. In these conditions, the MEF set of equations reads

$$\frac{\partial \tilde{n}_p}{\partial t} + \frac{\partial}{\partial x} \tilde{n}_p \tilde{u}_p = 0 \quad (2.1)$$

$$\frac{\partial}{\partial t} \tilde{n}_p \tilde{u}_p + \frac{\partial}{\partial x} \tilde{n}_p \tilde{u}_p \tilde{u}_p = -\frac{2}{3} \frac{\partial}{\partial x} \tilde{n}_p \delta \theta_p \quad (2.2)$$

$$\frac{\partial}{\partial t} \tilde{n}_p \delta \theta_p + \frac{\partial}{\partial x} \tilde{n}_p \delta \theta_p \tilde{u}_p = -\frac{2}{3} \tilde{n}_p \delta \theta_p \frac{\partial \tilde{u}_p}{\partial x}. \quad (2.3)$$

By analogy with the equations of dilute gases, Kaufmann [63] interprets the RHS term of Eq. 2.2 and Eq. 2.3 as a pressure term, the so called RUM pressure $\tilde{p}_{RUM} = 2/3 \tilde{n}_p \delta \theta_p$. Moreover, a particle sound-speed is defined as

$$\tilde{c}_p = \sqrt{\frac{10}{9} \delta \theta_p}. \quad (2.4)$$

The eigenvalues of the system 2.1-2.3 are $(\tilde{u}_p + \tilde{c}_p, \tilde{c}_p, \tilde{u}_p - \tilde{c}_p)^T$. They are all different, so the simplified system is hyperbolic like that of the fluid. Thus, similar convective schemes can be used for both phases.

If the drag force is now accounted for, Kaufmann [63] proposes a physical explanation of the particle clusters depending on the particle inertia and \tilde{c}_p . In the case of small Stokes numbers, particles follow closely the carrier and $\delta \theta_p$ is small, so that the mesoscopic velocity is much larger than the particle sound speed $|\tilde{u}_p| \gg \tilde{c}_p$. The dispersed phase may be compared to a supersonic flow where shock-like structures appear. At very small St_K , the drag force prevents the compressibility effects [63]. At large St_K , the mesoscopic kinetic energy (MKE) is smaller than the RUM kinetic energy. In this case, the RUM pressure counteracts the accumulation of particles. Finally, maximal preferential concentration occurs when $St_K \sim 1$, when neither drag

nor RUM pressure are sufficient to redistribute the clusters of particles.

In other words, even if the droplets themselves are incompressible, a cloud of droplets acts as a highly compressible phase. Therefore, two-phase flows may be harder to simulate than subsonic gaseous flows and require specific numerical methods [54].

2.1.2 Crossing trajectories

The set of equations of the MEF has been derived assuming that the refined-grid PDF, defined in Eq. 1.14, remains a delta function in the velocity phase centered at \mathbf{u}_p . This hypothesis is violated when two particles cross. That causes a singularity, called a δ -shock [27]. It corresponds to a discontinuity in velocity and leads to Dirac delta function concentrations in density (all the mass density concentrates in one cell). This phenomenon is emphasized in Fig. 2.1 with the

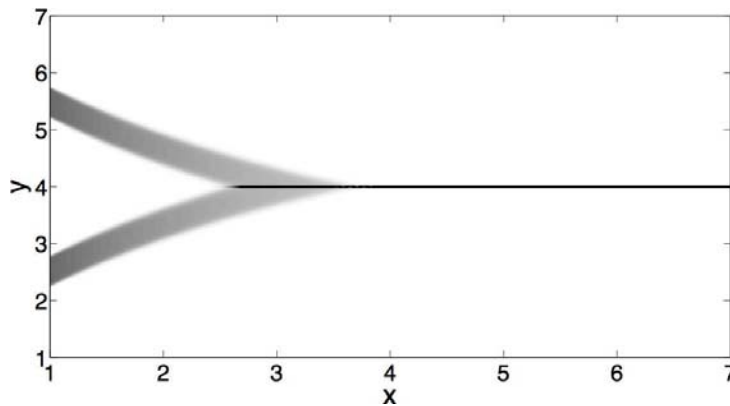


Figure 2.1: Mass density for the simulation of two crossing jets using the standard multi-fluid approach (excerpted from [27]). When the two jets cross, the assumption that the PDF remains a delta function centered at a mean velocity is not fulfilled and a δ -shock occurs.

simulation of two crossing jets. When they cross, the assumed “Gaussian-shape” of the PDF is not fulfilled and a δ -shock occurs. It results in an infinitely thin jet with a velocity equal to the averaged velocity of the two jets. Note that recently, a high-order moment formalism has been introduced for PTC [16] in the LES framework.

At the intersection of the jets, particle velocities are spatially uncorrelated. In the MEF, it causes a large production of RUM kinetic energy at the crossing of two jets. Again, numerical methods should be sufficiently robust to handle this high number density gradient and the stiff source terms associated to the RUM stress tensor, Eq. 1.59.

2.2 Numerical structure of AVBP with the MEF

The precedent section underscored that numerical methods are a cornerstone in two-phase flow simulations. This section exposes the numerical structure of AVBP and how each component has been adapted to two-phase flow calculations.

As mentioned in Sec 1.3.4, the final set of MEF equations (Eq. 1.50-1.54) can be written in compact form

$$\frac{\partial \mathbf{U}_p}{\partial t} + \vec{\nabla} \cdot \vec{\mathcal{F}}(\mathbf{U}_p) = \mathbf{S}_p, \quad (2.5)$$

where the flux tensor is decomposed in two components $\vec{\mathcal{F}} = \vec{\mathcal{F}}_p^C(\mathbf{U}_p) + \vec{\mathcal{F}}_p^V(\mathbf{U}, \vec{\nabla} \mathbf{U}_p)$. Using this decomposition and Eq. 1.55, the numerical backbone of AVBP may be represented as in Fig. 2.2. Remind that all the numerical approaches in AVBP lie in the context of high fidelity unsteady

$$\underbrace{\frac{\partial \mathbf{U}}{\partial t}}_{\text{Temporal advancement}} + \underbrace{\vec{\nabla} \cdot \vec{\mathcal{F}}^C(\mathbf{U})}_{\text{Convective scheme}} + \underbrace{\vec{\nabla} \cdot \vec{\mathcal{F}}^V(\mathbf{U}, \vec{\nabla} \mathbf{U})}_{\text{Diffusive terms}} = \underbrace{\mathbf{S}}_{\text{Source terms}}$$

cell-vertex approach

Figure 2.2: Numerical backbone of AVBP. Each box represents an important piece of the code, from the volume finite cell-vertex approach to the different terms of the transport equations in compact form.

simulations (DNS or LES). Consequently, the smallest resolved scales of the turbulence should not be dissipated nor deformed due to numerical errors. This is ensured by specific numerical schemes, as it will be discussed later. Moreover, the issue of complex geometries means complex meshes with a large number of nodes. Therefore, AVBP was built (1) as an unstructured solver to handle any type of grid cells so that meshes can be refined locally and (2) to work on massively parallel architectures. Each box of Fig. 2.2 represent an important piece of the code and is now discussed in details.

2.2.1 Cell-vertex approach

AVBP uses a finite volume (FV) approach to solve the fluid transport equations and more specifically the *cell-vertex* method [89, 110, 111]. The originality of this approach is to store the discrete value of the conservative variables at the nodes while the transport equations are solved in the control volume defined by the mesh cell. The *cell-vertex* approach shares “its roots” with the family of the residual distribution schemes and has close relations with Galerkin finite element (FE) methods (See [69] and reference therein.).

This method was shown to be more accurate than the *cell-centered* or *vertex-centered* FV approaches and more robust to grid deformations [85, 107, 137]. Moreover, this method is well adapted to the parallelism due to a compact stencil. The resolution of the transport equation in the cell-vertex approach can be decomposed in two steps, depicted in Fig. 2.3.

- *gather* operation: The residual (or fluctuation) \mathbf{R}_e is computed at the center of each element K_e [111].

$$\mathbf{R}_e = \frac{1}{V_e} \int_{K_e} \vec{\nabla} \cdot \vec{\mathcal{F}}_h dV \quad (2.6)$$

Applying the Green-Gauss theorem to Eq. 2.6, the residuals are defined as the integral of

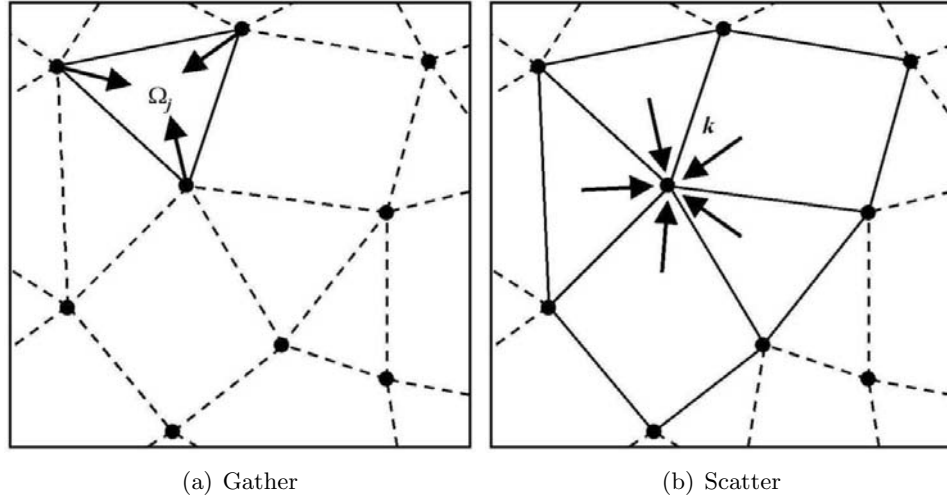


Figure 2.3: Diagram of the two steps of the cell-vertex approach (excerpted from [86]). Gather (Fig. 2.3(a)): the residuals are solved at the center of the control volume. Scatter (Fig. 2.3(b)): the residuals are scattered back to the nodes.

the fluxes through the surface of the element K_e

$$\mathbf{R}_e = \frac{1}{V_e} \oint_{\partial K_e} \vec{\mathcal{F}}_h \cdot \vec{n} dS, \quad (2.7)$$

where $\vec{\mathcal{F}}_h$ is the numerical approximation of the flux $\vec{\mathcal{F}}$ and V_e is the volume of the cell K_e .

Then, the integral of 2.7 is numerically calculated using a trapezoid method. After having defined the normal associated with the vertex k [69], \vec{S}_k , the residuals read

$$\mathbf{R}_e = -\frac{1}{dV_e} \sum_{k \in K_e} \vec{\mathcal{F}}_k \cdot \vec{S}_k, \quad (2.8)$$

where d is the number of space dimensions and $\vec{\mathcal{F}}_k = \vec{\mathcal{F}}_h(\vec{x}_k) = \vec{\mathcal{F}}(\mathbf{U}_k)$ is the flux approximation at vertex k .

- *scatter* operation: The residuals, defined for each element, are distributed to the nodes using the matrix $\underline{\mathbf{D}}_{j,e}$. The residual at node j is then defined as

$$\mathbf{N}_j = \frac{1}{V_j} \sum_{e \in \mathcal{D}_j} \underline{\mathbf{D}}_{j,e} V_e \mathbf{R}_e, \quad (2.9)$$

where $V_j = \sum_{e \in \mathcal{D}_j} V_e / n_v^e$ is the measure of \mathcal{D}_j , defined as the set of cells adjacent to j .

The scatter operation is the most computationally consuming operation in AVBP, representing 10% to 20% of the total CPU time. This is due to the communication and transfer at the interfaces between processors as well as between the cell groups.

After the gather-scatter operation, the system of the dispersed phase equations, written in compact form in Eq. 1.55, may be written in the semi-discrete form:

$$\frac{d\mathbf{U}_p}{dt} = -\mathbf{N}_j + \mathbf{S}_j, \quad (2.10)$$

where \mathbf{S}_j is the source term value at the node j . How to compute \mathbf{S}_j will be tackled in Sec. 2.2.2.

2.2.2 Source terms

As detailed by Lamarque [69], the source terms can be computed in two different ways in AVBP, either using a finite volume *vertex-centered* or a finite element approach following the *cell-vertex* method.

- *vertex-centered* source terms: Source terms are directly computed at the nodes

$$\mathbf{S}_j = \int_{c_j} \mathbf{S} dV = \mathbf{S}_j V_j, \quad (2.11)$$

where V_j is the volume at node j . This formulation is easy to implement as the source terms are calculated with the variable already stored at the nodes. However, it may be less accurate and source terms may vary strongly between neighboring nodes, triggering spurious oscillations in the solution.

- *cell-vertex* source terms: Source terms can be computed in a finite element way, being coherent with the *cell-vertex* approach. This operation is similar to the gather-scatter method. The source terms are first computed at the center of the element K_e with gathered variables from the vertices. Then, they are scattered back to the nodes. Then,

$$\mathbf{S}_j = \int_{\Omega} \mathbf{S} \phi_j dV = \sum_{e \in \mathcal{D}_j} \frac{\mathbf{S}_e V_e}{n_v^e}, \quad (2.12)$$

where \mathbf{S}_e denotes the source terms at the center of the element K_e . This formulation is computationally more expensive as it uses the scatter operation. However, it is more accurate.

In AVBP, gaseous-phase source terms are computed with the *cell-vertex* approach. However, the source terms of the dispersed phase are still computed with the *vertex-centered* approach, mainly due to historical and code structure. Indeed, the numerous source terms of the dispersed phase (Eq. 1.59) are computed in different areas of the code¹. Then, apply a *cell-vertex* approach (*i.e.* *gather-scatter* operations) is less obvious than for the carrier phase.

2.2.3 Convective scheme

Transporting a dispersed phase with an Eulerian framework is a numerical challenge for the convective scheme. On the one hand, small structures and steep gradients of particle volume fraction are created by the preferential concentration phenomenon, as discussed in Sec. 2.1. These small-scale structures should be convected without being dissipated by the convective

¹This could be improved using the object-oriented genericity allowed by Fortran 90 but has not been done yet.

scheme. On the other hand, the transport of these steep gradients causes numerical *wiggles* at their vicinity, which must be dissipated to ensure stability. Zones of very small α_p may become negative, which is not physical. Thus, convective schemes should be sufficiently robust to withstand strong gradients, dissipate the least possible the smallest physical structures and limit the apparition of *wiggles* at the same time.

With this idea in mind, the so-called kinetic schemes, first created to solve pressureless gas dynamics equations [13], have been successfully applied in the context of academic two-phase flow simulations [27]. These schemes proved to conserve the positiveness of particle volume fraction, capture the δ -shocks and treat zone of vacuum. However, they were implemented using a *cell-centered* finite-volume method in [27] and their implementation in the *cell-vertex* approach is not straightforward.

Another possibility is the use of Taylor-Galerkin (TG) schemes such as TTGC [22], which has been specifically constructed to yield low dissipation errors for gaseous LES simulations. It is third-order accurate both in space and time. TTGC was successfully implemented in AVBP by Cuenot and Riber [103] for the dispersed phase. Its application to a 3D homogeneous isotropic turbulence (HIT) laden with solid particles showed a good ability to capture the main physical properties, such as the total particle kinetic energy q_p^2 and particle concentration level. It showed better results than the Lax-Wendroff scheme [73]. This scheme should be coupled with artificial dissipation terms, similar to an artificial viscosity (AV) to handle numerical *wiggles* and steep gradients. The main challenge is then to localize accurately where to apply AV. This is the objective of AV sensors, which are presented in Sec. 2.3. Since then, this strategy has been successfully applied in complex configurations [112, 118] but the application of AV remains a crucial point.

Lamarque [69] and Roux [108] implemented an upwind and positive scheme in AVBP for the dispersed phase. This scheme, called Positive Streamwise Invariant (PSI) [134], belongs to the family of the *fluctuation-splitting* or residual distribution schemes [1]. Its formulation is close to the *cell-vertex* approach and thus natural to implement in AVBP. It was first designed for steady state problems [134]. As a first step towards unsteady problems, a simple Euler time-integration has been tested in AVBP. Moreover, the current implementation of a lumped mass matrix leads to an important numerical diffusion. As suggested in [69], the inversion of the exact mass matrix would improve the results but has not been implemented yet. Nevertheless, its capacity to handle steep gradients make this scheme very promising [112, 145]. The PSI scheme for the dispersed phase was first coupled with the Lax-Wendroff (LW) scheme for the carrier phase [73]. It was easier to implement as PSI and LW have both just one residual calculation per time step². However, the dispersive properties of the LW scheme [69] impacts the accuracy of two-phase flow simulations. That is the reason why the PSI scheme was plugged with the TTGC scheme during the present thesis. The good properties of the TTGC scheme are kept for the carrier phase whereas PSI provides a robust solution for the dispersed phase. Moreover, using the same scheme for the carrier phase (here TTGC) allows us to discriminate the scheme employed for the dispersed phase as the carrier phase are the same. In the present work, the carrier phase is always resolved with the TTGC scheme.

²TTGC has two residual calculations per time step.

To conclude, two numerical strategies will be used in this work for the resolution of the dispersed phase: PSI and “TTGC+AV”. These strategies are evaluated on academic test cases of increasing complexity in Part. II.

2.2.4 Temporal advancement

Three time integration methods are available in AVBP. All are explicit, which is favorable for the parallelism. The time marching method used in the present work is a variation of the Lax and Wendroff method [72] where temporal derivatives are function of spatial derivatives thanks to a Taylor expansion. It follows the Taylor-Galerkin two-step method³ specific to the TTG schemes [22, 31, 69]. The important point is that the stability of the convective scheme is driven by the Courant-Friedrichs-Lewy (CFL) number. In practice, the time step of the convective scheme must be lower than the critical time step:

$$\Delta t_{crit} = \frac{\nu \Delta x}{u_{character}}, \quad (2.13)$$

where ν , Δx and $u_{character}$ denote the CFL number, the local space step of the mesh and the characteristic speed at which the considered physics is transported, respectively. In the present work, the time step of the convective scheme is chosen so that the local CFL number never exceeds 0.7, which is below the critical CFL number [69].

Characteristic time step of the carrier and dispersed phase

This section tackles the issue of the reference time step of the carrier and dispersed phases.

As mentioned in Chap. 1, the fluid follows the compressible Navier-Stokes equations in AVBP. The reference CFL number of the carrier fluid, and thus the reference time step, is triggered by the acoustics:

$$\Delta t_{ac} = \frac{\nu_{ac} \Delta x}{|u_f + c|}, \quad (2.14)$$

where ν_{ac} , u_f and c are the acoustic CFL number, local fluid velocity and speed of sound, respectively.

The characteristic velocity of the dispersed phase is \tilde{u}_p so that the CFL number of the dispersed phase may be defined as⁴:

$$\nu_{p,conv} = \frac{\tilde{u}_p \Delta t}{\Delta x} \quad (2.15)$$

Because in AVBP the carrier and dispersed phase are advanced with the same time step, as illustrated in Fig. 2.5(a), one has the following relation between ν_{ac} and $\nu_{p,conv}$:

$$\nu_{p,conv} = \frac{\tilde{u}_p}{|u_f + c|} \nu_{ac}. \quad (2.16)$$

In most cases, $\tilde{u}_p/|u_f + c| \ll 1$, so that the $\nu_{p,conv}$ is several order of magnitude smaller than ν_{ac} , which has two consequences:

³These two steps may be seen as a prediction-correction.

⁴Theoretically the velocity that appears in $\nu_{p,conv}$ should be $\tilde{u}_p + \tilde{c}_p$ but \tilde{c}_p is often neglected

- It is a dead loss of CPU time if the dispersed phase is computed at the acoustic time step Δt_{ac} . The dispersed phase is over computed. Moreover, the particle volume fractions considered in this work implies that the dispersed phase has no impact on the carrier phase (*one-way* coupling). In other words, there are no source terms in the fluid equations to be computed every fluid time steps. Thus, there are no physical reasons to impose the same time step between both phases. This is specific to compressible solvers where acoustics is resolved (*i.e.* the smallest time scale is Δt_{ac}).
- The convective scheme does not dissipate enough the smallest length-scale (*wiggles*) and spurious oscillations appear. Indeed, the convective scheme properties depend on the CFL number, as shown in Fig. 2.4. This figure shows that TTGC has very small dissipation at low convective CFL numbers, whatever the wave number. When ν increases, the dissipation of the highest frequencies by TTGC increases. The impact of the CFL number is stronger for other convective schemes, like TTG4A.

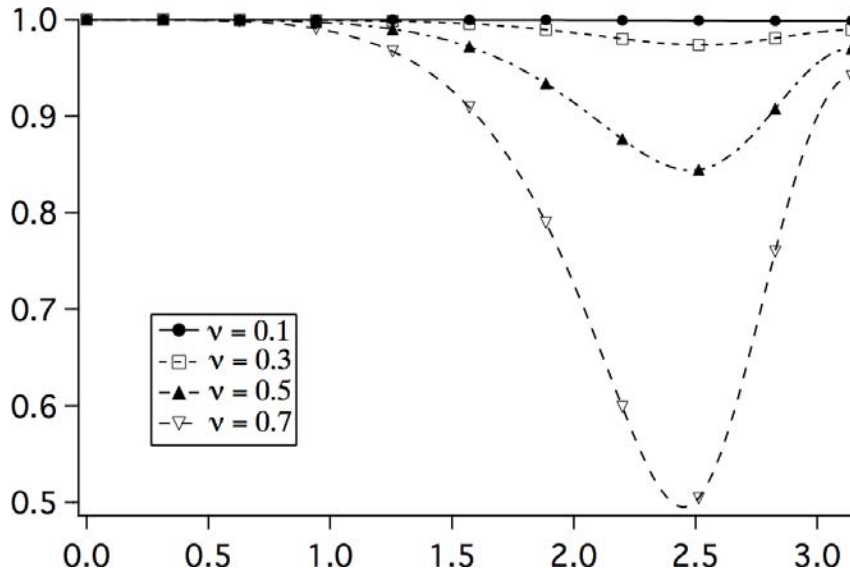


Figure 2.4: Numerical diffusion of the TTGC scheme (modulus of the amplification coefficient) as a function of the normalized wave number $k\Delta x$, for increasing convective CFL numbers ν . Excerpted from [69].

To circumvent these problems, one possibility is to “over” cycle the computation of the dispersed phase. This procedure, denoted Fast-TPF, is detailed in the next section.

Fast-TPF procedure

The idea is to increase the convective time step of the dispersed phase $\Delta t_{p,conv}$, computing the dispersed phase every N_{FTPF} time iteration of the carrier-phase, as illustrated Fig. 2.5. A similar procedure may be used in Lagrangian solvers where discrete particles properties are not computed every acoustic time steps.

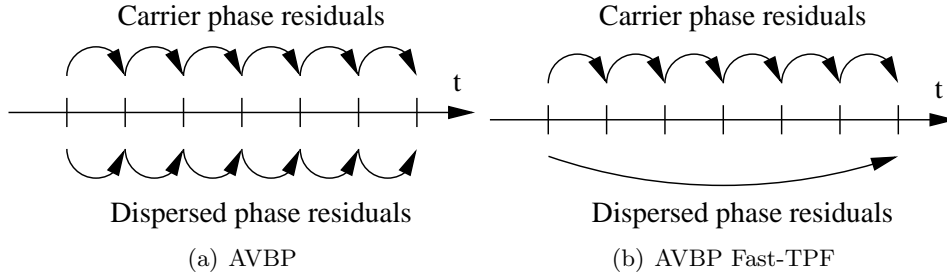


Figure 2.5: Diagram of the Fast-TPF procedure. Instead of computing the dispersed phase residuals every acoustic time steps (left), they are computed every $N_{\text{FTPF}} \Delta t_{\text{ac}}$ (right).

Without the Fast-TPF procedure, the CPU time T^* of a two phase flow simulation can be split as the sum of the CPU time of the carrier and of the dispersed phase, denoted t_f^* and t_p^* :

$$T^* = t_f^* + t_p^*, \quad (2.17)$$

where the superscript “*” means that the time step of the simulation is Δt_{ac} (no Fast-TPF). The consequence of the Fast-TPF procedure is to divide t_p^* by N_{FTPF} , so that the resulting total CPU time of a two-phase flow simulation becomes

$$T^{\text{FTPF}} = t_f^* + \frac{t_p^*}{N_{\text{FTPF}}}. \quad (2.18)$$

Note that t_f^* cannot be lowered since the carrier phase must be solved every acoustic time step. The CPU time of the sole dispersed phase t_p^* is *a priori* unknown and depends of the configuration (number of dispersed-phase variables, source terms, numerical scheme of the dispersed phase, etc..). An interesting information is the additional cost of a two-phase flow simulation in comparison with a single-phase simulation, *i.e.* the ratio between T^* and t_f^* . Combining Eq. 2.17 and Eq 2.18, the ratio of T^{FTPF} and t_f^* is:

$$\frac{T^{\text{FTPF}}}{t_f^*} = 1 - \frac{1}{N_{\text{FTPF}}} + \frac{1}{N_{\text{FTPF}}} \frac{T^*}{t_f^*}. \quad (2.19)$$

Fig. 2.6 illustrates the theoretical gain of CPU time provided by the Fast-TPF procedure. By way of example, T^* has been arbitrarily chosen as twice larger than t_f^* , which is roughly the case for an EE simulation. It can be seen that the cost of a two-phase flow simulation quickly decreases as a function of N_{FTPF} . The maximum N_{FTPF} is imposed by the stability condition: $\nu_{p,\text{conv}} = \nu_{\text{ac}}$. Therefore, the theoretical maximum number of iterations at which the dispersed phase can be computed, denoted $N_{\text{FTPF}}^{\text{max}}$, is

$$N_{\text{FTPF}}^{\text{max}} = \frac{\max(|u_f + c|)}{\max(\tilde{u}_p)} \quad (2.20)$$

As a matter of fact, just a few N_{FTPF} is necessary if the Fast-TPF procedure is only used to accelerate a two-phase flow simulation. Indeed, $N_{\text{FTPF}} = 4$ already yields a gain of CPU time of 80% in the representative example where $t_p^* \simeq t_f^*$ (Fig. 2.6). This procedure would be particularly interesting when more than one set of dispersed-phase equations are solved, as for the Multi-fluid MEF [145], in which a set of equation is solved for each class (diameter) of particles.

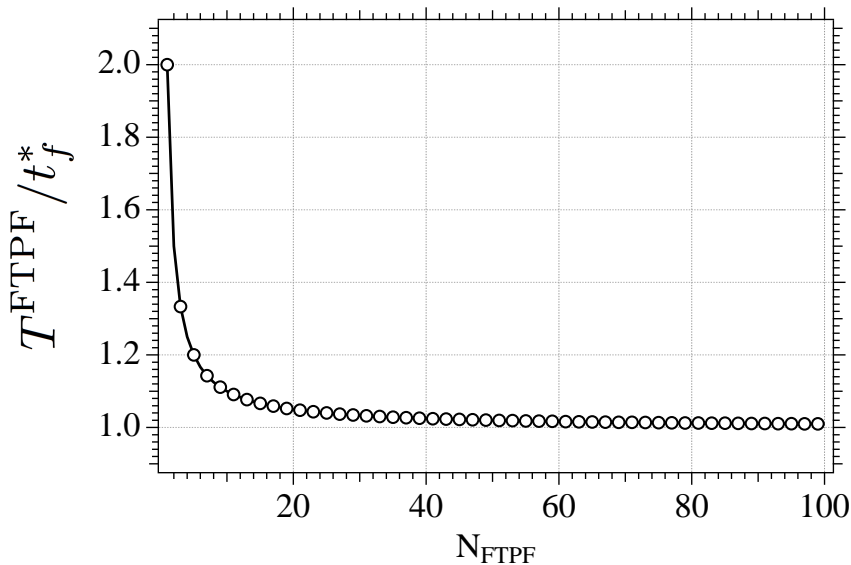


Figure 2.6: Gain of CPU time of a two-phase flow simulation provided by the Fast-TPF procedure.

2.2.5 Diffusive terms

Two methods are implemented in AVBP to compute the diffusive terms in Fig. 2.2. Their main characteristics are summarized in Tab. 2.7.

	4Δ	2Δ
Method	<i>cell-vertex</i> [26]	FE-Galerkin [21]
Stencil width	$4\Delta x$	$2\Delta x$
Dissipation of the smallest length-scale	No	Yes

Figure 2.7: Main characteristics of the diffusion operators available in AVBP

The first diffusion operator stems from a *cell-vertex* formulation and is denoted 4Δ due to a $4\Delta x$ stencil in one dimension. That means that the diffusion operator at one node requires the information of its neighbors and of the neighbors' neighbors. The flaw of this operator is that it does not diffuse the smallest length-scales, whether they are physical or *wiggles*. For example, a typical kinetic energy spectrum obtained in a DNS of a homogeneous isotropic turbulence with the 4Δ diffusion operator is shown in Fig. 2.8. Energy accumulates at smallest scales, which is not physical and can lead to the crash of computation.

Therefore, Colin [21] implemented another diffusion operator, denoted 2Δ , constructed from a FE Galerkin method. This leads to a smaller stencil of $2\Delta x$. This operator diffuses the smallest scales, hence the *wiggles*. The 2Δ operator has been recently implemented [77] for the dispersed phase and is the one used in the present work.

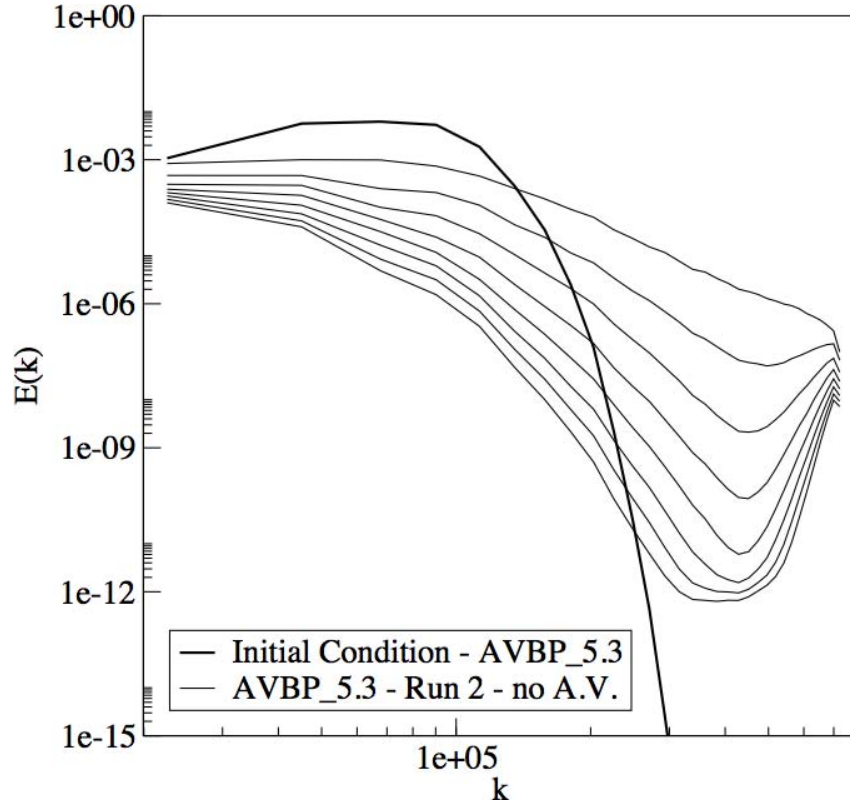


Figure 2.8: Energy spectra of a HIT in DNS with the 4Δ diffusion operator. Excerpted from [15].

2.3 Artificial viscosity

This section details the various components of the stabilization technique used jointly with the high-order scheme TTGC, the so-called artificial viscosity (AV). The computational simulation of flows with discontinuities have required specific stabilization techniques to withdraw, or at least limit, the apparition of wiggles close to strong gradients. The use of artificial viscosity stems from the seminal work of Von Neumann and Richtmeyer [147], who introduced an additional pressure term in Euler equations to withstand strong shocks. Further studies [60] improved this technique, using a combination of a second and fourth-order viscosity operator. These operators have been adapted to the *cell-vertex* approach [133] and are directly added to the nodal equation (Eq. 1.55).

$$\frac{d\mathbf{U}_p}{dt} = -(\mathbf{N}_j + \mathbf{D}_j^{(2)} + \mathbf{D}_j^{(4)}) + \mathbf{S}_j, \quad (2.21)$$

where $\mathbf{D}_j^{(2)}$ and $\mathbf{D}_j^{(4)}$ denote the 2nd and 4th-order AV operators. These two operators are thoroughly detailed in [69] and briefly recalled below:

$$\mathbf{D}_j^{(2)} = \frac{1}{V_j} \sum_{e \in \mathcal{D}_j} -\frac{\epsilon^{(2)} \zeta_e V_e}{n_v^e \Delta t} (\bar{\mathbf{U}}_e - \mathbf{U}_j) \quad (2.22)$$

$$\mathbf{D}_j^{(4)} = \frac{1}{V_j} \sum_{e \in \mathcal{D}_j} -\frac{\epsilon^{(4*)} V_e}{n_v^e \Delta t} \left[\left(\frac{1}{n_v^e} \sum_{k \in K_e} \vec{\nabla} \mathbf{U}_k \right) \cdot (\vec{x}_e - \vec{x}_j) - (\bar{\mathbf{U}}_e - \mathbf{U}_j) \right], \quad (2.23)$$

where $\bar{\mathbf{U}}_e = \sum_k \mathbf{U}_k / n_v^e$ is the average of \mathbf{U}_p at cell K_e , ζ_e denotes the AV sensor and n_v^e is the number of vertices in K_e . Moreover, $\epsilon^{(4*)} = \max(0, \epsilon^{(4)} - \zeta_e \epsilon^{(2)})$ [60] where $\epsilon^{(2)}$ and $\epsilon^{(4)}$ are user parameters.

The 2nd-order AV operator can be seen as a “shock-capturing” term (called 2nd-order AV) which smoothes under-resolved gradients whereas the 4th order AV operator acts as a “background dissipation” term (called 4th order AV) which dissipates the wiggles. These two operators depend on the two user-defined parameters $\epsilon^{(2)}$ and $\epsilon^{(4)}$ and one sensor ζ_e . Therefore, the AV methodology is carried out in two steps:

- First, a sensor detects if AV must be applied, *i.e.* quantifies the local non-linearity of well-chosen dispersed-phase variables.
- Then, a certain amount of 2nd and 4th-order AV is effectively applied, depending on the choice of $\epsilon^{(2)}$ and $\epsilon^{(4)}$. The value of $\epsilon^{(2)}$ and $\epsilon^{(4)}$ must be a good balance between robustness and accuracy, and depends of the configuration (user experience).

The results of a two-phase flow simulation mostly depends of these two steps. The sensors used in this work are defined in Sec. 2.3.1.

2.3.1 Sensors

A sensor ζ_e is a scaled parameter defined in each cell K_e of the mesh that is normalized between zero and one. A value of ζ_e close to zero means that the solution is smooth enough and that no AV must be applied. On the contrary, the closer to one, the stiffer variations are detected and AV must be applied. Then, AV sensors should be accurately computed to be as local as possible, to minimize artificial diffusion of the solution.

It is more difficult to detect local strong variations in the dispersed phase than in the fluid. Indeed, gaseous phase sensors are computed from the pressure, which is supposed to be very sensitive to any perturbation. We already mentioned that there is no such variable in the dispersed phase. The difficulty is thus to find a set of well chosen variables from which to compute the sensors. All the sensors are, at least, computed as a function of the particle volume fraction. Most of the two-phase flow simulations carried out with AVBP take into account the evaporation of particles. In AVBP, the particle diameter is not transported but reconstructed from the particle volume fraction and number density

$$d_p = \left(\frac{6\tilde{\alpha}_p}{\tilde{n}_p \pi} \right)^{1/3}. \quad (2.24)$$

When the particle volume fraction and the number density are proportional, their numerical error is also proportional and particle diameter is constant. However, when particles evaporate, the relation linking $\tilde{\alpha}_p$ and \tilde{n}_p becomes non-linear. These variables are transported differently and their numerical errors have no more the same shape. Spurious oscillations of d_p may appear after its reconstruction with Eq. 2.24 because of dispersion errors. Particle diameter is thus a

good variable to evaluate the sensors if droplets evaporate.

They are two families of sensors for the dispersed phase.

- A sensor based on the extrema, denoted ζ_{extr} . This sensor checks if the dispersed-phase variables stays bounded in the physical domain (*e.g.* positiveness of the particle volume fraction, diameter and number density).
- A sensor based on the gradients, denoted ζ_{grad} . This sensor⁵ detects under-resolved gradients.

The final AV sensor, which is used to effectively apply AV in the equations, is the maximum between the two sub-family sensors:

$$\zeta_e = \max(\zeta_{\text{extr},e}, \zeta_{\text{grad},e}). \quad (2.25)$$

Both ζ_{extr} and ζ_{grad} have specific models which are combined. The name of the resulting AV sensor follows the convention: “acronym of ζ_{grad} model”-“acronym of ζ_{extr} model”. For example, the Colin-Martinez (CM) model for ζ_{grad} used in combination with the Total sensor model (T) for ζ_{extr} yields the name CM-T. The various sensors and operators are detailed in the handbook of AVBP [15]. The parts concerning the sensors used in the present work are briefly presented hereafter.

Sensors based on the extrema

- **T sensor**, denoted $\zeta_{\text{extr}}^{\text{T}}$. This sensor has been developed by Kaufmann [63] and S. Pascaud [91]. The sensor $\zeta_{\text{extr}}^{\text{T}}$ is computed from the particle volume fraction and number density in the cell Ω_j as

$$\zeta_{\text{extr},e}^{\text{T}} = \max[\zeta_{\text{extr},e}(\tilde{\alpha}_p), \zeta_{\text{extr},e}(\tilde{n}_p)] \quad (2.26)$$

The sensor $\zeta_{\text{extr},e}$ applied to any variable x is defined as

$$\zeta_{\text{extr},e}(x) = \begin{cases} 1 & \text{if } x \in]-\infty, B_{\min}(x)] \cup [B_{\max}(x), \infty[\\ \max(\zeta_e^0(x), \zeta_e^1(x)) & \text{otherwise} \end{cases} \quad (2.27)$$

where $B_{\min}(x)$ and $B_{\max}(x)$ are minimum and maximum thresholds of the variable x . B_{\max} is a fixed parameter in the code and corresponds to an unrealistic value of particle volume fraction or number density:

$$B_{\max}(\tilde{\alpha}_p) = 0.3, \quad B_{\max}(\tilde{n}_p) = 10^{16}.$$

However, $B_{\min}(\tilde{\alpha}_p)$ and $B_{\min}(\tilde{n}_p)$ are user-defined parameters. Their value is of paramount importance since they define a “hard limit” under which a maximum AV is applied ($\zeta_{\text{extr},e} = 1$).

⁵It was denoted ζ_{tpf} in previous works [15, 103, 112, 145].

The function ζ_e^0 is an estimation of the relative variation of x in the cell, and reads

$$\zeta_e^0(x) = 2 \left| \frac{x_{min} + x_{max} - 2x_e}{x_{min} + x_{max} + 2x_e} \right|, \quad (2.28)$$

where x_{min} , x_{max} are the minimum and maximum values of x at the vertices i of the current cell K_e .

The function ζ_e^1 estimates the distance to the minimum bound value B_{min} :

$$\zeta_e^1(x) = \frac{1}{1 + |x_e|/(\epsilon + B_{min})}. \quad (2.29)$$

- **The S sensor**, denoted ζ_{extr}^S . This sensor was designed by Sanjose [112] to tackle evaporation cases. It is a simplification of the Total sensor and aims at being as small as possible in the dense zones and being maximum in the zone of low $\tilde{\alpha}_p$ and d_p . Then, it is evaluated from these two variables as

$$\zeta_{extr,e}^S = 2\sqrt{\zeta_e^1(\tilde{\alpha}_p) \cdot \zeta_e^1(d_p)}, \quad (2.30)$$

where ζ_e^1 is defined in Eq. 2.29.

Here again, the minimal threshold of $\tilde{\alpha}_p$ and d_p are required for the evaluation of ζ_e^1 . However, this sensor lacks of a hard limit similar to the total sensor in Eq. 2.27, depending on $B_{min}(\tilde{\alpha}_p)$ or $B_{min}(d_p)$. Therefore, it is less robust when the particle volume fraction becomes very close to zero.

Sensors based on the gradients

Various sensors based on the gradients exist and are adapted from sensors designed for the fluid. The basic idea is to compare two evaluations of the gradient at the cell

$$\Delta_1^i = x_e - x_i \quad (2.31)$$

$$\Delta_2^i = (\vec{\nabla} x)_i \cdot (\vec{x}_e - \vec{x}_i), \quad (2.32)$$

where x_i and x_e are the value of the variable x at the node i and at the cell K_e , respectively. Δ_1^i represents the variation of x inside the cell whereas Δ_2^i stands for the variation of x with a larger stencil. The objective is to find the best mathematical functions using Δ_1^i and Δ_2^i to localize under-resolved gradients.

For example, Riber [103] adapted the Jameson sensor [60] to the dispersed phase, yielding the Jameson-Riber (JR) sensor. This Jameson sensor was initially derived for steady-state aerodynamics computations. It proves to be too smooth and activated too often, resulting in an over application of AV. For these reasons, the JR sensor was not used in this work. Evaluation of the JR sensor on the academic test case of the convection of a particle-volume fraction gaussian is available in [112, 145].

The Colin sensor was initially designed for unsteady turbulent gaseous simulations and is sharper than the Jameson sensor. This sensor was adapted to the dispersed phase and slightly modified by Martinez [77], using a cell value for normalization instead of a vertex value.

- The CM sensor, denoted $\zeta_{\text{grad}}^{\text{CM}}$. Its exact definition is

$$\zeta_{\text{grad},e}^{\text{CM}} = \max [\zeta_{\text{grad},e}(\tilde{\alpha}_p), \zeta_{\text{grad},e}(d_p)], \quad (2.33)$$

where

$$\zeta_{\text{grad},e}(x) = \frac{1}{2} \left(1 + \tanh \left(\frac{\psi(x) - \psi_0}{\delta} \right) \right) - \frac{1}{2} \left(1 + \tanh \left(\frac{-\psi_0}{\delta} \right) \right), \quad (2.34)$$

x being either the particle volume fraction α_p or particle diameter d_p . In eq. 2.34,

$$\psi(x) = \max_{i \in K_e} \left(0, \frac{\Delta^i}{|\Delta^i| + K(x)\epsilon_1 x} \zeta_i^{\text{J}}(x) \right) \quad (2.35)$$

$$\zeta_i^{\text{J}}(x) = \frac{|\Delta_1^i - \Delta_2^i|}{|\Delta_1^i| + |\Delta_2^i| + x} \quad (2.36)$$

$$\Delta^i = |\Delta_1^i - \Delta_2^i| - \epsilon^k \max(|\Delta_1^i|, |\Delta_2^i|) \quad (2.37)$$

$$\epsilon^k = \epsilon_2 \left(1 - \epsilon_3 \frac{\max(|\Delta_1^i|, |\Delta_2^i|)}{|\Delta_1^i| + |\Delta_2^i| + x} \right). \quad (2.38)$$

The parameters have been fixed by Colin [20] and are recalled bellow.

ψ_0	δ	ϵ_1	ϵ_2	ϵ_3	K
2.10^{-2}	1.10^{-2}	1.10^{-2}	0.95	0.5	1

- The CM5 sensor⁶. The CM sensor can be modified using the user-defined parameter K in Eq. 2.35 [77]. When the value of K is increased, the CM sensor activates slightly later but stronger, so does the AV. As a result, local non-linearities develops more.

The influence of $K(\alpha_p)$ has been studied in a particle-laden HIT [145]. With $K(\alpha_p) = 10$, Eulerian simulations was found to capture better the preferential concentration than with the normal CM sensor ($K(\alpha_p) = 1$) in homogeneous isotropic turbulence laden with particles. However, this value is case-dependant. If K is too high, the simulation is less robust. The best set of parameters, providing both accuracy and robustness was found to be $K(\alpha_p) = 5$ and $K(d_p) = 2$. This set of parameters has been used in academic [145] as well as industrial applications [77, 112]. The resulting sensor is denoted CM5 in the present work, following the notation of [145].

⁶also referred to as CM-lite in [112, 145]

Part II

Evaluation of the numerical strategies

This part evaluates the numerical strategies detailed in Chap. 2 on canonical test cases of increasing complexity. The objective is to find one numerical strategy, defined as the best, and use it to carry out *a posteriori* tests of the MEF in Part III. Parts II and III can be read independently from each other.

The choice of the convective scheme and AV model used for a simulation will be referred to as the “numerical strategy” in the rest of the manuscript. This numerical strategy drives the quality of the numerical results of Eulerian/Eulerian two-phase flow simulations. It is important to evaluate what is the most adequate strategy regarding robustness and accuracy.

Several methods exist to study separately the convective schemes and the AV. The best known method to study the stability of convective schemes is the Von Neumann method, also called Fourier analysis [25]. Recently, Lamarque [69] applied the modified equation method [150] to study the schemes implemented in AVBP (cf. Fig. 2.4). However, the issue of numerical stabilization was not tackled in this study. Concerning that specific point, a one-dimensional stability analysis of the AV applied in AVBP is proposed in [15]. This analysis brings insight of the minimal and maximal bounds of the AV coefficients for a stable simulation but is independent of the convective scheme and of the context of two-phase flows (positiveness of particle volume fraction for example). To our knowledge, a general theoretical method that takes into account the whole system: convective scheme + AV, has not been devised yet.

Therefore, academic test cases are often used to evaluate numerical strategies as a whole. First, academic test cases may be classified as a function of their complexity (number of dimensions, physical phenomena taken into account, etc). Second, they can be separated whether an analytical solution is available or not. Analytical solutions allow to quantify the intrinsic error of the numerical strategies but only exist for few simple academic cases. For example, Chap. 3 considers the classical test case of the one-dimensional convection of a particle volume-fraction crenel to illustrate the problem of the apparition of *wiggles* and transport of steep gradients. A first comparison of the two numerical strategies identified in Chap. 2 is proposed. As a first step toward more complex configurations, a new analytical solution of a two-dimensional particle-laden vortex is proposed in Chap. 4. Contrary to the 1D configuration, the particle-laden vortex takes into account the drag force, so that the influence of particle inertia can be investigated. When there is no analytical solution, Lagrangian simulations are taken as the reference and macroscopic quantities are directly used to discriminate the numerical strategies. Thus, Chap. 5 considers the simulation a three-dimensional decaying homogeneous isotropic turbulence (HIT) laden with solid particles.

Chapter 3

Convection of a 1D particle volume fraction crenel

Contents

3.1	Presentation of the configuration	50
3.1.1	Methodology	51
3.2	How to get rid of spurious oscillations?	52
3.3	How to withstand stiff gradients?	54
3.3.1	Set up of the AV sensor	55
3.3.2	Comparison of the two numerical strategies: PSI scheme and “TTGC+AV”	58

Accuracy and robustness of the numerical scheme is a bottleneck of two-phase flow simulations with an Eulerian approach. As mentioned in Sec. 2.1.1, the particle preferential concentration invariably leads to the creation of steep gradients and no pressure-like term exists in the dispersed-phase equations to diffuse them if RUM is not to be modeled. Therefore, all the robustness of the simulation lies on the convective scheme and on a possible stabilization technique. The objective of this chapter is to illustrate two numerical issues we have to deal with and to propose adapted solutions. The main numerical problems are (1) the apparition of high wavenumber oscillations (a.k.a *wiggles*) when gradients are transported and (2) the transport itself of these steep gradients when the mesh resolution is poor. These issues are illustrated on the simple test case of a one-dimensional convection of a particle volume fraction profile at constant speed. This test case has been widely used in the literature [69, 112, 145] to discriminate numerical strategies. Indeed, it combines the advantages to be a purely convective test case and that a straightforward analytical solution is available.

After a brief presentation of the configuration and methodology in Sec. 3.1, a few numerical strategies presented in Ch. 2 are used to handle the two issues listed above. First, the issue of the *wiggles* is dealt with in Sec. 3.2. Then, an artificial viscosity sensor is chosen in Sec. 3.3.1. Finally, the problem of the transport of under-resolved gradients is tackled in Sec. 3.3. A first comparison of the two numerical strategies considered in this work, namely the PSI scheme and “TTGC + AV”, is carried out in this section.

3.1 Presentation of the configuration

Let us suppose that the particle velocity is constant: $\tilde{u}_p = 1 \text{ m.s}^{-1}$, that there is no coupling between the carrier and the dispersed phase (no drag force nor heat transfer) and that particle temperature is constant. The dispersed phase is then entirely governed by the continuity equation

$$\frac{\partial \tilde{\alpha}_p}{\partial t} + \tilde{u}_p \frac{\partial \tilde{\alpha}_p}{\partial x} = 0. \quad (3.1)$$

In the rest of this chapter, the tilde of $\tilde{\alpha}_p$ is dropped. This equation is solved on a one-dimensional mesh of 1m long. Boundary conditions are periodic in the streamwise direction.

The initial particle volume-fraction profile is defined by the equation:

$$\alpha_p^{t=0}(x) = \alpha_p^{\min} + f(x)(\alpha_p^{\max} - \alpha_p^{\min}) \quad (3.2)$$

$$f(x) = \frac{1}{2} \left(1 + \tanh \frac{L_{ref} - 2|x|}{\theta/2} \right), \quad (3.3)$$

where α_p^{\min} and α_p^{\max} stand for the minimum and maximum value of the particle volume-fraction crenel. L_{ref} denotes the crenel width and θ the width of the initial gradient, as illustrated in Fig. 3.1. The two relevant parameters are the amplitude ratio of the profile, defined by

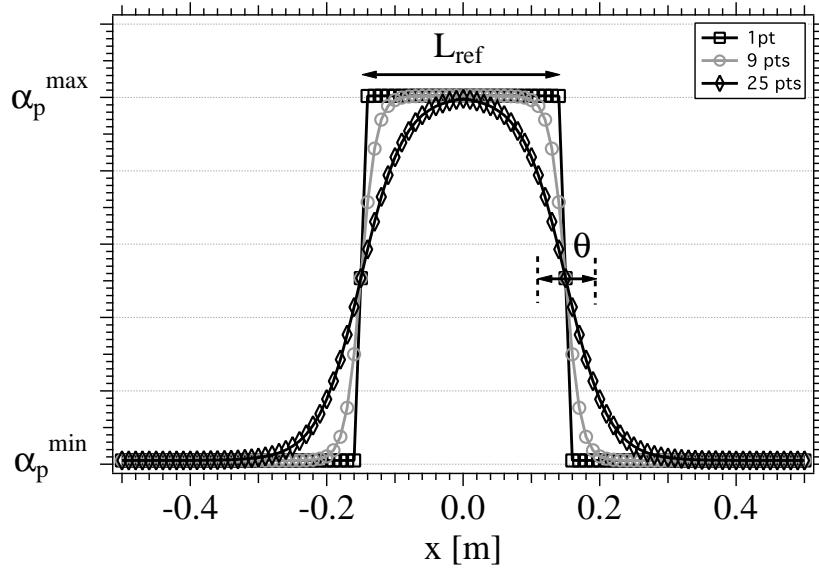


Figure 3.1: Initial solution of the particle volume-fraction as a function of the number of points in the gradient

$$R\alpha_p = \frac{\alpha_p^{\max}}{\alpha_p^{\min}}, \quad (3.4)$$

and the initial number of points inside the gradient

$$N_{grad}^0 = \theta / \Delta x \quad (3.5)$$

where Δx is the space step in the streamwise direction.

For a fixed $R\alpha_p$, Fig. 3.1 shows the wide range of particle volume-fraction shapes which can be obtained as a function of N_{grad}^0 , from a top-hat to a smooth function. The less points in the gradient and the higher amplitude of the crenel, the higher the numerical difficulties. Therefore, this profile function allows to tune easily the level of numerical stiffness. Moreover, the analytical solution is simply:

$$\alpha_p(x, t) = \alpha_p(x - \tilde{u}_p t, t = 0) \quad (3.6)$$

3.1.1 Methodology

Two test cases are considered in this chapter, depending on the amplitude of the particle volume-fraction crenel and number of points inside the gradient of the initial solution. Their main characteristics are summarized in Tab. 3.1. A mesh of 1m long with 100 cells in the streamwise direction is used for both test cases.

keyword	α_p^{min}	α_p^{max}	$R\alpha_p$	N_{grad}^0
C1	1.10^{-4}	5.10^{-4}	5	3
C2	1.10^{-4}	1.10^{-2}	100	7

Table 3.1: Characteristics of the 1D test cases

Case C1 consists in the convection of a low-amplitude α_p crenel. This low-amplitude allows the apparition of *wiggles* but their intensity remains limited (at least after one convective time) so that no 2nd-order AV is necessary. Two solutions for this problem are presented: (1) the use of 4th-order AV or (2) increasing the convective CFL number of the dispersed phase with the Fast-TPF procedure (*cf.* Sec. 2.2.4), defining two sub cases: C1-S0a and C1-S0b (*cf.* Tab. 3.2). Next, the amplitude of the α_p crenel is increased (case C2) so that specific numerical solutions are compulsory to prevent the crash of the simulation. This test case is used to test the two families of numerical strategies presented in Ch. 2, *i.e.* the PSI and TTGC scheme used with an AV term. First, the choice of the AV sensor (used jointly with TTGC) is discussed, comparing C2-S1a and C2-S1b cases. Then, the convective schemes PSI and TTGC are compared with cases C2-S2, C2-S1b and C2-S1c, respectively.

keyword	scheme	ζ_{extr}	ζ_{grad}	$\epsilon^{(2)}$	$\epsilon^{(4)}$	$B_{min}(\alpha_p)$	ν_{CFL}
C1-S0a	TTGC	T	CM	0	$5 \cdot 10^{-3}$	$1 \cdot 10^{-8}$	$2 \cdot 10^{-3}$
C1-S0b	TTGC	T	CM	0	0	$1 \cdot 10^{-8}$	0.7
C2-S1a	TTGC	T	CM	0.5	0	$1 \cdot 10^{-8}$	$2 \cdot 10^{-3}$
C2-S1b	TTGC	T	CM5	0.5	0	$1 \cdot 10^{-8}$	$2 \cdot 10^{-3}$
C2-S1c	TTGC	T	CM5	0.5	$5 \cdot 10^{-3}$	$1 \cdot 10^{-8}$	$2 \cdot 10^{-3}$
C2-S2	PSI	T	CM5	$5 \cdot 10^{-3}$	0	$1 \cdot 10^{-8}$	$2 \cdot 10^{-3}$

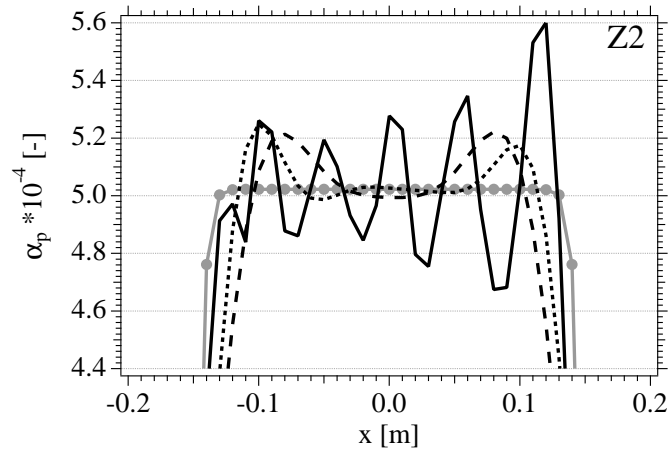
Table 3.2: Parameters of the sub test cases

3.2 How to get rid of spurious oscillations?

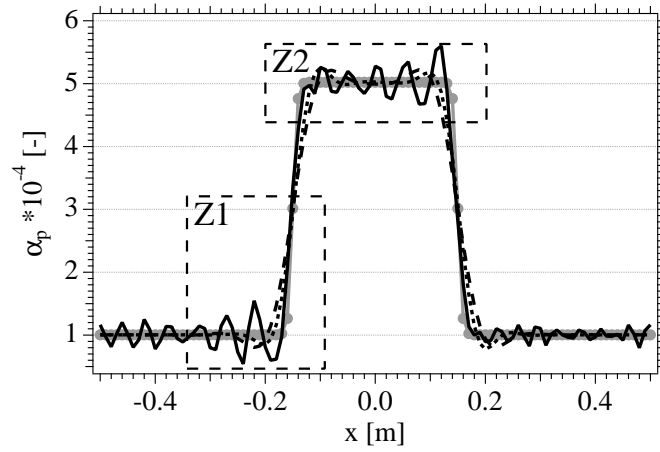
As mentioned in the previous section, spurious oscillations appear when a steep gradient is convected by a centred scheme like TTGC. The amplitude of these *wiggles* depends of that of the gradient and increases along time if not dissipated by a physical or numerical term. Since the dispersed phase equations have no-pressure term (*i.e.* physical dissipation) in the momentum equations, these non-physical oscillations must be eliminated by a numerical term. Two solutions are presented in this section (1) the use of an hyper-viscosity operator, a.k.a 4th-order viscosity or (2) use the Fast-TPF procedure to increase the convective CFL number of the dispersed phase. These two strategies have been detailed in Sec. 2.3 and Sec. 2.2.4, respectively.

The particle volume fraction profile after one convective time is shown in Fig. 3.2. Without any artificial viscosity, the initial profile is scattered with node-to-node oscillations. Note that their amplitude remains limited as the amplitude ratio of the crenel $R\alpha_p$ (Eq. 3.4) is low for this configuration.

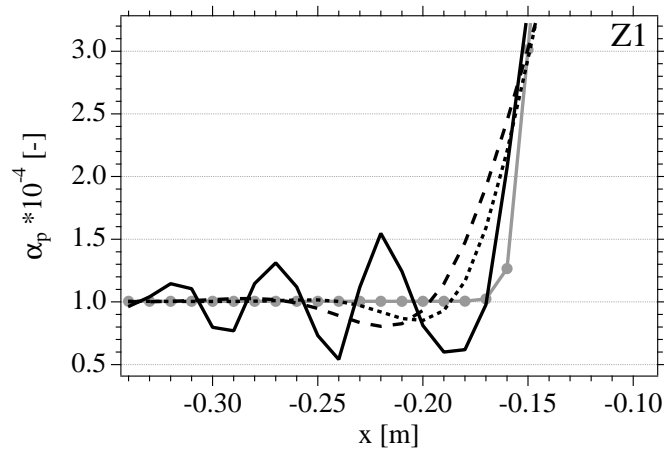
Adding a small amount of 4th-order AV is sufficient to eliminate these wiggles, as shown in Fig. 3.2(a) for example. Different values of $\epsilon^{(4)}$ have been tested iteratively and $\epsilon^{(4)} = 5 \cdot 10^{-3}$ was found to be the best balance between accuracy and dissipation. However, the minimum and maximum of the volume fraction are not conserved and the profile is slightly diffused. These results are consistent with Sanjose [112] where the impact of the 4th-order AV was studied on the convection of a Gaussian.



(a)



(b)



(c)

Figure 3.2: Particle volume-fraction crenel after one convective time (case C1). Comparison between the exact solution ($\text{---}\bullet\text{---}$) and Eulerians simulation carried out with the TTGC scheme. Without any AV (---), with $\epsilon^{(4)}$ at small CFL number (case C1-S0a, ---) or without $\epsilon^{(4)}$ at high CFL number with the Fast-TPF procedure (case C1-S0b, ---). The top and bottom figures correspond to the zooms Z2 and Z1 of the wide figure (medium), respectively.

Another solution is to use the Fast-TPF procedure to increase the convective CFL number of the dispersed phase, $\nu_{p,\text{conv}}$ (Eq. 2.16). Indeed, $\nu_{p,\text{conv}} \simeq 2 \cdot 10^{-3}$ in this configuration since the acoustic CFL of the gaseous phase equals $\nu_{\text{ac}} = 0.7$ and $u_g = \tilde{u}_p = 1 \text{ m}\cdot\text{s}^{-1}$. At this convective CFL, the TTGC scheme does not dissipate high frequencies very much. However, it dissipates more high frequencies when $\nu_{p,\text{conv}}$ is high enough, around 0.5, according to theory (*cf.* Fig. 2.4 or [69]). Then, case C1-S0b consists in setting $\nu_{p,\text{conv}} = 1$ without any artificial viscosity ($\epsilon^{(2)} = \epsilon^{(4)} = 0$). With that technique, all the *wiggles* are eliminated. However, it does not conserve either the minimum or maximum of the particle volume fraction. As a matter of fact, particle volume fraction profiles of cases C1-S0a and C1-S0b are similar and both agree satisfactorily with the exact solution. Nevertheless, increasing $\nu_{p,\text{conv}}$ is interesting as it yields the same result of C1-S1a without an insight of the value of $\epsilon^{(4)}$ and the computational time of the simulation is highly reduced (-60 %).

In order to study the gain of CPU given by the Fast-TPF procedure, several simulations have been carried out with a wide range of N_{FTPF} . Fig. 3.3 presents the total CPU time of a two-phase flow simulation divided by the cost of a sole gaseous simulation with the same configuration, as a function of N_{FTPF} . The case C1-S0b corresponds to $N_{\text{FTPF}} = 346$ and is not represented in the figure since we wanted to highlight the quick gain of CPU time for small values of N_{FTPF} . Here, the distinction is made between the cost of the carrier-phase simulation, which is incompressible, and the cost of the dispersed phase simulation, which is reduced by the Fast-TPF procedure. By way of example, “over-cycling” only twice the dispersed phase ($N_{\text{FTPF}} = 3$) cuts the additional cost of its simulation by 60%. Note that in application, T^* does not exactly converge toward t_f^* but has a slight offset of 5% with the theoretical CPU time (Eq. 2.19). This offset corresponds to the time spent in the internal routines of the dispersed phase for each iteration of the carrier phase¹.

Cases C1 consisted in the transport of a low-amplitude crenel, with sufficient mesh resolution. There was no problem of stability apart of the apparition of *wiggles*. In the next sections, the amplitude of the crenel is increased and adequate numerical strategies are proposed. This second case is more restrictive for the numerical scheme than case C1 so that the Fast-TPF procedure cannot be used to dissipate the spurious oscillations by increasing the CFL number. Indeed, the simulation can be “over-cycled” by only a few N_{FTPF} ($N_{\text{FTPF}} = 3$) before it becomes unstable, much lower than its theoretical maximum value (Eq. 2.20). Therefore, spurious oscillations will be dissipated thanks to the 4th-order AV as in Case C1-S0a ($\epsilon^{(4)} = 5 \cdot 10^{-3}$).

3.3 How to withstand stiff gradients?

In many two-phase flow simulations, the particle volume-fraction gradients are not sufficiently resolved (not enough points). The configuration C2 is representative of the transport of an under-resolved α_p steep front created by the particle preferential concentration. It allows a meaningful investigation of the two numerical strategies defined in Ch. 2: the PSI scheme and the “TTGC + AV” strategy. Since it is one basic component of the “TTGC + AV” strategy, the set up of the AV sensor is detailed in Sec. 3.3.1.

¹Note that it is related to the actual implementation of Fast-TPF in AVBP and may be reduced with a more appropriated structure of the code.

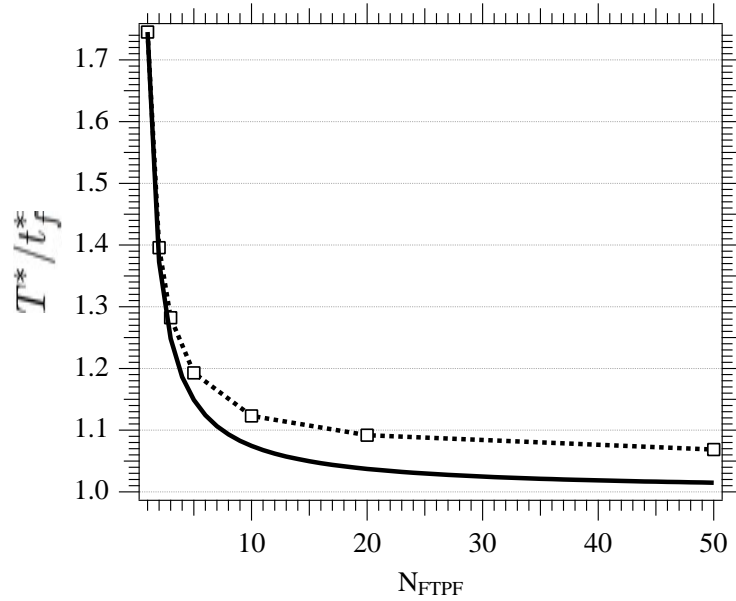


Figure 3.3: Impact of the Fast-TPF procedure on the CPU time. The ratio of CPU time of the two-phase flow simulation to the sole carrier phase ($\cdots\square\cdots$) is compared with the theoretical acceleration (—) (Eq. 2.19).

3.3.1 Set up of the AV sensor

The artificial viscosity sensors and coefficients are the two fundamental components of the strategy “TTGC+AV”. Since the value of $\epsilon^{(2)}$ and $\epsilon^{(4)}$ depends on the configuration, this section only tackles the question of the choice of the sensor.

This issue has been already discussed in the context of AVBP [103, 112, 145] and almost every author created a new sensor. For example, the CM-S and CM5-S sensors were tested on the problematic case of 1D Burger’s equation [112], but the resulting AV was not sufficient to prevent a negative α_p . One reason for the AV method to fail in this non-linear situation is that the S sensor is not sharp enough when α_p has a strong overshoot. A numerical clipping was applied on the particle volume-fraction and on the number density to circumvent this problem. Although efficient, this technique is not optimal as it causes numerical errors on the particle diameter and a loss of mass.

In the present work, no new sensor has been created. On the contrary, we looked for the best combination of already existing sensors and define some guidelines to set their parameters ($B_{\min}(\alpha_p)$, $\epsilon^{(2)}$). The objective is to provide a suitable stabilization term when the TTGC scheme is used, without any non-physical clipping. Consequently, the T sensor was preferred to the S sensor (*cf.* Sec. 2.3.1) since it has a threshold under which ζ_{extr} is maximal. This sensor on the extrema, used with a high $\epsilon^{(2)}$ is sufficiently robust to prevent a negative α_p . It must be used with a very sharp sensor on the gradients. Then, sensors belonging to the CM family seem good candidates. The following strategy is considered:

- Set a threshold value on α_p and \tilde{n}_p four order of magnitude lower than their initial minimum values, $\alpha_p^{\min,0}$ and $\tilde{n}_p^{\min,0}$, respectively.

- The value of $\epsilon^{(2)}$ must be sufficiently high to diffuse any undershoot of particle-volume fraction below $B_{min}(\alpha_p^{min,0})$.
- Use a sufficiently sharp sensor on the gradients.

Then, two sensors on the gradients of the CM's family are evaluated on the case C2. No 4th-order AV is applied, in order to quantify only the effect of the 2nd-order AV. Note that without any stabilization technique (no AV), a simulation carried out with TTGC on C2 crashes after a few iterations due to a negative α_p . Fig. 3.4 presents the profile of α_p after one convective time, comparing the cases C2-S1a and C2-S1b with the exact solution. First, both simulations are similar and in good agreement with the analytical solution. The particle volume fraction profile seems mildly sensitive to the sensor on the gradient. Incidentally, the CM5-T sensor dissipates slightly more the high frequency oscillations than CM-T, even though no 4th-order AV is applied (Fig. 3.4(a)). The key area concerning the stability of the simulation is the uphill foot of the crenel, indicated in Fig. 3.4(b) by Z1. In this zone, the TTGC scheme leads to a strong undershoot of α_p which is actually contained by the artificial viscosity, as shown in Fig. 3.4(c).

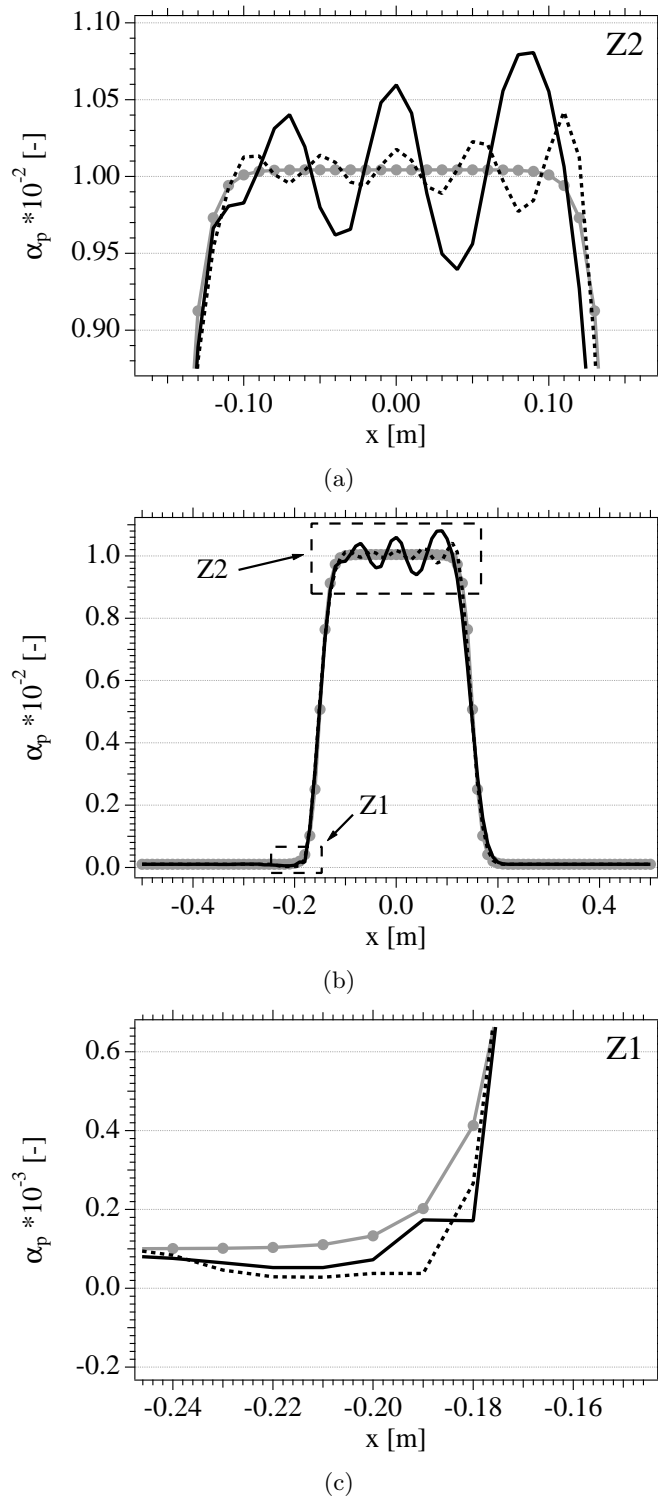


Figure 3.4: Impact of the AV sensor on the transport of a particle volume-fraction crenel after one convective time (case C2). Comparison between the exact solution ($\text{---}\bullet\text{---}$) and Eulerians simulation carried out with different AV sensors (*cf.* Tab. 3.2). CM-T (case C2-S1a, ---) and CM5-T (case C2-S1b, ). The top and bottom figures correspond to the zooms Z2 and Z1 of the wide figure (medium), respectively.

Fig. 3.5 indicates that both ζ_{extr} and ζ_{grad} activate in this zone. As expected, the sensor CM5 is sharper than CM, as it can be seen in Fig. 3.5(a). It activates only around the gradient location ($x \simeq -0.18$) whereas CM activates even when the solution is smooth ($x \sim -0.28$). The sensor on the extrema is shown in Fig. 3.5(b). The threshold $B_{\text{min}}(\alpha_p)$ defines a background dissipation of low amplitude in the tails of the crenel which wipe out the *wiggles*. Note that ζ_{extr} is three order of magnitude lower than ζ_{grad} . The sensor on the extrema behaves as expected, increasing just before the gradient, where an undershoot occurs. Both CM-T and CM5-T sensors work satisfactorily, but CM5 is definitely sharper than CM. Consequently, CM5-T is chosen to be used with TTGC for the rest of this work.

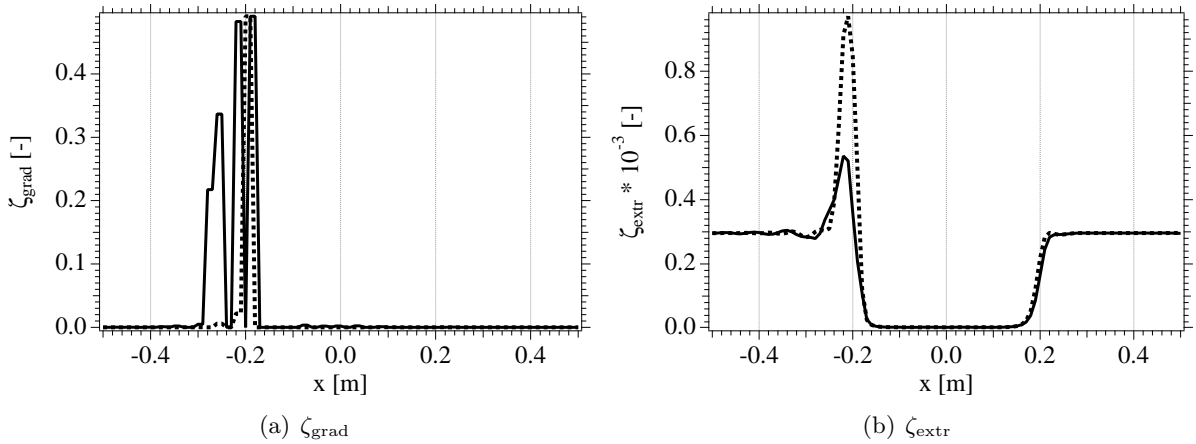


Figure 3.5: Effect of the AV sensor, comparison between CM-T (—) and CM5-T (⋯⋯). Axial profiles of ζ_{grad} (left) and ζ_{extr} (right) at one convective time.

3.3.2 Comparison of the two numerical strategies: PSI scheme and “TTGC+AV”

Now that the AV sensor has been chosen, the two numerical strategies defined in Ch. 2 are compared on case C2. First, case C2-S2 is carried out with the PSI scheme [134], an upwind and positive scheme recently implemented in AVBP [108, 69] whereas case C2-S1b uses the TTGC scheme with the AV sensor set up in Sec. 3.3.1: the CM5-T sensor. Note that the positiveness of PSI is not entirely fulfilled on the dispersed phase system so that a very small amount of 2nd-order AV is applied in case of a strong undershoot of α_p . Characteristics of C2-S2 and C2-S1b are detailed in Tab 3.2.

The α_p profiles of cases C2-S2 and C2-S1b are plotted in Fig. 3.6. First, the distinct characteristics of PSI is to substantially dissipate the initial crenel but conserve the minimum of α_p . That confirms the robustness of PSI for a two-phase flow simulation and is consistent with previous study on similar academic configurations [69, 112]. Of course, this dissipation decreases progressively if the mesh is refined, as remarked by Sanjose [112]. On the contrary, the TTGC scheme, used jointly with the CM5-T sensor is in satisfactory agreement with the exact solution. Moreover, adding a small amount of 4th-order AV further improves the results, as shown in Fig. 3.6(a) with case C2-S1c.

Note that PSI converges in space at the first order (*cf.* remarks in Sec. 2.2.3) whereas TTGC converges in space at the third order. Therefore, the comparison of these two schemes at the same mesh resolution is relatively unfair. As stressed by Lamarque [69], the performances of PSI are understandable as the mass matrix is lumped in AVBP, which reduces the order in space. One important remark is that PSI only dissipates in the streamwise direction, contrary to the AV which dissipates in every direction. Nevertheless, the robustness of PSI is unquestionable, which is valuable for industrial applications.

To conclude, the two main numerical problems encountered in two-phase flow simulations with an Eulerian approach were illustrated on the one-dimensional convection of a crenel of α_p , *i.e.* the apparitions of spurious oscillations at the vicinity of steep gradients and the convection of under-resolved gradients of α_p . The simplicity of this test case allows us to separately discriminate adapted numerical strategies. First, either the use of 4th-order AV or increasing the convective CFL number with the Fast-TPF procedure, are efficient ways to dissipate non-physical *wiggles*. Moreover, the Fast-TPF procedure reduces dramatically the cost of a two-phase flow simulation by over-cycling the resolution of the dispersed-phase. However, it proves to be more unstable when the configuration is more restrictive, so that only the 4th-order AV is retained to deal with spurious oscillation in the rest of this work. Although it is an interesting way to fasten an EE simulation, the Fast-TPF procedure needs further investigations regarding its robustness so that it will not be used further in this work. Finally, the two numerical strategies defined in Ch. 2 were compared on an under-resolved crenel of α_p : the positive and robust scheme PSI and the high order scheme TTGC used jointly with a stabilization technique. First, an artificial viscosity strategy has been proposed combining existing AV sensors implemented in AVBP, with a special attention to prevent negative α_p . The resulting sensor (CM5-T) and set up were used with the TTGC scheme and yield very reasonable robustness and accuracy. However, this test case shows that in its current implementation (low order temporal accuracy and lumped mass matrix), the PSI scheme diffuses more the solution than TTGC.

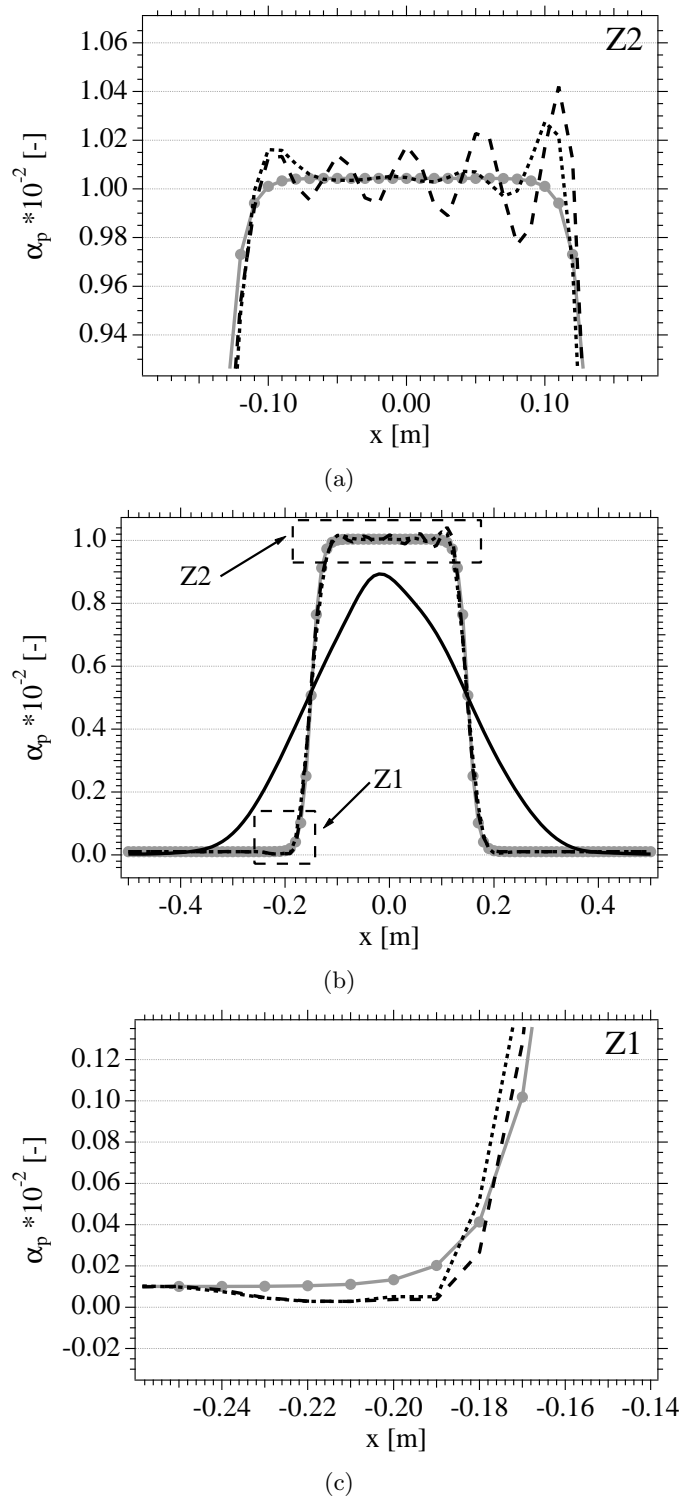


Figure 3.6: Particle volume-fraction crenel after one convective time (case C2). Comparison between the exact solution ($\text{---}\bullet\text{---}$) and Eulerians simulation carried out with different numerical strategies (*cf.* Tab. 3.2). PSI scheme (case C2-S2, —), TTGC scheme without $\epsilon^{(4)}$ (case C2-S1b, ---) and TTGC scheme with $\epsilon^{(4)}$ (case C2-S1c, ). The top and bottom figures correspond to the zooms Z2 and Z1 of the wide figure (medium), respectively.

Chapter 4

Particle-laden vortex

Contents

4.1	Description of the configuration	62
4.2	Governing equations of the carrier phase	63
4.3	Governing equations of the dispersed phase	63
4.3.1	Normalization procedure	65
4.3.2	Analytical solution when $St \ll 1$	66
4.4	Methodology	66
4.5	Particle-laden vortex simulations at low inertia	67
4.5.1	Comparison of EE and EL results with the analytical solution	67
	Evaluation of the CM5-T sensor along time	69
4.5.2	Effect of the mesh resolution	70
	Comparison with the analytical solution	71
	Discrete budget of the particle volume fraction	72
4.6	Vortex laden with inertial particles ($St = 1$)	74

As mentioned before, one key phenomenon in two-phase flows is the preferential concentration of particles. Depending on their inertia, particles heavier than the fluid are ejected from vortices and gather in high shear and weak vorticity areas. As a first step toward more complex multi-dimensional configurations, the test case of a two-dimensional vortex laden with solid particles is considered in this section. This test case gives some clues about how an initial homogenous field of α_p evolves in vortex characteristic of a turbulent flow. It can be considered as complementary to other two-dimensional test cases, such as particle-laden Taylor-Green vortices [27].

This test case allows us to investigate specifically the impact of particle inertia and to propose adapted numerical strategies. The two numerical strategies defined in Ch. 2 –the positive and robust scheme PSI and the high order scheme TTGC used jointly with a stabilization technique– are compared in this context. These two numerical strategies will be compared with two reference solutions, depending on the particle inertia. Indeed, an analytical solution of the particle

volume-fraction is proposed in the limit of small inertia. At moderate inertia, when the analytical solution is no longer valid, Lagrangian simulations are carried out from which Eulerian fields are interpolated with an adequate strategy [65].

After a detailed description of the configuration and of the analytical solution in Sec. 4.3.2, the methodology and test cases characteristics are summarized in Sec. 4.5. Then, the two numerical strategies are evaluated in Sec. 4.5, first at low inertia in Sec. 4.5.1 and finally at moderate inertia in Sec. 4.6. A specific attention is done on the mesh-resolution sensitivity of the results in Sec. 4.5.2.

4.1 Description of the configuration

A schematic representation of the test case is shown in Fig. 4.1. It consists in the simulation of an isotropic vortex, fixed at the center of a square box of length L_x . At $t = 0$, the field of α_p is homogeneous and the particle velocity is set equal to that of the carrier phase. The simulation is carried out on a mesh with $N_x \times N_x$ cells and all boundaries are periodic. The

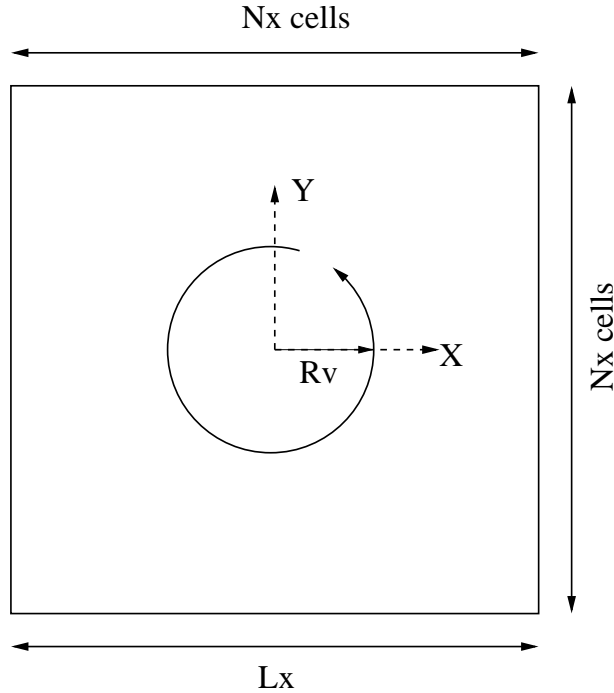


Figure 4.1: Schematic representation of the two-dimensional particle-laden vortex.

main characteristics of the vortex are summarized in Tab. 4.1.

Hereafter, the equations are written in cylindrical coordinates $(\vec{e}_x, \vec{e}_r, \vec{e}_\theta)$. The subscripts “f” and “p” will refer to the carrier and dispersed phase, respectively.

L_x	N_x	R_v	Γ_v	μ
$2 \cdot 10^{-2}$ m	100	$2 \cdot 10^{-3}$ m	$1.1472 \cdot 10^{-2}$ m ² .s ⁻¹	$1 \cdot 10^{-5}$ kg.m ⁻¹ .s ⁻¹

Table 4.1: Main parameters of the particle-laden vortex.

4.2 Governing equations of the carrier phase

The definition of carrier-phase governing equations of an isolated vortex is a classical problem. The stream function of an isotropic vortex is given by:

$$\Psi(r, \theta) = \Gamma_v e^{-\frac{r^2}{2R_v^2}} \quad (4.1)$$

where Γ_v and R_v are respectively the vortex strength and its characteristic radius (Tab. 4.1). The resulting velocity distribution is obtained through the velocity stream function relationship,

$$u_{f,r} = \frac{\partial \psi}{\partial \theta}, \quad u_{f,\theta} = -\frac{\partial \psi}{\partial r}. \quad (4.2)$$

Then, the radial and tangential velocity fields are given by:

$$u_{f,r} = 0 \quad (4.3)$$

$$u_{f,\theta} = \frac{\Gamma_v r}{R_v^2} e^{-\frac{r^2}{2R_v^2}}. \quad (4.4)$$

The maximum velocity induced by the vortex is $U_{f,max} = \sqrt{\max(u_{f,r})^2 + \max(u_{f,\theta})^2}$ and is obtained at $r = R_v$. Then,

$$U_{f,max} = \frac{\Gamma_v}{R_v \sqrt{e}}. \quad (4.5)$$

The vorticity distribution, defined as

$$\begin{aligned} \omega_g &= \frac{\partial}{\partial r} u_{f,\theta} - \frac{1}{r} \frac{\partial}{\partial \theta} u_{f,r} \\ &= \frac{\Gamma_v}{R_v^2} e^{-\frac{r^2}{2R_v^2}} \left[1 - \frac{r^2}{R_v^2} \right] \end{aligned} \quad (4.6)$$

is plotted in Fig. 4.2. According to [132], particles should concentrate in the region of low vorticity, around its minimal value at $r = \sqrt{3}R_v \simeq 3.46 \cdot 10^{-3}$ m. To conclude on the set up of the configuration, the gaseous field is simply frozen since we particularly address the evolution of the dispersed phase and since we assume a one-way coupling from the carrier to the dispersed phase. Consequently, the drag force induced by the carrier velocity is a constant source term.

4.3 Governing equations of the dispersed phase

The symmetric configuration of the test case ensures that the particle radial and tangential velocities, $u_{p,r}$ and $u_{p,\theta}$, are only function of the radial coordinate. In order to obtain a simple approximate solution, it is assumed that the tangential velocity of the particles remains equal

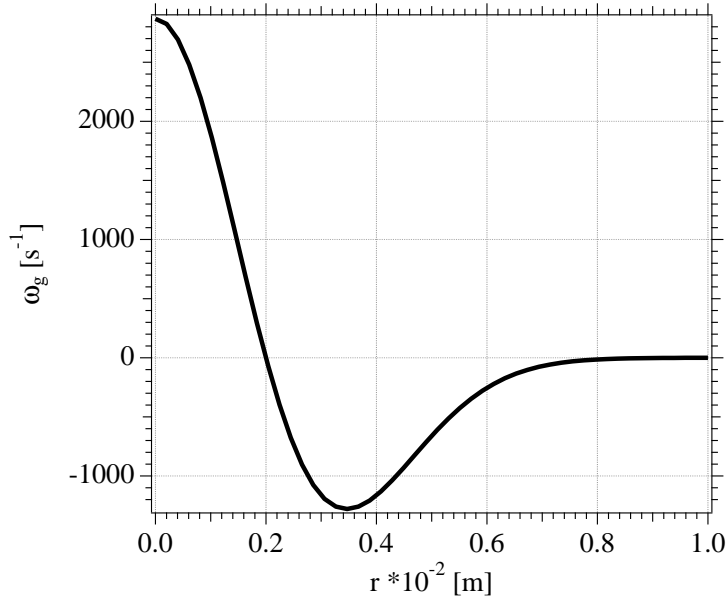


Figure 4.2: Vorticity of the carrier phase

to that of the gas: $u_{p,\theta} = u_{f,\theta}$. The problem is then reduced to find the volume fraction α_p and radial velocity $u_{p,r}$ of the dispersed phase satisfying the conservation equations. The particle velocity is defined as:

$$\mathbf{u}_p = u_{p,r}(r)\vec{e}_r + u_{f,\theta}(r)\vec{e}_\theta. \quad (4.7)$$

As a first step, the RUM is neglected and the particle temperature is assumed to be constant. The general continuity equation (Eq. 1.36) yields:

$$\frac{\partial}{\partial t}\rho_p\alpha_p + \frac{\partial}{\partial x}(\rho_p\alpha_p u_{p,x}) + \frac{1}{r}\frac{\partial}{\partial r}(\rho_p\alpha_p r u_{p,r}) + \frac{1}{r}\frac{\partial}{\partial \theta}(\rho_p\alpha_p u_{p,\theta}) = 0. \quad (4.8)$$

The general momentum conservation equations Eq. 1.37 written in non-conservative form and in cylindrical coordinates is:

$$\rho_p\alpha_p \left[\frac{\partial}{\partial t}u_{p,r} + u_{p,x}\frac{\partial}{\partial x}u_{p,r} + u_{p,r}\frac{\partial}{\partial r}u_{p,r} + u_{p,\theta}\frac{1}{r}\frac{\partial}{\partial \theta}u_{p,r} - \frac{u_{p,\theta}u_{p,\theta}}{r} \right] = \rho_p\alpha_p \frac{u_{f,r} - u_{p,r}}{\tau_p} \quad (4.9)$$

$$\rho_p\alpha_p \left[\frac{\partial}{\partial t}u_{p,\theta} + u_{p,x}\frac{\partial}{\partial x}u_{p,\theta} + u_{p,r}\frac{\partial}{\partial r}u_{p,\theta} + u_{p,\theta}\frac{1}{r}\frac{\partial}{\partial \theta}u_{p,\theta} + \frac{u_{p,\theta}u_{p,r}}{r} \right] = \rho_p\alpha_p \frac{u_{f,\theta} - u_{p,\theta}}{\tau_p} \quad (4.10)$$

Using Eq. 4.7 and the definition of the tangential gaseous velocity Eq. 4.4, Eqs. 4.8-4.9 reduce to the two simplified equations:

$$\frac{\partial}{\partial t}\alpha_p + \frac{1}{r}\frac{\partial}{\partial r}(\alpha_p r u_{p,r}) = 0 \quad (4.11)$$

$$\frac{\partial}{\partial t}u_{p,r} + u_{p,r}\frac{\partial}{\partial r}u_{p,r} + \frac{u_{p,r}}{\tau_p} = \frac{\Gamma_v^2 r}{R_v^4} e^{-\frac{r^2}{R_v^2}}. \quad (4.12)$$

Then, the radial velocity of particles (Eq. 4.12) is governed by a Burgers' equation with a stiff source term. This type of equation is typical of non-linear problems leading to shocks. That means that $u_{p,r}$ will inevitably lead to discontinuities, even if it is initialized with a smooth function. That discontinuity will impact the particle volume fraction through Eq. 4.11. Moreover, the particle radial velocity depends on the particle response time (third LHS of Eq. 4.12). That highlights the role of the particle inertia in the radial deviation of a particle, embedded in a vortex. This equation can be normalized in order to exhibit the Stokes number.

4.3.1 Normalization procedure

The normalized variables are:

- The normalized particle radial velocity: $u^* = \frac{u_{p,r}}{U_{f,max}}$ where $U_{f,max}$ is the maximum gaseous velocity defined in Eq. 4.5.
- The normalized radius: $r^* = \frac{r}{R_v}$
- The normalized time: $t^* = \frac{t}{r_v/U_{f,max}}$
- The normalized volume fraction: $\alpha_p^* = \frac{\alpha_p}{\alpha_0}$, where α_0 is the initial homogeneous particle volume fraction.

Then, the normalized equations of continuity and momentum equations read:

$$\frac{\partial}{\partial t^*} \alpha_p^* + \frac{1}{r^*} \frac{\partial}{\partial r^*} (\alpha_p^* r^* u^*) = 0 \quad (4.13)$$

$$\underbrace{\frac{\partial}{\partial t^*} u^*}_{(1)} + \underbrace{u^* \frac{\partial}{\partial r^*} u^*}_{(2)} + \underbrace{\frac{u^*}{St}}_{(3)} = r^* e^{-(r^*)^2+1}. \quad (4.14)$$

In Eq. 4.14, St denotes the Stokes number, defined as the ratio between the particle and the fluid characteristic time τ_p and τ_f , respectively (Eq. 1.11). The definition of the particle relaxation time in Stokesian regime is recalled:

$$\tau_p = \frac{\rho_p d_p^2}{18\mu_f}. \quad (4.15)$$

In this configuration, the characteristic time of the fluid τ_f is taken as one eddy-turnover time:

$$\tau_f = \frac{R_v}{U_{f,max}}. \quad (4.16)$$

Three limiting cases can be distinguished as a function of the Stokes number. In particular, an analytical solution of α_p^* and u^* can be found in the limit case of small particle inertia ($St \ll 1$).

4.3.2 Analytical solution when $St \ll 1$

When $St \ll 1$, the unsteady (term (1)) and non-linear (term (2)) contributions in Eq. 4.14 are negligible compared to the drag force (term (3)). Then, the radial velocity equation follows the steady equation:

$$u^* = Str^* e^{-(r^*)^2+1}, \quad (4.17)$$

which intensity is only driven by the Stokes number. When injected in Eq. 4.13, the volume fraction evolution follows the equation:

$$\frac{\partial}{\partial t^*} \alpha_p^* + f(r^*) \frac{\partial}{\partial r^*} \alpha_p^* + g(r^*) \alpha_p^* = 0, \quad (4.18)$$

where

$$f(r^*) = Str^* e^{-(r^*)^2+1} \quad (4.19)$$

$$g(r^*) = 2St(1 - (r^*)^2) e^{-(r^*)^2+1}. \quad (4.20)$$

It is reasonable to assume that α_p^* has a finite tangent at the center of the vortex. Then, when $r^* \rightarrow 0$, the product $f(r^*) \frac{\partial}{\partial r^*} \alpha_p^* \rightarrow 0$ and $g(0) = 2eSt$. Thus, the particle volume-fraction follows the simple ODE at the center of the vortex:

$$\frac{\partial}{\partial t^*} \alpha_p^* + 2eSt \alpha_p^* = 0, \quad (4.21)$$

which analytical solution is straightforward

$$\alpha_p^*(r^* = 0, t^*) = e^{-2eStt^*}. \quad (4.22)$$

Then, the particle volume-fraction continuously decreases at the center of a vortex and the higher the Stokes number, the faster it occurs. Moreover, Eq. 4.21 can be solved numerically using a simple forward in time, centered in space (FTCS) scheme to have an estimation of the solution in the whole domain. This solution is referred to as semi-analytical hereafter.

4.4 Methodology

Two main configurations of the particle-laden vortex are carried out, denoted V1 and V2, depending on the inertia of the particles (Tab. 4.2 and 4.3). Two sub cases, denoted V1a and V1b, are set up from V1 as a function of the mesh resolution N_x . Fluid characteristics, particle initial α_p and diameter are fixed for all configurations so that only the density of the particles sets the Stokes number via the particle relaxation time. The two numerical strategies presented in Ch. 3 are used: an high order scheme (TTGC [22]) stabilized with AV dissipation and a robust scheme (PSI [134]) with almost no AV. These two strategies are denoted S1 and S2 in this chapter, respectively, and their parameters are summarized in Tab. 4.4. The AV sensor employed for both strategies is CM5-T, with an α_p threshold $B_{min}(\alpha_p)$ four order of magnitudes lower than the initial particle-volume fraction α_p^0 (*cf.* Sec. 3.3.1).

In case V1, the particles inertia is sufficiently low ($St = 10^{-2}$) for the analytical solution to be valid. First, the resolution of the mesh is chosen relatively high so that the gradients of α_p are

expected to be sufficiently resolved (sub case V1a). The objective of V1a is to compare Eulerian and Lagrangian simulations (denoted V1a-EE and V1a-EL, respectively) to the analytical solution. Then, the mesh is coarsened to study the deviation of the Eulerian simulations from the analytical solution and the impact of the mesh resolution in the budget of α_p . This sub test case is denoted V1b. Finally, the particle inertia is increased ($St = 1$) so that the vortex empties faster and gradients of α_p are stiffer. This test case, denoted V2, is more restrictive for the numerical strategies and S1a is no longer sufficient to prevent a negative particle volume fraction. Then, the coefficient $\epsilon^{(2)}$ is slightly increased to prevent a negative α_p . This numerical set-up is denoted S1b. Thus, case V2 is a relevant test case to compare the two numerical strategies presented in Ch. 3: S1b and S2. Since the analytical solution is no longer valid at this mild inertia, Eulerian simulations will be compared with Lagrangian simulations (denoted V2-EL) which will be considered as the reference.

$U_{f,max}(\text{m}\cdot\text{s}^{-1})$	$\tau_f(\text{s})$	α_p^0	$d_p(\text{m})$
3.48	$5.75 \cdot 10^{-4}$	10^{-4}	10^{-5}

Table 4.2: Characteristics of the particle-laden vortex common for the three test cases.

	N_x	ρ_p (kg·m ⁻³)	τ_p (s)	St	Numerical strategy
V1a	100	10.348	$5.75 \cdot 10^{-6}$	10^{-2}	S1a
V1b	50	10.348	$5.75 \cdot 10^{-6}$	10^{-2}	S1a
V2	100	1034.8	$5.75 \cdot 10^{-4}$	1	S1b & S2

Table 4.3: Dispersed-phase parameters of the particle-laden vortex.

	scheme	AV sensor	$\epsilon^{(2)}$	$\epsilon^{(4)}$	$B_{min}(\alpha_p)$
S1a	TTGC	CM5-T	$5 \cdot 10^{-3}$	$5 \cdot 10^{-4}$	10^{-8}
S1b	TTGC	CM5-T	$1 \cdot 10^{-2}$	$5 \cdot 10^{-4}$	10^{-8}
S2	PSI	CM5-T	$5 \cdot 10^{-4}$	0	10^{-8}

Table 4.4: Numerical strategies used for the particle-laden vortex simulations.

4.5 Particle-laden vortex simulations at low inertia

4.5.1 Comparison of EE and EL results with the analytical solution

The evolution of α_p along time is presented in Fig. 4.3. First, particles are progressively ejected outside the vortex, positioned at the center of the box. While the vortex gets empty, particles accumulate at the fringe of the vortex, in a region of low vorticity. The gradient of particle volume fraction inside the vortex stiffens progressively. Then, particle accumulation reaches a steady state around $70 \tau_f$, where there are no more particles in the vortex, and no forces to diffuse

the particle accumulation. The qualitative agreement between the Eulerian and Lagrangian simulations is quite good.

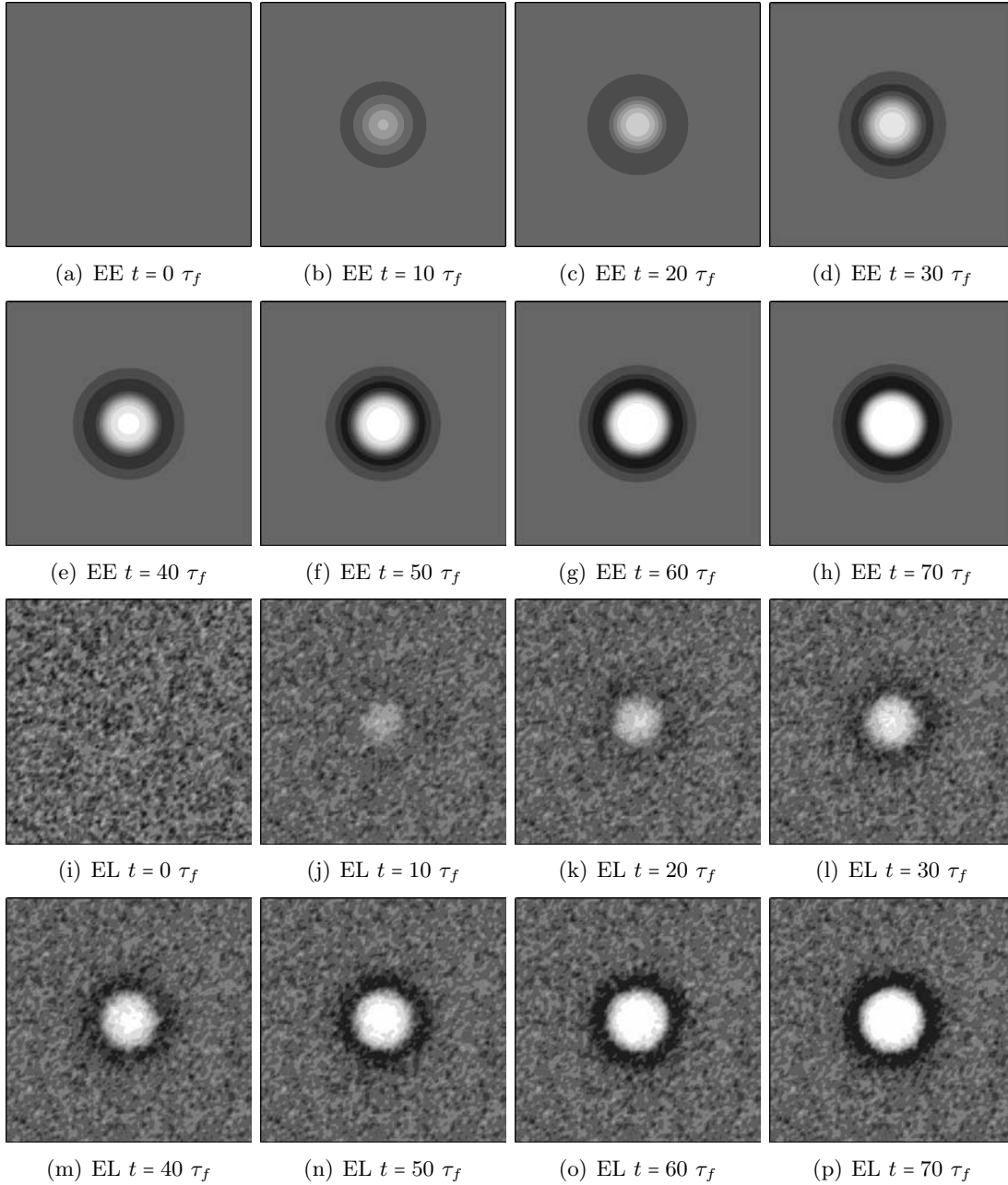


Figure 4.3: Comparison of Lagrangian (Bottom) and Eulerian (Top) particle volume-fraction fields for test case V1. Particle volume-fraction is proportional to darkness.

For a quantitative comparison, the particle volume fraction of cases V1a-EE and V1a-EL are plotted versus the analytical solution (Eq. 4.22) in Fig. 4.4. The particle volume fraction at the center of the vortex decreases rather slowly due to the low inertia of particles. Both Lagrangian

and Eulerian simulations agree satisfactorily with the analytical solution. As mentioned in

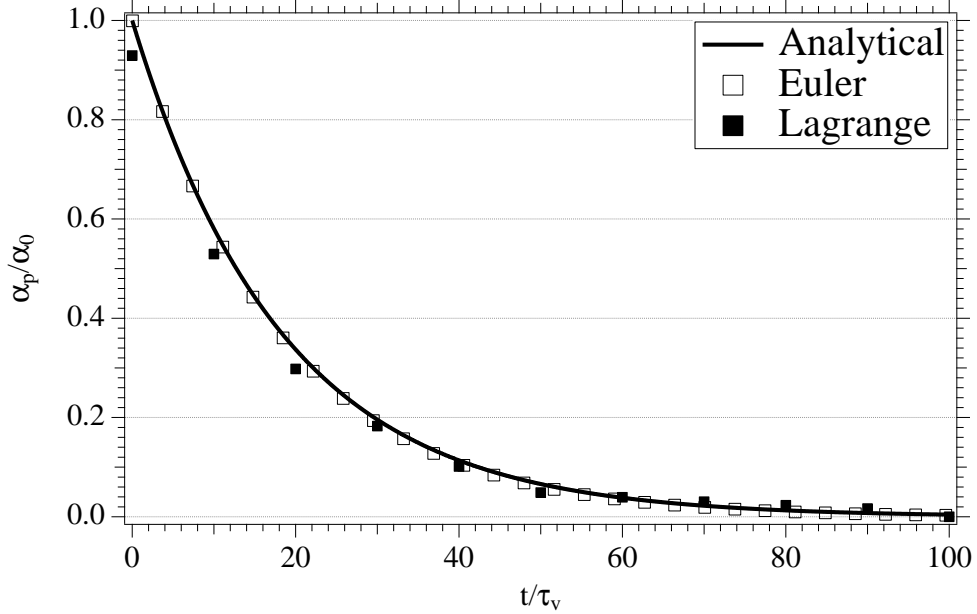


Figure 4.4: Particle volume fraction at the center of the vortex. Simulations V1a-EE and V1a-EL are compared to the analytical solution (Eq. 4.22).

Sec. 4.3.2, it is possible to obtain the solution of α_p in all the computational domain (not only at the center), resolving Eq. 4.13 with a simple finite-difference scheme. Note that the mesh must be sufficiently fine to ensure a good convergence and accuracy of this low-order scheme. This semi-analytical solution is compared with radial-averaged α_p of profiles at different times in Fig. 4.5(a). Overall, AVBP compares very well with the semi-analytical solution. It predicts the right position of the preferential accumulation of particles and its intensity. In particular, the agreement between V1a-EE and the semi-analytical solution is very good inside the vortex, where the particle volume fraction decreases as a function of time. Then, as the time increases, we observe a slight discrepancy in the maximum of α_p . For example, maximal α_p of V1a-EE at $t = 90$ is 15% smaller than the analytical solution. Accordingly with the literature [129], particles accumulate in region of minimal vorticity, which corresponds in this case to $r \simeq 3.46 \cdot 10^{-3}$ m (*cf.* Fig. 4.2). Radial averages of particle radial velocities agree also very well with the analytical solution, Fig. 4.5(b). Small differences of maximal $u_{p,r}$ are visible for later times.

Evaluation of the CM5-T sensor along time

The radial-averaged profiles of the two AV sensors, shown in Fig. 4.6(b) and Fig. 4.6(a) give some hints of how V1a-EE is stabilized. For the one-dimensional pure convection of a crenel of α_p , presented in Sec. 3.2, ζ_{grad} was several orders of magnitude larger than ζ_{extr} . That meant that the low resolution of the gradient of α_p was more problematic for the stability of the computation than the minimal α_p . Here, the issue is somewhat different. At this low inertia, the particle preferential concentration is limited, *i.e.* the gradient of α_p stays relatively smooth. Moreover,

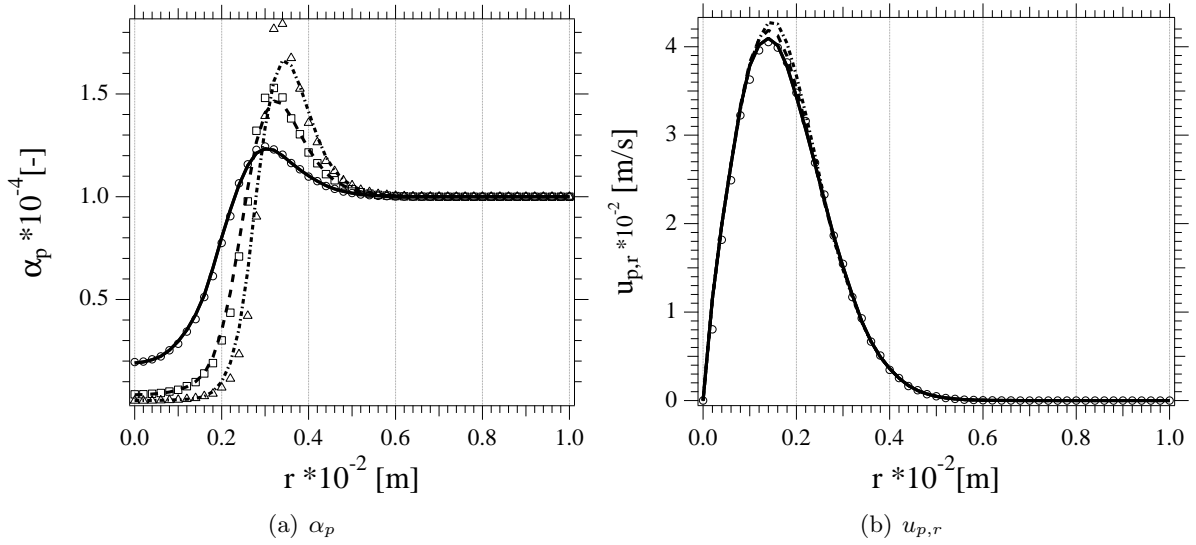


Figure 4.5: Quantitative comparison between V1a-EE results and the semi-analytical solution (symbols). Radial-averaged profiles of particle volume fraction (left) and radial velocity (right) at different times: $t = 30 \tau_f$ (—), $60 \tau_f$ (----) and $90 \tau_f$ (-.-).

the mesh resolution is relatively high (seven points in the inner gradient of α_p). Furthermore, contrary to the 1D test case, the particle-volume fraction is driven by the drag force. As the gas is frozen, α_p constantly decreases inside the vortex. The main numerical matter is then to prevent a negative α_p inside the vortex, more than to withstand a strong gradient of α_p . The profiles of ζ_{extr} and ζ_{grad} in Fig. 4.6(b) and Fig. 4.6(a) are coherent with this analysis. ζ_{extr} is one order of magnitude larger than ζ_{grad} , which shows that the numerical issue of close-to-zero α_p is more important than a possible under-resolved gradient. ζ_{extr} logically increases while times advances (α_p is decreasing, becoming closer to the threshold value $B_{\text{min}}(\alpha_p)$). Even if ζ_{grad} is small, it detects satisfactorily the gradient of α_p , around $r = R_v = 2 \cdot 10^{-3} \text{m}$. Thus, the CM5-T sensor behaves adequately in this configuration, which may be explained by a good choice of its parameters ($\epsilon^{(2)}, \epsilon^{(4)}$ and $B_{\text{min}}(\alpha_p)$).

This section compared EE and EL results with the analytical solution. It would be interesting to quantify the effect of the mesh resolution on the accuracy and stability of this sub-test case, all parameters being unchanged. This is to be done in Sec. 4.5.2.

4.5.2 Effect of the mesh resolution

The first mesh contains 100^2 cells, which yields around twenty nodes for one vortex diameter. This high resolution is unrealistic for most two-phase flow simulations and was only chosen to compare EE results with the analytical and EL solutions. For example, the case of homogeneous isotropic turbulence of Ch. 5 has around three points along one diameter for the smallest vortex. Then, it may be interesting to investigate the impact of a coarser mesh on the numerical strategy S1a. Case V1b is then performed on a 50^2 cell mesh, all parameters being unchanged.

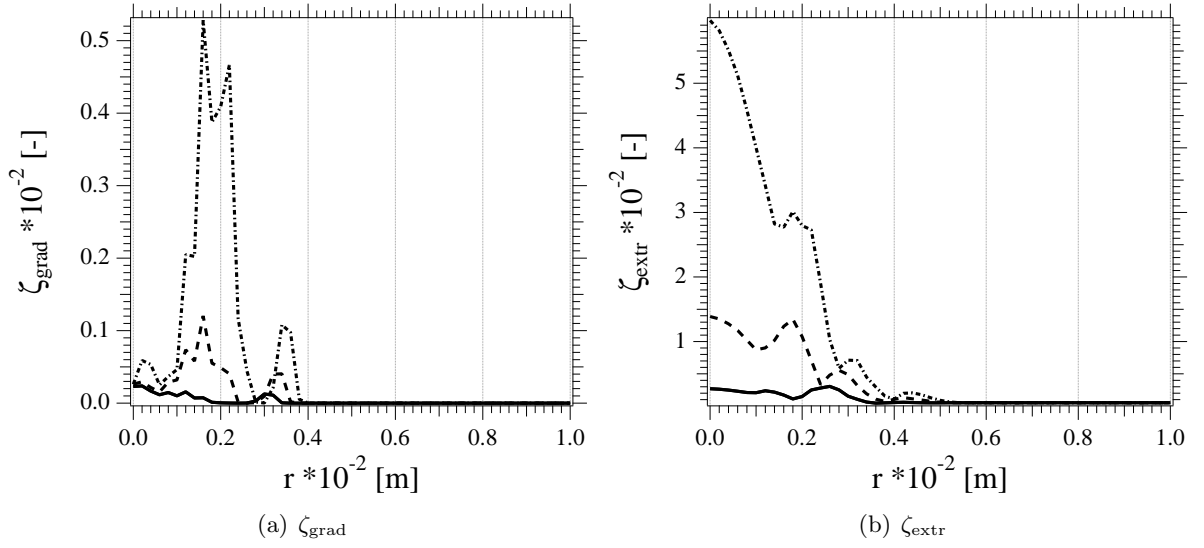


Figure 4.6: Radial-averaged profiles of ζ_{extr} (Fig. 4.6(b)) and ζ_{grad} (Fig. 4.6(a)) at different times for the V1a-EE simulation: 30 τ_f (—), 60 τ_f (---) and 90 τ_f (-.-).

Comparison with the analytical solution

First, the particle volume fraction and radial velocities of V1b are compared with their corresponding semi-analytical solutions in Fig. 4.7 at $t = 90 \tau_f$. Note that the semi-analytical solution is computed on the 100^2 cell mesh since the FTCS scheme is unstable on a 50^2 cell mesh.

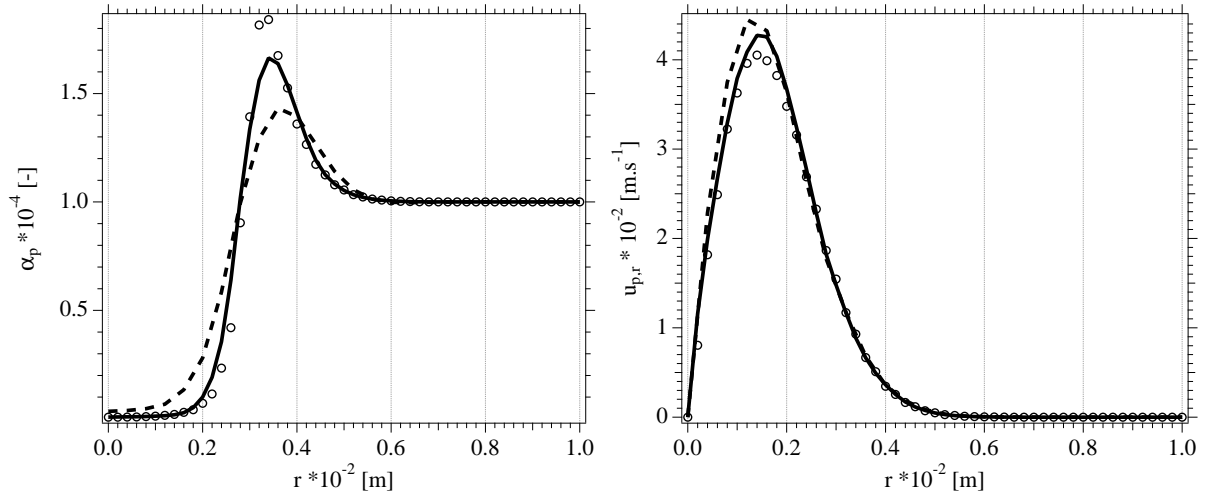


Figure 4.7: Influence of the mesh resolution on the particle volume fraction (left) and on the radial velocity at $t = 90 \tau_f$. The numerical strategy is the same for V1a-EE and V1b-EE. Comparison between V1a-EE (—), V1b-EE (---) and the analytical solution (○). The profiles are radial averaged.

As mentioned in Sec. 4.5.1, the profile of α_p (Fig. 4.7(a)) agrees very well with the semi-analytical solution for the fine mesh. Inner and outer gradients of α_p s are well captured. Only the maximal concentration at $r = 3.5 \cdot 10^{-3}$ m is slightly under-estimated. When the mesh is coarsened, the agreement between V1b-EE and the semi-analytical solution is still acceptable. The zones of vacuum and preferential concentration are satisfactorily reproduced. However, the inner and outer gradients of α_p are diffused and the concentration peak is around half that of the analytical solution. This is mainly due to the AV diffusion but is the price to pay for stability.

Particle radial velocities are similar between V1a-EE and V1b-EE. The agreement is satisfactory between EE simulations and the analytical solution, with only a slight discrepancy in the maximum $u_{p,r}$. V1b-EE over-estimates twice more $u_{p,r}$ than V1a-EE, with a 10% discrepancy. Now, the impact of the mesh resolution is quantified with the discrete budget of the transport equation of the particle-volume fraction.

Discrete budget of the particle volume fraction

The analysis of AV sensor profiles (as in Sec. 4.5.1) is helpful to check if they behave as expected, *i.e.* if their parameters are well chosen ($\epsilon^{(2)}, \epsilon^{(4)}$ and $B_{min}(\alpha_p)$). However, this diagnostic is not sufficient to quantify the real impact of the AV on the simulation. An estimation of the effective viscosity that is added by the AV operator is possible for the one-dimensional pure-convection test case [69]. This method was used by Sanjose [112] to discriminate numerical strategies (mesh resolution, AV sensors). However, it provides few informations about the AV weight in the transport of particle-volume fraction. Only the discrete budget of the α_p equation could do it, which has been done in the present work and is presented in this section.

The dispersed-phase governing equations are written in their nodal form in Eq. 2.21. Then, the nodal equation of the particle volume fraction reads:

$$\frac{\partial \alpha_p}{\partial t} = -(\mathbf{N}_j(\alpha_p) + \mathbf{D}_j^{(AV)}(\alpha_p)), \quad (4.23)$$

where $\mathbf{D}_j^{(AV)} = \mathbf{D}_j^{(2)} + \mathbf{D}_j^{(4)}$ is the global AV residual at node j .

These different terms have been extracted from AVBP in order to quantify their effective weight in the α_p equation. The discrete budget of α_p for the vortex at $t = 90 \tau_f$ is shown in Fig. 4.8 for both mesh resolutions.

First, the temporal derivative term is coherent with the profiles of α_p in Fig. 4.7(a). For example, four zones can be delimited for V1a-EE (Fig. 4.8(a)):

- $0 < r < 0.1 \cdot 10^{-2}$ m: $\partial \alpha_p / dt \sim 0$, meaning that α_p no longer decreases.
- $0.1 < r < 0.32 \cdot 10^{-2}$ m: $\partial \alpha_p / dt < 0$, α_p is decreasing. That corresponds to the emptying side of the vortex. $\partial \alpha_p / dt$ has a minimum around $r = 0.26 \cdot 10^{-2}$ m, just before the inner gradient of α_p , meaning that the gradient is stiffening.
- $0.32 \cdot 10^{-2} m < r < 0.54 \cdot 10^{-2}$ m: $\partial \alpha_p / dt > 0$. Particle volume fraction increases at the outer fringe of the vortex.
- $r > 0.54 \cdot 10^{-2}$ m: $\partial \alpha_p / dt = 0$, α_p is not perturbed by the rotation.

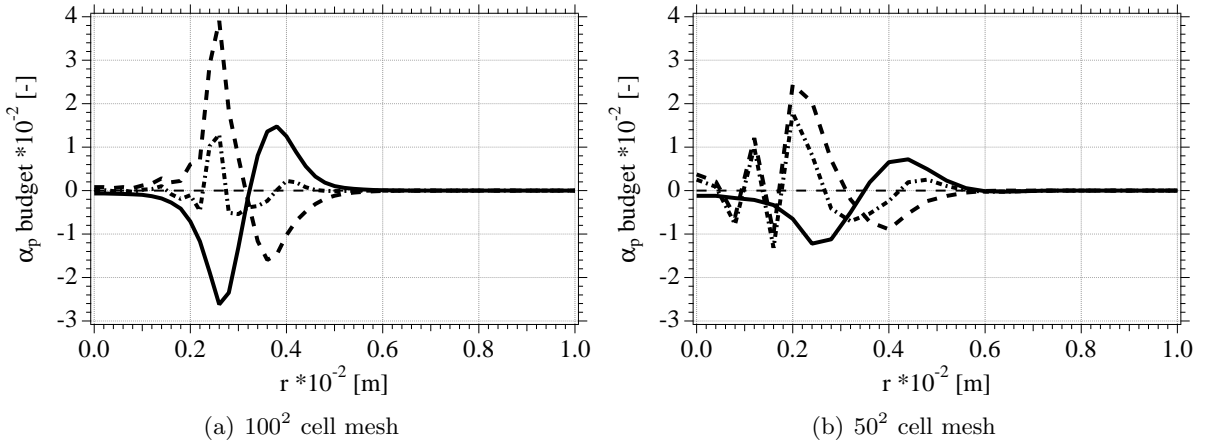


Figure 4.8: Discrete budget of the particle volume fraction at $90 \tau_f$. Influence of the mesh resolution. Comparison between V1a-EE (left) and V1b-EE (right) test cases. $\partial\alpha_p/\partial t$ (—), $\mathbf{N}_j(\alpha_p)$ (----), $-\mathbf{D}_j^{(AV)}(\alpha_p)$ (-.-.) and budget (-.-.-).

If no AV was added, $\partial\alpha_p/\partial t$ would be exactly equal and of opposite sign to \mathbf{N}_j , since there is no other term in the α_p transport equation in this case (no evaporation).

The AV residuals $-\mathbf{D}_j^{(AV)}$ seem to balance the convective residuals \mathbf{N}_j . Our personal understanding is that the effective weight of the AV in the α_p transport equation may be indicated by the ratio between $|\mathbf{D}_j^{(AV)}(\alpha_p)|$ and $|\mathbf{N}_j(\alpha_p)|$. By way of example, $|\mathbf{D}_j^{(AV)}(\alpha_p)|$ reaches almost one quarter of the nodal residual in V1a-EE. Moreover, the two peaks of $\mathbf{D}_j^{(AV)}(\alpha_p)$ locate at the same abscissa than the two peaks of $\partial\alpha_p/\partial t$, meaning that a maximum AV is actually applied where α_p increases or decreases the most.

The budget of α_p is also a powerful tool to quantify the impact of the mesh resolution. First, $\partial\alpha_p/\partial t$ extrema of V1b-EE (Fig. 4.8(b)) are half those of V1a-EE. Then, the conjugate emptying/accumulation of α_p at the inner and outer sides of the vortex will be lower for V1b-EE than for V1a-EE, which is coherent with the analysis of the α_p of profiles (Fig. 4.7). Note that $\partial\alpha_p/\partial t$ is not null and negative at the center of the vortex for V1b-EE, meaning that it is still emptying. Another difference between V1a and V1b is the quantity of AV applied in the simulation. For V1b, $\mathbf{D}_j^{(AV)}(\alpha_p)$ has almost the same amplitude than the convective residuals while it is limited for V1a, meaning that the AV yields as numerical dissipations as the convective scheme for the coarse mesh.

Remark that the effective application of AV is not fully correlated with the sensor amplitude (Fig. 4.6). That agrees with the theoretical definition of the AV operators in Sec. 2.3. The AV operators are linear functions of the sensor but also depends of the gradient of the conservative variables. AV is not applied if there are no gradients, even if the AV sensors are high.

4.6 Vortex laden with inertial particles ($St = 1$)

At low inertia, the vortex empties smoothly and gradients of α_p are then sufficiently well resolved with a 100^2 cell mesh. Then, particle density is increased to have a higher dynamic inertia, with a Stokes number –based on one eddy-turnover time– close to unity¹. This test case is denoted V2 (Tab. 4.3). Lagrangian simulations are carried out to validate the Eulerian results, since the analytical solution is no longer valid.

Fig. 4.9 presents the time evolution of α_p of the Lagrangian simulation (V2-EL). At this intermediate inertia, particles are ejected from the center of the vortex faster and further than at low inertia. The vortex is emptied in only six eddy-turnover time, which is about ten times less than at $St = 10^{-2}$. The particle concentration peak has a very high amplitude and is narrower than at low inertia. At $t = 8 \tau_f$, it represents seven times the initial α_p in amplitude. The resulting gradient of α_p is extreme, with several orders of magnitude between the maximal and minimal α_p at the inner part of the vortex and only one grid point (highlighted by solid circles at $t = 8 \tau_f$ in Fig. 4.9). Interestingly, at a certain time, the concentration peak begins to decrease. At $t = 10 \tau_f$, it is lower and wider than at $8 \tau_f$. One has to mention that particle collisions are not taken into account in this test case. With collisions, particle preferential concentration increases and the size of the cluster decreases (Fede and Pastis [51]), so that the concentration peak at $t = 8 \tau_f$ may have higher amplitude.

Now, Eulerian simulations of V2 are performed with the two strategies determined in Ch. 3. Note that case V2-EE crashes with the S1a strategy (TTGC+AV) before one eddy-turnover time. A negative α_p occurs at the center of the vortex, where the vorticity is maximum (Fig. 4.2). The AV sensor ζ_{extr} activates but $\epsilon^{(2)}$ is not high enough to withstand the quick vortex emptying. When $\epsilon^{(2)}$ is twice higher, V2-EE does not fail, which defines the S1b strategy in Tab. 4.4. This underscores one weakness of the S1 strategy: the coefficient $\epsilon^{(2)}$ is case sensitive. The same simulation is performed with the S2 strategy (PSI scheme + a small amount of 2nd-order AV). These two numerical strategies are compared with the reference solution in Fig. 4.10. At $t = 2\tau_f$, the gradients of α_p are mild and have enough grid resolution (Fig. 4.10(a)). Then, V2-EE with the strategy S1b is in perfect agreement with Lagrangian results. Eulerian simulation with S2 are comparatively not as good as S1b. The particle concentration peak is underestimated by 50%². As discussed previously, the particle concentration is maximum at $t = 8 \tau_f$ (Fig. 4.10(b)). This situation is challenging for numerical strategies as the gradient of α_p is high with only one grid point inside. At $t = 8\tau_f$, both numerical strategies S1b and S2 yield similar results, and both underestimate α_p by around 60% in comparison with the Lagrangian reference. The disappointing performance of S1b is assumed to be due to the large amount of $\epsilon^{(2)}$ necessary to stabilize the computation.

In this chapter, the test case of a two-dimensional particle-laden vortex has been presented. The originality of this test case is that an analytical solution of the particle volume fraction can

¹This threshold value is somehow indicative in this chapter. We are not trying to be in a regime where preferential concentration is maximal. This phenomenon is maximal for Stokes number around unity, but when the fluid characteristic time is based on the Kolmogorov scale [148] and not on one eddy-turnover time.

²Note that the miscalculation of α_p at the center of the vortex is due to an artefact of the PSI scheme. This scheme cannot distribute the residuals if the velocity equals exactly zero at a node, which is the case at $r = 0$. This situation seldom occurs in realistic situations.

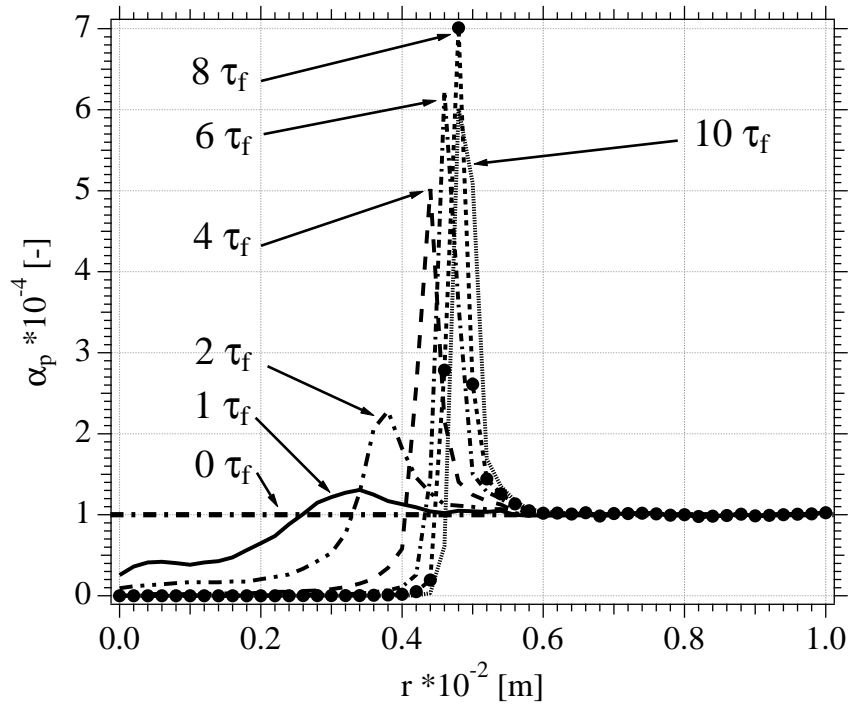


Figure 4.9: Lagrangian results (V2-EL). Radial-averaged profiles of particle volume fraction along time.

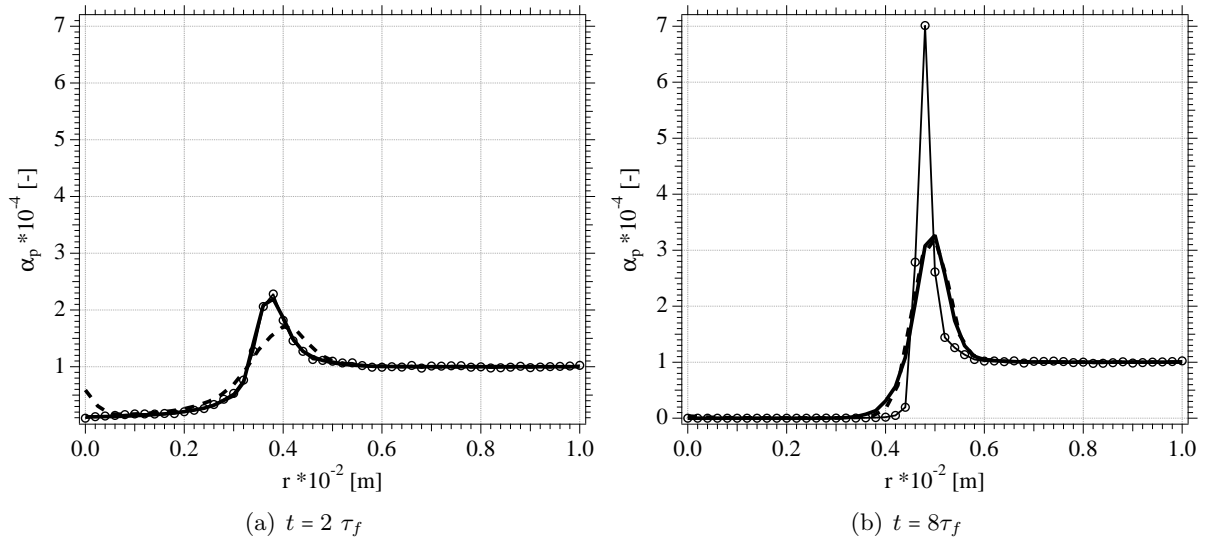


Figure 4.10: Particle volume fraction profiles at $t = 2 \tau_f$ and $t = 8 \tau_f$. Comparison between Lagrangian simulation ($\text{---}\circ\text{---}$) and Eulerian simulations with two different numerical strategies defined in Tab. 4.4. S1(TTGC scheme + AV): — and S2 (PSI scheme): - - - .

be derived at low inertia. Eulerian simulations carried out with the “TTGC + AV” strategy agree very well with this analytical solution. Moreover, a discrete budget of the equation of α_p allowed us to thoroughly quantify the impact of the AV and of the mesh resolution. Finally, numerical strategies were evaluated at higher inertia, where gradients of α_p are stiffer. The conclusion is that the “TTGC+AV” strategy can be as robust as the PSI scheme if the user parameter $\epsilon^{(2)}$ is well chosen. Moreover, the “TTGC+AV” strategy yields better or similar results than the PSI scheme, depending on how the gradient of α_p is resolved. The agreement between “TTGC+AV” strategy and the Lagrangian reference is remarkable for well resolved gradients of α_p , whereas it is alleviated for (very) stiff gradients.

Chapter 5

Particle-laden decaying Homogeneous Isotropic Turbulence

Contents

5.1	Brief theoretical background	78
5.2	Description of the test case	81
5.2.1	Initialization procedure	81
	Carrier phase	81
	Dispersed phase	83
5.3	Methodology	84
5.3.1	Previous work with the MEF with this test case	84
5.3.2	Present work: presentation of the test cases	85
5.4	Macroscopic evaluation of numerical strategies	86
5.5	Discrete kinetic energy balance of the dispersed phase	89
5.5.1	Analytical derivation	89
5.5.2	Application of this diagnostic to the test cases	91
5.6	Conclusions	93

Particle-laden Homogeneous Isotropic Turbulence (HIT) is a canonical test case to study the dynamics of two-phase flows. This configuration is academic, but contains a lot of the physics that occurs in a wide range of industrial applications. Numerous theoretical, experimental and numerical investigations have been carried out on this configuration. One can mention the fundamental work of Tchen [138] and Hinze [52] about the diffusion of passive scalars in stationary HIT and the extension to inertial particles. Seminal experimental and numerical investigations brought light on the particle dispersion in turbulent flows [106, 127]. Fundamental physical phenomena have been studied and understanding has been gained such as the particle preferential concentration [82, 131], the effect of particle collisions [149], the effect of the mass loading on the carrier turbulence [35, 130] or more recently the effect of particle concentration on evaporating sprays [100].

The numerical setup of this particle-laden HIT test case is one of those used by Kaufmann [63] to study the dispersion of particles as a function of their inertia. The Stokes number based the Kolmogorov scale is sufficiently high ($St_K \sim 2.5$) to be in regime of preferential concentration. Particle volume fraction gradients are very steep and the dispersed phase acts as a highly compressible phase. This setup has been used afterwards by Riber and Vié [103, 145] to investigate one step further the MEF and discriminate numerical strategies. It is now a validation test case for AVBP. Eulerian results are compared with a Lagrangian simulation performed by Moreau [83] (referred to as case A) with the NTMIX code [14]. Eulerian mesoscopic variables are extracted from these simulations using an adequate gaussian projection procedure [64] and are considered as the reference.

In this chapter, the test case of particle-laden decreasing HIT is used to discriminate the numerical strategies one step further than the two previous academic test cases in Chap. 3 and Chap. 4. First, the numerical setup of the gaseous field will be recalled in Sec. 5.2. Then, numerical strategies will be investigated using two diagnostics: (1) the particle concentration function $g_{pp} = \langle \tilde{n}_p^2 \rangle / \langle \tilde{n}_p \rangle^2$ in Sec. 5.4 and (2) the discrete budget of $\alpha_p \rho_p \tilde{u}_p^2$ in Sec. 5.5.

5.1 Brief theoretical background

The HIT configuration provides a theoretical framework where the scales of the turbulence can be defined analytically. Indeed, the assumed homogeneity (invariance by translation) and isotropy (invariance by rotation and reflexion) of the statistics greatly simplifies the definition of two-points correlations which are a powerful tool to describe the turbulence [18, 95]. Hereafter, the various scales of the turbulence are detailed to define the macroscopic quantities and dimensionless numbers used in this chapter. This section is partly excerpted from the fundamental book of Hinze [52].

The Eulerian spatial correlation tensor of fluid velocities defined at two points located at distance \mathbf{r} is defined as

$$\mathcal{R}_{f,ij}^E = \frac{\langle u_{f,i}(\mathbf{x} + \mathbf{r}, t) u_{f,j}(\mathbf{x}, t) \rangle}{2q_f^2(\mathbf{x}, t)} \quad (5.1)$$

where $\langle \cdot \rangle$ is the ensemble average operator and

$$q_f^2(\mathbf{x}, t) = \frac{1}{2} \langle u_{f,i}(\mathbf{x}, t) u_{f,i}(\mathbf{x}, t) \rangle \quad (5.2)$$

is the turbulent kinetic energy (TKE) of the fluctuating velocity $u_{f,i}$. The characteristic velocity of the turbulence is then defined as

$$u'_f = \sqrt{\frac{2}{3} q_f^2}. \quad (5.3)$$

A consequence of homogeneity is that $\mathcal{R}_{f,ij}^E$ is independent of the location \mathbf{x} and only depends of the radial distance \mathbf{r} between the two points x_i and x_j . Moreover, in isotropic configuration, $\mathcal{R}_{f,ij}^E$ can be written as a function of the Eulerian longitudinal and transverse autocorrelation

functions f and g of the fluid:

$$f(r, t) = \mathcal{R}_{f,11}^E \quad (5.4)$$

$$g(r, t) = \mathcal{R}_{f,22}^E \quad (5.5)$$

$$\mathcal{R}_{f,ij}^E = g(r, t)\delta_{i,j} + \frac{f(r, t) - g(r, t)}{r^2}r_i r_j, \quad (5.6)$$

where $r = |\mathbf{r}|$ in an orthonormal basis e_i . Then, longitudinal and transverse integral length scales of the fluid, denoted L_f^f and L_f^g , respectively, are:

$$L_f^f = \int_0^\infty f(r, t) dr \quad (5.7)$$

$$L_f^g = \int_0^\infty g(r, t) dr. \quad (5.8)$$

These integral length scales represent the distance from where two velocities are not correlated anymore. They are representative of large scales of the turbulence. On the contrary, Taylor scales are representative of dissipative scales of the turbulence and are defined as

$$\lambda_f^f(t) = \left(-\frac{1}{2} \frac{\partial^2 f}{\partial r^2} \Big|_{r=0, t} \right) \quad (5.9)$$

$$\lambda_f^g(t) = \left(-\frac{1}{2} \frac{\partial^2 g}{\partial r^2} \Big|_{r=0, t} \right). \quad (5.10)$$

Finally, the longitudinal and transverse integral and Taylor scales can be related [56] in isotropic incompressible flows by the relations:

$$L_f^f = 2 L_f^g \quad (5.11)$$

$$\lambda_f^f = \sqrt{2} \lambda_f^g. \quad (5.12)$$

In HIT, the TKE decreases progressively due the viscous dissipation, following the equation:

$$\frac{dq_f^2}{dt} = -\varepsilon_f. \quad (5.13)$$

In Eq. 5.13, ε_f refers to the dissipation rate of the TKE, defined as

$$\varepsilon_f = \frac{\nu_f}{2} \left\langle \frac{\partial u_{f,i}}{\partial x_j} + \frac{\partial u_{f,j}}{\partial x_i} \right\rangle, \quad (5.14)$$

where ν_f is the kinematic viscosity of the fluid. In HIT, the dissipation rate can be computed thanks to the transverse Taylor scale:

$$\varepsilon_f = \frac{15\nu_f u_f'^2}{(\lambda_f^g)^2}. \quad (5.15)$$

Then, the Eulerian integral length scale L_f^f may be approximated as a function of the macroscopic quantities

$$L_f^f \approx \frac{(u_f')^3}{\varepsilon_f}. \quad (5.16)$$

Finally, the turbulent Reynolds number is defined as the ratio of the inertia over the viscous effects:

$$\text{Re}_t = \frac{L_f^f u'_f}{\nu_f}. \quad (5.17)$$

The turbulent Reynolds number is based on the integral scale L_f^f , and consequently characterizes the turbulence of large eddies. The energy contained at these large scales is progressively transferred through the “energy cascade” to the smallest scales of the turbulence, characterized by the Kolmogorov scale η_K , and is finally dissipated by the viscosity. If the separation of scales between the largest and smallest scales of the turbulence is sufficient, the size, timescale τ_K and velocity v_K of the smallest eddies only depend on the kinematic viscosity and of the dissipation rate as:

$$\eta_K = \left(\frac{\nu_f^3}{\varepsilon_f} \right)^{1/4} \quad (5.18)$$

$$\tau_K = \left(\frac{\nu_f}{\varepsilon_f} \right)^{1/2} \quad (5.19)$$

$$v_K = (\nu_f \varepsilon_f)^{1/4}. \quad (5.20)$$

By definition, inertia is totally balanced by the viscous effect at the Kolmogorov scale, so that

$$\text{Re}_K = \frac{\eta_K v_K}{\nu_f} = 1 \quad (5.21)$$

Combining Eq. 5.16, 5.17, 5.20 and 5.21, the ratio of the largest scale of the turbulence to the Kolmogorov scale equals

$$\frac{L_f^f}{\eta_K} = \text{Re}_t^{3/4}. \quad (5.22)$$

Then, the separation of scales increases when the turbulent Reynolds number increases. Finally, the Eulerian integral time scale can be defined as

$$T_f^E = \frac{L_f^f}{u'_f}, \quad (5.23)$$

and represents one eddy turnover time of a large eddy of size L_f^f . Moreover, a Lagrangian characteristic time of the turbulence τ_f^t can be introduced as the time necessary for a fluid particle to be entirely uncorrelated. Haworth and Pope [48] suggest to model the general equation of the fluid particle velocity increment by a Langevin equation and proposes

$$\tau_f^t = \frac{q_f^2}{\beta_1 \varepsilon_f}, \quad (5.24)$$

where $\beta_1 = 2.075$ in a forced HIT. In this chapter, the characteristic time scale of the fluid is τ_f^t .

5.2 Description of the test case

All the simulations are performed on a cubic box of edge $2\pi L_{ref}$ where $L_{ref} = 10^{-3}$ m, with periodic boundary conditions in all directions. The carrier phase is composed of a synthetic gas similar to the air of density ρ_f and speed of sound U_{ref} . The kinematic viscosity ν_f has been chosen to yield the same acoustic Reynolds number $Re_{ac} = U_{ref}L_{ref}/\nu_f$ than the reference simulation (*cf.* Tab.5.1). Hereafter, all the physical parameters will be normalized by the

Re_{ac}	ν_f (m ² .s ⁻¹)	ρ_f (kg.m ⁻³)	μ_f (kg.m ⁻¹ .s ⁻¹)
200	$1.735 \cdot 10^{-3}$	1.164	$2.02 \cdot 10^{-3}$

Table 5.1: Characteristic variables of the carrier phase

variables summarized in Tab. 5.2. Normalized variables will be denoted by the superscript “+”.

U_{ref} (m.s ⁻¹)	L_{ref}	t_{ref} (s)
347	10^{-3}	$2.8818 \cdot 10^{-6}$

Table 5.2: Normalization variables of the carrier phase

Decaying HIT is a statistically unsteady test case and depends entirely on the initial conditions and parameters of the carrier and dispersed phases. First, the initialization procedure is detailed in Sec. 5.2.1.

5.2.1 Initialization procedure

The initialization of the two-phase flow simulations is performed in two steps, depicted in Fig. 5.1.

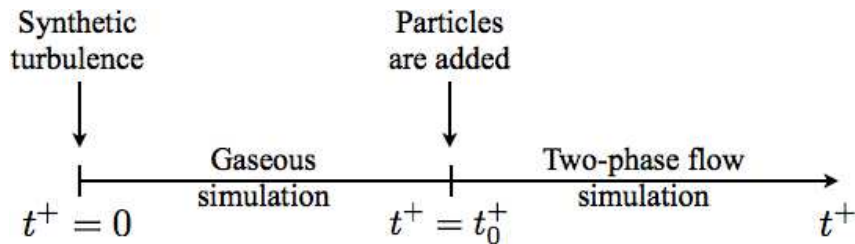


Figure 5.1: Methodology to initialize the particle-laden HIT configuration.

Carrier phase

First, a synthetic turbulent kinetic energy spectrum is created in the spectral space. The velocity field in the physical space is then computed from a reverse Fourier transform of the velocity field

in the spectral space. Most of the models consist in the approximate solution of the TKE equation in the Fourier space [18]:

$$\frac{\partial}{\partial t} E_f(k, t) = T_f(k, t) - 2\nu_f k^2 E_f(k, t), \quad (5.25)$$

where $E_f(k, t)$ is the TKE as a function of the wave number k and time t . In Eq. 5.25, T_f refers to the energy transfer from the largest scales to the smallest scales. Two models are widely used to create the TKE spectrum in the spectral space, namely the Passot-Pouquet (PP) [92] and the von Kármán Pao (VKP) [146] spectrum. As stressed by Riber [103], the VKP model is only valid for $Re_t > 200$, which is larger than the turbulent Reynolds number of the present configuration ($Re_t = 13.6$ at $t_0^+ = 4.233$). Therefore, the velocity field is initialized with the PP spectrum defined by the following approximation of the TKE:

$$E_f(k, t) = \frac{16u_{f,t}'^2}{k_e} \sqrt{\frac{2}{\pi}} \left(\frac{k}{k_e}\right)^4 e^{-2[k/k_e]^2}, \quad (5.26)$$

where $k_e = 2\pi/l_e$ is the characteristic wave number based on the most energetic length scale l_e and $u_{f,t}'$ is its associated velocity fluctuation. For this test case, these parameters have been chosen as $l_e^+ = 2.2$ and $u_{f,t}' = 0.1$.

Contrary to the VKP model, the PP spectrum only takes into account the most energetic eddies. Consequently, the TKE is gathered around k_e , so that the resulting spectra lacks of the most dissipative scales, as shown in Fig. 5.2. Moreover, this model yields a velocity field

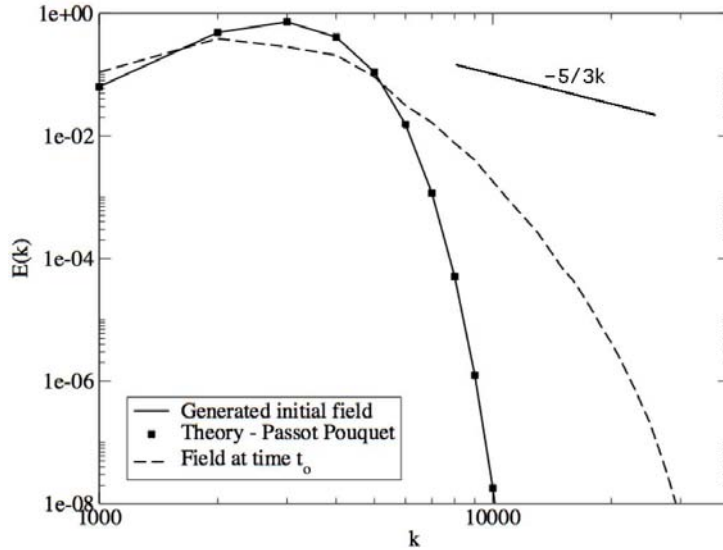


Figure 5.2: Comparison of the turbulent kinetic energy spectra at time $t^+ = 0$ (—) and at time $t^+ = t_0^+$ (-----).

that satisfies the continuity equation but not the momentum equation. Therefore, a common procedure is to carry out a gaseous simulation during a certain time to retrieve a solution satisfying the Navier-Stokes equations. Then, the simulation is carried out during roughly one

eddy turnover time of the large scales ($t_0^+ = 4.233$). Tab. 5.3 summarizes the main parameters of the carrier phase at $t_0^+ = 4.233$. After this time interval, the TKE spectrum presents a wider

quantity	# equation	
Re_t	(5.17)	13.6
q_f^2	(5.2)	$9.37 \cdot 10^{-3}$
ε_f	(5.14)	$1.08 \cdot 10^{-3}$
u_f	(5.3)	0.079
L_f^f	(5.4) or (5.16)	0.861 or 0.458
η_K	(5.18)	0.104
T_f^E	(5.23)	10.8
τ_K^+	(5.19)	2.15
$\tau_f^{t,+}$	(5.24)	4.19

Table 5.3: Main parameters of the carrier phase at $t_0^+ = 4.233$, when the particles are added. Excerpted from [83].

range of scales (Fig. 5.2) than the initial condition. Part of the energy has been transferred from the largest eddies to the smallest scales of the turbulence. However, the separation of scales is moderate at this relatively low Re_t , so that the TKE spectra lacks of the inertial subrange where $E_f(k) \propto k^{-5/3}$. Nevertheless, the carrier phase is considered sufficiently relevant of a turbulent flow at $t = t_0^+$ to add the particles.

Dispersed phase

The dispersed phase is sufficiently diluted to assume that it has no impact on the carrier phase (one-way coupling). Moreover, the ratio of the density of the dispersed to the carrier phase is sufficiently high to assume that only drag force acts upon the dispersed phase and that other forces are negligible. With these assumptions, the dispersed phase dynamics only depends of the particle inertia and of the initial condition.

The main particles properties are summarized in Tab. 5.4. The Stokes number used in this chapter is based upon the particle relaxation time τ_p (Eq. 1.9) and the fluid Lagrangian time scale τ_f^t (Eq. 5.24) evaluated when the particles are embedded in the gaseous flow (*cf.* Tab. 5.3). It is roughly one half of the Stokes number based on the Kolmogorov time scale.

The initial distribution of particles is uniform with $\alpha_p = 2.7 \cdot 10^{-2}$. Since particles are injected at the same velocity than the carrier phase. Then, there is no drag at $t = t_0^+$. Note that this particle volume fraction is larger than the previous one-dimensional and two-dimensional test cases in this manuscript Chap. 3 and Chap. 4. This has no impact on the dynamics of the particles as collisions are not taken into account. The initial RUE is arbitrarily fixed at a non-null value of 0.1 so that it can increase during the computation. Indeed, the production and destruction terms in the RUE equation (Eq. 1.52) are linearly related with the RUE. The RUE would remain zero if it is initialized at zero.

τ_p^+	$St = \tau_p^+ / \tau_f^{t,+}$	$St_K = \tau_p^+ / \tau_K^+$	$\rho_p (\text{kg} \cdot \text{m}^{-3})$
5.47	1.3	2.54	1916
$d_p (m)$	$\tilde{n}_p (\text{m}^{-3})$	$\tilde{u}_{p,i} (\text{m} \cdot \text{s}^{-1})$	$\delta\theta_p (\text{m}^2 \cdot \text{s}^{-2})$
$17.3 \cdot 10^{-6}$	10^{13}	$u_{f,i}$	0.1

 Table 5.4: Dispersed phase properties when solid particles are embedded at $t = t_0^+$.

5.3 Methodology

5.3.1 Previous work with the MEF with this test case

The simulations performed by Kaufmann [63] used the Lax-Wendroff (LW) scheme [73] for both the carrier and the dispersed phase. At this time, it was the only scheme available for the dispersed phase in AVBP and AV models had not been implemented for the dispersed phase. The LW scheme is known to smooth the gradients and to be dispersive [69]. For the simulations with the high compressible effect, the LW scheme was not sufficiently stable to handle the steep gradients due to the particle concentration. To deal with this numerical difficulty, Kaufmann introduced a subgrid bulk viscosity in the momentum equations to act on the compressible part of the mesoscopic velocity. The mesoscopic and RUM particle kinetic energy were in good agreement with the Lagrangian reference. However, the particle concentration, characterized by the dispersion function [124]

$$g_{pp} = \frac{\langle \tilde{n}_p^2 \rangle}{\langle \tilde{n}_p \rangle^2} \quad (5.27)$$

was strongly under-estimated, as shown in Fig. 5.3.

Riber [103] showed the superiority of the TTGC scheme in comparison with the LW scheme, if an adequate AV model (JR model) was used. The stability and accuracy of the simulation were increased. In particular, the LW and TTGC dissipations of the gaseous TKE were compared thanks to the discrete budget of the TKE equation, following [86]. A RUE flux limiter was introduced to prevent non-physical negative value of RUE. With that strategy, the subgrid bulk viscosity of Kaufmann was shown to be no longer necessary. The RUM model VISCO (presented in Sec. 1.3.3) predicted accurately the RUE levels. Although better than with the LW scheme, the maximum segregation of particles computed with the TTGC scheme was still under-estimated (*cf.* Fig. 5.3).

Similarly to Riber [103], Vié [145] used the time evolution of g_{pp} to discriminate Eulerian simulations with different AV models in comparison with the Lagrangian reference. It was shown that the modification of the CM AV sensor (*cf.* Sec. 2.3.1), coupled with the TTGC scheme, improved significantly the Eulerian simulations. In particular, Eulerian simulations with the CM10-S AV model captured very well the particle segregation (*cf.* Fig. 5.3). A numerical clipping of α_p was used to prevent negative values. The influence of the mesh resolution was not studied.

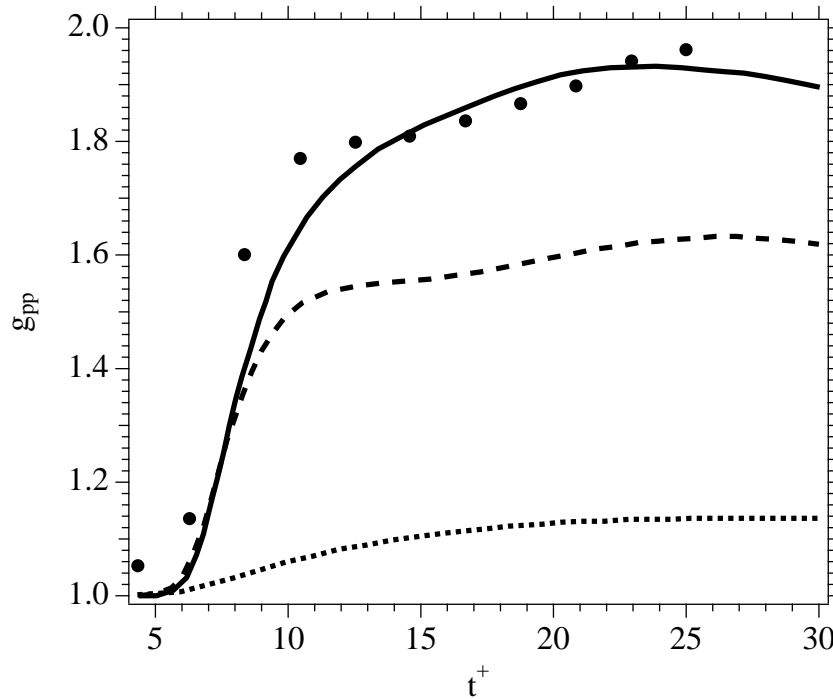


Figure 5.3: Time evolution of the particle concentration, characterized by the function g_{pp} . Comparison between Lagrangian results (\bullet) and non-exhaustive “best” results of Kaufmann [63] (.....), Riber [103] (-----) and Vié [145] (—).

5.3.2 Present work: presentation of the test cases

As mentioned before, this test case already brought insights about the numerical strategies used to perform two-phase flow simulations with AVBP. However, several points have not been studied yet.

For example, the PSI scheme performance has only been quantified on simple test cases by Lamarque [69] and Sanjose [112] and in Chap. 3 and Chap. 4 of the present work. It could be interesting to evaluate this scheme on a more realistic turbulent test case. Moreover, as mentioned in Sec. 2.2.3, the PSI scheme is now plugged with the TTGC scheme for the carrier phase. Thus, two-phase flow simulations carried out with PSI and TTGC for the dispersed phase can be directly compared as the carrier phase is the same. Then, two Eulerian simulations are performed with the two numerical strategies outlined in Chap. 3 and Chap. 4, denoted T1 and T2 in Tab. 5.5. Cases T1 and T2 are performed on two different meshes¹, denoted M1H and M1T, respectively. The only difference between M1H and M1T is the type of elements, as it can be seen in Tab. 5.6. Indeed, the PSI scheme has not been implemented yet for hexahedral elements in AVBP. Note that the mean space step is the same between M1H and M1T. Furthermore, the influence of the AV sensor is investigated (case T3), similarly to Vié [145]. All parameters are

¹It has been verified that case T1 yields the same results on M1H and M1T. The TTGC scheme performances are rather the same on hexahedral and tetrahedral meshes [15] if the space step is similar.

unchanged between configurations T1 and T3 except the sensor on the gradients. Finally, the mesh is refined to study its influence on Eulerian simulations (case T4).

keyword	mesh	scheme	AV sensor	$\epsilon^{(2)}$	$\epsilon^{(4)}$
T1	M1H	TTGC	CM5-T	0.115	$5 \cdot 10^{-3}$
T2	M1T	PSI	CM5-T	$1 \cdot 10^{-2}$	0
T3	M1H	TTGC	CM10-T	0.115	$5 \cdot 10^{-3}$
T4	M2H	TTGC	CM5-T	0.115	$5 \cdot 10^{-3}$

Table 5.5: Characteristics of the particle-laden HIT test cases

keyword	type	resolution	Δx_{min}	Δx_{max}	# of elements
M1H	hexa	64^3	$9.82 \cdot 10^{-5}$	$9.82 \cdot 10^{-5}$	262144
M1T	tetra	64^3	$3.89 \cdot 10^{-5}$	$2.99 \cdot 10^{-4}$	1479900
M2H	hexa	128^3	$4.91 \cdot 10^{-5}$	$4.91 \cdot 10^{-5}$	2097152

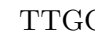
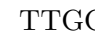
Table 5.6: Mesh characteristics

The four test cases are performed with the same initial condition, detailed in Sec. 5.2. The RUM model is VISCO (presented in Sec. 1.3.3). Note that the AV parameter $\epsilon^{(2)}$ has been minimized to ensure both robustness and accuracy of the computations.

First, the particle concentration function g_{pp} (Eq. 5.27) is used to compare the test cases. The particle concentration function of the test case Tx, denoted g_{pp}^{Tx} , will be compared with that from a Lagrangian simulation, denoted g_{pp}^{EL} , carried out by Moreau [83] with the NTMIX code [14].

5.4 Macroscopic evaluation of numerical strategies

The time evolution of g_{pp}^{Tx} and g_{pp}^{EL} is shown in Fig. 5.4. First, g_{pp}^{EL} exhibits two inflection points. It increases quickly after that particles have been added, reaches a plateau around $t^+ = 10$ and increases again around $t^+ = 17$. Unfortunately, no Lagrangian data are available after $t^+ = 25$. Then, the decline of α_p after having reached a maximum, observed in the particle-laden vortex (Sec. 4.6), cannot be confirmed in the HIT with the Lagrangian data. Nevertheless, Eulerian simulations agree satisfactorily with the Lagrangian reference. However, none of the Eulerian results capture the two inflections. The Eulerian results may be compared step by step:

- **Impact of the convective scheme:** TTGC (T1, ) vs PSI (T2, ). Eulerian results are similar with the TTGC and PSI scheme when the value of $\epsilon^{(2)}$ is tuned ($\epsilon_{T1}^{(2)} \ll \epsilon_{T2}^{(2)}$). At the beginning of the computation, preferential concentration is slightly lower with PSI than with TTGC. This trend reverses around $t^* = 13$. This is coherent with the results of the particle-laden vortex in Sec. 4.6, where PSI initially under-estimated the maximal α_p and then agreed satisfactorily with TTGC.

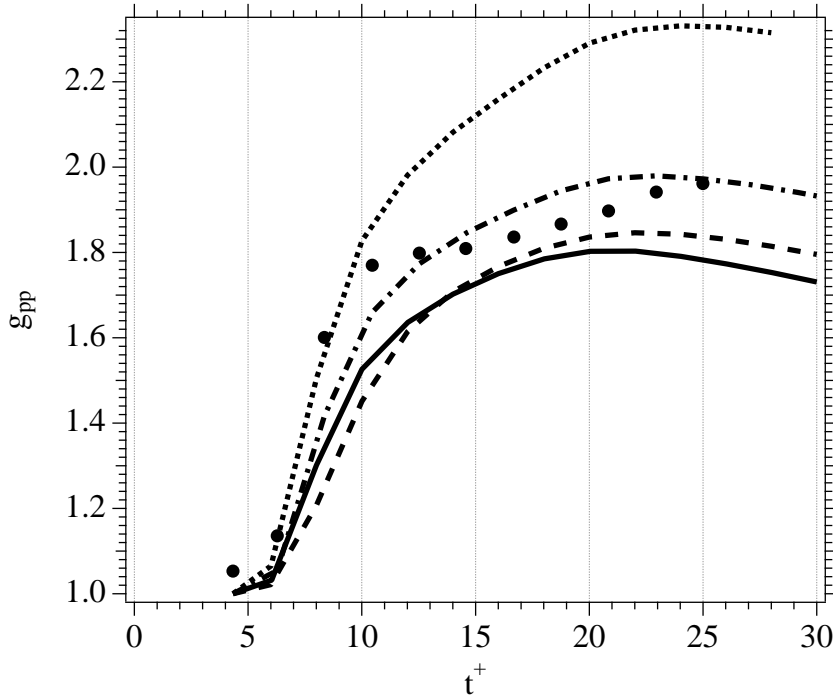


Figure 5.4: Time evolution of the particle concentration, characterized by the function g_{pp} (Eq. 5.27). Comparison between Lagrangian results (\bullet) and Eulerian simulations: T1 (—), T2 (---), T3 (-.-) and T4 (.....)

- **Influence of the AV sensor:** CM5-T (T1, —) vs CM10-T (T3, -.-). The tuning of the CM family of AV sensors (Sec. 2.3.1) does have an impact on the particle preferential concentration, as reported by Vié [145]. Eulerian results with the CM10-T sensor are in better agreement with the Lagrangian reference than the T1 test case. The increase of g_{pp} at the early stage of the simulation is well captured by T3. That underscores again the importance of the AV in the strategy “TTGC + AV”. Results can be very good with an adapted sensor and a tuned $\epsilon^{(2)}$. Note that case T2 (PSI) yields the same results with the sensor CM5-T and CM10-T.
- **Effect of the mesh resolution:** coarse mesh M1H (T1, —) vs fine mesh M2H (T4,). First, the CM10-T sensor no longer provides enough stability when the mesh is refined. The computation crashes after a few iterations. That is the reason why the CM5-T sensor is used in T4. While the particle concentration is under-estimated for $t^* < 9$ with the coarse mesh, it is in good agreement with the Lagrangian reference with a finer mesh. However, the over-estimation of g_{pp}^{T4} for $t^* > 9$ in comparison with g_{pp}^{EL} (+20%) is disappointing. Several reasons may explain this result.

On the one hand, Lagrangian simulations have been performed on M1H whereas T4 is carried out on M2H. Comparing Eulerian results carried out on a 128^3 cell mesh with Lagrangian results performed on a 64^3 cell mesh may be questioned. Unfortunately, La-

Lagrangian data are not available on the finer mesh. The particle segregation is driven by the intricate relationship between the particle inertia and the surrounding turbulent structures. Since the particle inertia is fixed between cases T1 and T4, an increase of preferential concentration could be explained by different carrier phases. However, the carrier phase is already converged on M1H, as shown in Fig. 5.5 where the mean and local TKE of the carrier phase obtained with T1 and T4 are compared. Discrepancies between the two meshes are negligible. There is no physical reason that the Lagrangian particle field would not be the same between M1H and M2H. Nevertheless, Lagrangian data are actually projections of Lagrangian fields on a Eulerian mesh. If particle clusters are thinner than the mesh space step, the interpolation on a coarse mesh would yield a lower projected particle field. Thus, available Lagrangian data on M1H may be lower than the “true” field.

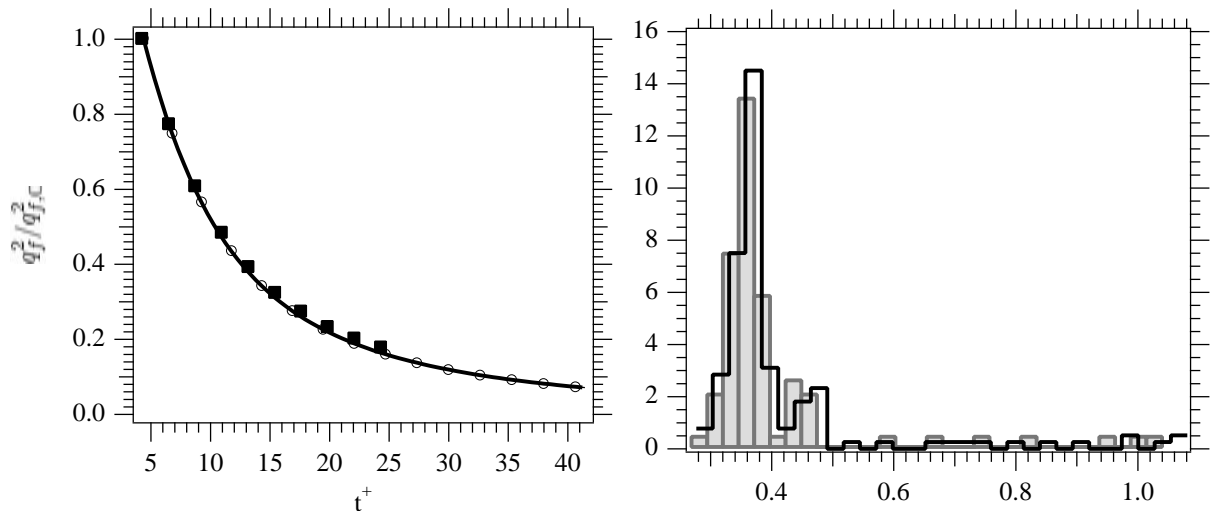


Figure 5.5: Influence of the mesh resolution on the carrier phase. Left: Normalized mean turbulent kinetic energy. (T1 (coarse mesh): \blacksquare , T4 (fine mesh): \circ , EL: \blacksquare). Right: PDF of the turbulent kinetic energy at the center of the domain (T1 (coarse mesh): \square , T4 (fine mesh): \blacksquare).

On the other hand, assuming that the Lagrangian data are ok, the over-estimation of the particle preferential concentration on the finer mesh may come from the Eulerian approach. Contrary to the Lagrangian approach, where particles are tracked individually and only depend on the carrier phase, Eulerian particle fields are conditioned by the resolution of the mesh. Indeed, there is no equivalent of the Kolmogorov scale for the dispersed phase at which smallest scales are dissipated by the viscosity. The dissipation of the smallest structures is driven by the mesh step through the natural dissipation of the convective scheme or through the stabilization strategies (AV). The discrete budget of particle volume fraction in Sec. 4.5.2 showed that the AV decreases when the mesh gets finer. Then, the dissipation due to numerics may be lower with M2H than with M1H.

An other reason could be the RUM model. On average, the VISCO model provides –in this configuration– very good results of mesoscopic and uncorellated kinetic energy compared

with Lagrangian data [103]. However, preferential concentration is a local phenomenon and the VISCO model has not been validated with local comparison of RUE in this HIT. Masi [78] showed recently that a good evaluation of the RUE by the RUM model in average does not mean directly that the local transfer between mesoscopic and uncorrelated energy is well captured. Moreover, it is now known that the AV strategy used in the former Eulerian simulations of this configuration [103] were not adapted [145]. Then, AV may do part of the RUM model's job locally. These are only assumptions. One way to thoroughly confirm them is to write the discrete budget of particle MKE, which is done in Sec. 5.5.

5.5 Discrete kinetic energy balance of the dispersed phase

The particle dispersion function g_{pp} is undoubtedly useful to compare numerical setups. However, it hardly differentiates the impact of numerics (scheme, AV, mesh) from that of physics (drag force, RUM). These terms can be isolated with the derivation of the discrete MKE balance of the dispersed phase.

5.5.1 Analytical derivation

The discrete balance equation of the total kinetic energy of the carrier phase was proposed by Moureau [86] to quantify the effect of the numerical scheme and artificial viscosity in the context of LES. Following the same methodology, the discrete balance of the MKE of the dispersed phase is derived².

The starting point is the splitting of the temporal derivatives of $\rho_p \alpha_p \tilde{u}_{p,i}^2$ as a function of the temporal derivatives of the particle volume fraction and momentum as:

$$\frac{1}{2} \frac{\partial \rho_p \alpha_p \tilde{u}_{p,i}^2}{\partial t} = \tilde{u}_{p,i} \frac{\partial \rho_p \alpha_p \tilde{u}_{p,i}}{\partial t} - \frac{\tilde{u}_{p,i}^2}{2} \frac{\partial \rho_p \alpha_p}{\partial t}. \quad (5.28)$$

The time derivatives of the RHS of Eq. 5.28 are written in their nodal form, taking into account the AV terms as presented in Eq. 2.21:

$$\frac{\partial \rho_p \alpha_p}{\partial t} = -(\mathbf{N}_j(\rho_p \alpha_p) + \mathbf{D}_j^{(AV)}(\rho_p \alpha_p)) \quad (5.29)$$

$$\frac{\partial \rho_p \alpha_p \tilde{u}_{p,i}}{\partial t} = -(\mathbf{N}_j(\rho_p \alpha_p \tilde{u}_{p,i}) + \mathbf{D}_j^{(AV)}(\rho_p \alpha_p \tilde{u}_{p,i})) + \mathbf{S}_{j,drag} + \mathbf{S}_{j,RUM}, \quad (5.30)$$

where $\mathbf{S}_{j,drag}$ and $\mathbf{S}_{j,RUM}$ are the nodal residuals of the drag force and RUM terms in the momentum equation at node j . The AV operator $\mathbf{D}_j^{(AV)}$ is the sum of the 2nd and 4th-order AV terms

$$\mathbf{D}_j^{(AV)} = \mathbf{D}_j^{(2)} + \mathbf{D}_j^{(4)}. \quad (5.31)$$

²It is actually the MKE multiplied by the particle volume fraction. The budget of this quantity is easier to obtain in AVBP as it transports the conservative variables α_p and $\alpha_p \tilde{u}_{p,i}$. Their respective residuals are directly available in the code.

Then, the particle velocity $\tilde{u}_{p,i}$ and square velocity $\tilde{u}_{p,i}^2$ in Eq. 5.28 are approximated by the arithmetic and geometric means, denoted respectively $v_i^{(1)}$ and $v_i^{(2)}$:

$$\tilde{u}_{p,i} \simeq \frac{\tilde{u}_{p,i}^{n+1} + \tilde{u}_{p,i}^n}{2} = v_i^{(1)} \quad (5.32)$$

$$\tilde{u}_{p,i}^2 \simeq \frac{\tilde{u}_{p,i}^{n+1} \tilde{u}_{p,i}^n}{2} = v_i^{(2)}. \quad (5.33)$$

Finally, the discrete equation of the particle kinetic energy budget is obtained combining Eq. 5.28-5.33:

$$\begin{aligned} \frac{\partial \rho_p \alpha_p \tilde{q}_p^2}{\partial t} &= -\left(v_i^{(1)} \mathbf{N}_j(\rho_p \alpha_p \tilde{u}_{p,i}) - v_i^{(2)} \mathbf{N}_j(\rho_p \alpha_p)\right) \\ &\dots -\left(v_i^{(1)} \mathbf{D}_j^{(AV)}(\rho_p \alpha_p \tilde{u}_{p,i}) - v_i^{(2)} \mathbf{D}_j^{(AV)}(\rho_p \alpha_p)\right) \\ &\dots +v_i^{(1)} \mathbf{S}_{j,RUM}(\rho_p \alpha_p \tilde{u}_{p,i}) \\ &\dots +v_i^{(1)} \mathbf{S}_{j,drag} \end{aligned} \quad (5.34)$$

The budget equation of the mean particle kinetic energy is obtained by a spatial average over the computational box of Eq. 5.35, yielding:

$$-\left\langle \frac{\partial \rho_p \alpha_p \tilde{q}_p^2}{\partial t} \right\rangle = \varepsilon_{scheme} + \varepsilon_{drag} + \varepsilon_{RUM} + \varepsilon_{AV}, \quad (5.35)$$

where ε_{scheme} , ε_{drag} , ε_{RUM} and ε_{AV} refer to the dissipation due to convection (numerical scheme), drag force, RUM and artificial viscosity. These dissipation terms are defined as

$$\begin{aligned} \varepsilon_{scheme} &= \left\langle v_i^{(1)} \mathbf{N}_j(\rho_p \alpha_p \tilde{u}_{p,i}) - v_i^{(2)} \mathbf{N}_j(\rho_p \alpha_p) \right\rangle \\ \varepsilon_{drag} &= -\left\langle v_i^{(1)} \mathbf{S}_{j,drag} \right\rangle \\ \varepsilon_{RUM} &= -\left\langle v_i^{(1)} \mathbf{S}_{j,RUM}(\rho_p \alpha_p \tilde{u}_{p,i}) \right\rangle \\ \varepsilon_{AV} &= \left\langle v_i^{(1)} \mathbf{D}_j^{(AV)}(\rho_p \alpha_p \tilde{u}_{p,i}) - v_i^{(2)} \mathbf{D}_j^{(AV)}(\rho_p \alpha_p) \right\rangle. \end{aligned} \quad (5.36)$$

The normalized dissipation ε^+ is defined as

$$\varepsilon^+ = \frac{\varepsilon_{\bullet}}{-\left\langle \frac{\partial \rho_p \alpha_p \tilde{q}_p^2}{\partial t} \right\rangle}.$$

Then, the normalized budget equation of particle kinetic energy reads:

$$\varepsilon_{scheme}^+ + \varepsilon_{drag}^+ + \varepsilon_{AV}^+ + \varepsilon_{RUM}^+ = 1 \quad (5.37)$$

Note that $\partial \rho_p \alpha_p \tilde{q}_p^2 / \partial t$ is explicitly computed in the code using a simple centred method

$$\frac{\partial \rho_p \alpha_p \tilde{q}_p^2}{\partial t} \simeq \frac{1}{2} \frac{\rho_p \alpha_p^{n+1} (\tilde{u}_{p,i}^{n+1})^2 - \rho_p \alpha_p^n (\tilde{u}_{p,i}^n)^2}{\Delta t} \quad (5.38)$$

to check that the budget is closed.

5.5.2 Application of this diagnostic to the test cases

The terms of Eq. 5.37 have been extracted from AVBP for the four test cases (*cf.* Tab. 5.5). The time evolution of these normalized dissipations is plotted in Fig. 5.6. A special attention has been given to highlight numerical and physical dissipations. Similarly to Sec. 5.4, T1 will be successively compared with the other test cases.

- **Impact of the convective scheme:** TTGC (T1, Fig. 5.6(a)) vs PSI (T2, Fig. 5.6(b)). The major difference between TTGC and PSI is the numerical dissipation, highlighted by continuous lines with symbols in Fig. 5.6. Dissipation due the convective scheme and that due to the AV behave in opposite ways between T1 and T2. On the one hand, for TTGC, it is ε_{AV}^+ that dissipates the most the MKE. The dissipation of the scheme is almost null. On the other hand, for PSI, the MKE is solely dissipated by the scheme at the beginning of the computation, whereas ε_{AV}^+ is negligible.

The shape of ε_{RUM}^+ may be explained roughly as the following. The particles are injected with the same velocity of the gas, so that RUE would be null at $t^+ = 0$ if we have not imposed $\delta\theta_p = 0.1$ for numerical reasons (*cf.* Sec. 5.2.1). After a transient time corresponding to one τ_p , preferential concentration becomes visible. The clusters of particles are composed of particles coming from different areas of the domain with spatially decorrelated velocities. Thus, the augmentation of preferential concentration observed in Fig. 5.4 logically implies an increase of the RUE, and consequently of ε_{RUM}^+ . Then, the turbulence is progressively damped out by the viscosity so that RUE decreases.

One important remark is that the numerical dissipation (ε_{AV}^+ for T1 or ε_{scheme}^+ for T2) is higher than the dissipation associated to the RUM model for both test cases. In these conditions, the evaluation of the RUM models is questionable.

- **Influence of the AV sensor:** CM5-T (T1, Fig. 5.6(a)) vs CM10-T (T3, Fig. 5.6(c)). It was shown in Sec. 3.3.1 that the increase of the K parameter (Eq. 2.35) sharpens the CM sensor, so that the activation of the AV is delayed. Consequently, the mean dissipation associated to the CM10-T sensor (in Fig. 5.6(c)) is lower than that associated to CM5-T (in Fig. 5.6(a)). As ε_{scheme}^+ is similar between T1 and T3, the decrease for ε_{AV}^+ is favorable to the physical dissipations ε_{drag}^+ and ε_{RUM}^+ . Consequently, the maximum dissipation associated with the RUM model is slightly higher in T3 and than in T1.
- **Effect of the mesh resolution:** coarse mesh M1H (T1, Fig. 5.6(a)) vs fine mesh M2H (T4, Fig. 5.6(d)). Comparing Fig. 5.6(a) and Fig. 5.6(d), the dissipation associated to the AV drastically decreases when the mesh is refined, consistently with what suggested the analysis of the discrete budget of α_p equation in Sec. 4.5.2. For case T4, ε_{AV}^+ quickly falls to a constant value of 18% after a one τ_p . Interestingly, the physical dissipations are now higher than those related to the numerics.

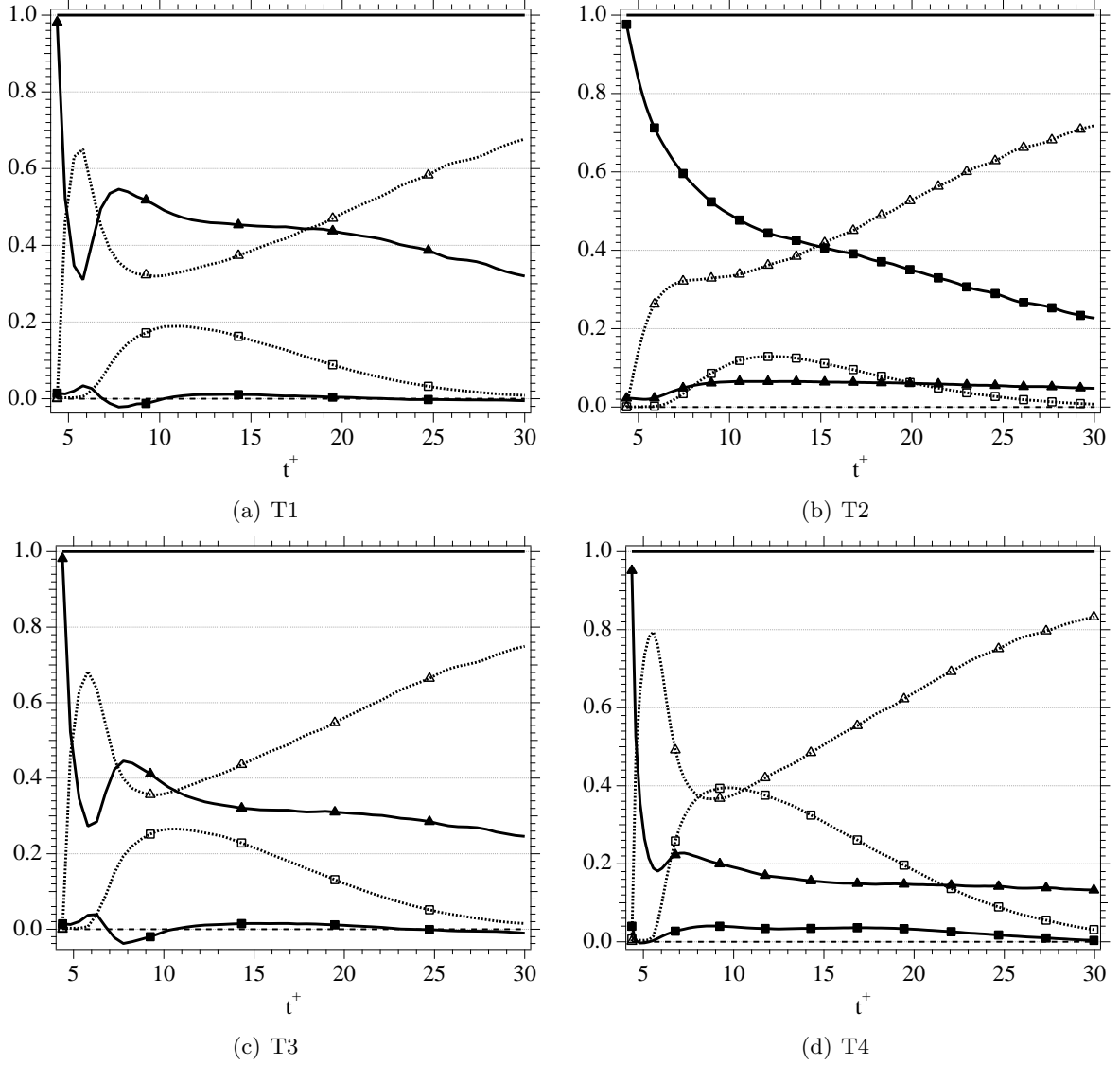


Figure 5.6: Discrete kinetic energy balance of the dispersed phase for the different test cases. The normalized dissipations of Eq. 5.37 are plotted. Numerical dissipations are represented by symbol-continuous lines (ϵ_{scheme}^+ : \blacksquare — and ϵ_{AV}^+ : \blacktriangle —) where physical dissipations are plotted with dotted lines (ϵ_{drag}^+ : $\triangle\dots\dots$ and ϵ_{RUM}^+ : $\square\dots\dots$). Budget: $1 - \sum \epsilon^+$ (— — —)

5.6 Conclusions

The numerical aspects of the MEF used in this work have been studied on a particle-laden HIT configuration in regime of preferential concentration. Following the consecutive studies performed on the same configuration [63, 83, 103, 145], the two numerical strategies detailed in Chap. 2 have been evaluated using the particle dispersion function [124]. The conclusions are the following:

- The two numerical schemes used for the dispersed phases, TTGC and PSI, provide similar results when $\epsilon^{(2)}$ is tuned.
- At constant $\epsilon^{(2)}$, TTGC results can be nonetheless improved when the AV sensor is modified, whereas this procedure has no effect on PSI.
- Preferential concentration is unexpectedly over-predicted with a finer mesh and the best numerical strategy.

Then, the discrete budget of the MKE equation has been written to discriminate more quantitatively the numerical strategies, quantifying thoroughly the balance between numerical and physical dissipations in the Eulerian simulations.

- For TTGC, the particle MKE is mainly dissipated by the AV at the onset of the simulation and the dissipation due to the scheme is negligible.
- It is the contrary for PSI, where the dissipation of the scheme is larger than the dissipation of drag and RUM at the beginning of the simulation.
- Increasing the mesh resolution has a big impact on the budget of the particle MKE, decreasing the weight of the numerical dissipations. With a sufficiently fine mesh, numerical dissipations can be lower than the physical dissipations.

Therefore, these diagnostics highlighted one fundamental issue in EE simulations: the simulation of a two-phase flow requires more mesh resolution than the turbulent flow. For a meaningful study of physical models, one has to verify that the numerical dissipations are below the physical ones and most of all when a stabilization technique is used. This is a crucial information to study RUM models in more complex configurations like in Part. III.

Part III

A posteriori tests of the MEF extended to non-isothermal flows

Chapter 6

Influence of the thermal inertia in dispersed-phase flows - 2D non-isothermal particle-laden jet

Contents

6.1	Introduction	96
6.2	Description of the solvers and modeling equations	97
6.2.1	Carrier phase flow solvers	98
6.2.2	Eulerian/Lagrangian formulation	98
6.2.3	Eulerian/Eulerian formulation: the Mesoscopic Eulerian Formalism	99
	General presentation	99
	Governing equations	100
	Models for the RUM	100
6.3	Configuration and boundary conditions	101
6.3.1	Computational domain	101
6.3.2	Mesh and boundary conditions	102
6.3.3	Turbulence injection	102
6.3.4	Dispersed phase characteristics	103
6.4	Results and analysis	104
6.4.1	Carrier phase	104
6.4.2	Dynamics of the dispersed phase	106
6.4.3	Influence of thermal inertia: analysis of Lagrangian simulations	108
6.4.4	Influence of thermal inertia: validation of the Eulerian simulations	108
6.5	Conclusions	111
6.6	Influence of the RUM model and coupling with the RUM heat fluxes	112
6.6.1	Dynamics of the dispersed phase	112
6.6.2	Temperature statistics of the dispersed phase	119
6.6.3	Additional conclusions	123

This chapter is a first *a posteriori* validation of the MEF extended to non-isothermal flows [78]. It focuses on the influence of the thermal inertia of particles on their temperature statistics. DNS using the MEF are compared to reference Lagrangian simulations for a two-dimensional non-isothermal turbulent jet laden with solid particles. Note that Eulerian uncorrelated variables (velocities, heat fluxes) are not presented as their Lagrangian counterpart were not available in this configuration.

The numerical strategy used in this chapter is the one identified as the most promising in Part. II: the TTGC scheme coupled with an adapted AV model, which characteristics are summarized in Tab. 7.4.

scheme	AV sensor	$\epsilon^{(2)}$	$\epsilon^{(4)}$	$B_{min}(\alpha_p)$
TTGC	CM5-T	0.5	$5 \cdot 10^{-4}$	$1 \cdot 10^{-8}$

Table 6.1: Numerical parameters of the simulations in Chap 6.

The first sections of this chapter (Sec. 6.1 to 6.5) are the content of a paper submitted to the International Journal of Heat and Mass Transfer [30]. The reader can skip Sec. 6.2 where the main equations of the Lagrangian and the MEF are summarized. These are the same than in Chap. 1. Additional results, not presented in the paper, are added in Sec. 6.6. In particular, the influence of the RUM model on the dynamics and temperature statistics and the coupling with the RUM heat fluxes are investigated.

6.1 Introduction

A variety of industrial devices involve two-phase flows and many of them are non-isothermal. In combustion chambers, for example, fuel is injected in liquid state at a relatively low temperature into a hot, turbulent flow. Due to hydrodynamic forces, the liquid is atomized into droplets. The subsequent evaporation of the droplets' cloud is driven by heat exchange between the carrier and the dispersed phase. Moreover, temperature fluctuations may have a strong impact on the local evaporated fuel mass fraction as evaporation is a non-linear phenomenon. The resulting fluctuations of local equivalence ratio are known to have a negative impact on ignition, flame propagation or even combustion instabilities [66, 75, 88]. An accurate description of heat transfer to the dispersed phase is therefore necessary.

Very few studies have directly tackled the issue of particle temperature dispersion, which is mainly due to the lack of experimental data of non-isothermal two-phase flows [155]. Recent experimental techniques –such as rainbow thermometry– seem promising but further improvements are required [144]. An alternative is to use Direct Numerical Simulations (DNS): a few studies of non-isothermal academic configurations, coupled with lagrangian tracking of particles, have been carried out. The mechanism of two-phase heat and turbulent transport by particles was investigated in an decaying isotropic turbulence with an imposed temperature gradient in the fluid [113]: it was found that the particle temperature fluctuation and velocity are well correlated in the direction of the imposed temperature gradient. Jaber *et al.* [57] investigated the

effects of the particle dynamical response time, τ_p , the Prandtl number, Pr , the Reynolds number, Re and mass-loading ratio, r_{ml} , on the statistics of particle temperature in a non-isothermal isotropic turbulence with stationary velocity and temperature fluctuations. They showed that particle temperature fluctuations decrease as τ_p , Pr , Re and r_{ml} increase. An extension of this work [58] showed that the response of particle temperature is different when the fluid and particle temperature decay in isotropic turbulence. In this case, the variance of the fluid and particle temperatures increase when the magnitude of $r_{ml} \times \text{Pr}$ increases. Shotorban *et al.* [119] studied the dispersed-phase temperature statistics in particle-laden turbulent homogeneous shear flow in the presence of mean temperature gradient. They found that the particle temperature variance increases when the ratio of specific heat increases.

The Eulerian-Lagrangian (EL) approach is as a powerful tool to understand and simulate two-phase flows in academic configurations. However, the lagrangian tracking of individual particles for the simulation of a realistic industrial configuration is still beyond reach because of the large number of droplets. An alternative is to model the dispersed phase as a continuum, like the carrier: this approach is called Eulerian-Eulerian (EE). The equilibrium Eulerian approach, recently extended to non-isothermal flows gives promising results [38] but is adapted only to particles with sufficiently small dynamical and thermal inertia. The statistical approach proposed by Février *et al.* [41], called the Mesoscopic Eulerian formalism (MEF), is able to reproduce local and instantaneous properties of particles embedded in a turbulent fluid flow [104]. The cornerstone of the MEF is the partitioning of the particle velocity field into two contributions: a continuous, self-coherent velocity shared by all particles called the mesoscopic field and a spatially uncorrelated contribution referred to as Random Uncorrelated Motion (RUM). This formalism showed its ability to simulate correctly turbulent two-phase flows in a complex geometry [105] and was recently extended to non-isothermal conditions [78]. *A priori* tests in a non-isothermal droplet-laden turbulent planar jet [80] show the ability of this approach to describe an evaporating dispersed phase interacting with a turbulent flow. The objective of the present work is twofold:

1. study the influence of the particles' thermal inertia in a configuration representative of a spray injection in a combustion chamber.
2. and propose an *a posteriori* validation of the MEF extended to non-isothermal flows.

The organization of the paper is as follows: the two solvers and modeling equations are described in Sec. 6.2; the configuration and boundary conditions are then presented in Sec. 6.3; finally the results are presented in Sec. 6.4 with detailed validation of the dynamics and temperature of the dispersed phase.

6.2 Description of the solvers and modeling equations

These simulations are carried out by two different codes developed at CERFACS and CORIA:

- a dilatable low-Mach solver (Asphodele - CORIA) with lagrangian tracking of individual particles.
- a compressible code (AVBP - CERFACS), where the MEF has been implemented.

6.2.1 Carrier phase flow solvers

Numerical methods used for the carrier-phase flow solvers have been already described in the literature [87, 116, 101] and are only summarized here. Boundary conditions are treated in Sec. 6.3.2. AVBP solves the compressible Navier-Stokes equations. A third-order in time and space, finite-element scheme TTGC [22] is used for the carrier and dispersed phase. Asphodele is a DNS structured low-Mach solver. It uses a fourth-order finite-difference scheme for the gas and a third-order explicit Runge-Kutta scheme with a minimal data storage method [154] for both carrier and dispersed phases. A third-order interpolation is employed for the determination of gaseous phase properties at the location of a particle.

6.2.2 Eulerian/Lagrangian formulation

As described by Reeks [98], it is possible to take into account many forces to characterize the particle dynamics. However, because of the high density ratio between dispersed and gas phases, only the drag force, which is prevalent, has been retained. Additionally, several usual assumptions have been made: some of them are given in the following, but details may be found in a reference paper of Sirignano [125]. First, the spray is supposed dispersed and each particle is unaware of the existence of the others. Any internal heterogeneity or particle rotation is neglected and an infinite heat conduction coefficient is assumed in the particle. As a consequence, the particle temperature remains uniform but evolves with time. As a first approach and because of the dispersed nature of the flow, a one-way coupling has been considered. By denoting \mathbf{V}_p and \mathbf{X}_p the velocity and position vectors of a particle, respectively, the following relations are used to track particles throughout the computational domain:

$$\frac{d\mathbf{V}_p}{dt} = \frac{1}{\tau_p} (\mathbf{U}(\mathbf{X}_p, t) - \mathbf{V}_p) \quad (6.1)$$

$$\frac{d\mathbf{X}_p}{dt} = \mathbf{V}_p \quad (6.2)$$

The vector $\mathbf{U}(\mathbf{X}_p, t)$ represents the gas velocity at the particle \mathbf{X}_p . The right hand side term of Eq. (6.1) stands for a drag force applied to the particle and τ_p is the kinetic relaxation time:

$$\tau_p = \frac{\rho_p d_p^2}{18\mu_f} \quad (6.3)$$

where d_p is the particle diameter, ρ_p is the dispersed phase density and μ_f is the gas viscosity. The heating of each particle is characterized through

$$\frac{dT_p}{dt} = \frac{1}{\tau_\theta} (T(\mathbf{X}_d) - T_p) \quad (6.4)$$

where the characteristic relaxation time τ_θ is defined as:

$$\tau_\theta = \frac{Pr}{12} \frac{C_p}{C_f} \frac{\rho_p d_p^2}{\mu} = \frac{3}{2} Pr \alpha \tau_p \quad (6.5)$$

where the gas and particle constant heat capacities are denoted C_f and C_p , respectively. Pr is the Prandtl number. The particle-to-fluid heat capacity ratio is $\alpha = C_p/C_f$.

6.2.3 Eulerian/Eulerian formulation: the Mesoscopic Eulerian Formalism

General presentation

The MEF was originally presented by Février *et al.* [41]: using Direct Numerical Simulations, they observed that two arbitrarily-close particles may have drastically different velocities. In other words, the ratio of the two-point correlation between particle velocities and the particle kinetic energy does not reach unity when the distance goes to zero (c.f. their Fig. 3). Based on this observation, the cornerstone of the MEF is a statistical-average operator, $\langle \bullet | \mathcal{H}_f \rangle$ that corresponds to the average over all particle realizations for a fixed carrier-fluid realization \mathcal{H}_f . This operator splits the particle velocity, u_p , in two contributions: a continuous, self-coherent velocity, $\tilde{u}_p = \langle u_p | \mathcal{H}_f \rangle$, shared by all particles called the mesoscopic field and a spatially uncorrelated contribution, δu_p , referred to as Random Uncorrelated Motion. One has

$$u_p(t) = \tilde{u}_p(x_p(t), t) + \delta u_p(t), \quad (6.6)$$

where $x_p(t)$ is the position of the particle at time t . Similarly, one can decompose the particle temperature T_p into its mesoscopic, \tilde{T}_p , and uncorrelated, δT_p , components:

$$T_p(t) = \tilde{T}_p(x_p(t), t) + \delta T_p(t). \quad (6.7)$$

From the perspective of particle dynamics, it can be simply said that the mesoscopic velocity and temperature are related to the coupling with the carrier phase, through drag and heat transfer, and that the RUM is caused by the inertia of the particles. Indeed, because of inertial effects, two particles may get to neighboring locations with different trajectories and therefore different properties (velocity, temperature, etc.). Consequently, for particle dynamics, the ratio of the inertial and viscous time scales acting on the particles is central for the evaluation of the relative importance of the mesoscopic and uncorrelated contributions. This ratio is the Stokes number, St , defined as

$$St = \frac{\tau_p}{\tau_f} \quad (6.8)$$

where τ_p is the particle relaxation time and τ_f a time scale typical of the carrier phase. Using the particle thermal time scale τ_θ a thermal Stokes number, St_θ , may be also defined as

$$St_\theta = \frac{\tau_\theta}{\tau_f}. \quad (6.9)$$

The dynamical and thermal particle relaxation times, τ_p and τ_θ , have been defined in Eq. 6.3 and Eq. 6.5, respectively. However, the choice of a characteristic time, τ_f , for the carrier fluid can be ambiguous depending on the configuration [5]. For the present configuration (c.f. Sec. 6.3), the momentum thickness at the inlet boundary condition, δ_θ , is chosen as the reference length and the maximum of the rms of the inlet velocity, $u_f'^{max}$, is chosen as the reference velocity, leading to:

$$\tau_f = \frac{\delta_\theta}{u_f'^{max}}. \quad (6.10)$$

Governing equations

The set of Eulerian equations for a non-isothermal dilute particle flow in the mesoscopic formalism was derived by Masi [78]:

$$\frac{\partial \tilde{n}_p}{\partial t} + \frac{\partial \tilde{n}_p \tilde{u}_{p,j}}{\partial x_j} = 0, \quad (6.11)$$

$$\frac{\partial \tilde{n}_p \tilde{u}_{p,i}}{\partial t} + \frac{\partial \tilde{n}_p \tilde{u}_{p,i} \tilde{u}_{p,j}}{\partial x_j} = -\frac{\tilde{n}_p}{\tau_p} (\tilde{u}_{p,i} - u_{f,i}) - \frac{\partial \tilde{n}_p \delta R_{p,ij}}{\partial x_j}, \quad (6.12)$$

$$\frac{\partial \tilde{n}_p C_p \tilde{T}_p}{\partial t} + \frac{\partial \tilde{n}_p C_p \tilde{u}_{p,j} \tilde{T}_p}{\partial x_j} = -\frac{\tilde{n}_p C_p}{\tau_\theta} (\tilde{T}_p - T_f) - \frac{\partial \tilde{n}_p C_p \delta \Theta_{p,j}}{\partial x_j}, \quad (6.13)$$

where \tilde{n}_p is the mesoscopic particle number density and u_f and T_f the fluid velocity and temperature, respectively. There are two unclosed terms in these equations corresponding to the RUM velocity stress tensor, $\delta R_{p,ij}$, and the RUM heat flux, $\delta \Theta_{p,j}$, defined as:

$$\delta R_{p,ij} = \langle \delta u_{p,i} \delta u_{p,j} | \mathcal{H}_f \rangle, \quad (6.14)$$

$$\delta \Theta_{p,j} = \langle \delta T_p \delta u_{p,j} | \mathcal{H}_f \rangle. \quad (6.15)$$

Models for the RUM

The RUM velocity stress tensor is decomposed into its spherical and deviatoric parts as

$$\delta R_{p,ij} = \delta R_{p,ij}^* + \frac{2}{3} \delta \theta_p \delta_{ij}, \quad (6.16)$$

where $\delta \theta_p = 1/2 \delta R_{p,kk}$ is the RUM kinetic energy.

Recently, Masi *et al.* [79] proposed a viscosity-like model for the deviatoric part $\delta R_{p,ij}^*$, assuming the axisymmetry of tensors, their alignment and a one-component limit state:

$$\delta R_{p,ij}^* = \text{sign}(III_s) \left(\frac{2}{3} \right)^{1/2} 2 \delta \theta_p \frac{S_{p,ij}^*}{S}, \quad (6.17)$$

where $S_{p,ij}^*$ is the deviatoric part of the mesoscopic particle rate-of-strain tensor, S the square root of its second invariant, and III_s its third invariant. This RUM model, denoted AXISY-C, was found to improve significantly the prediction of RUM stresses in comparison with the previous model [63, 79, 105]. The main difference is that it now accounts for positive and negative local viscosity and use a more appropriate timescale $\mathcal{F}(S^{-1})$, predicting a better mean dissipation.

Then, a transport equation is solved for the RUM kinetic energy:

$$\frac{\partial \tilde{n}_p \delta \theta_p}{\partial t} + \frac{\partial \tilde{n}_p \tilde{u}_{p,j} \delta \theta_p}{\partial x_j} = -2 \frac{\tilde{n}_p}{\tau_p} \delta \theta_p - \tilde{n}_p \delta R_{p,ij} \frac{\partial \tilde{u}_{p,i}}{\partial x_j} - \frac{1}{2} \frac{\partial \tilde{n}_p \delta Q_{p,ij}}{\partial x_j}. \quad (6.18)$$

The third-order velocity correlation $\delta Q_{p,ijk} = \langle \delta u_{p,i} \delta u_{p,j} \delta u_{p,k} | \mathcal{H}_f \rangle$ in Eq. 6.18 is modeled as suggested by Kaufmann *et al.* [65]:

$$\delta Q_{p,ijj} = -2 \kappa_{p,RUM} \frac{\partial \delta \theta_p}{\partial x_j}, \quad (6.19)$$

$$\kappa_{p,RUM} = \frac{5 \tau_p}{3} \delta \theta_p. \quad (6.20)$$

With this, Eq. 6.12 is closed so the last contribution to model is the RUM heat flux $\delta\Theta_p$ in Eq. 6.13. The present work being an *a posteriori* evaluation of the influence of RUM heat fluxes on an academic configuration, it was decided to use as little additional modeling as possible for $\delta\Theta_p$. Consequently, we opted for a resolution of the conservation equations for $\delta\Theta_p$ derived by Masi [78]:

$$\begin{aligned} \frac{\partial \tilde{n}_p C_p \delta\Theta_{p,i}}{\partial t} + \frac{\partial \tilde{n}_p C_p \tilde{u}_{p,j} \delta\Theta_{p,i}}{\partial x_j} &= -\tilde{n}_p C_p \left(\frac{1}{\tau_p} + \frac{1}{\tau_\theta} \right) \delta\Theta_{p,i} - \tilde{n}_p C_p \delta\Theta_{p,j} \frac{\partial \tilde{u}_{p,i}}{\partial x_j} \\ &\quad - \tilde{n}_p C_p \delta R_{p,ij} \frac{\partial \tilde{T}_p}{\partial x_j} - \frac{\partial \tilde{n}_p \delta \Delta_{p,ij}}{\partial x_j}, \end{aligned} \quad (6.21)$$

with the only assumption that the third-order contribution $\delta\Delta_{p,ij} = \langle \delta u_{p,i} \delta u_{p,j} \delta T_p | \mathcal{H}_f \rangle$ could be neglected. This last assumption is solely based on pragmatism as we do not yet have models available for this term.

6.3 Configuration and boundary conditions

6.3.1 Computational domain

The configuration (Fig. 6.1) is a two-dimensional cold jet, laden with solid particles and surrounded by a hot co-flow. The jet width, $L_{ref} = 0.79 \cdot 10^{-2}$ m, is used throughout the paper for normalization. The streamwise (x -axis) extent of the computational domain is $L_x = 12 L_{ref}$ and its cross-stream (y -direction) dimension is $L_y = 6 L_{ref}$. The carrier gas is composed of pure air (density ρ_f and kinematic viscosity μ_f) at a mean pressure P_{ref} . The parameters common to all computations (velocity u , temperature T and mass loading α) are presented in Tab. 6.2, where the superscript ‘ j ’ (respectively ‘ c ’) denotes jet (respectively co-flow) properties and the subscript ‘ f ’ (respectively ‘ p ’) denotes carrier fluid (respectively particles) properties. With these parameters, the Reynolds number based on the momentum thickness is $Re_\theta = \rho_f \delta_\theta \Delta U / \mu_f = 125$, where $\Delta U = u_f^j - u_f^c$ is the initial velocity difference between the two gaseous streams. Finally, one defines a convective time $t_c = 12 L_{ref} / \Delta U$ so that the results can be presented as a function of the normalized variables: $t^* = t/t_c$, $x^* = x/L_{ref}$ and $y^* = y/L_{ref}$. It should be pointed out

L_{ref} [m]	Re_θ	ρ_f [kg.m ⁻³]	μ_f [kg.m ⁻¹ .s ⁻¹]
$0.79 \cdot 10^{-2}$	125	1.177	$1.86 \cdot 10^{-5}$
δ_θ	T_f^j, T_f^c [K]	u_f^j, u_f^c [m.s ⁻¹]	T_p^j [K], u_p^j [m.s ⁻¹], α_p^j
$L_{ref}/40$	300, 600	20, 10	300, 20, 10^{-2}

Table 6.2: Parameters for the simulations.

that the two-dimensional character of the configuration is not limiting for the MEF: the RUM formulation was tested successfully in a three-dimensional test case by Masi *et. al* [80]. Here, to focus on the effects of heat transfer, using two-dimensional simulations is sufficient to investigate the effects of the RHS terms in Eq. 6.13.

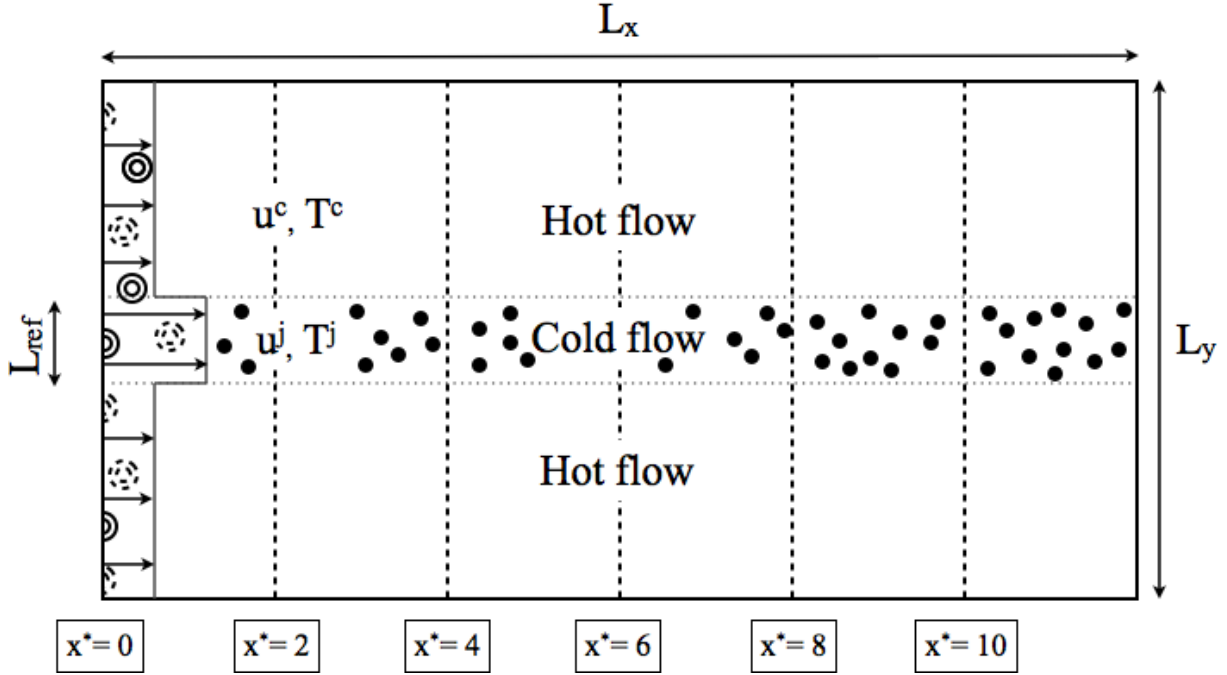


Figure 6.1: Scheme of the two-dimensional non-isothermal jet. The cold jet at the center is embedded with cold particles while the co-flow is a hot gas void of particles. The vertical dashed lines represent the location of the transverse cuts for the analysis.

6.3.2 Mesh and boundary conditions

Both solvers use a cartesian mesh with 1024 cells in x direction and 512 cells in y direction. Mesh independency was thoroughly checked with both solvers: the results presented here are the same with half the current resolution in both directions. Because Asphodele is a low-Mach solver while AVBP is fully compressible, the treatments of inlet and outlet boundary conditions differ: Asphodele uses Dirichlet conditions while AVBP uses characteristic boundary conditions [93] and their recent extension accounting for transverse terms at outlets [45]. Finally, the upper and lower boundary conditions are treated as symmetries.

Axial velocity and temperature of the carrier and dispersed phase, as well as particle volume fraction, are injected with the general hyperbolic profile

$$\phi(y) = \phi^c + f(y)(\phi^j - \phi^c) \quad (6.22)$$

$$f(y) = \frac{1}{2} \left(1 + \tanh \frac{L_{ref}/2 - |y|}{2\delta_\theta} \right), \quad (6.23)$$

where ϕ^j and ϕ^c denote the considered quantity in the jet and co-flow, respectively. All quantities are injected with the same profile in both codes.

6.3.3 Turbulence injection

For a meaningful comparison of the dispersed-phase properties in the two solvers, it is mandatory that they both compute the same carrier phase. It is necessary that the statistics of the carrier

to be identical but we have chosen a more conservative approach by imposing exactly the same inlet velocity signal, including the turbulent fluctuations. Mean inlet conditions are presented in Sec. 6.3.2 and in order to favor the destabilization of the jet, a turbulent velocity fluctuation was added to the mean flow following the procedure proposed by Celik and Kraichan [67, 126]. In this particular method, a number of random modes with an average spectrum corresponding to the Passot-Pouquet spectrum are added to the mean velocity. The Passot-Pouquet spectrum is defined by its most energetic length scale set at $L_{ref}/3$ and a turbulent intensity of 2.5% of the velocity profile. The equivalence of the velocity signals was ensured by imposing in Asphodele the random modes from AVBP.

AVBP being a compressible code, it is only in the absence of acoustic perturbation that the velocity signals can be expected to be identical. Fig. 6.2 compares the axial and transverse velocities at $x^* = 0$ in the middle of the jet for both codes. The agreement is excellent with minor discrepancies caused by the presence of acoustic waves in AVBP.

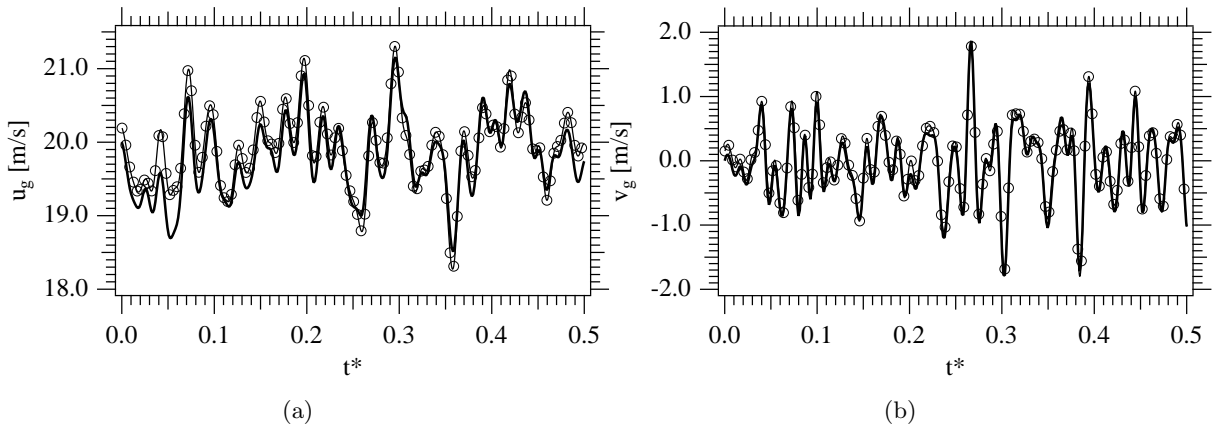


Figure 6.2: Comparison of AVBP (—) and Asphodele (—○—) gaseous velocities as a function of t^* at $x^* = 0$ in the middle of the jet. (a) Axial velocity, (b) Transverse velocity.

6.3.4 Dispersed phase characteristics

The dynamics of the dispersed phase is governed by the Stokes number, St , while its temperature is driven by the thermal Stokes number St_θ . Following Eq. 6.3 one has to prescribe a particle diameter d_p and density ρ_p . For this particular flow, with our choice of fluid characteristic time (Eq. 6.10), it was found that significant preferential concentration (c.f Fig. 6.4) was produced for $St=2$, corresponding to $d_p = 11.5 \cdot 10^{-6}$ m and $\rho_p = 1999.2$ kg.m $^{-3}$. All simulations are carried out for this Stokes number, meaning that the dynamics of the jet is fixed for all cases. St_θ is modulated by changing the particle heat capacity (c.f Eq. 6.5) to explore its influence on the temperature of the particles. Three values for St_θ are considered: from thermal tracers ($St_\theta = 0.2$) to ‘thermally ballistic’ particles ($St_\theta = 8$) with an intermediate value ($St_\theta = 2$) maximizing the effect of RUM heat fluxes. These parameters are summarized in Tab. 6.3.

Mesoscopic Eulerian quantities are obtained from the Lagrangian simulations by projection on the Eulerian grid. It is possible to circumvent the intrinsic filtering and statistical error of the projection method by using a sufficient number of particles and a well chosen projector [65].

d_p [m]	ρ_p [kg.m ⁻³]	Pr
$11.5 \cdot 10^{-6}$	1999.2	0.7194
$\alpha = C_p/C_f$	St	St _{θ}
0.093	2	0.2
0.93	-	2
3.7	-	8

Table 6.3: Characteristics of the three dispersed-phase simulation

Following these recommendations, ten particles per cell are injected. This procedure allows for a direct validation of the Eulerian simulations conducted in AVBP.

Hereinafter, all the statistics of the dispersed-phase used for the validation procedure are conditional averages. The conditional-average operator of a mesoscopic quantity, $\langle \tilde{\phi} \rangle_p$ is defined as

$$\langle \tilde{\phi} \rangle_p = \frac{\{\tilde{n}_p \tilde{\phi}\}}{\{\tilde{n}_p\}}, \quad (6.24)$$

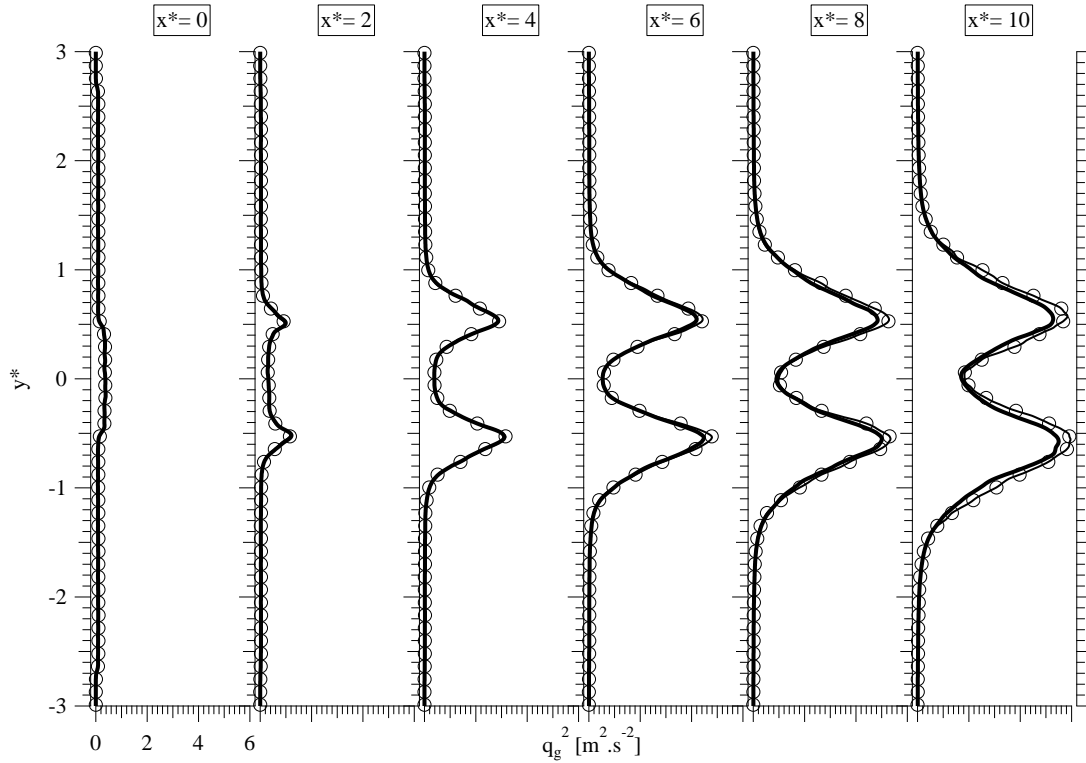
where $\{\bullet\}$ is the time-average operator and \tilde{n}_p the mesoscopic number density. For the sake of simplicity, the brackets are dropped in the rest of the paper.

6.4 Results and analysis

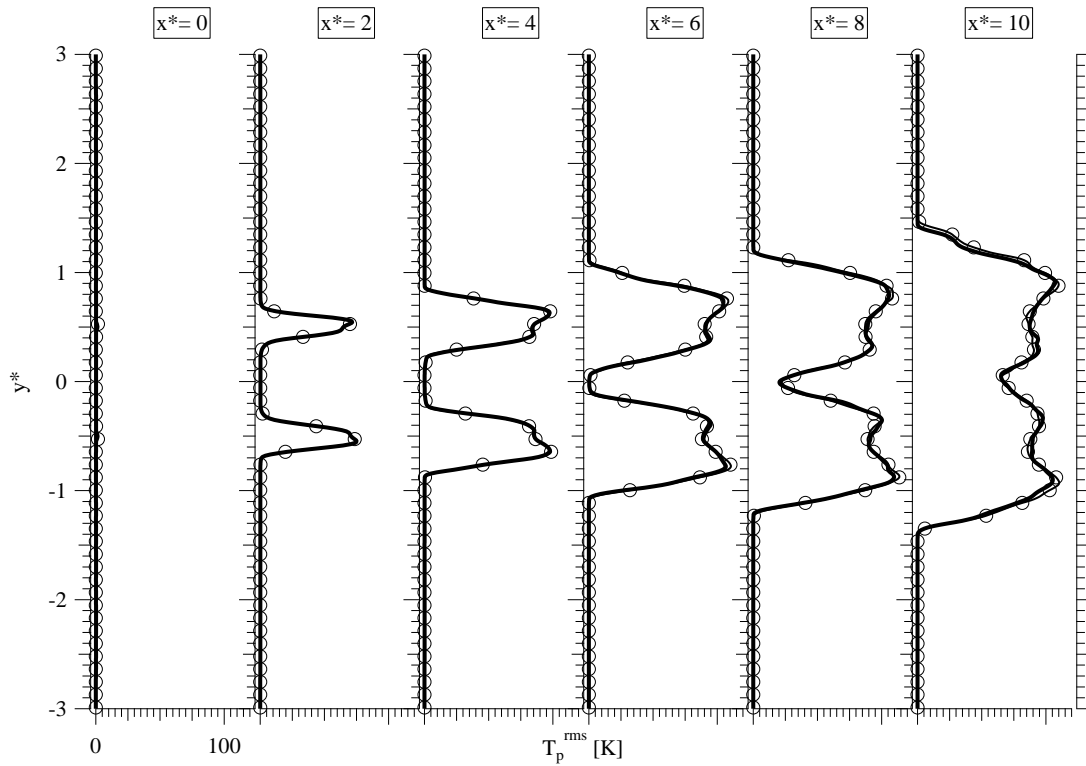
6.4.1 Carrier phase

As described in Sec. 6.3.3, it is mandatory that the gaseous phase in both solvers be identical, which is verified in this section. For the sake of compactness, only two statistics, most relevant for the present study are presented: the kinetic energy and rms of the temperature. These variables are important for the preferential concentration and temperature dispersion of the particles but all other gaseous variables compare accordingly between the two solvers.

The kinetic energy of the gas along six transverse cuts of the domain is presented in Fig. 6.3(a). Mixing layers at the edges of the jet spread with a slight preference into the low-speed streams, which is consistent with theory [95]. The maximum of the kinetic energy increases with x^* , first rapidly from the inlet to $x^* = 6$ and then more slowly. At $x^* = 6$, the kinetic energy at the center of the jet, begins to increase. The agreement between the two solvers (AVBP and Asphodele) is excellent. Then, the rms of gas temperature is shown Fig. 6.3(b). As for the kinetic energy, two regions can be distinguished: for $x^* < 6$ the level of rms increases in the outskirts of the jet while for $x^* > 6$ the center of the jet is contaminated and the maximum of rms remains roughly constant. Again, the agreement between the two solvers is excellent, which allows for meaningful analysis of the dispersed phase.



(a)



(b)

Figure 6.3: Comparison between AVBP (—) and Asphodele (—○—) at six transverse cuts. (a) Kinetic energy and (b) rms of temperature for the carrier phase.

6.4.2 Dynamics of the dispersed phase

Since the three runs of Tab. 6.3 differ only through the thermal Stokes number, the particle positions and velocity fields are the same for the three runs. A qualitative comparison of the particle field at $t^* = 2$ is shown in Fig. 6.4. As observed in other configurations [132], particles concentrate in regions of high shear and low vorticity. The qualitative agreement between the two codes is remarkable. In particular, thanks to the identical turbulent velocity at the inlet, both fields show the same features at the same location.

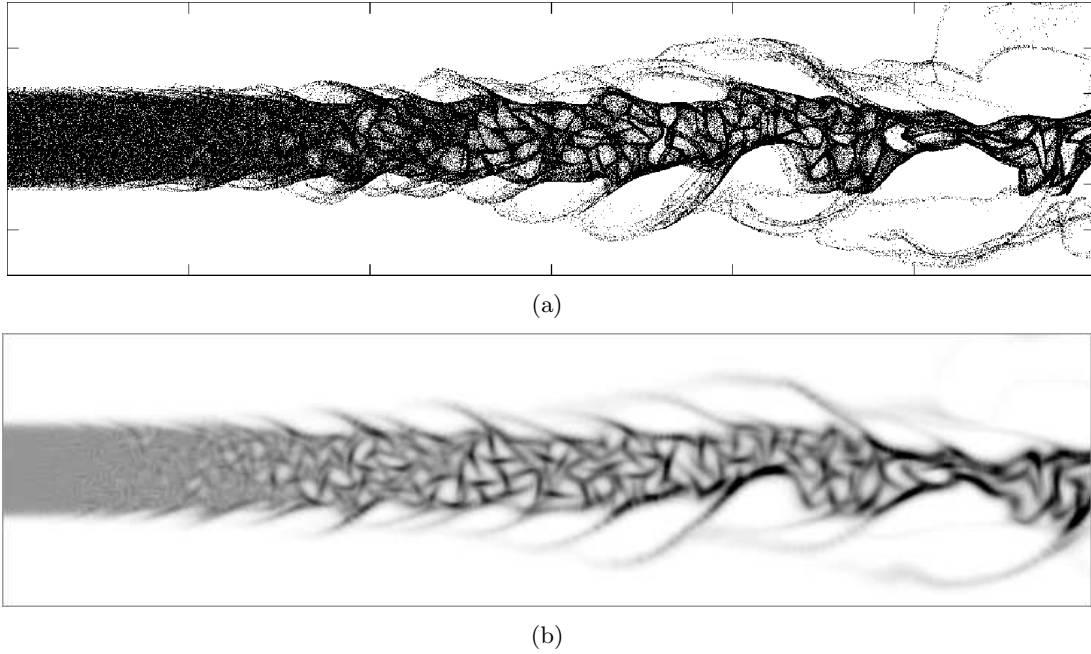
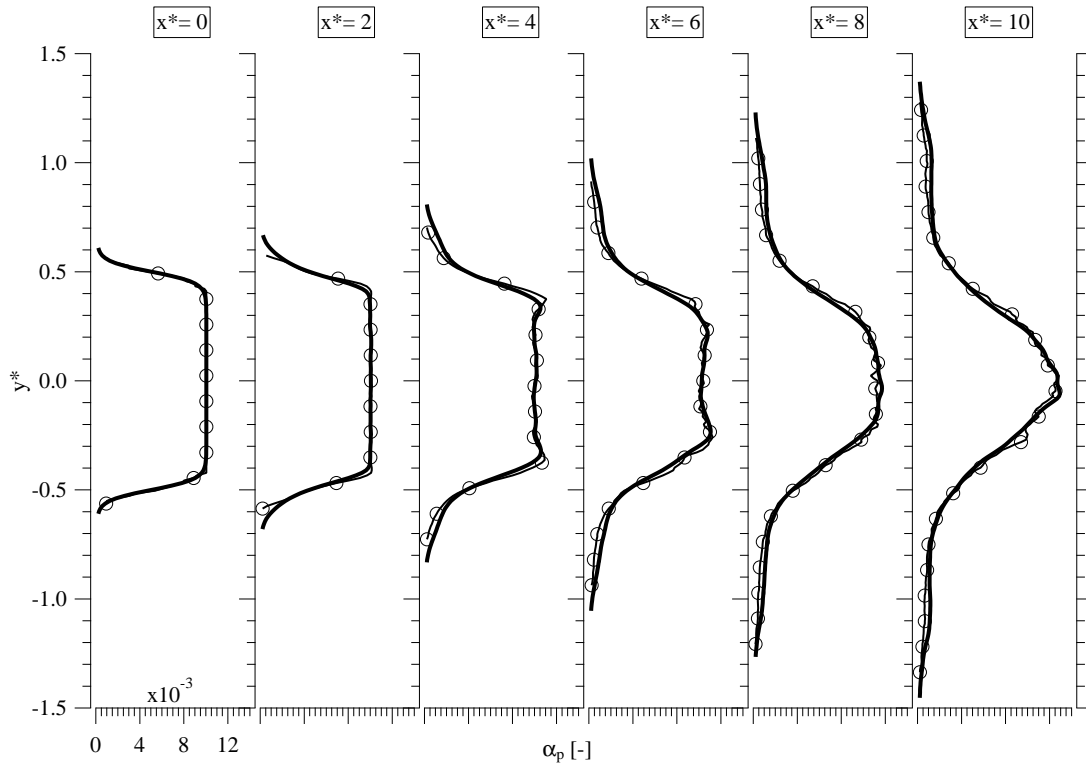
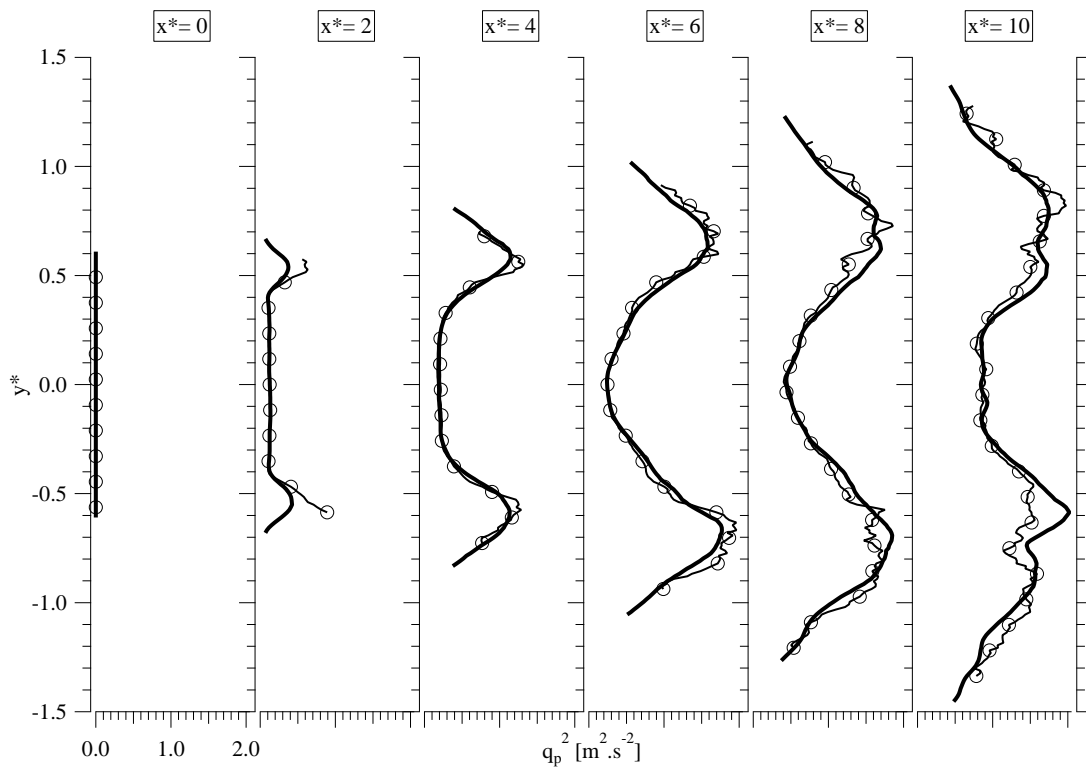


Figure 6.4: Particle-laden jet at time $t^* = 2$. (a) Lagrangian field of particles. (b) Eulerian particle volume fraction.

For a quantitative validation, the time average of the volume fraction over transverse cuts is presented in Fig. 6.5(a). The agreement is excellent between the Eulerian and Lagrangian simulations. For a validation of the dynamics of the dispersed phase in the Eulerian solver, the time-averaged mesoscopic turbulent kinetic energy, $\tilde{q}_p^2 = 1/2 \langle \tilde{u}'_{p,i} \tilde{u}'_{p,i} \rangle_p$, is displayed in Fig. 6.5(b). At the inlet boundary condition, there is no agitation in the dispersed phase so that $\tilde{q}_p^2 = 0$. The transfer of turbulent kinetic energy from the carrier yields an increase in \tilde{q}_p^2 , first on the edges, eventually spreading to the entire jet. The level of fluctuation in the dispersed phase reaches third of the fluid kinetic energy, displayed in Fig. 6.3(a). Such levels, as well as the strong preferential concentration observed in the jet, are consistent with the Stokes number of the particles. The details of the mean and rms of the velocity components are not presented here but the agreement between the two solvers is similar. The comparison of the dynamics of the dispersed phase between the Eulerian solver and the Lagrangian reference is excellent, which is a validation of the AXISY-C model (Eq. 6.17) and now allows for a detailed investigation of heat transfer to the dispersed phase.



(a)



(b)

Figure 6.5: Comparison between AVBP (—) and Asphodele (—○—) at six transverse cuts. (a) particle volume fraction α_p and (b) mesoscopic turbulent kinetic energy \bar{q}_p^2 .

6.4.3 Influence of thermal inertia: analysis of Lagrangian simulations

As presented in Tab. 6.3, the dynamical Stokes number is kept constant while the thermal Stokes number St_θ is varied. In this section, only the Lagrangian results are presented for an analysis of the influence of St_θ , while Sec. 6.4.4 is devoted to the validation of the Eulerian simulations and the study of the influence of the RUM heat transfer.

The time-averaged mesoscopic temperature, \tilde{T}_p , and its rms, \tilde{T}_p^{rms} , are shown in Fig. 6.6 for the three thermal inertia. The corresponding quantity for the gaseous phase is shown in order to quantify the deviation between both phases. The thermal Stokes number St_θ has a strong impact, both on the mean (Fig. 6.6(a)) and rms (Fig. 6.6(b)) of the particle temperature. As expected, for low values of St_θ , the temperature of the particles follows that of the gas yielding identical mean and rms. As the characteristic thermal time of the particles is increased, particles keep the memory of their temperature at injection. The fluctuations are affected accordingly, levels falling down to one fourth of the gas temperature rms for the higher thermal Stokes number. In the early development of the jet, only the particles with the lowest thermal inertia have the same statistics as the gas. However, as the jet evolves, the intermediate value of St_θ gets closer to the gaseous phase while the most inertial particles keep the memory of their initial state and show drastically different statistics. These observations are consistent with the study of temporal evolution of particle temperature variance in decaying non-isothermal homogeneous turbulent configuration [58].

6.4.4 Influence of thermal inertia: validation of the Eulerian simulations

The objective of this section is to validate the Eulerian simulations by comparing them to the Lagrangian reference. The influence of the RUM heat flux on the statistics of the dispersed phase is also analyzed.

Figure 6.7 presents the mean and rms of particle mesoscopic temperature at $x^* = 6$ for the three values of St_θ . First, the Eulerian simulations are carried out without the RUM heat flux term (second term in the r.h.s of Eq. 6.13). With this simplification, there is no direct coupling between the RUM and the heat transfer to the particles. Then the simulations are conducted with the RUM heat flux term and the resolution of its transport equation (Eq. 6.21). As shown in Fig. 6.7(a), at the lowest thermal inertia ($St_\theta = 0.2$), the Eulerian simulation recovers the Lagrangian result for the time-averaged mesoscopic temperature. However, as St_θ is increased, the Eulerian results depart from their Lagrangian counterpart at the edges of the jet. Accounting for the RUM heat flux marginally reduces the discrepancy, but overall, it seems that the mean mesoscopic temperature is mildly sensitive to the RUM heat flux term. It should be pointed out that the differences occur in a region of very small mass loading (c.f. Fig. 6.5(a)). Particle temperature fluctuations, \tilde{T}_p^{rms} , are presented in Fig. 6.7(b). For low and intermediate values of St_θ , neglecting the RUM heat flux leads to a deviation of the order of 10 K in the temperature fluctuations. It is important to note that while the fluctuations are underestimated at $St_\theta = 0.2$, they are overestimated at $St_\theta = 2$. Accounting for RUM heat fluxes allows to recover the correct fluctuation levels. For the case with a very large thermal inertia ($St_\theta = 8$), the comparison with the lagrangian reference is not favorable, especially at the edges of the jet. Accounting for RUM heat fluxes unfortunately does not yield measurable improvement. For very large values of the thermal inertia, it is likely that the particles are quite far from equilibrium, which is not favorable to the present Eulerian description. This could explain the lack of precision of the present results at $St_\theta = 8$.

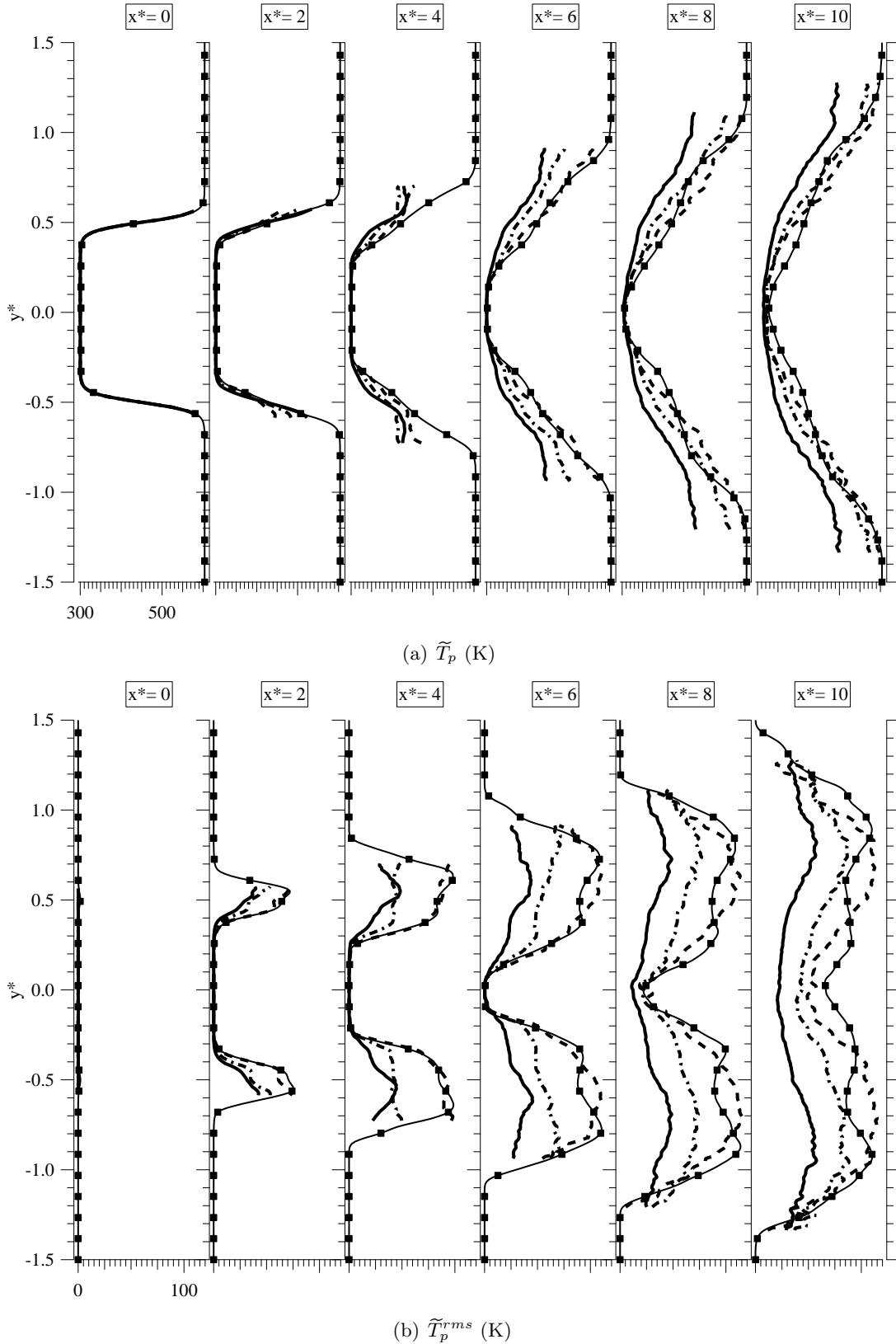


Figure 6.6: Lagrangian simulation results: 6.6(a) time-averaged mesoscopic temperature of the particles, and 6.6(b) rms of temperature fluctuations, for different values of the thermal inertia. —: $St_\theta = 8$; ---: $St_\theta = 2$ and - · - ·: $St_\theta = 0.2$. The corresponding quantity for the carrier fluid is presented for reference: —■—.

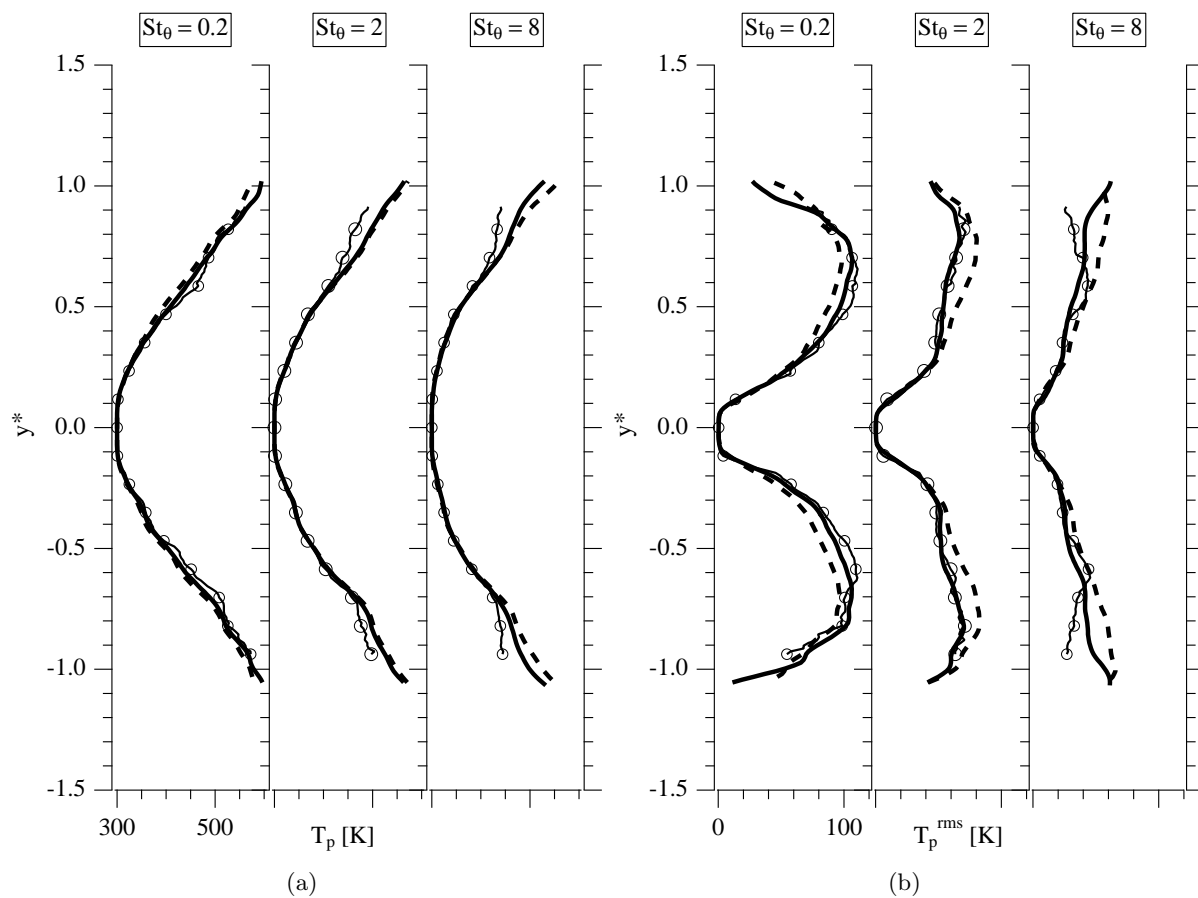


Figure 6.7: Comparison of Eulerian and Lagrangian mesoscopic quantities at $x^* = 6$. (a) Mean particle temperature \tilde{T}_p , (b) rms \tilde{T}_p^{rms} . Influence of the RUM-HF on the Eulerian statistics: —: with RUM-HF, - - - -: without RUM-HF, Lagrangian reference (—○—).

6.5 Conclusions

The simulation of a two-dimensional turbulent non-isothermal jet laden with solid particles has been carried out using Eulerian-Eulerian and Eulerian-Lagrangian approaches, in two different solvers. A special care has been taken to implement the same injection of turbulence in the two solvers so that time-wise comparison could be performed. The carrier-phase was compared between both codes and a perfect agreement was found.

Cold solid particles were then injected at regime of Stokes number where significant preferential concentration occurs. Again, a very good agreement was found between Eulerian and Lagrangian approaches allowing for a detailed scrutiny of heat transfer.

The influence of the thermal inertia of particles on their temperature was then investigated. The mean and rms of particle temperature showed a strong dependence on the thermal Stokes number. At low, thermal inertia, both mean and rms of particle temperature follow that of the fluid. At high thermal inertia, particles keep the memory of their injection temperature so that their statistics differ from that of the surrounding fluid.

Finally, the influence of the RUM heat fluxes in the Mesoscopic Eulerian Formalism was investigated. The mean temperature is satisfactorily predicted by the MEF, comparing to the Lagrangian reference. Under the conditions of the present study, the RUM heat fluxes have a marginal influence on the mean particle temperature. But a significant impact was observed on the magnitude of particle temperature fluctuations. Neglecting the RUM heat fluxes leads to erroneous results while the Lagrangian statistics are recovered when they are accounted for in the regimes of low to moderate thermal Stokes number. However, for particles with a very large thermal inertia ($St_\theta = 8$), the predictions of the temperature fluctuations deteriorate, even when RUM heat fluxes are accounted for.

6.6 Influence of the RUM model and coupling with the RUM heat fluxes

The influence of the RUM model was not presented in the paper (Sec. 6.1 to 6.5) for the sake of simplicity as it focused on the thermal dispersion of the particles. Actually, the AXISY-C model was chosen as it yielded the best agreement with Lagrangian simulations. However, the *a posteriori* evaluation of the RUM model in this mean-sheared configuration is valuable and is presented in this section. Moreover, RUM models may impact the particle temperature through the RUM heat fluxes if they are turned on as $\delta R_{p,ij}$ is a source term of the transport equation of the RUM heat fluxes (Eq. 1.54). Therefore, this section is divided in two parts. First, the influence of the RUM model (VISCO vs AXISY-C) on the dynamics of the particles is investigated in Sec. 6.6.1. Then, the joint effect of the RUM model and the RUM heat fluxes is studied in Sec. 6.6.2.

Four test cases are carried out, their characteristics are summarized in Tab. 6.4. Cases J3 and J4 correspond to the the two sets of parameters used in the paper. In this section, dynamic and

keyword	RUM model	RUM heat fluxes
J1	VISCO	No
J2	VISCO	Yes
J3	AXISY-C	No
J4	AXISY-C	Yes

Table 6.4: Numerical parameters for the simulations.

thermal Stokes numbers are respectively $St = 1$ and $St_\theta = 2$, which corresponds to the medium thermal inertia used in the paper (Tab. 6.3): the one with the most impact of the RUM HF term.

6.6.1 Dynamics of the dispersed phase

Time-averaged particle volume fraction profiles are shown in Fig. 6.9(a). First, the agreement between the Lagrangian reference and the Eulerian simulations is remarkable, for both RUM models. Small discrepancies are nonetheless visible at the border of the jet (high shear) at $x^* = 2$ and $x^* = 4$. The VISCO model slightly over estimates the particle volume fraction in comparison with the AXISY-C model. This problem is known and has been observed by Riber [103] in a vertical particle-laden turbulent confined jet flow [55] where the VISCO model caused a relaminarization of the dispersed phase flow. This is due to the light-anisotropy assumption of the VISCO model (c.f. Sec. 1.3.3) that is not fulfilled in mean-sheared flow. In this configuration, the RUM model has limited influence on the particle volume fraction fluctuation, shown in Fig. 6.9(b). Both Eulerian simulations underestimate α_p^{rms} by 50% in comparison with the Lagrangian reference. This is disappointing, since the mesh resolution is particularly fine. Numerical dissipation effects are expected to be lower than the dissipation due to the RUM model (*cf.* the discussion in Sec. 5.5.2). Thus, the discrepancy of α_p^{rms} between EE and EL simulations is assumed to be solely due to the RUM model. That means that there is still room

for improvement in the RUM model.

Moreover, Riber [103] pointed out that the VISCO model leads to a significant underestimation of the total agitation of particles in this type of configurations. Part of this statement is confirmed by the analysis of the mesoscopic particle kinetic energy, shown in Fig. 6.8(a). Whereas \tilde{q}_p^2 is well captured by the AXISY-C model, it is underestimated by VISCO for $0 \leq x^* \leq 6$. Both RUM models yield satisfactory agreement at $x^* = 8$ and $x^* = 10$ compared with the exact solution. Despite the fact that Lagrangian data are not available, the comparison of δq_p^2 between Eulerian simulations sheds light on the RUM models. As expected, the RUE is much larger with VISCO than with AXISY-C for $0 \leq x^* \leq 6$. In particular, δq_p^2 is abnormally high at $x^* = 2$ compared to \tilde{q}_p^2 ($\delta q_p^2 \simeq 7\tilde{q}_p^2!$). There is no physical reason why particle velocities would be so spatially uncorrelated after the injection of particles without RUM fluctuations. This must be due to the viscosity assumption of VISCO. This model does not capture the fact that the RUM agitation develops in one preferred direction while it is damped in the other, as analyzed by Masi [78] in a similar configuration. On the contrary, with AXISY-C, the RUE increases progressively from its (almost) null initial value to $x^* = 8$, proportionally to \tilde{q}_p^2 , which seems more physical.

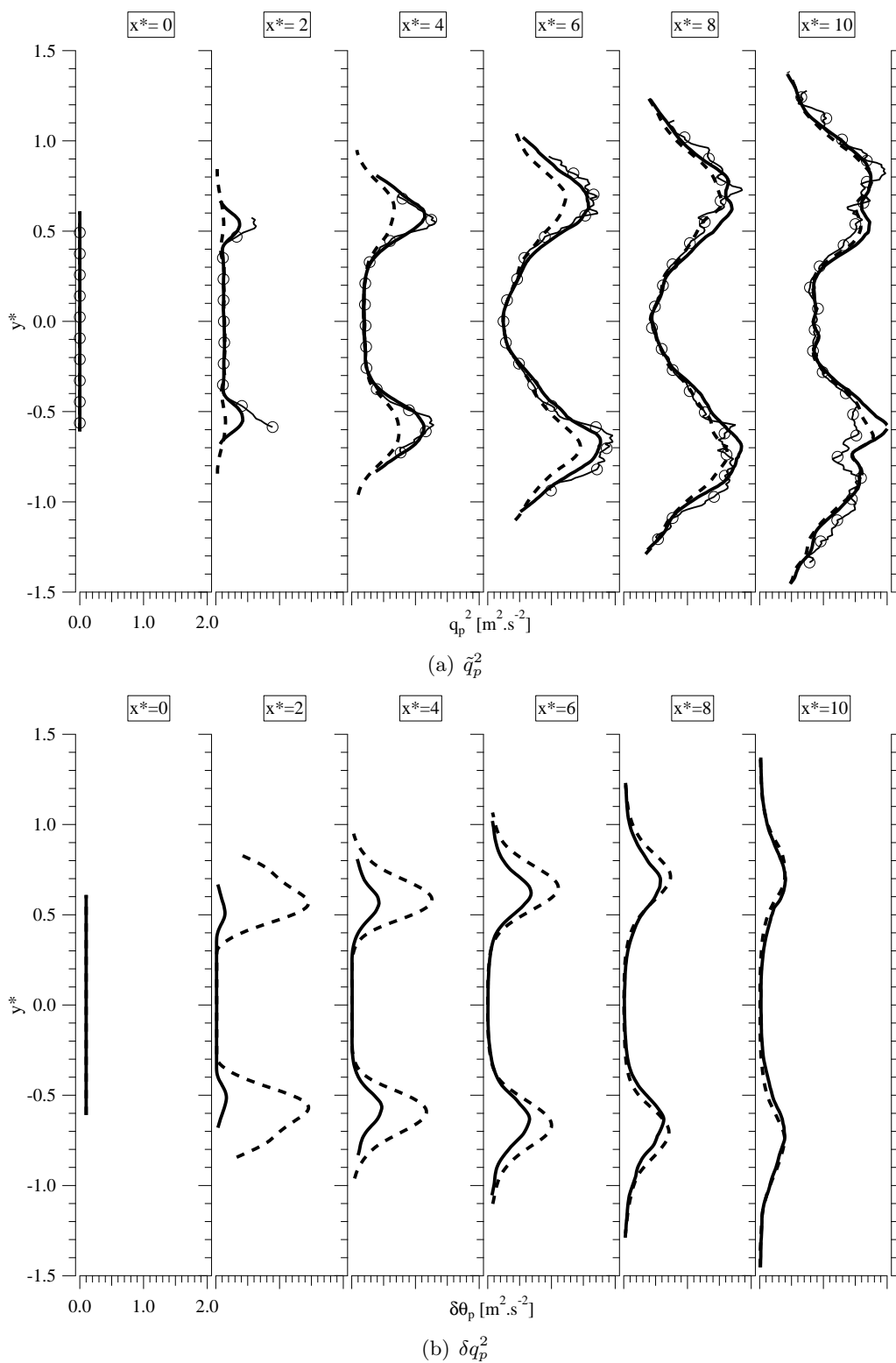


Figure 6.8: Impact of the RUM models on the dispersed phase statistics. (a) mesoscopic turbulent kinetic energy \tilde{q}_p^2 and (b) RUM particle kinetic energy δq_p^2 . Comparison between AXISY-C (—) and VISCO (---) models *vs* the Lagrangian reference (—○—).

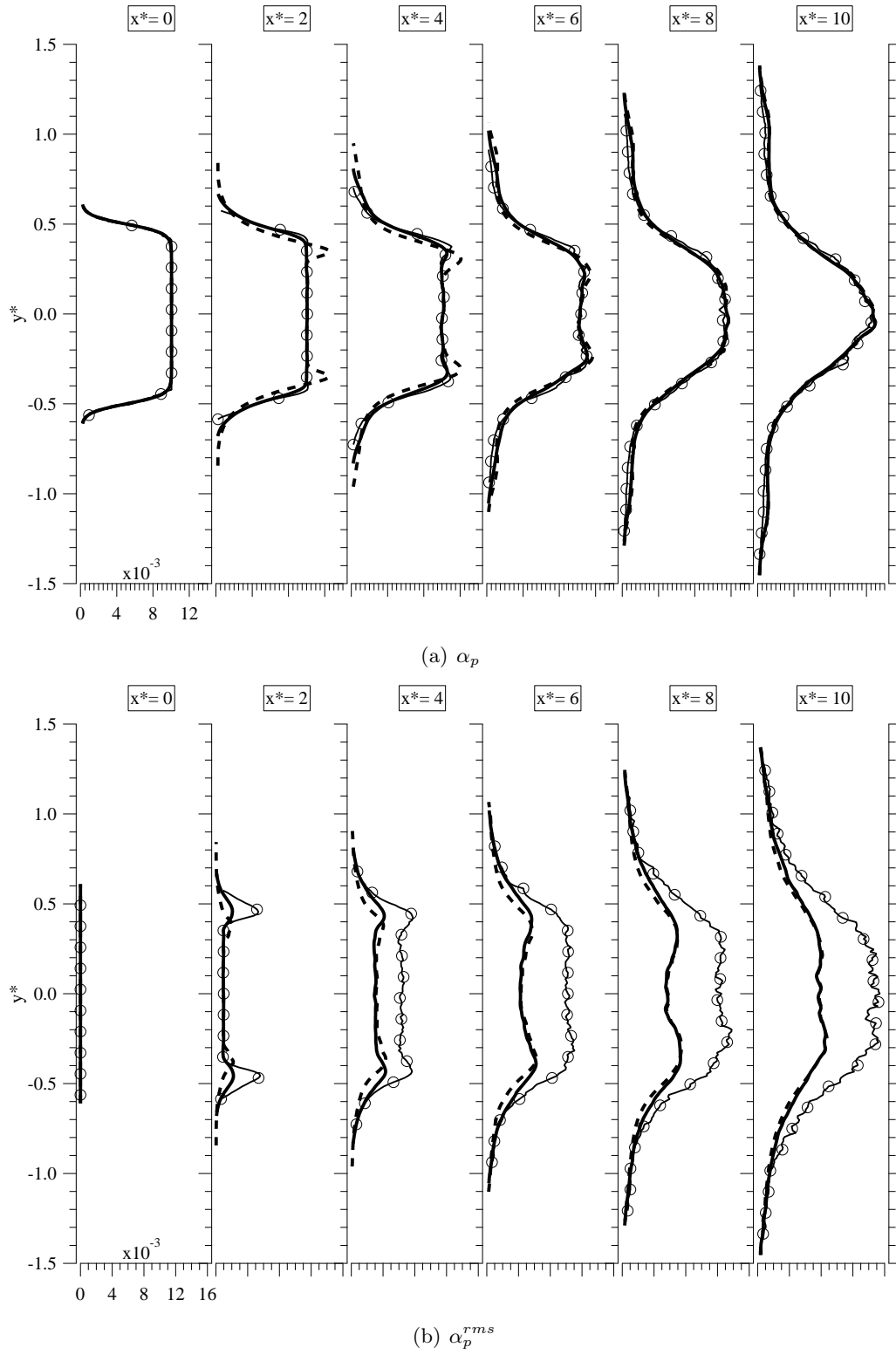


Figure 6.9: Impact of the RUM models on the dispersed phase statistics. (a) mean particle volume fraction and (b) rms particle volume fraction . Comparison between AXISY-C (—) and VISCO (---) models *vs* the Lagrangian reference (—○—).

Finally, the PDFs of the streamwise and spanwise particle mesoscopic velocities are presented in Fig. 6.11 and 6.12, comparing the two Eulerian simulations to the Lagrangian reference. The position of the six probes, plotted in Fig. 6.10, has been chosen as a function of the jet expansion. First, the superiority of the AXISY-C over the VISCO model is clearly visible at P1,

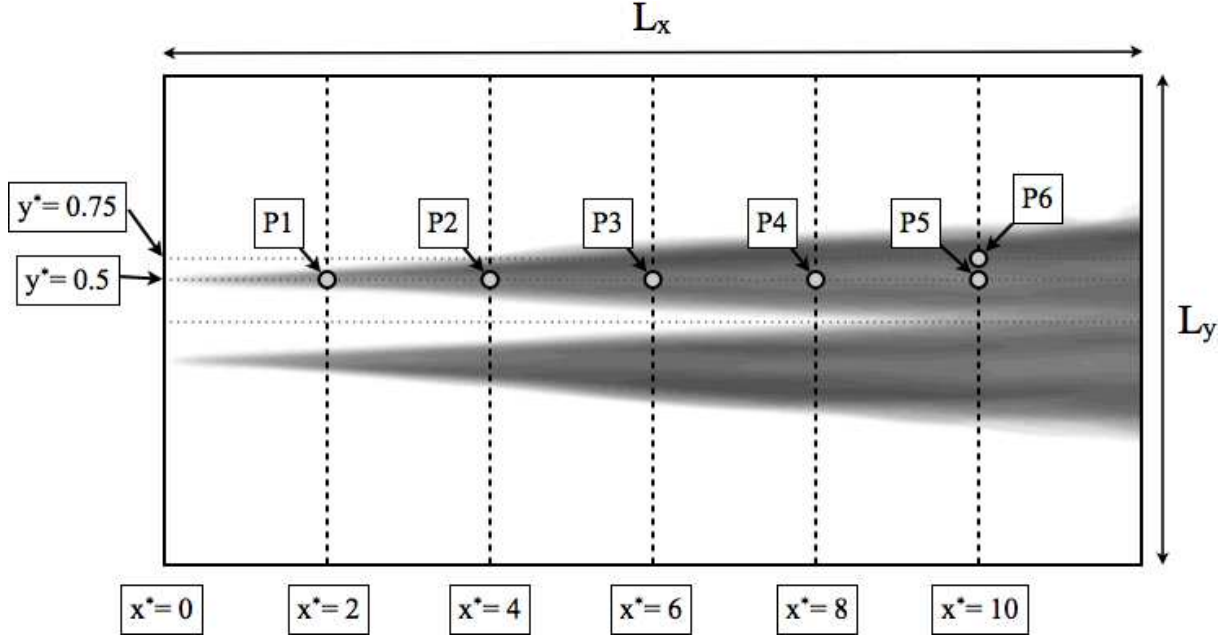


Figure 6.10: Diagnostics used for the two-dimensional non-isothermal jet. The vertical dashed lines represent the location of the transverse cuts for the analysis. The white bullets represent the probes where velocity and temperature signals were recorded. Their positions have been chosen as a function of the mean particle temperature shown in the background.

consistently with the previous statistics. With VISCO, the PDF of \tilde{u}_p and \tilde{v}_p are too narrow, with a mean slightly over-estimated whereas the agreement is very good between AXISY-C and the EL simulation. For the other probes, both Eulerian simulations agree satisfactorily with the Lagrangian reference. Note that the MEF is able to predict non gaussian PDF of velocities, which means that higher moments are also well predicted.

The influence of the RUM model on the thermal dispersion is investigated in the next section.

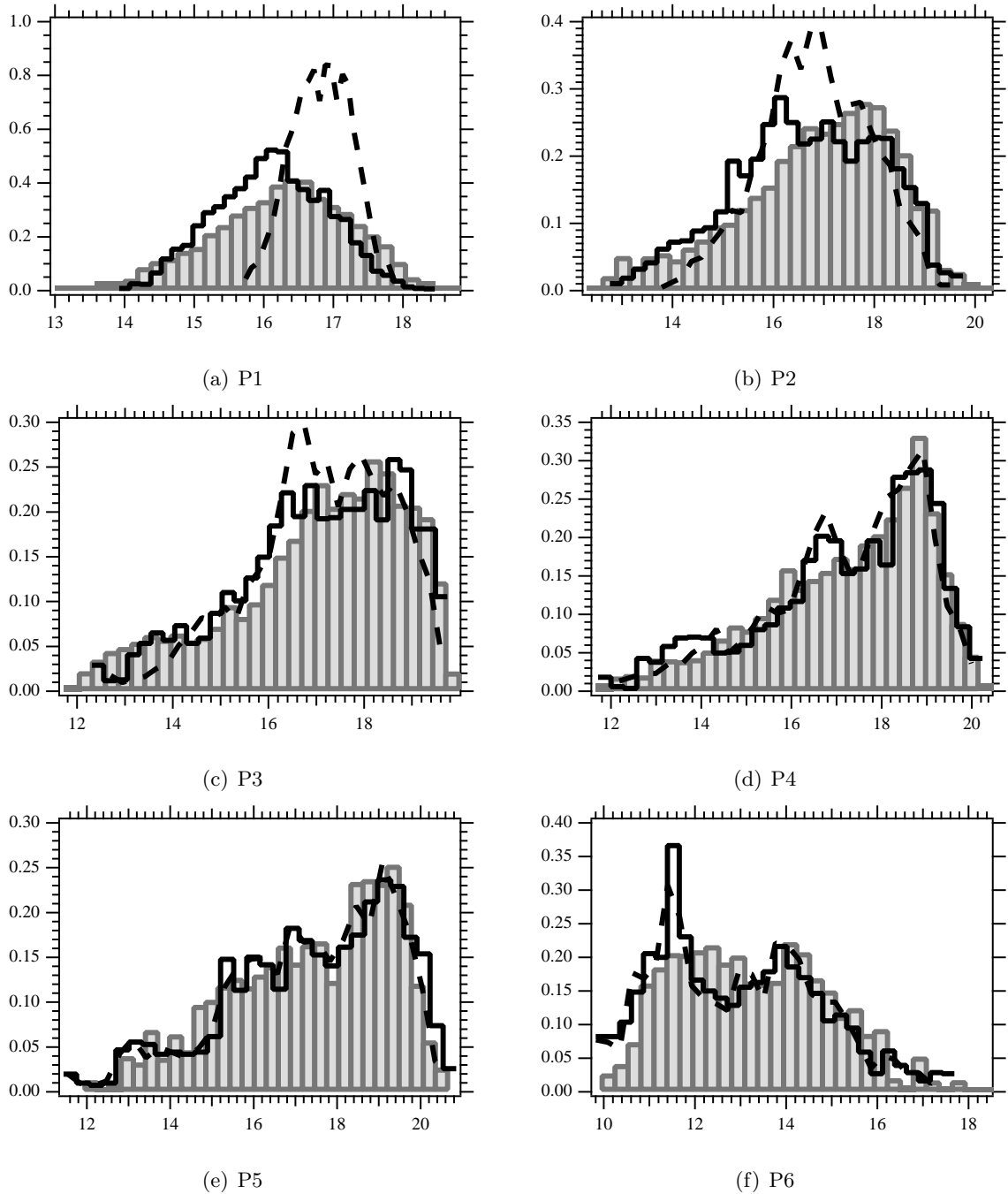


Figure 6.11: Impact of the RUM models on the PDF of the streamwise velocity \tilde{u}_p at the different locations defined in Fig. 6.10. Comparison between AXISY-C (—) and VISCO (---) models vs the Lagrangian reference (\square).

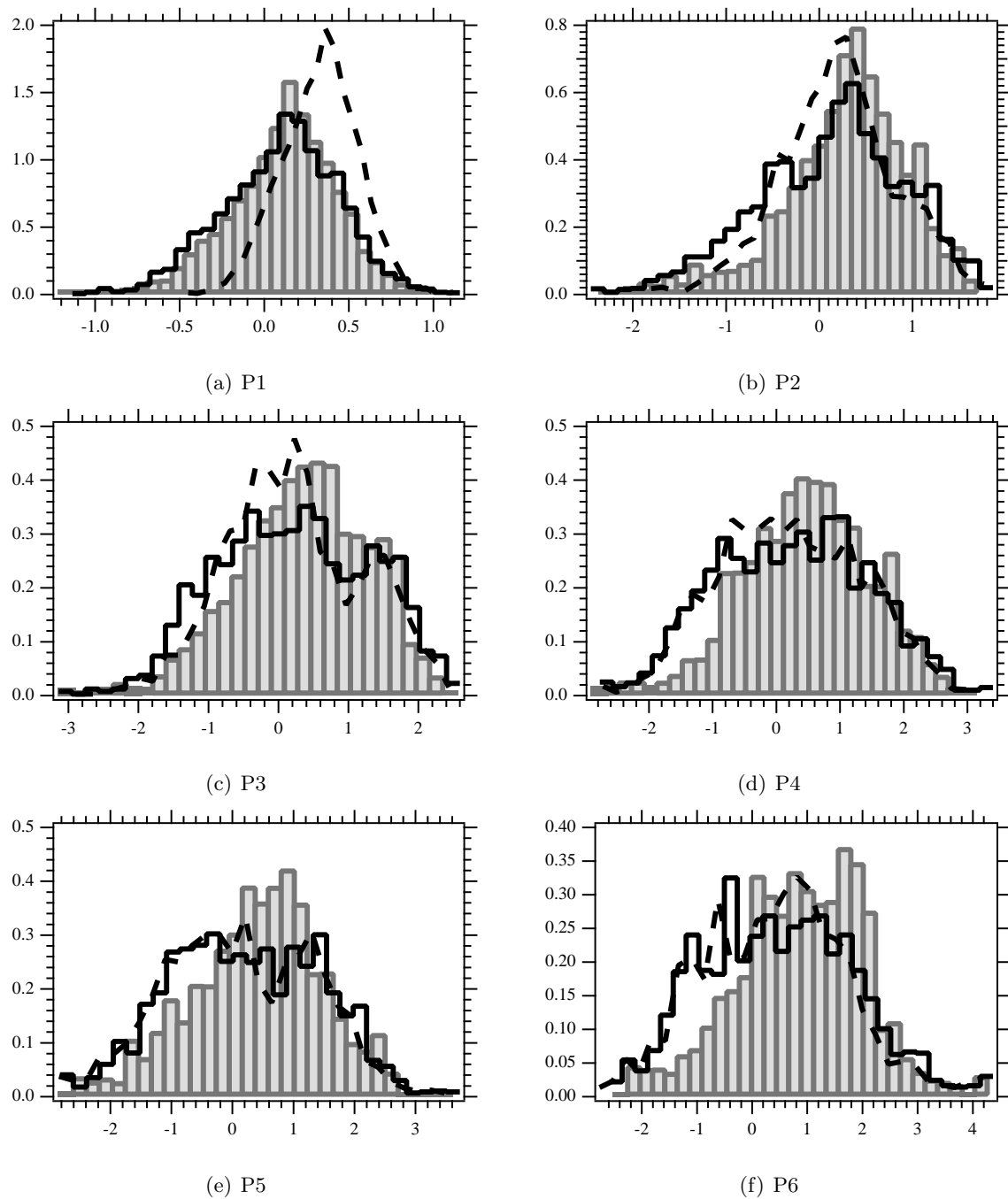


Figure 6.12: Impact of the RUM models on the PDF of the spanwise velocity \tilde{v}_p at the different locations defined in Fig. 6.10. Comparison between AXISY-C (—) and VISCO (---) models vs the Lagrangian reference (■).

6.6.2 Temperature statistics of the dispersed phase

The RUM models may impact the temperature statistics by two means: (1) through the particle dynamics only and (2) through the RUM heat fluxes if they are turned on. First, it is intuitive that thermal dispersion is altered when the dynamics of the dispersed phase is modified (for the same carrier phase). Particles with different trajectories have a different heat transfer with the gas. Secondly, particles have a thermal inertia which is not negligible in this configuration ($St_\theta = 2$). That means that their temperature does not adapt instantaneously to the surrounding carrier phase. Then, two neighboring particles coming from two distinct zones of the jet may have different temperature, spatially uncorrelated. This is taken into account in the MEF by the RUM heat fluxes, which are function of the particle uncorrelated velocities and consequently depend of the RUM model. Then, all parameters being unchanged, two different RUM models yield two distinct uncorrelated temperatures. Mathematically, the RUM impacts the particle temperature through the RUM heat fluxes since $\delta R_{p,ij}$ appear in their transport equations as a source term (Eq. 1.54).

First, the impact of the RUM model without RUM heat fluxes is evaluated comparing the test cases J1 (---) and J3 (----) in Fig. 6.13. Inside the jet, the mean particle temperature (Fig. 6.13(a)) is similar for both RUM models and agree satisfactorily with the exact solution. However, results between the two Eulerian simulations slightly differ at the border of the jet for $x^* \geq 4$, where \tilde{T}_p is over-estimated by around 50 K with the VISCO model in comparison with AXISY-C. These discrepancies between both RUM models are also visible on the particle temperature rms statistics (Fig. 6.13(b)). \tilde{T}_p^{rms} is overestimated by both RUM models in comparison with EL results. The deviation is almost twice larger with VISCO than with AXISY-C. Finally, the two RUM models are compared with the PDF of \tilde{T}_p , plotted in Fig. 6.14. At P1, the PDF of \tilde{T}_p is slightly shifted toward the lower temperatures with VISCO, whereas the agreement is very good between AXISY-C and the EL simulation. This could be explained by the over-estimation of the jet expansion with VISCO at P1 (the spanwise velocity is overestimated Fig. 6.12(a)). There are more particles coming from the cold center of the jet. At the other probes, both models yield similar results. Incidentally, the tails of the PDF are better predicted by VISCO than AXISY-C at P2, P3 and P4. That means that the particle dynamic dispersion –driven by the RUM model– has a strong impact on the thermal statistics. This is another motivation to develop advanced RUM models for the simulation of evaporating sprays, where thermal dispersion of particles is of paramount importance [10].

Then, the influence of the RUM heat fluxes may be investigated for a given RUM model in Fig. 6.13, comparing cases J1 (---) vs J2 (.....) or J3 (----) vs J4 (—). The mean particle temperature is almost not impacted by the RUM heat fluxes at this thermal inertia. Large deviation of \tilde{T}_p is visible at $x^* = 2$ with the VISCO model, probably due to the overestimation of δq_p^2 at this particular location (Fig. 6.8(b)). However, the RUM heat fluxes have a strong influence on the particle temperature rms. Turning on the RUM heat fluxes improves the agreement with the Lagrangian reference, for both RUM models. Note that the impact of the RUM heat fluxes on the PDF of \tilde{T}_p (Fig. 6.15) is minor. Only the tail of the PDF at P2, P3 and P4 is slightly better predicted when the RUM heat flux term is switched on.

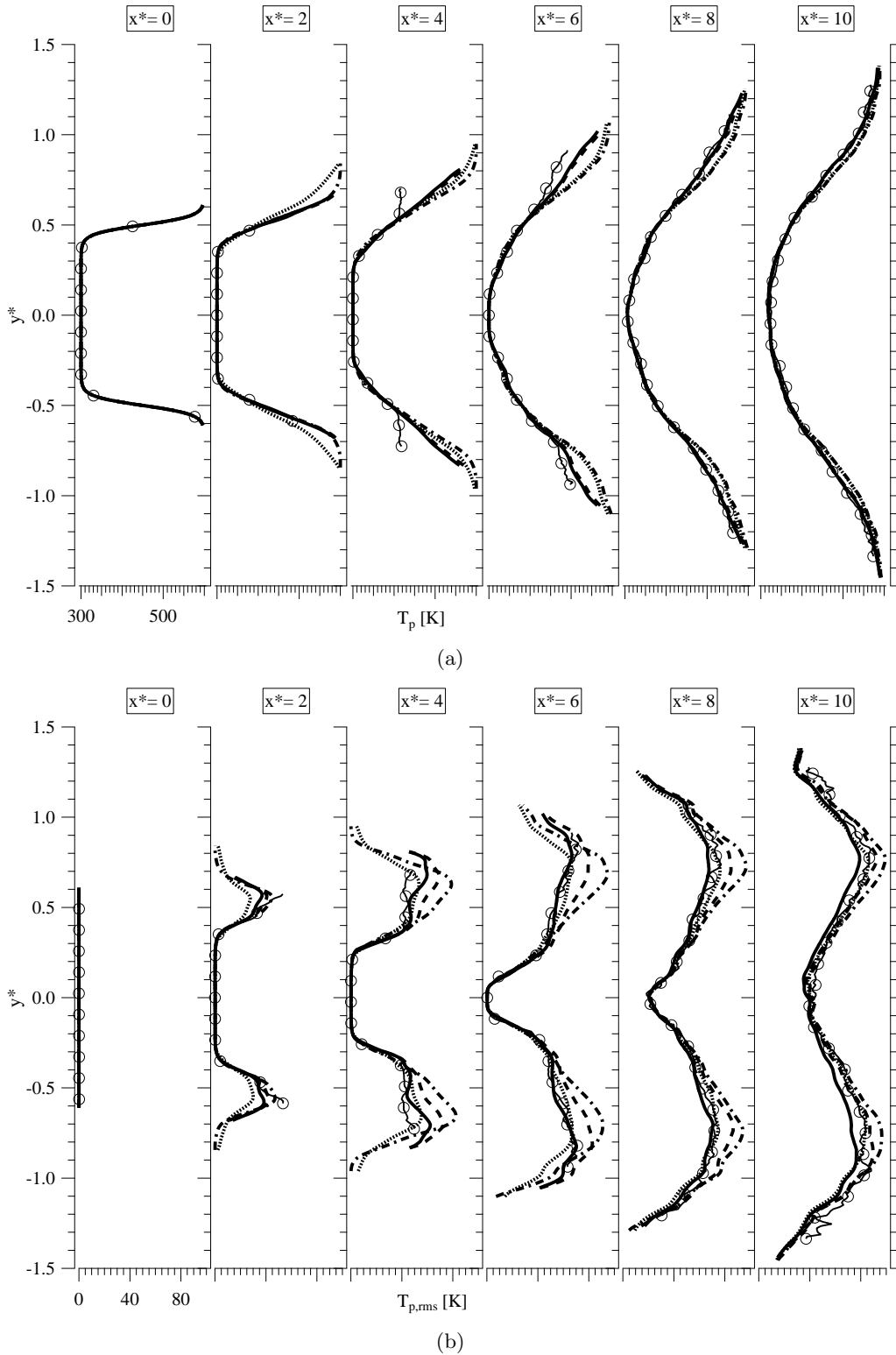


Figure 6.13: Comparison between Eulerian test cases defined in Tab. 6.4 ($St_\theta = 2$) and the Lagrangian reference (—○—). VISCO model without and with RUM HF (J1:--- and J2:....., respectively). AXISY-C model without and with RUM HF (J3:-.-.- and J4:—, respectively). (a) Mean particle temperature \tilde{T}_p , (b) rms \tilde{T}_p^{rms} .

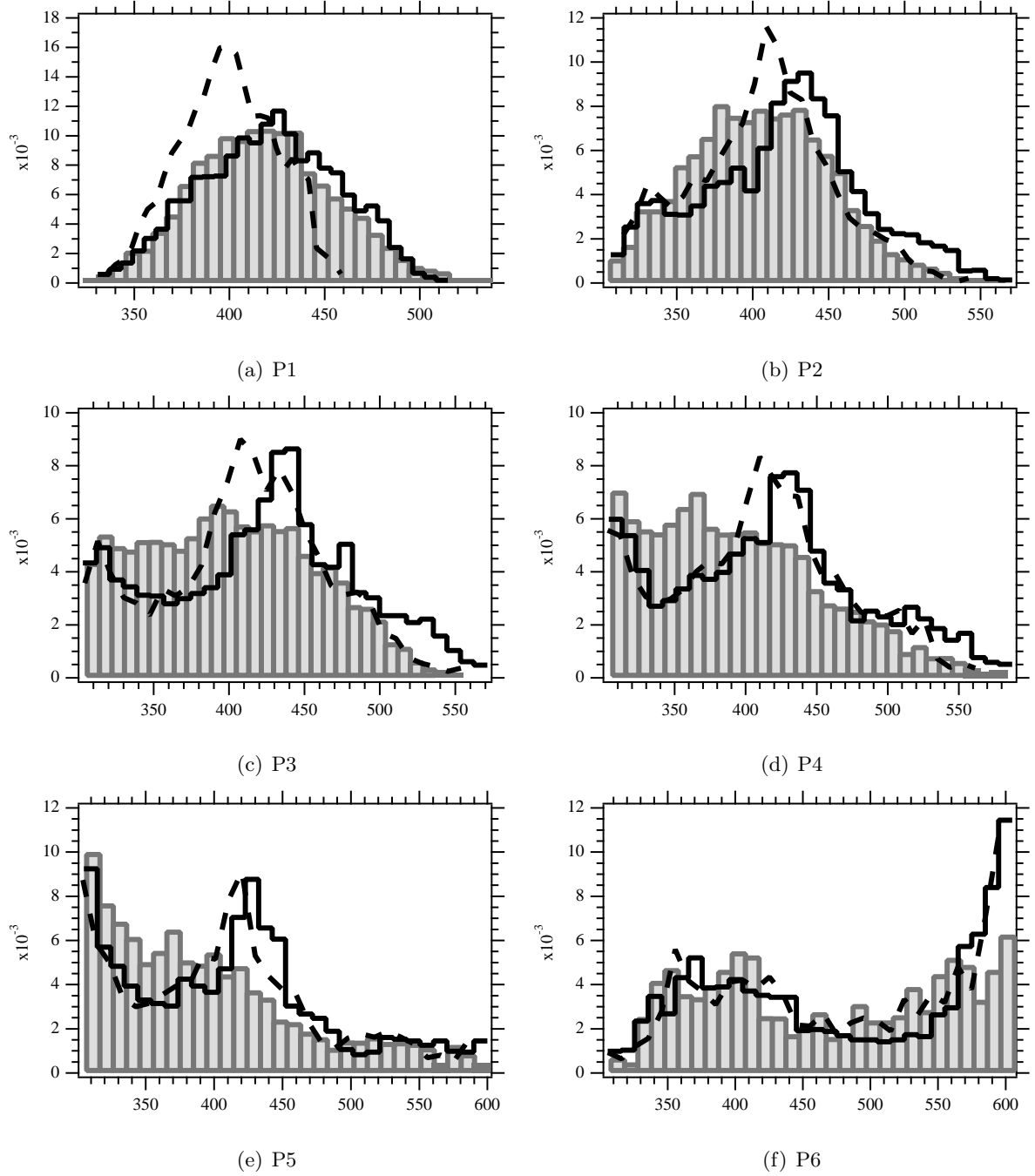


Figure 6.14: Impact of the RUM model (no RUM HF term) on the PDF of the particle mesoscopic temperature \tilde{T}_p at the different probes (*cf.* Fig. 6.10 for their locations). Comparison between AXISY-C (—) and VISCO (---) models vs the Lagrangian reference (□).

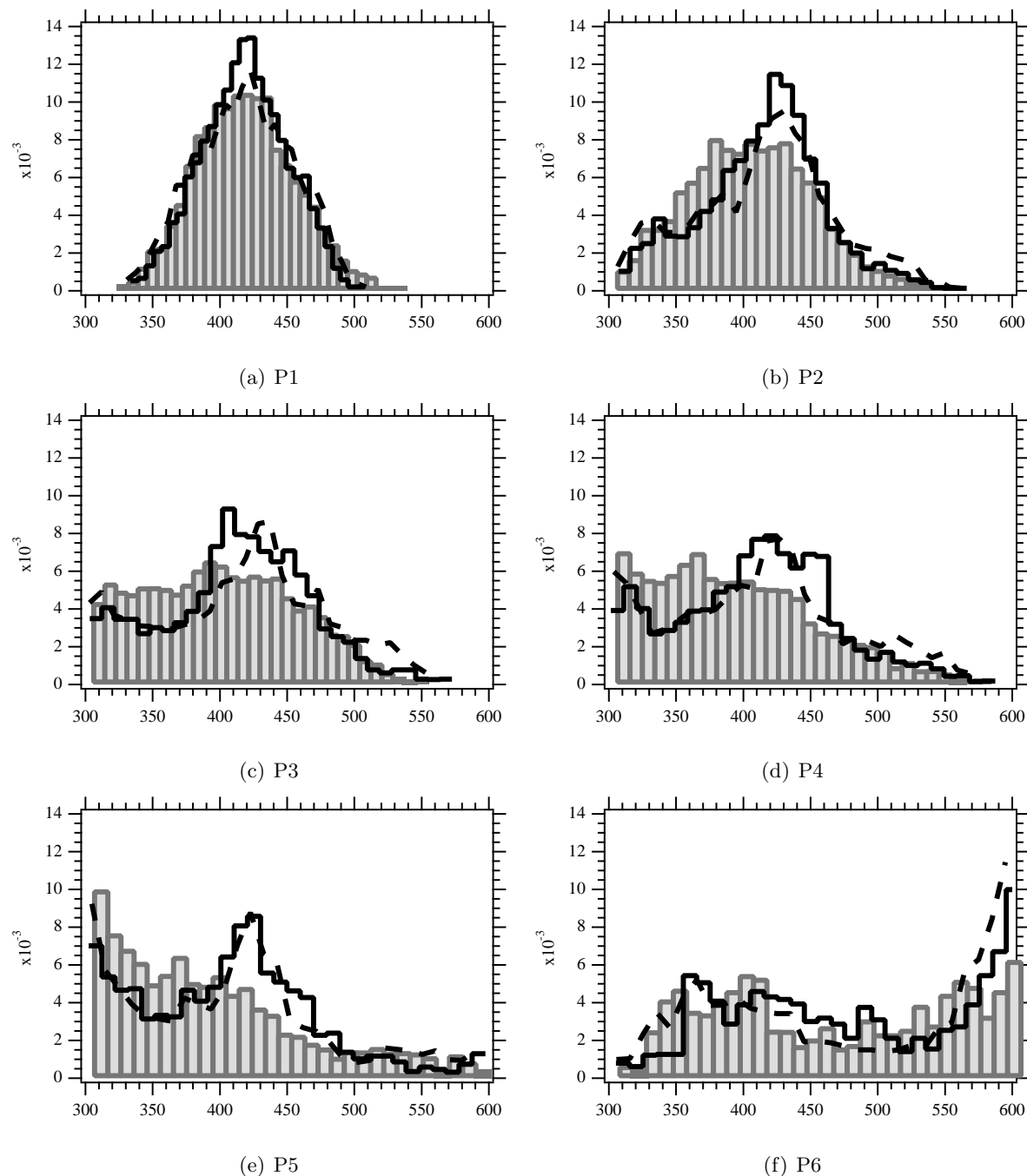


Figure 6.15: Impact of the RUM HF term when the AXISY-C model is used for the dynamics. PDF of the particle temperature \tilde{T}_p at the different probes (*cf.* Fig. 6.10 for their locations). Eulerian simulation with (—) and without RUM HF (---) vs the Lagrangian reference (▒).

6.6.3 Additional conclusions

This section presented additional results carried out on the two-dimensional non-isothermal turbulent jet laden with solid particles.

- First, the two RUM models available in this work, namely the VISCO and AXISY-C models (*cf.* Sec. 1.3.3), have been compared. The AXISY-C model clearly overcomes VISCO in this configuration, capturing satisfactorily the dynamics of the particles.
- Furthermore, it was shown that the dynamics only of the particles (driven by the RUM models) has a large impact on the thermal statistics at the edges of the jet. Both mean and fluctuations of the particle mesoscopic temperature are better predicted with the AXISY-C model in comparison with the exact solution.
- Finally, the influence of the RUM heat flux term was investigated with both RUM models. In this configuration, no impact is noticeable on the mean mesoscopic temperature. However, accounting for the RUM heat fluxes clearly improves the prediction of \widetilde{T}_p^{rms} , for both RUM models.

Unfortunately, the Lagrangian database did not contain RUM variables, so that only Eulerian and Lagrangian mesoscopic quantities were compared. The configuration of Chap. 7 overcomes this issue and also allows to extend tests to a full three-dimensional configuration.

Chapter 7

Evaluation of the MEF extended to non-isothermal flows - 3D non-isothermal particle-laden jet

Contents

7.1	Configuration	125
7.1.1	Initial conditions	125
7.1.2	Definition of the normalization numbers	127
7.1.3	Numerical setup and methodology	128
7.2	Analysis of the carrier phase	130
7.3	Analysis of the dispersed phase	132
7.3.1	Analysis of the Lagrangian database	132
7.3.2	Mesh convergence of the Eulerian simulations	132
7.3.3	Evaluation of the RUM models	137
7.3.4	Influence of the RUM heat fluxes	143
7.4	Conclusions	145

The objective of this chapter is to *a posteriori* validate the MEF extended to non-isothermal flows in a configuration more realistic of a fuel injection in a combustion engine. It consists in a three-dimensional non-isothermal particle-laden turbulent planar jet [80, 142]. The specificity of this configuration is the mean shear and the particle temperature gradient. Low particle volume fraction allows us to assume that the dispersed phase has no impact on the carrier (one-way coupling), neither on the momentum nor the energy equations. This enables an independent investigation of the effects of the RUM model and RUM heat flux term on the dynamic and thermal dispersion of the particles.

Eulerian simulations carried out with AVBP will be compared to Eulerian particle fields computed from a DNS EL simulation performed by Masi [78] with the NTMIX code [14]. Contrary to the configuration of Chap. 6, uncorrelated particle-velocity and particle-temperature moments

are available in the Lagrangian database¹. This is the most complete database available at IMFT to thoroughly compare mesoscopic and uncorrelated variable statistics between Eulerian and the exact solution. Moreover, this configuration is three dimensional, contrary to the one of Chap. 6.

First, the configuration is presented in Sec. 7.1, with specific attention on the normalization procedure of the parameters in Sec. 7.1.2. Then, the carrier-phase statistics of both solvers are analyzed in Sec. 7.2, along with their sensitivity to the grid resolution. After that mandatory step, some Lagrangian fields of the dispersed phase are displayed in Sec. 7.3.1 to present the physical features of the particle-laden jet. Finally, the effects of the two RUM models available in this work and the impact of the RUM heat flux term are investigated in Sec. 7.3.3 and Sec. 7.3.4, respectively.

7.1 Configuration

The configuration consists in a three-dimensional cold planar turbulent jet, embedded with solid particles and surrounded by a hot decaying turbulent flow. The reference length $L_{ref} = 10^{-3}$ m is used throughout this chapter for normalization. The computational domain is a cubic box of size $L_{box} = 2\pi L_{ref}$ with periodic conditions in all directions. The carrier phase is composed of pure air (density ρ_f , kinematic viscosity μ_f and specific heat at constant pressure $C_{p,f}$) at constant mean pressure P_{ref} and reference temperature T_{ref} . This yields the reference speed of sound

$$c = \sqrt{\gamma \frac{P_{ref}}{\rho_f}}, \quad (7.1)$$

where $\gamma = C_{p,f}/C_{v,f}$ is the ratio of the specific heats of the gas at constant pressure and constant volume ($\gamma = 1.4$). The particle-laden jet is statistically unsteady and depends solely on the initial conditions and parameters of the carrier and dispersed phase.

7.1.1 Initial conditions

The initial condition of the carrier phase is the same between NTMIX and AVBP. The initial mean profile of the velocity and temperature of the carrier phase are imposed with the general hyperbolic profile

$$\phi(y) = \phi^c + f(y)(\phi^j - \phi^c) \quad (7.2)$$

$$f(y) = \frac{1}{2} \left(1 + \tanh \frac{L_{slab}/2 - |y|}{2\delta_\theta} \right), \quad (7.3)$$

where ϕ^c and ϕ^j denote the considered quantity in the jet and in the coflow, respectively. L_{slab} and δ_θ refer to the initial width and initial momentum thickness of the slab. The parameters of the initial solution are summarized in Tab. 7.1. The mean velocity profile is added to an initial statistical homogeneous isotropic turbulence initialized by a Passot-Pouquet spectrum [92]. It is defined by the most energetic length scale $l_e = 0.4 L_{ref}$ and by the fluctuating velocity u' defined in Sec. 7.1.2. With that, the jet is already turbulent at the initial time. On the contrary, the

¹In this chapter and for the sake of conciseness, the terms ‘‘Lagrangian database’’ or ‘‘Lagrangian reference’’ refer to the Eulerian fields extrapolated from the Lagrangian simulation.

temperature of the carrier phase has no fluctuation at $t^* = 0$. The initial velocity field of the carrier phase is shown in Fig. 7.1. It can be seen that the choice of l_e yields initial turbulent eddies which size are around one quarter of the initial slab width. As stressed by Masi [78], that allows the jet to develop additional turbulent velocity fluctuations from the mean gradient. With a too large value of l_e , the eddies of the initial turbulence would damp out the jet.

The initial conditions of the dispersed phase of the Eulerian solution (AVBP) were chosen

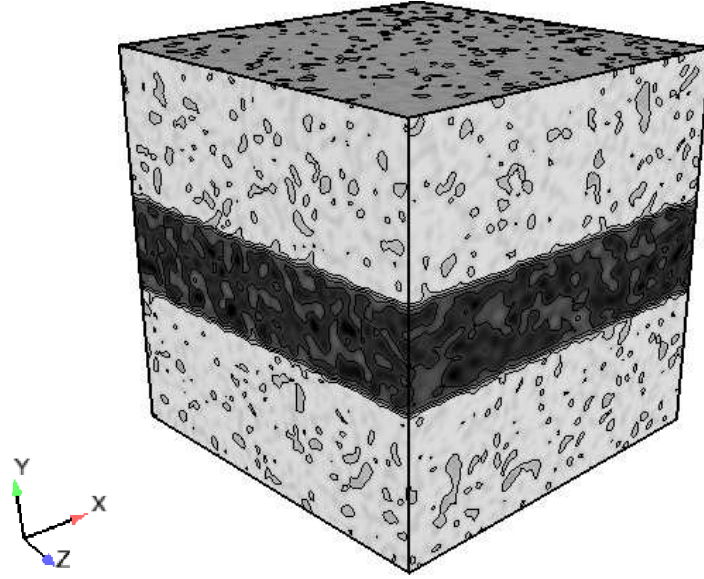


Figure 7.1: Initial velocity field of the carrier phase of the three-dimensional particle-laden slab. Velocity is proportional to darkness.

as close as possible to that of the Lagrangian solution (NTMIX). They only slightly differ for the initial particle volume-fraction profile shape. Whereas particles are randomly seeded with a crenel profile in NTMIX, the dispersed phase of the Eulerian initial solution consists in an homogeneous particle volume fraction following the hyperbolic profile of Eq. 7.2. That allows AVBP to handle the initial transient time where the particle volume-fraction profile is very steep (*cf.* Part. II). Note that AVBP crashes with the crenel-type profile of the Lagrangian initial solution. Apart of that difference, the Eulerian and Lagrangian initial solutions of the dispersed phase are rigorously identical. Particles are embedded with the same mean velocity and temperature than the carrier phase

$$\tilde{u}_p = \overline{u}_g \quad (7.4)$$

$$\tilde{v}_p = v'_g \quad (7.5)$$

$$\tilde{w}_p = w'_g \quad (7.6)$$

$$\tilde{T}_p = T_g \quad (7.7)$$

Incidentally, the particles have no velocity fluctuation in the streamwise direction at $t^* = 0$. The parameters of the carrier and dispersed phase at $t^* = 0$ are summarized in Tab. 7.1 and are written as a function of the normalized parameters detailed in Tab. 7.3.

δ_θ	L_{slab}	u_f^j, u_f^c [m.s ⁻¹]	T_f^j, T_f^c [K]	α_p^j [-]	u_p^j [m.s ⁻¹]	T_p^j [K]
$\frac{\pi}{50} L_{ref}$	$\frac{\pi}{2} L_{ref}$	$U + u', u'$	$T_{ref}, 1.25 T_{ref}$	10^{-4}	U	T_{ref}

Table 7.1: Characteristics of the initial condition. Variables are written as a function of the normalized parameters detailed in Tab. 7.3.

The reference database has been computed with NTMIX, which uses normalized variable, unlike AVBP. Common normalization numbers ensure the similarity of the solutions between both codes. Their choice and definition are detailed in Sec. 7.1.2.

7.1.2 Definition of the normalization numbers

The four following normalization numbers characterize the carrier phase (Tab. 7.2):

- The acoustic Reynolds number

$$\text{Re}_{ac} = \frac{c L_{ref}}{\nu_f}, \quad (7.8)$$

where $\nu_f = \rho_f / \mu_f$ is the kinematic viscosity of the carrier phase.

- The Mach number

$$\text{M} = \frac{U}{c}, \quad (7.9)$$

where U is the mean velocity of the carrier phase.

- The turbulence intensity

$$\text{I}_{turb} = \frac{u'}{U}, \quad (7.10)$$

where u' is the fluctuating velocity.

- The Prandtl number

$$\text{Pr} = \frac{C_{p,f} \mu_f}{\lambda_f}, \quad (7.11)$$

where λ_f is the thermal conductivity of the fluid.

The four free parameters ν_f , U , u' and λ_f are computed from Eqs. 7.8-7.11. Moreover, the dispersed phase is determined by the two following normalization numbers (Tab. 7.2):

- The dynamic Stokes number

$$\text{St} = \frac{\tau_p}{\tau_f}, \quad (7.12)$$

where τ_p is the particle dynamic relaxation time (Eq. 1.4). In this configuration, the characteristic time scale of the fluid has been chosen based on the initial HIT as it was thought to be the most relevant for the initial particle segregation inside the slab. It is defined as the ratio of the integral length scale of the turbulence $l_e = 0.4 L_{ref}$ and the fluctuating velocity u' :

$$\tau_f = \frac{l_e}{u'}. \quad (7.13)$$

- The thermal Stokes number

$$St_\theta = \frac{\tau_\theta}{\tau_f}, \quad (7.14)$$

where τ_θ is the particle thermal relaxation time (Eq. 1.5).

Carrier phase				Dispersed phase	
Re_{ac}	M	I_{turb}	Pr	St	St_θ
5500	0.15	0.1	0.7	0.46	0.93

Table 7.2: Normalization parameters of the carrier and dispersed phase shared by the two solvers.

The particle diameter is a degree of freedom of the configuration. It was chosen to be smaller than the smallest turbulent fluid scale, triggered by the smallest grid size Δx . It was arbitrarily fixed at $d_p = 2 \cdot 10^{-6}$ m, which corresponds to $\Delta x/25$ or $\Delta x/12$ for the two mesh resolutions used in this chapter (*cf.* Tab. 7.6). Finally, the particle density ρ_p is obtained combining the particle dynamic relaxation time in Stokesian regime (Eq. 1.4) and Eq. 7.12:

$$\rho_p = \frac{18\mu_f St \tau_f}{d_p^2}. \quad (7.15)$$

Similarly, the specific heat at constant pressure of the particles, $C_{p,p}$, is computed combining the definition of τ_θ at small Re (Eq. 1.5) and Eq. 7.14:

$$C_{p,p} = \frac{2}{3} \frac{C_{p,f}}{\text{Pr}} \frac{St_\theta}{St}. \quad (7.16)$$

The characteristics of the carrier and dispersed phase are summarized in Tab. 7.3.

ρ_f [kg.m ⁻³]	c [m.s ⁻¹]	P_{ref} [Pa]	T_{ref} [K]
1.138	352.9	101325	300
$C_{p,f}$ [J.kg ⁻¹ .K ⁻¹]	ν_f [m ² .s ⁻¹]	U [m.s ⁻¹]	u' [m.s ⁻¹]
1041.3	$6.4163 \cdot 10^{-5}$	52.9	5.29
λ_f [W.m ⁻¹ .K ⁻¹]	d_p [m]	ρ_p [kg.m ⁻³]	$C_{p,p}$ [J.kg ⁻¹ .K ⁻¹]
$1.09 \cdot 10^{-1}$	$2 \cdot 10^{-6}$	$11.45 \cdot 10^3$	2005

Table 7.3: Characteristics of the carrier and dispersed phases.

7.1.3 Numerical setup and methodology

The numerical strategy used in this chapter is the one identified as the most promising in Part. II. It consists in the TTGC scheme [22] coupled with adapted AV sensors and coefficients $\epsilon^{(2)}$ and

$\epsilon^{(4)}$, which characteristics are summarized in Tab. 7.4. This strategy has already been validated in the configuration of Chap. 6 and provided sufficient robustness and accuracy. The minimum threshold $B_{min}(\alpha_p)$ has been adapted to the minimum value of α_p in the coflow of this configuration ($\alpha_p^c = 10^{-8}$).

scheme	AV sensor	$\epsilon^{(2)}$	$\epsilon^{(4)}$	$B_{min}(\alpha_p)$
TTGC	CM5-T	0.5	$5 \cdot 10^{-4}$	$1 \cdot 10^{-10}$

Table 7.4: Numerical parameters for the simulations.

Five runs have been carried out in this chapter, recapitulated in Tab. 7.5. First, the impact of the mesh resolution on the carrier and dispersed phase will be investigated with M2H-V and M3H-V cases. The only difference between these two cases is the mesh. In particular, the mesh M3H is twice finer than M2H, as shown in Tab. 7.6. Note that the Lagrangian simulation has been carried out on a mesh of similar resolution than M2H (128^3). Then, we will study the influence of the RUM model on the dynamic and thermal statistics of the dispersed phase (cases M3H-V and M3H-AXI). The notation “-V” and “-AXI” refer to the VISCO and AXISY-C RUM models, which are presented in Sec. 1.3.3. Finally, the impact of the RUM heat flux term in Eq. 1.53 is investigated with the two cases M3H-AXI and M3H-AXI-HF.

keyword	mesh	RUM model	RUM heat flux term
M2H-V	M2H	VISCO	No
M3H-V	M3H	VISCO	No
M3H-AXI	M3H	AXISY-C	No
M3H-AXI-HF	M3H	AXISY-C	Yes

Table 7.5: Characteristics of the runs carried out in this chapter

keyword	type	resolution	Δx
M2H	hexa	128^3	$4.91 \cdot 10^{-5}$
M3H	hexa	256^3	$2.45 \cdot 10^{-5}$

Table 7.6: Mesh characteristics

In this chapter, statistics of any dispersed phase variable ϕ is density-weighted averaged over planes parallel to the streamwise direction (plane ZX)

$$\{\phi\}_p = \frac{\langle \tilde{n}_p \tilde{\phi} \rangle_{ZX}}{\langle \tilde{n}_p \rangle_{ZX}}. \quad (7.17)$$

The bracket notation $\{\cdot\}_p$ is dropped in the rest of the chapter for the sake of clarity. Statistics of the carrier phase are not density-weighted as the gas is considered as weakly compressible due

to the low Mach number. As stressed out by Masi [78], the volume average over these planes of homogeneity gives an estimation of the theoretical ensemble average computed over a large number of particle-and-fluid flow realizations, *i.e.* mean quantities. In the rest of the chapter, the time will be normalized by the initial particle dynamic relaxation time.

$$t^* = \frac{t}{\tau_{p,t=0}} \quad (7.18)$$

Now that the configuration has been described, results of the carrier phase are presented in Sec. 7.2.

7.2 Analysis of the carrier phase

The first requisite before studying the dispersed phase is to verify that the carrier phase is identical between the two solvers NTMIX and AVBP. Moreover, it is important to check that the results are independent of the mesh, *i.e.* that the statistics are converged for a given mesh resolution. For the sake of compactness, only two statistics are shown in this section: the turbulent kinetic energy the rms of the temperature. These variables are thought the most relevant for the physical phenomena of the dispersed phase as the particle concentration and the temperature dispersion. Note that the other variables, not shown here, compare accordingly between both solvers. The analysis of q_g^2 and T_g^{rms} is very similar to that of the two-dimensional jet configuration of Chap. 6.

First, the turbulent kinetic energy at five normalized times is presented in Fig. 7.2(a). The initial homogeneous turbulence created by the Passot-Pourquet spectrum is progressively damped by the viscous effects so that q_g^2 is null outside the mixing layers at $t^* = 40$. Accordingly to theory [95], the mixing layers at the edges of the jet spread with a slight preference into the lighter streams. The turbulent kinetic energy begins to increase at the center of the jet for $t^* > 60$. The agreement is excellent between the simulations carried out with AVBP and NTMIX. Moreover, the statistics of q_g^2 are converged with the M2H mesh. Then, the rms of the gas temperature is shown in Fig. 7.2(b). The maximum of T_g^{rms} remains approximatively constant at the fringe of the jet whereas it increases progressively at its center. At the end of the simulation, the maximum rms of the temperature represents almost one fifth of the initial jet-to-coflow mean temperature difference. Again, both solvers agree very well and no differences are visible between the fine and coarse meshes. The dispersed phase is now analyzed having verified that (1) both solvers yield the same carrier phase and (2) the carrier phase statistics are converged on the coarse mesh M2H.

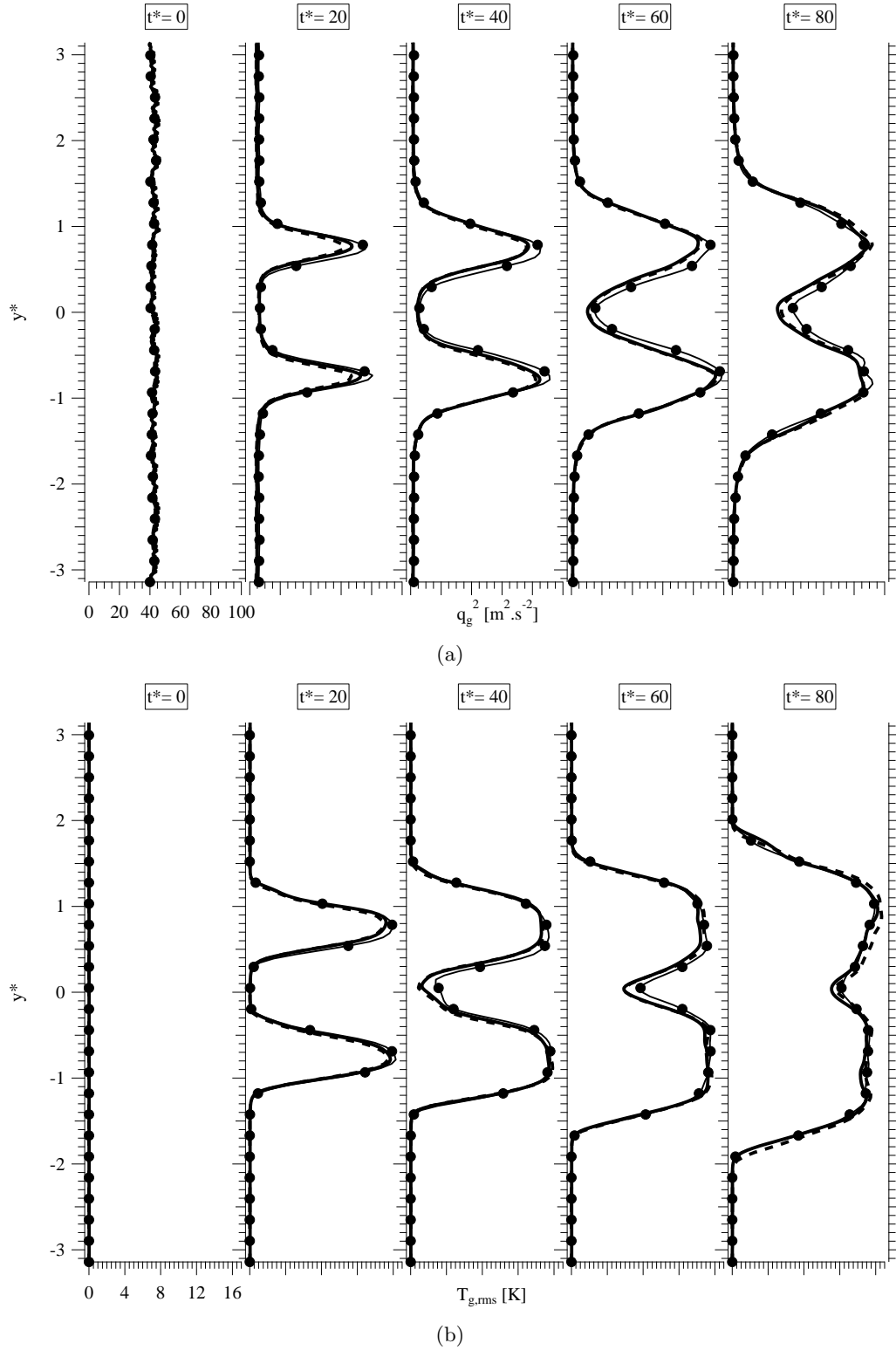


Figure 7.2: Comparison of Eulerian and Lagrangian quantities of the carrier phase. (a) Turbulent kinetic energy q_g^2 and (b) rms T_g^{rms} . Simulations carried out with AVBP (fine mesh M3H (—) and coarse mesh M2H (---)) are compared with NTMIX (—●—).

7.3 Analysis of the dispersed phase

7.3.1 Analysis of the Lagrangian database

The time evolution of the particle volume fraction, extracted from the Lagrangian database, is presented in Fig. 7.3. At $t^* = 0$, particles are randomly embedded in the plane jet at the same mean velocity and temperature than the carrier phase. In the early stages of the simulation, the zone inside the particle-laden slab is similar to a particle-laden HIT (as presented in Chap. 5). Particles quickly accumulate inside the slab in regions of weak vorticity and high shear, coherently with the Stokes number value ($St = 0.46$). While the initial small eddies are damped by viscosity (*cf.* Fig. 7.2(a)), the number of small clusters decreases. At the same time, the mean velocity gradient creates large scale structures at the edges of the jet. Under the effect of these large eddies, some part of the particles concentrates at the center of the jet whereas another part is dispersed in large “finger-shapes” at the edges.

The time evolution of the RUM kinetic energy is presented in Fig. 7.3. It is null at the beginning of the simulation as the particles are injected at the same mean velocity as the gas. According to theory [78], the RUM kinetic energy is produced by the mean motion and by the fluctuating contributions. This is verified in Fig. 7.3(j), where δq_p^2 is very high at the edges of the jet and presents some spots of mild intensity inside the slab similar to what is observed in a particle-laden HIT. RUM kinetic energy quickly vanishes at the center of the jet since the fluctuating contributions no longer exist to produce δq_p^2 . However, the mean motion is strong enough to produce δq_p^2 at the edges of the jet until the end of the simulation.

As expected, the results show that the mean shear introduced here increases one step further the complexity of a particle-laden HIT. A large range of scales appears, from the small clusters of particles at the beginning of the simulation to the large structures at the end. Steep fronts of particle-volume fraction develop at the edges of the jet. The previous chapters showed that these steep gradients of particle volume fraction are difficult to handle with an Eulerian approach. The numerical strategy designed and evaluated on simple test cases in Part. II is expected to circumvent this issue. Moreover, the RUM kinetic energy is continuously created by the mean motion, contrary to an “ordinary” particle-laden HIT. The RUM model will have to be accurate enough to reproduce this unsteady and local phenomenon.

First of all, Sec. 7.3.2 investigates the impact of mesh resolution on the dispersed phase.

7.3.2 Mesh convergence of the Eulerian simulations

The discrete balance of particle MKE of a particle-laden HIT (Chap. 5) pinpointed the importance of the mesh resolution in two-phase flow simulations with an Eulerian approach. Even if the carrier phase is converged for a given mesh, it might not be the case for the dispersed phase. Numerical dissipation effects (convective scheme, stabilization techniques) could be higher than physical dissipation terms (drag, RUM model). For quantitative results, it is then mandatory to verify the mesh convergence of the dispersed phase in the present configuration before investigating the impact of the RUM models and/or RUM heat fluxes.

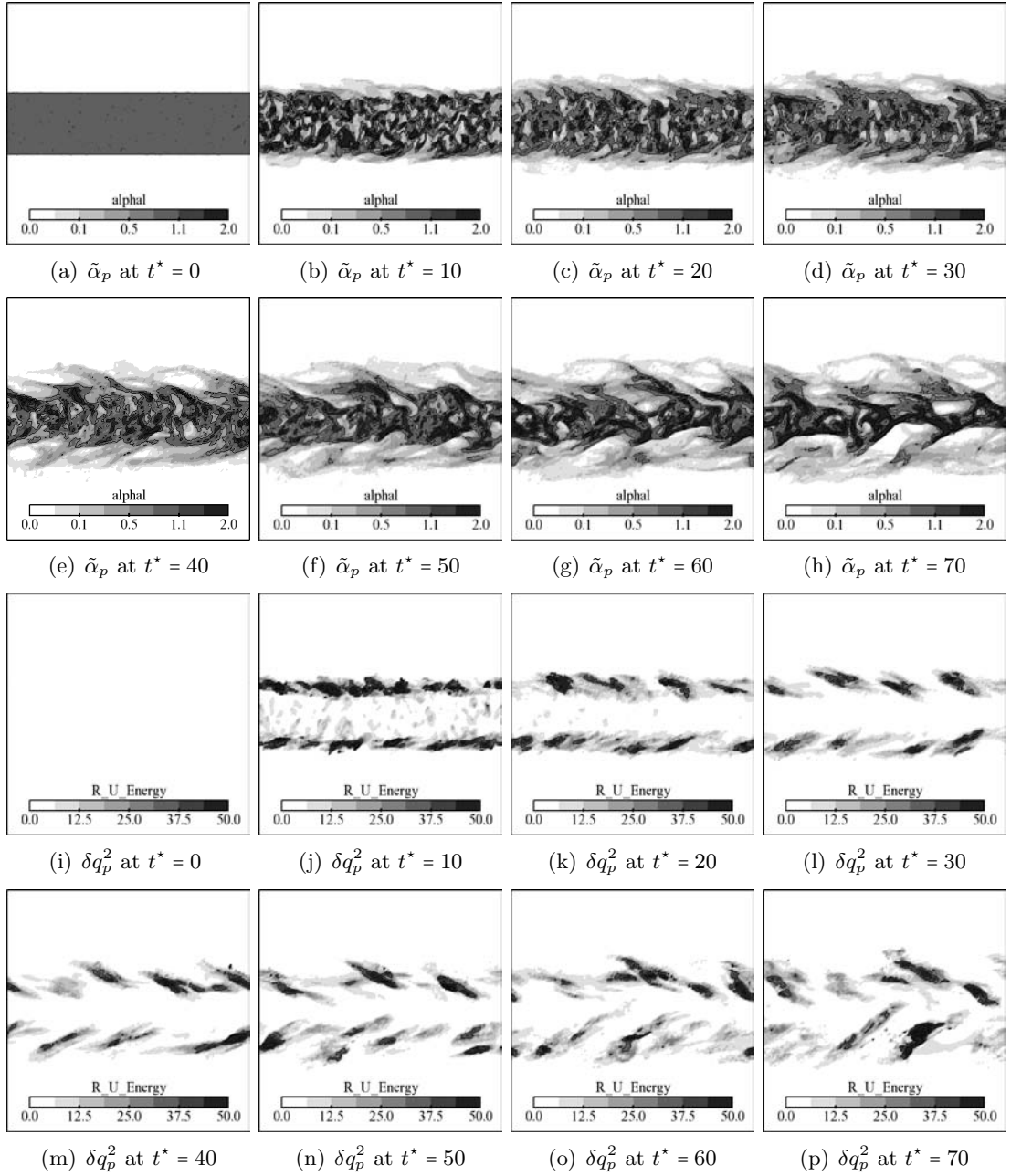


Figure 7.3: Time evolution of the normalized particle volume fraction $\tilde{\alpha}_p/\tilde{\alpha}_p^0$ (top) and RUM particle kinetic energy δq_p^2 (bottom) of the Lagrangian simulation. Cut at $Z = 0$.

Previous chapters of this work showed that the particle volume fraction is a good choice to quantify the effect of the mesh and/or the effect of numerical strategies. Thus, Fig. 7.4 shows the impact of the mesh resolution on the mean and rms of the normalized particle volume fraction at $t^* = 40$. The two simulations M2H-V and M3H-V yield the same mean $\tilde{\alpha}_p$. Moreover, mean $\tilde{\alpha}_p$ agree reasonably well with the Lagrangian reference. For all the other variables (mean and

rms) –not shown here for the sake of conciseness– statistics are the same for M2H and M3H at any time. There is one exception: the particle volume fraction fluctuations $\tilde{\alpha}_p^{rms}$, displayed in Fig. 7.4(b). Particle volume fraction fluctuations are under-estimated by roughly 50% at the center of the jet with the coarser mesh. On the contrary, $\tilde{\alpha}_p^{rms}$ is in better agreement with the Lagrangian reference on the finer mesh. It is surprising that the particle volume fraction field

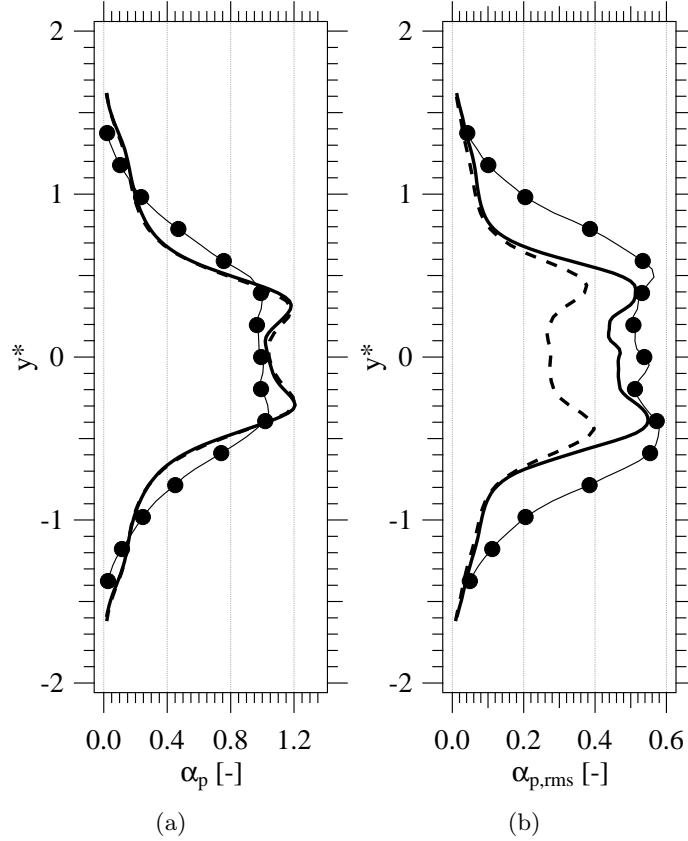


Figure 7.4: Impact of the mesh resolution on the normalized particle volume fraction at $t^* = 40$. (a) Mean $\tilde{\alpha}_p/\tilde{\alpha}_p^0$ and (b) rms $\tilde{\alpha}_p^{rms}/\tilde{\alpha}_p^0$. Eulerian simulations performed on the fine mesh M3H (—) and coarse mesh M2H (----) are compared with the Lagrangian reference (—●—).

differs between M2H-V and M3H-V whereas the particle mesoscopic velocities $\tilde{u}_{p,i}$, which drive $\tilde{\alpha}_p$, are extremely similar between both meshes. To illustrate this point, the time signal of $\tilde{\alpha}_p$ and of the streamwise velocity is plotted in Fig. 7.5. Streamwise mesoscopic velocities are almost super-imposed between M2H-V and M3H-V simulations whereas the particle volume fraction signals differ significantly as a function of the mesh.

One cause of this paradox may be the artificial viscosity terms added in the dispersed-phase equations to stabilize the simulations (Eq. 2.21), *i.e.* the numerical dissipation. Indeed, it was shown in Part. II that the numerical dissipation is related to the mesh resolution. The discrete budget of the equation of $\tilde{\alpha}_p$ applied to the particle-laden vortex, showed that the AV contribution diminishes when the mesh is refined (*cf.* Fig. 4.8). Similar conclusions were

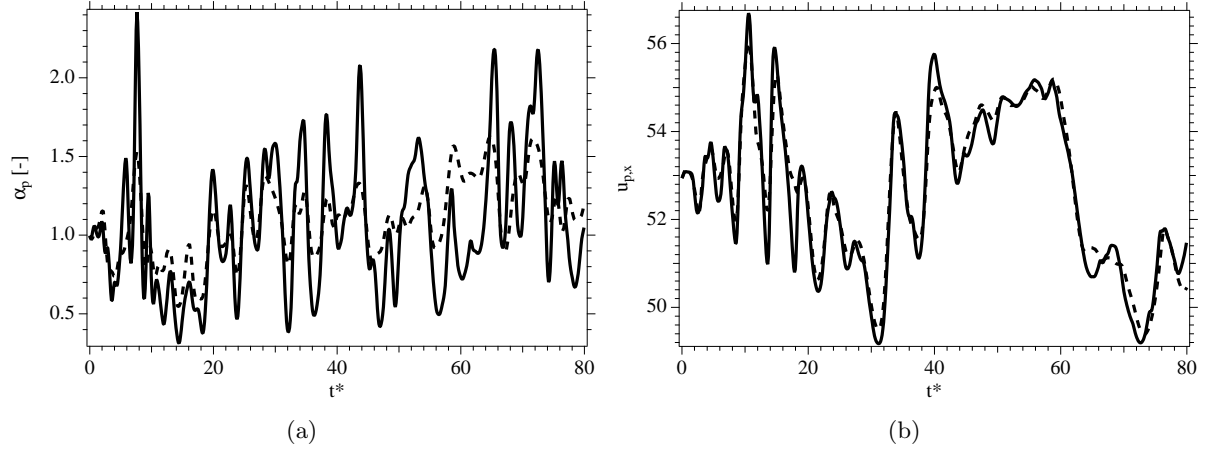


Figure 7.5: Comparison of particle volume fraction (a) and streamwise mesoscopic velocity (b) between the coarse (-----) and the fine (————) mesh as a function of t^* at the center of the computational domain.

drawn with the discrete balance of the mean weighted MKE applied to the particle-laden HIT in Chap. 5. Since this last diagnostic is an efficient mean to quantify the balance between numerical and physical dissipations, it is applied to the present configuration. Note that Eq. 5.35 is averaged in homogeneous planes, parallel to the streamwise direction rather than over the whole computational domain, which would be meaningless in this configuration. The final budget equation of the mean particle MKE is then

$$-\left\langle \frac{\Delta \alpha_p \rho_p \tilde{q}_p^2}{\Delta t} \right\rangle_{ZX} = \underbrace{\varepsilon_{scheme}^{ZX} + \varepsilon_{AV}^{ZX}}_{\text{numerical dissipations}} + \underbrace{\varepsilon_{drag}^{ZX} + \varepsilon_{RUM}^{ZX}}_{\text{physical dissipations}}, \quad (7.19)$$

where $\varepsilon_{scheme}^{ZX}$, ε_{AV}^{ZX} , ε_{drag}^{ZX} and ε_{RUM}^{ZX} refer to the plane-averaged dissipations due to the numerical scheme, artificial viscosity, drag force and RUM, respectively (*cf.* Eq. 5.36). Fig. 7.6 shows the impact of the mesh resolution on the MKE balance. Dissipation due to the artificial viscosity ε_{AV}^{ZX} is compared with the physical dissipations due to drag ε_{drag}^{ZX} and RUM ε_{RUM}^{ZX} . Residuals of the MKE and of the convective scheme $\varepsilon_{scheme}^{ZX}$ are not plotted for the sake of clarity but it was checked that the balance was closed (fine dashed line in Fig. 7.6). First, the peaks of the various dissipations do not have the same location. The position of the AV residual peaks corresponds to the particle volume fraction gradient (*cf.* Fig. 7.4) whereas ε_{drag}^{ZX} and ε_{RUM}^{ZX} are substantial in the region of mean shear. ε_{drag}^{ZX} and ε_{RUM}^{ZX} are rather similar between both meshes. On the contrary, the mesh resolution has a significant impact on the AV contribution. Whereas the amplitude of ε_{AV}^{ZX} is twice more important than the physical dissipations with M2H, it is at worse of the same order with M3H. No simulations have been performed with a mesh finer than 256^3 , but the AV contribution should lower again. Unfortunately, carrying out two-phase flow simulations on more than 256^3 cells was beyond the reach of the present work. Indeed, the inner structure of the code should be modified to adapt the memory management. The conclusion of this section is that numerical dissipations are at least of the same order than the physical dissipations with M3H, which enables a meaningful investigation of the RUM models.

Therefore, the Eulerian simulations presented in the rest of the chapter have been carried out on the finer mesh, M3H.

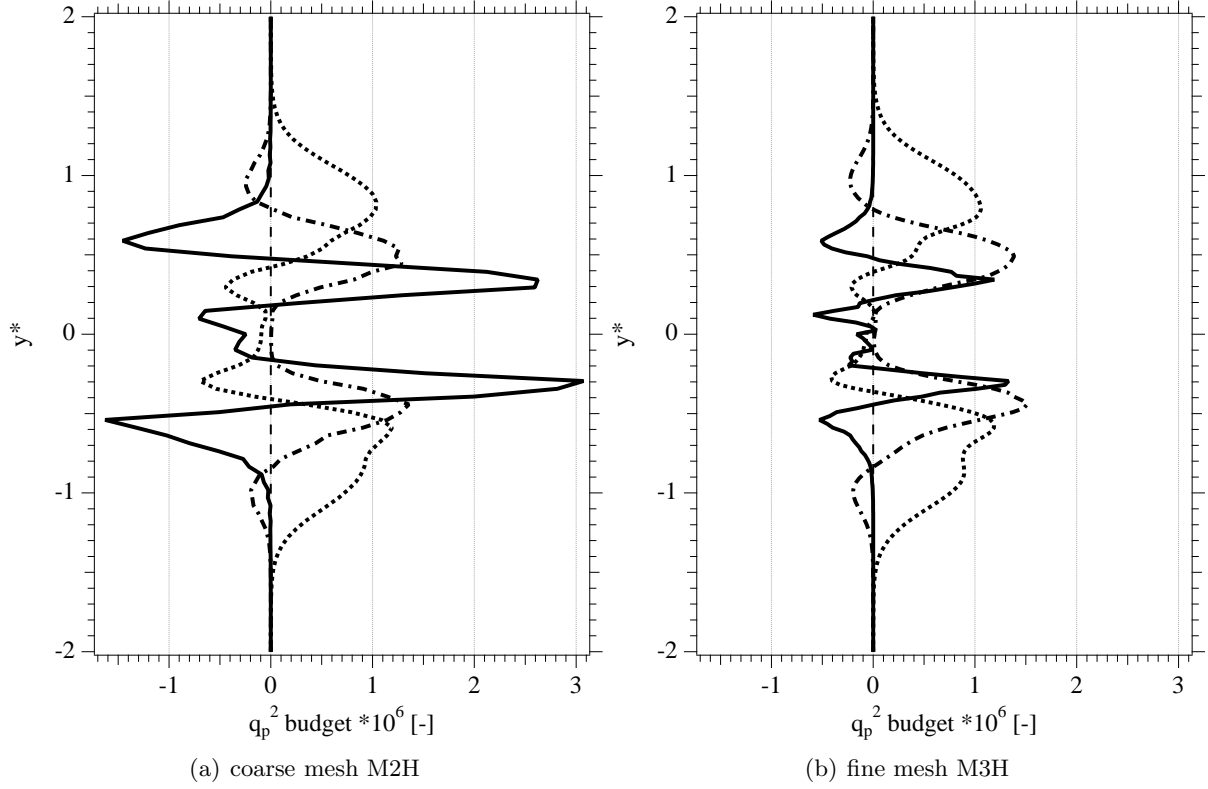


Figure 7.6: Discrete MKE balance of the dispersed phase at $t^* = 40$ of the Eulerian simulations carried out on the coarse mesh M2H (a) and fine mesh M3H (b). Dissipation due to the artificial viscosity ε_{AV}^{ZX} (—) is compared with the physical dissipations due to drag ε_{drag}^{ZX} (.....) and RUM ε_{RUM}^{ZX} (-.-). Residuals of the kinetic energy and of the convective scheme $\varepsilon_{scheme}^{ZX}$ are not plotted for the sake of clarity but the balance is closed ($\left\langle \frac{\Delta \alpha_p \rho_p \tilde{q}_p^2}{\Delta t} \right\rangle_{ZX} - \sum \langle \varepsilon \cdot \rangle_{ZX}$: - - -).

7.3.3 Evaluation of the RUM models

Part. II and Sec. 7.3.2 showed that an adapted numerical strategy, coupled with a fine-enough mesh (M3H in Tab. 7.6) minimizes the numerical dissipations in comparison with those related to the physical models. Then, the effect of the RUM models on the particle dispersion can now be investigated. Two Eulerian simulations performed with the VISCO and AXISY-C RUM models are compared with the Lagrangian database.

For a first validation of the dynamics between both solvers, the mesoscopic and uncorrelated particle kinetic energy are displayed in Fig. 7.7. At the initial condition, $\tilde{q}_{p,t^*=0}^2$ equals roughly two third of $q_{g,t^*=0}^2$ since the particles are added to the carrier phase without fluctuations in the streamwise direction ($\tilde{u}'_p = 0$). Next, the transfer of kinetic energy from the carrier-phase by drag yields an increase in \tilde{q}_p^2 , first at the edges of the jet and then at its center. \tilde{q}_p^2 is about one half of q_g^2 , which is coherent with the range of the dynamic Stokes number ($St = 0.46$) [41]. The two Eulerian simulations yield similar \tilde{q}_p^2 at the center of the jet, and agree rather well with the Lagrangian reference for $t^* \leq 40$. This is consistent with previous results in mean-shear free turbulent flows [63, 83, 103], where the VISCO model produces very good results. However, this model fails where the mean velocity gradient is important. In this configuration, VISCO produces under-estimated \tilde{q}_p^2 at the edges of the jet, whereas the AXISY-C model is in very good agreement with the reference in this region.

The uncorrelated variables can be computed from the Lagrangian database, which allows a comparison of the uncorrelated particle kinetic energy δq_p^2 , shown in Fig. 7.7(b). The RUE, almost null at $t^* = 0$ ($\delta q_{p,t^*=0}^2 = 0.1$), quickly increases at the beginning of the simulation as the particle velocities become uncorrelated under the effect of the velocity fluctuations and mean gradient. At $t^* = 20$, δq_p^2 has the same amplitude than \tilde{q}_p^2 at the edges of the jet. Then, it decreases progressively and the ratio $\delta q_p^2 / \tilde{q}_p^2$ converges to one third for $t^* \geq 60$. Overall, the RUM particle kinetic energy is over estimated by the VISCO model at the edges of the jet by approximately 50% for the whole simulation. On the contrary, δq_p^2 is first underestimated by AXISY-C but the gap between the Eulerian simulation and the Lagrangian reference progressively narrows. For $t^* \geq 60$, the agreement is excellent between M3H-AXI and the EL database.

The under-estimation of \tilde{q}_p^2 , together with the over-estimation of δq_p^2 by the VISCO model is relevant of a miscomputation of the reverse energy exchange between the uncorrelated and the mesoscopic contributions. Indeed, an *a priori* study showed that the VISCO model reproduces the transfer of energy in one-way only from the mesoscopic to the RUM component, whereas it occurs in both ways in reality [78]. On the contrary, the correction of the AXISY model (*cf.* Sec. 1.3.3) takes into account the reverse energy exchange. Consequently, both particle mesoscopic and uncorrelated kinetic energy are satisfactorily captured with the AXISY-C model.

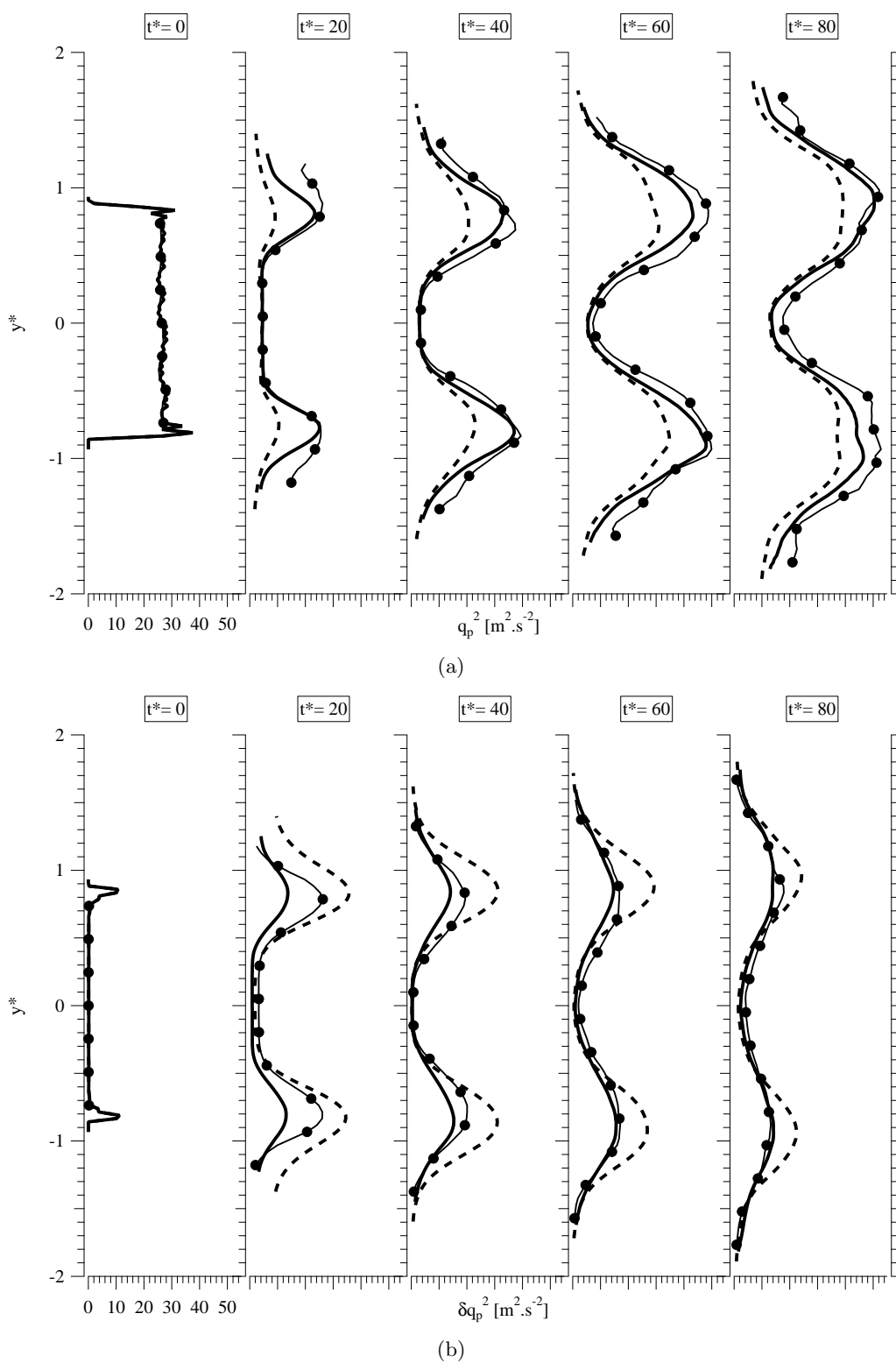


Figure 7.7: Influence of the RUM models on the Eulerian statistics at $t^* = 40$. (top) Mesoscopic turbulent kinetic energy \tilde{q}_p^2 and (bottom) RUE δq_p^2 . Eulerian simulations performed with AXISY-C (—) and VISCO (----) are compared with the Lagrangian reference (—●—).

The effect of the RUM model can also be evaluated directly through the particle dispersion. A qualitative comparison of the particle volume fraction field at $t^* = 40$ is shown in Fig. 7.8. The two Eulerian simulations M3H-V and M3H-AXI compare satisfactorily with the EL data

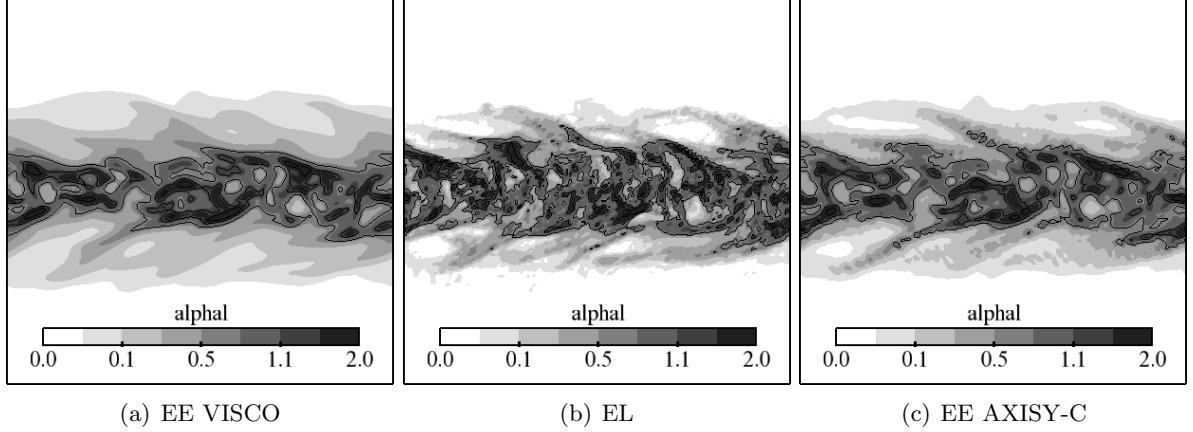


Figure 7.8: Influence of the RUM model on the mean particle volume fraction $t^* = 40$. Cut at $Z = 0$. Comparison between the Lagrangian reference (center) and the Eulerian simulations carried out with VISCO (left) and AXISY-C (right) RUM models.

at the center of the jet, with a slight preference for the AXISY-C model. The position of the particle clusters and vacuum zones are well captured by the Eulerian simulations. This result was expected at the center of the jet. Indeed, this region is similar to a particle-laden HIT, in which the VISCO model has been previously validated [63, 83, 103]. However, the particle volume fraction gradients at the edges of the jet are too smooth in M3H-V, due to the overestimation of the RUE by the VISCO model (Fig. 7.7(b)) in this region. On the contrary, the agreement between M3H-AXI and the EL database is qualitatively very good.

For a quantitative comparison, mean and rms of the normalized particle volume fraction are displayed in Fig. 7.9. Both Eulerian simulations yield mean $\tilde{\alpha}_p$ in good agreement with the Lagrangian reference. Some discrepancies are visible at the edges of the jet. The mean particle volume fraction is slightly underestimated in the mean-shear region and overestimated at the inner border of the jet with both RUM models. However, case M3H-AXI is in better agreement with the exact solution than case M3H-V. Furthermore, the particle fluctuations are reasonably captured at the center of the jet by both RUM models, with 10% fewer $\tilde{\alpha}_p^{rms}$ with both Eulerian simulations. None of the two RUM models considered in this work predicts the exact amount of particle fluctuations in the mean shear region. By way of example, the VISCO model underestimates by 70% the particle fluctuations at $y^* = 0.75$, whereas AXISY-C reduces half the gap towards the EL counterpart. Therefore, AXISY-C yields slightly better results than the VISCO RUM model, even if the prediction of particle fluctuations may be improved. Now, the influence of the RUM models on the thermal dispersion of the particles is evaluated.

The mean and rms of the particle mesoscopic temperature at $t^* = 40$ are shown in Fig. 7.10. The RUM heat fluxes are turned off, so that the sole influence of the particle dynamic dispersion is evaluated. In this configuration, \tilde{T}_p seems midly sensitive to the RUM models, contrary to the temperature fluctuations. Indeed, \tilde{T}_p^{rms} is satisfactorily predicted by the two Eulerian simula-

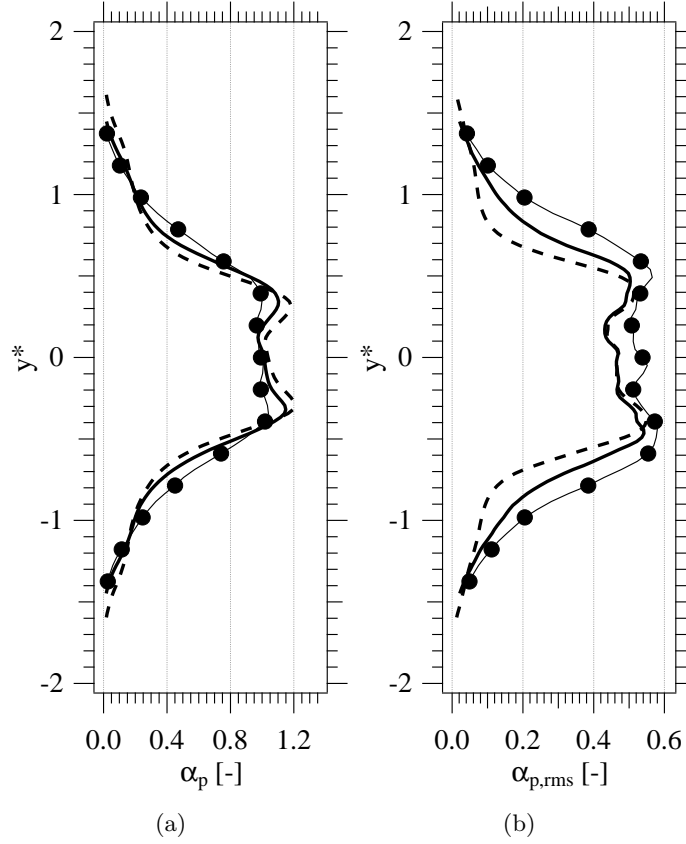


Figure 7.9: Influence of the RUM model on the normalized particle volume fraction at $t^* = 40$. (left) Mean $\tilde{\alpha}_p / \tilde{\alpha}_p^0$ and (right) rms $\tilde{\alpha}_p^{rms} / \tilde{\alpha}_p^0$. Eulerian simulations performed with AXISY-C (—) and VISCO (----) are compared with the Lagrangian reference (—●—).

tions inside the jet but large discrepancies are visible at its edges. In this region, the maximum \tilde{T}_p^{rms} is over estimated by roughly 50% and 25% in case M3H-V and M3H-AXI, respectively. Thus, a better prediction of the particle dynamic dispersion substantially improves the statistics of \tilde{T}_p^{rms} , which explains the better results with AXISY-C than with the VISCO RUM model.

Mean mesoscopic heat fluxes, defined as

$$\tilde{\mathbb{F}}_{p,i}(\mathbf{x}, t) = \frac{\langle \tilde{n}_p(\mathbf{x}, t) \tilde{u}'_{p,i}(\mathbf{x}, t) \tilde{T}'_p(\mathbf{x}, t) \rangle}{\langle \tilde{n}_p(\mathbf{x}, t) \rangle} \quad (7.20)$$

are plotted in Fig. 7.11 for the two RUM models. Spanwise $\tilde{\mathbb{F}}_{p,y}$ and cross-stream $\tilde{\mathbb{F}}_{p,z}$ mean mesoscopic heat fluxes of cases M3H-V and M3H-AXI compare reasonably well with the reference. However, $\tilde{\mathbb{F}}_{p,x}$ is in better agreement with the Lagrangian reference with the VISCO RUM model than with AXISY-C. This could be explained by the fact that RUM HF are not taken into account in M3H-V and M3H-AXI. Indeed, the last two terms in the RHS of the mean

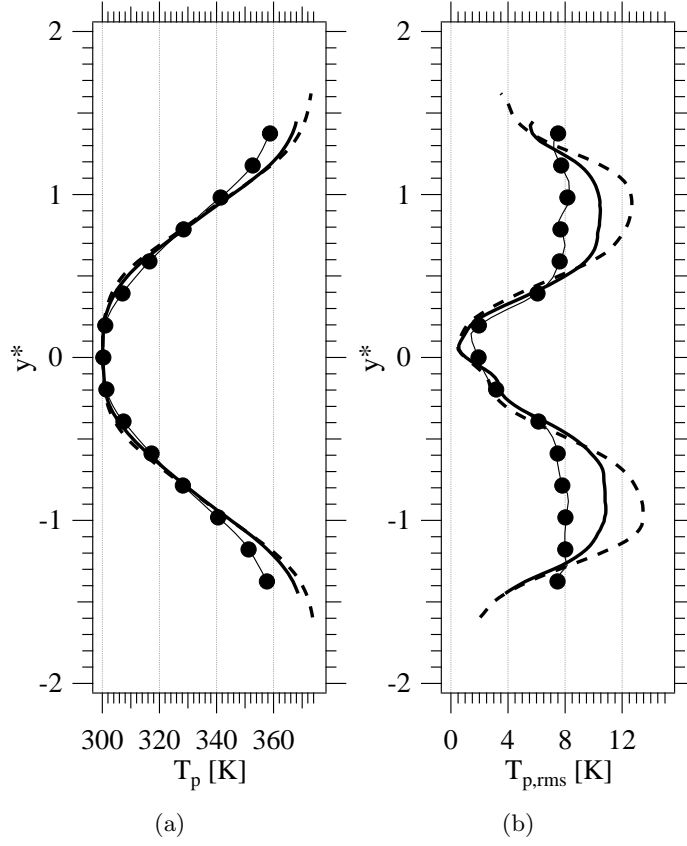


Figure 7.10: Influence of the RUM model on the mesoscopic particle temperature at $t^* = 40$. (left) Mean \tilde{T}_p and (right) rms \tilde{T}_p^{rms} . Eulerian simulations performed with AXISY-C (—) and VISCO (----) RUM models are compared with the Lagrangian reference (—●—).

mesoscopic HF transport equation (Eq. B.4):

$$\underbrace{n_p C_{p,p} \langle \delta R_{p,ij} \frac{\partial \tilde{T}_p'}{\partial x_j} \rangle_p}_{D1} + \underbrace{n_p C_{p,p} \langle \delta \Theta_{p,j} \frac{\partial \tilde{u}'_{p,i}}{\partial x_j} \rangle_p}_{D2} \quad (7.21)$$

are dissipative terms. Since the RUM HF are not taken into account, the mean mesoscopic HF “lacks” of a dissipative term ($D2 = 0$). Moreover, Fig. 7.7 showed that the VISCO RUM model over estimates $\delta R_{p,ij}$ whereas it is slightly under predicted by AXISY-C. Therefore, the VISCO RUM model may incidentally balance the lack of D2 by a larger D1.

Now, the impact of the RUM HF term in Eq. 1.39 on the thermal statistics of the particles is investigated.

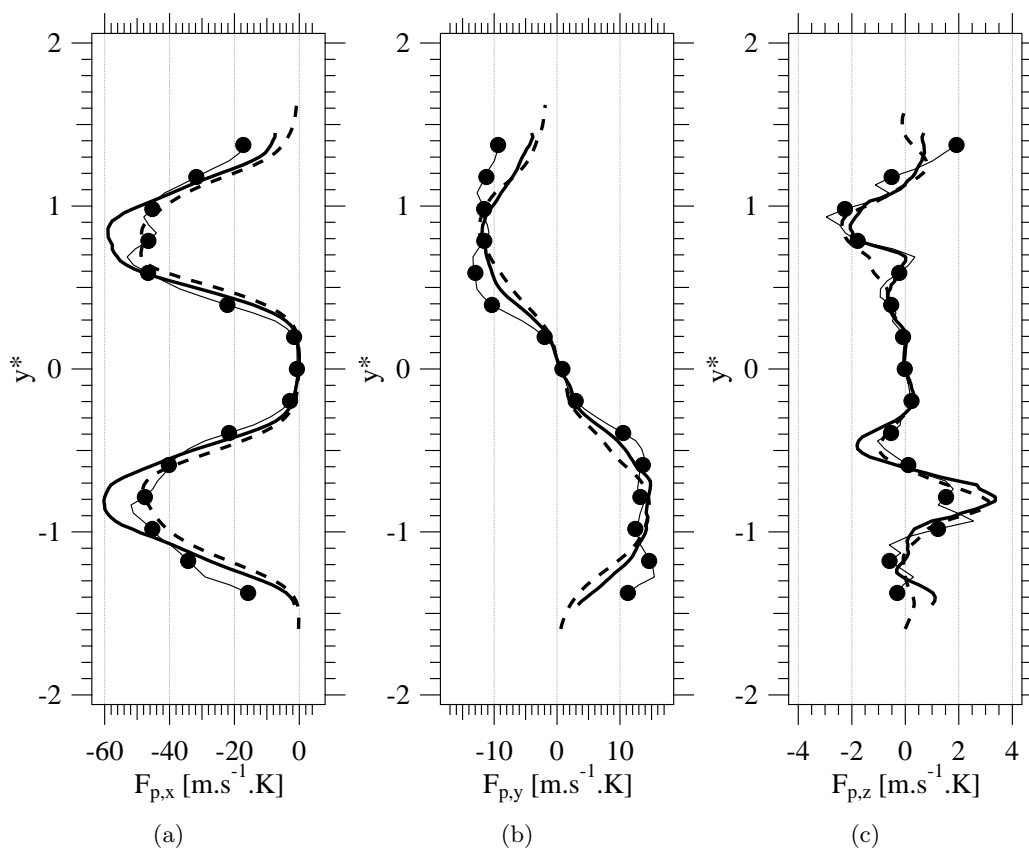


Figure 7.11: Influence of the RUM model on the mesoscopic heat fluxes of the dispersed phase at $t^* = 40$ (no RUM HF). (left) streamwise $\widetilde{F}_{p,x}$, (center) spanwise $\widetilde{F}_{p,y}$ and (right) cross-stream $\widetilde{F}_{p,z}$ heat fluxes. Eulerian simulations performed with AXISY-C (—) and VISCO (----) RUM models are compared with the Lagrangian reference (—●—).

7.3.4 Influence of the RUM heat fluxes

The objective of this section is to assess the impact of the RUM HF on the thermal statistics of the dispersed phase. First of all, the AXISY-C RUM model is used for the dynamics, since it was identified in Sec. 7.3.3 as the best of the two RUM models available in this work. The RUM HF is in the second RHS term of the transport equation of the particle mesoscopic temperature (Eq. 1.53). This term will be referred in this section as the “RUM HF term”. In order to evaluate the impact of the RUM HF, two Eulerian simulations are carried out for a given dynamics of the particles, denoted M3H-AXI and M3H-AXI-HF (*cf.* Tab. 7.5). That means that the particle dynamic dispersion is the same for the two EE simulations and only the thermal dispersion differs. In case M3H-AXI, the RUM HF term is not taken into account, so that there is no direct coupling between the mesoscopic and RUM temperature of the particles. Nevertheless, the transport equations of $\delta\Theta_p$ are solved to allow a sort of “one-way” evaluation of the RUM HF. On the contrary, the RUM HF term is switched on in case M3H-AXI-HF and the transport equations of the RUM HF are solved (Eq. 1.54).

First, a qualitative comparison of the particle mesoscopic temperature fields at $t^* = 40$ is presented in Fig. 7.12. Inside the jet, the two Eulerian simulations lead to similar temperature

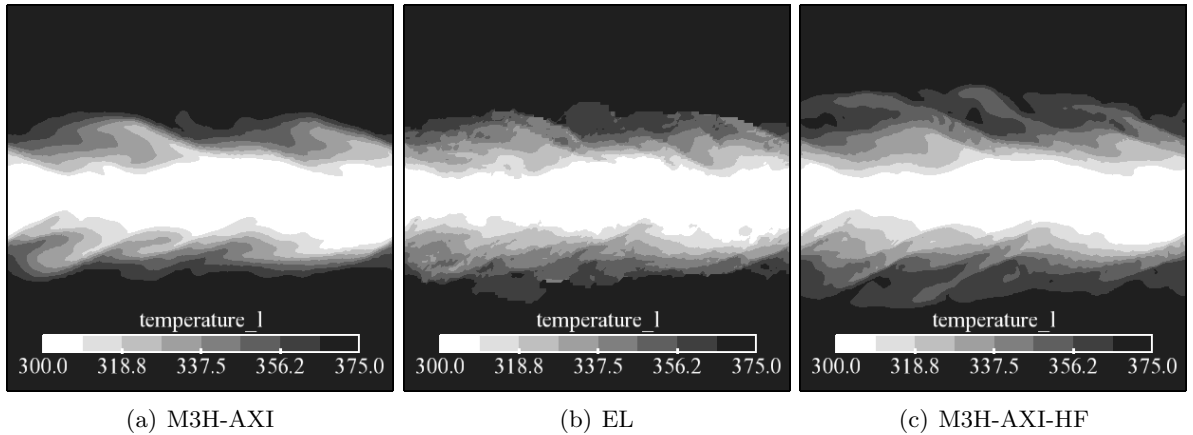


Figure 7.12: Impact of the RUM HF term on the particle mesoscopic temperature. Cut at $Z=0$ at $t^* = 40$. Eulerian simulations without (left) and with (right) RUM HF are compared with the Lagrangian reference (center).

fields and agree reasonably well with the Lagrangian reference. However, some discrepancies are visible at the edges of the jet when the RUM HF term is switched on. In this region, the particle temperature field of case M3H-AXI-HF has more fluctuations than that of case M3H-AXI, and agree qualitatively better with the Lagrangian solution.

For a quantitative comparison, the mean particle temperature and fluctuations are displayed at five normalized times in Fig. 7.13. The corresponding quantity of the carrier phase is presented to underscore the deviation between both phases. The mean and rms of particle temperature are lower than those of the carrier phase. This relatively large deviation is consistent with the study of the thermal inertia influence performed on the two-dimensional non-isothermal particle-laden jet in Sec. 6.4.3. At this thermal Stokes number ($St_\theta = 0.93$), particles keep

the memory of their initial temperature profile but do not follow exactly that of the carrier. Comparing cases M3H-AXI and M3H-AXI-HF, both Eulerian simulations recover the correct \tilde{T}_p at the center of the jet. However, the RUM HF have a clear impact on \tilde{T}_p at the edges of the slab in this configuration². Without RUM HF, the particle mesoscopic temperature of case M3H-AXI departs from the Lagrangian counterpart, with a maximum deviation of 10 K. On the contrary, mean \tilde{T}_p is satisfactorily predicted when the RUM HF are taken into account (case M3H-AXI-HF). Moreover, particle temperature fluctuations are plotted in Fig. 7.13(b). Again, the RUM HF have a favorable impact at the edges of the jet. When they are neglected, \tilde{T}_p^{rms} is over-estimated by roughly 25% in this region whereas it is adequately recovered when the RUM HF are taken into account.

Moreover, the RUM HF participate to one fundamental phenomenon in the thermal dispersion of particles, *i.e.* the reverse exchange of mesoscopic temperature variance between the RUM and the mesoscopic part³. Theoretically [78], the term responsible for the heat transfer between the two contributions appears with a reverse sign in the RHS of the transport equations of the mean mesoscopic and RUM temperature variance (Eq. B.2 and Eq. B.3, respectively):

$$\pm n_p C_{p,p} < \delta \Theta_{p,j} \frac{\partial \tilde{T}'_p}{\partial x_j} >_p. \quad (7.22)$$

The good prediction of $\delta \Theta_{p,i}$ is thus of paramount importance to have the correct fluctuations of particle temperature. The mean mesoscopic HF are also important since they drive the production term of the mean mesoscopic temperature variance (third term in the RHS of Eq. B.2). The completeness of the Lagrangian database allows a comparison of the mesoscopic and RUM HF with the Eulerian simulations. Then, the streamwise and spanwise mesoscopic and RUM heat fluxes are displayed in Fig. 7.14 and Fig. 7.15, respectively. Cross-stream heat fluxes are shown in Appendix in Fig. C.4. A common feature of the streamwise and spanwise HF is that the amplitude of the mesoscopic HF increases along time while that of the RUM HF progressively diminishes. This is consistent with the statistics of the mesoscopic and RUM kinetic energy (Fig. 7.7) and \tilde{T}_p^{rms} (Fig. 7.13(b)). By way of example, particles are highly spatially uncorrelated at the edges of the jet (*cf.* Fig. 7.7(b)) at $t^* = 20$. In this region, two neighboring particles could come from different sides of the jet and thus, have a very different temperature history, implying high RUM heat fluxes. Along the simulation, the decrease of δq_p^2 (*cf.* Sec. 7.3.3) at the edges of the jet directly leads to a decrease of the RUM HF.

First, the two Eulerian simulations recover satisfactorily the streamwise and spanwise mesoscopic HF when compared to the reference (Fig. 7.14(a) and Fig. 7.15(a), respectively). The spanwise mesoscopic HF seems mildly sensitive to the RUM HF term whereas the streamwise mesoscopic HF is slightly better predicted when the RUM HF are not taken into account (case M3H-AXI). As mentioned in Sec. 7.3.3, this could be incidental since mean mesoscopic HF lacks of a dissipative term when the RUM HF are neglected (Eq. 7.21). However, the RUM HF are satisfactorily predicted in the case M3H-AXI-HF, when the RUM HF term is switched on. The amplitude of $\delta F_{p,x}$ is in good agreement between M3H-AXI-HF and the exact solution. Only a slight deviation of the peak location of $\delta F_{p,x}$ is visible outside the jet, which may be due to the neglected diffusion term by the third-order moments in Eq. 1.54. Spanwise RUM heat fluxes are

²It was not the case in the two-dimensional configuration of Chap. 6.

³This phenomenon is the analog of the reverse exchange of MKE between the RUM and the mesoscopic part, discussed in Sec. 7.3.3.

slightly over estimated but still agree satisfactorily with the Lagrangian data. Nevertheless, the reverse exchange of mesoscopic temperature variance seems to be captured, since both mesoscopic and RUM HF are in good agreement with the reference. That means that the chosen approach to model the RUM HF in this work, *i.e.* transport $\delta\Theta_{p,i}$ and neglect the third order moment $\delta\Delta_{p,ij}$, is adapted for non-isothermal EE simulations.

7.4 Conclusions

The simulation of a three-dimensional turbulent jet laden with cold solid particles surrounded by a hot carrier gas has been carried out. The MEF extended to non-isothermal flows has been *a posteriori* validated against a complete Lagrangian database computed by Masi [78] with the NTMIX solver. This database contains both mesoscopic and RUM variables, allowing a thorough validation of the MEF.

First, it was verified that the carrier phase in both solvers were identical. A mesh of 128^3 cells was found to be sufficiently fine to yield converged carrier-phase statistics. However, a mesh sensitivity study of the dispersed phase showed that a finer mesh was necessary to capture the correct level of particle volume-fraction fluctuations. Having in mind the conclusions of Chap. 5, the numerical and physical dissipations were explicitly extracted. It was shown that the numerical dissipations due the artificial viscosity are not acceptable on the coarse mesh. Therefore, a finer mesh (256^3 cells) was used to conduct a meaningful study of the impact of the RUM model and of the RUM heat flux term.

Then, the impact of the RUM model on the dispersed phase statistics was investigated. The two RUM models available in this work, VISCO and AXISY-C, have been compared. It was shown that the VISCO model yields correct results at the center of the jet but fails in the region of mean-shear at its edges, consistently with previous studies [63, 83, 103]. Indeed, VISCO model under-estimates the particle MKE at the edges of the jet whereas it over predicts the RUM kinetic energy. On the contrary, the AXISY-C model⁴ recovers the correct level of these two quantities. The discrepancy between the two RUM models was partly explained by their ability to recover the reverse energy exchange from the RUM to the mesoscopic part. Whereas the correction of the AXISY model (acronym “-C”) allows this reverse energy exchange, the VISCO model cannot reproduce it.

Finally, the impact of the RUM HF term (appearing in the transport equation of the particle mesoscopic temperature) on the thermal particle dispersion was analyzed, which finalizes the *a posteriori* validation of the MEF extended to non-isothermal flows. It was shown that the RUM HF have a large favorable impact on both the mean and rms of particle mesoscopic temperature. Without the RUM heat flux term, the mean mesoscopic temperature and rms are over estimated at the edges of the jet whereas the agreement is excellent when it is accounted for. Moreover, it was shown that both mesoscopic and RUM HF are satisfactorily predicted when the RUM HF term is taken into account, which validates the modeling of the RUM HF used in this work. Thus, the fundamental phenomenon of reverse exchange of heat transfer between the mesoscopic and RUM components is well captured, which may have a large impact on the evaporation of particles.

⁴implemented in AVBP by Sierra [120]

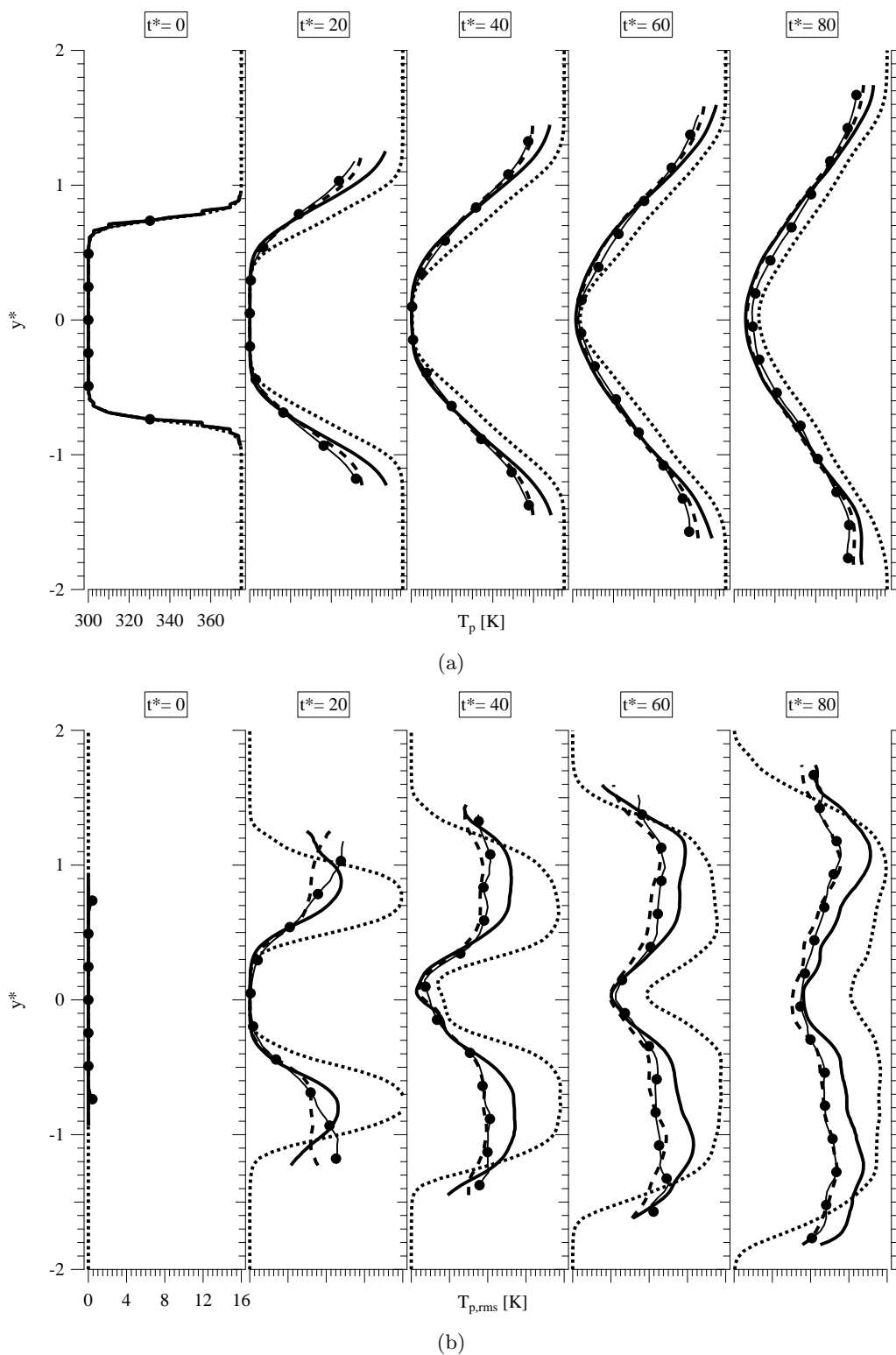


Figure 7.13: Influence of the RUM HF term on the particle mesoscopic temperature with the AXISY-C model. (Top) mean \tilde{T}_p and (Bottom) \tilde{T}_p^{rms} . Eulerian simulations without (—) and with (---) the RUM HF term are compared with the Lagrangian reference (—●—). The corresponding quantity of the carrier phase is plotted for reference (.....)

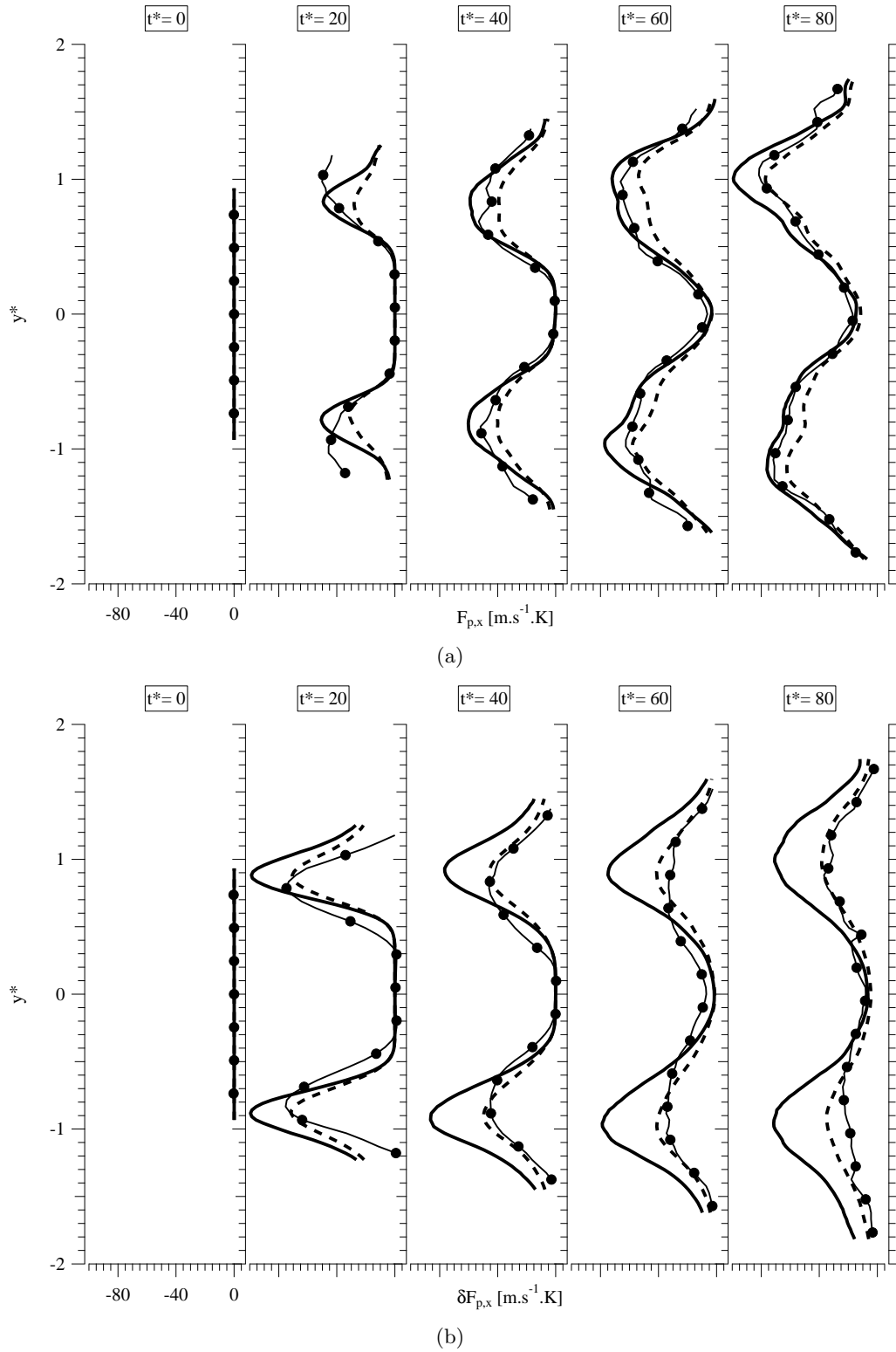


Figure 7.14: Influence of the RUM heat flux term on the particle streamwise heat flux statistics with the AXISY-C model. (Top) mesoscopic HF $\widehat{F}_{p,x}$ and (Bottom) RUM HF $\delta F_{p,x}$. Eulerian simulations without (—) and with (---) the RUM HF term are compared with the Lagrangian reference (—•—).

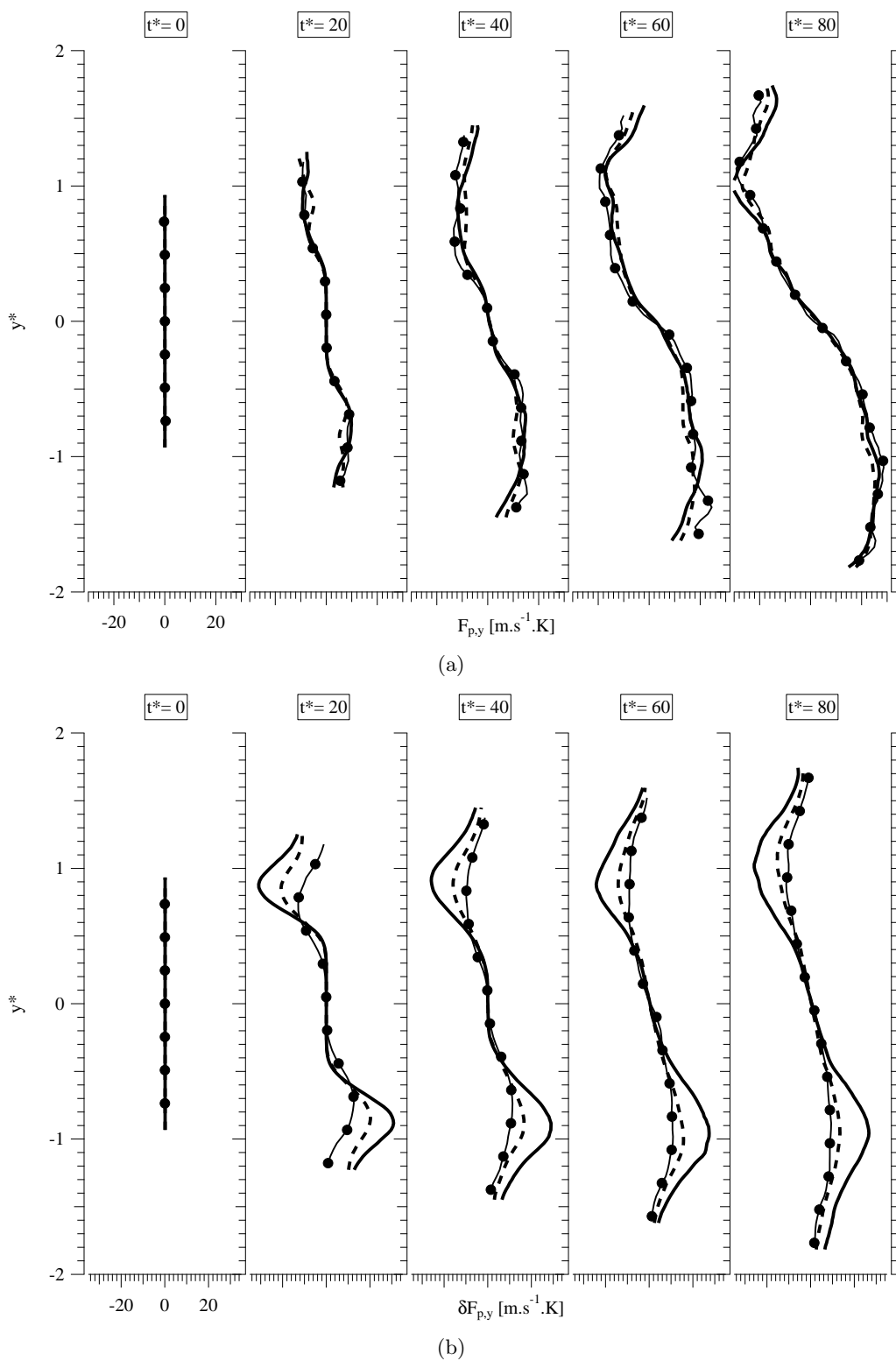


Figure 7.15: Influence of the RUM heat flux term on the particle spanwise heat flux statistics with the AXISY-C model. (Top) mesoscopic HF $\widehat{F}_{p,y}$ and (Bottom) RUM HF $\delta F_{p,y}$. Eulerian simulations without (—) and with (---) the RUM HF term are compared with the Lagrangian reference (—●—).

Conclusion

The context of the present work is DNS of non-isothermal dilute sprays in configurations relevant of fuel injection in a piston engine. The focus was set on the accurate prediction of the droplet dispersion and heat transfer between droplets and surrounding gas. Among other Eulerian approaches using a statistical description of the dispersed phase, the Mesoscopic Eulerian Formalism [41, 78] was chosen for its ability to capture the local and instantaneous behavior of inertial particles embedded in non-isothermal turbulent flows. The main objective of this work was to assess the ability of this formalism to accurately account for both dynamic and thermal inertia of particles in turbulent flows with a mean shear. The CFD code used in this work is AVBP⁵. Three main issues were addressed:

- **Numerics.** First, the numerical methods implemented in AVBP for two-phase flows [69, 103, 108] were tested and revisited to propose a robust and accurate numerical strategy, which withstands the steep gradients of particle volume fraction produced by preferential concentration [132] with limited numerical diffusion. The two numerical strategies available in AVBP: (1) the robust upwind scheme called PSI and (2) the high-order scheme TTGC used jointly with an AV term, were compared on academic test cases of increasing complexity. The configuration of a two-dimensional vortex laden with solid particles was suggested to simply illustrate the impact of the dynamic inertia of the particles on their concentration profile and compare the two numerical strategies. In particular, an analytical solution was derived in the limit of small St. Finally, it was shown that option (2) was the best with an appropriate set-up (*i.e.* AV sensor).

In order to compare thoroughly the two numerical strategies, the discrete budget of the kinetic energy of the dispersed phase was written and the dissipations due to numerics and physical effects were explicitly extracted. This diagnostic also highlighted an important issue in Eulerian approaches: the simulation of a two-phase flow may require more mesh resolution than necessary for the carrier phase alone. For a meaningful study of physical models, it is mandatory to ensure that the sources of numerical dissipations are below those corresponding to the physics.

- **Modeling of the particle dispersion in configurations with a mean-shear.** The issue of the closure model of the RUM stress tensor in the MEF, referred to as RUM model, has been tackled. A new RUM model proposed by Masi [78] and implemented by Sierra [120] in AVBP –denoted AXISY-C– has been validated in configurations with a mean shear. Contrary to the previous RUM models [83, 103], AXISY-C captured accurately the motion and concentration of particles both at the center and at the edges of a jet. Indeed,

⁵<http://pantar.cerfacs.fr/4-26334-The-AVBP-code.php>

both mean mesoscopic and uncorrelated kinetic energy were remarkably predicted. This was partly explained by the ability of AXISY-C to recover the reverse energy exchange from the RUM to the mesoscopic part. It is a major achievement for the MEF and a mandatory step before considering heat transfer between phases in configurations with a mean shear.

- The **modeling of the heat transfer** between phases with the MEF has been investigated in two configurations with a mean shear: a two-dimensional and a three-dimensional non-isothermal jet laden with solid particles, denoted in this conclusion J-2D and J-3D, respectively. For these two cases, AVBP was compared to a Lagrangian simulation performed by B. Leveugle at CORIA for J-2D and by E. Masi at IMFT for J-3D.

First, the impact of the thermal inertia of particles on their temperature has been investigated in J-2D. Lagrangian simulations⁶ showed that both mean and rms of the mesoscopic temperature were strongly dependent of the thermal Stokes number. At low thermal inertia, these two quantities follow that of the fluid. At high thermal inertia, the particles keep the memory of their injection temperature so that their statistics differ from those of the surrounding carrier phase. It is thus of paramount importance that the numerical approach describes correctly the thermal inertia of particles.

To do so, the extension of the MEF to non-isothermal conditions [78], *i.e.* the RUM heat fluxes, has been implemented in AVBP. Then, the influence of the RUM HF on the temperature statistics has been studied in the configurations J-2D and J-3D, with the following conclusions:

- At low to moderate thermal inertia, the RUM HF terms have a strong positive impact on the fluctuations of mesoscopic temperature in both configurations J-2D and J-3D. Neglecting the RUM HF leads to erroneous results while the Lagrangian statistics are recovered when they are accounted for.
- However, the accuracy of the MEF may be reduced for particles with large thermal inertia. In J-2D, the predictions of the temperature fluctuations are not satisfactory at large thermal Stokes number, even when the RUM HF are accounted for.
- The necessity of accounting for the RUM-HF in order to predict the mean temperature field turned out to be configuration dependent. In J-2D, the RUM HF have a marginal influence of this statistic. However, for J-3D the RUM-HF must be accounted for in order to recover the correct level for the mean mesoscopic temperature.
- The MEF has been thoroughly validated in J-3D where both mesoscopic and RUM Lagrangian statistics⁷ were available. It was shown that both mesoscopic and RUM HF are satisfactorily predicted when the RUM HF term is accounted for. This important achievement validates the modeling of the RUM HF used in this work.

The collaboration with CORIA on the modeling of the heat transfer in the J-2D configuration led to an article submitted to the International Journal of Heat and Mass Transfer [30]. This work has been supported by the ANR (National Research Agency) under the grant number ANR-07-PDIT-002-01.

⁶Carried out by B. Leveugle at CORIA using the Asphodele code

⁷The Lagrangian database has been performed by E. Masi [78] at IMFT using the NTMIX code

Concerning the continuation of this work, several issues remain critical:

- **Impact of the RUM HF on the evaporation process.** The *a priori* study of an evaporating non-isothermal jet [80] showed that the MEF with the RUM HF is able to describe the local behavior of the evaporating dispersed phase. Moreover, the complete Lagrangian database of J-3D also contains evaporation terms (mass transfer, fuel vapor, etc..). Then, a straightforward extension of the present work would be to *a posteriori* investigate the impact of the RUM HF on the evaporation process.
- **Modeling of the RUM stress tensor.** The RUM AXISY-C used in this work was one of the simplest models proposed by Masi [78]. Even if this RUM model captures satisfactorily the main statistics of the dispersed phase, the fluctuations of the particle volume fraction are still under-estimated in the regions of strong mean shear. Moreover, cases with particles with very large dynamic inertia have not been carried out in this thesis and AXISY-C may fail in such configurations. An ongoing thesis is carried out at CERFACS [120] that tests higher-order non-linear RUM models.
- **Modeling of the RUM heat fluxes.** In this work, a simple modeling of the RUM HF has been chosen: the transport equations have been explicitly solved and the third-order moments neglected. Other models proposed in [78] could be implemented in AVBP.
- **Large Eddy Simulation (LES).** The extension of the MEF to non-isothermal flows has been studied in this work in the framework of DNS. The next step towards simulations of industrial configurations in complex geometries is the extension of this formalism to Large Eddy Simulations (LES). Indeed, this issue has already been addressed with the derivation of the MEF in the LES framework [63], closure models [84, 103] and application to complex geometries [59, 105, 112, 145] but the RUM HF were not taken into account. Masi [78] presented an *a priori* investigation of the MEF extended to non-isothermal flows in the LES framework and proposed specific closure models that should be tested.
- **Robust numerical schemes.** For the resolution of the dispersed phase, the current choice of combining centered schemes and artificial viscosity relies on user experience in order to maintain the delicate balance between accuracy and positivity of the solution. However, the implementation of kinetic schemes [13] in AVBP is not obvious due to the cell-vertex formalism. Recent advances in the construction of high-order residual schemes on hybrid unstructured meshes that can withstand very strong shocks [2, 3] may represent an alternative path.

Appendix A

Carrier phase

The numerical code used in this work is AVBP¹. It has been jointly developed by CERFACS and Institut Français du Pétrole to carry out numerical simulations of reactive gaseous flows, with an emphasis on combustion instabilities. It is thus of importance that pressure waves were taken into account. Then, AVBP solves the compressible Navier-Stokes equations, as found in fundamental CFD text books as [6, 53]. This section briefly describes these equations and is a close transposition of the AVBP handbook [15].

From now on, the index notation is adopted for the description of the governing equations. The summation rule is subsequently implied over repeated indices. The set of conservation equation describing the evolution of a compressible flow without chemical reactions reads,

$$\frac{\partial \rho_f}{\partial t} + \frac{\partial}{\partial x_j} \rho_f u_{f,j} = 0 \quad (\text{A.1})$$

$$\frac{\partial}{\partial t} \rho_f u_{f,i} + \frac{\partial}{\partial x_j} \rho_f u_{f,i} u_{f,j} = -\frac{\partial}{\partial x_j} [P_f \delta_{ij} - \tau_{f,ij}] \quad (\text{A.2})$$

$$\frac{\partial}{\partial t} \rho_f E_f + \frac{\partial}{\partial x_j} \rho_f E_f u_{f,j} = -\frac{\partial}{\partial x_j} [u_{f,i} (P_f \delta_{ij} - \tau_{f,ij}) + q_{f,j}]. \quad (\text{A.3})$$

Eq. A.1-A.3 correspond to the conservation laws for the fluid density, momentum and total energy, where ρ_f , $u_{f,i}$ and E_f denote the fluid density, velocity vector and total energy, respectively. The symbols P_f , $\tau_{f,ij}$ and $q_{f,j}$ denote the hydrostatic pressure of the fluid, stress tensor and heat flux, respectively.

The conservative variable vector is introduced: $\mathbf{U} = (\rho_f, \rho_f u_{f,i}, \rho_f E_f)^T$ so that Eq. A.1-A.3 can be written in compact form:

$$\frac{\partial \mathbf{U}}{\partial t} + \vec{\nabla} \cdot \vec{\mathcal{F}} = 0, \quad (\text{A.4})$$

where the flux vector $\vec{\mathcal{F}}$ can be decomposed into a convective (inviscid) $\vec{\mathcal{F}}^C$ and a viscous component $\vec{\mathcal{F}}^V$. They are respectively noted for the three conservation equations:

¹<http://pantar.cerfacs.fr/4-26334-The-AVBP-code.php>

$$\vec{\mathcal{F}}_f^C = \begin{pmatrix} \rho_f u_{f,j} \\ \rho_f u_{f,i} u_{f,j} + P_f \delta_{ij} \\ u_{f,i} (\rho_f E_f + P_f \delta_{ij}) \end{pmatrix} \quad (\text{A.5})$$

$$\vec{\mathcal{F}}_f^V = \begin{pmatrix} 0 \\ -\tau_{f,ij} \\ -u_{f,i} \tau_{f,ij} + q_{f,j} \end{pmatrix} \quad (\text{A.6})$$

The hydrostatic pressure P_f is determined by the equation of state for a perfect gas: $P_f = \rho_f \frac{\mathcal{R}}{W_f} T_f$, where $\mathcal{R} = 8.3143 \cdot J \cdot mol^{-1} \cdot K^{-1}$ is the universal gas constant and W_f is the molecular weight of the fluid.

The fluid stress tensor $\tau_{f,ij}$ follows the relation:

$$\tau_{f,ij} = 2\mu_f \left(S_{f,ij} - \frac{1}{3} \delta_{ij} S_{f,kk} \right), \quad (\text{A.7})$$

where μ_f is the fluid dynamic viscosity and

$$S_{f,ij} = \frac{1}{2} \left(\frac{\partial u_{f,j}}{\partial x_i} + \frac{\partial u_{f,i}}{\partial x_j} \right) \quad (\text{A.8})$$

is the strain tensor.

In AVBP, μ_f can be computed thanks to the Sutherland and Power law. These laws assume μ_f to be independent of the gas composition and close to that of the air. They account for the variation of μ_f as a function of the gas temperature. In the present work, only the Power law is employed²:

$$\mu_f = \mu_{ref} \left(\frac{T}{T_{ref}} \right)^b. \quad (\text{A.9})$$

For the air at $T_{ref} = 273K$, $\mu_{ref} = 1.71 \cdot 10^{-5} kg \cdot m^{-1} \cdot s$ and $b = 0.76$.

The heat flux vector $q_{f,j}$ is given by the classical Fourier law:

$$q_{f,j} = -\lambda_f \frac{\partial T_f}{\partial x_j}, \quad (\text{A.10})$$

where λ_f is the heat conductivity coefficient of the fluid and is computed by introducing the molecular Prandtl number as:

$$\lambda_f = \frac{\mu_f C_{p,f}}{\text{Pr}}. \quad (\text{A.11})$$

The quantity $C_{p,f}$ is the fluid heat capacity at constant pressure. In AVBP, $C_{p,f}$ and the fluid heat capacity at constant volume $C_{v,f}$ depend on the fluid temperature and are supposed constant between T_i and $T_{i+1} = T_i + 100$. They are defined as the slope of the sensible enthalpy ($C_{p,f} = \partial h_s / \partial T_f$) and sensible energy ($C_{v,f} = \partial e_s / \partial T_f$), which are tabulated in AVBP.

²The range of temperature used in this work is narrow so the viscosity law has few importance.

Appendix B

Additional transport equations of high-order moments of the dispersed-phase

The following transport equations of higher moments of the dispersed phase have been excerpted from Masi [78]

- transport equation of the mean temperature variance:

$$\begin{aligned}
 n_p \frac{DQ_\theta^2}{Dt} = & -\frac{\partial}{\partial x_j} \left[n_p \bar{T}_p (\tilde{\mathbb{E}}_{p,j} + \delta \mathbb{E}_{p,j}) \right] - \frac{n_p}{\tau_{fp}^{F\theta}} (2Q_\theta^2 - \bar{T}_p \bar{T}_f) \\
 & - n_p \tilde{\mathbb{E}}_{p,j} \frac{\partial \bar{T}_p}{\partial x_j} - n_p \delta \mathbb{E}_{p,j} \frac{\partial \bar{T}_p}{\partial x_j}
 \end{aligned} \tag{B.1}$$

- transport equation of the mean mesoscopic temperature variance:

$$\begin{aligned}
 n_p C_{p,p} \frac{D\tilde{q}_\theta^2}{Dt} = & -\frac{\partial}{\partial x_j} \left[n_p C_{p,p} \langle \tilde{T}'_p \delta \Theta_{p,j} \rangle_p + \frac{1}{2} n_p C_{p,p} \langle \tilde{T}'_p \tilde{T}'_p \tilde{u}'_{p,j} \rangle_p \right] \\
 & - \frac{n_p C_{p,p}}{\tau_{fp}^{F\theta}} (2\tilde{q}_\theta^2 - q_{fp}^\theta) \\
 & - n_p C_{p,p} \tilde{\mathbb{E}}_{p,j} \frac{\partial \bar{T}_p}{\partial x_j} \\
 & + n_p C_{p,p} \langle \delta \Theta_{p,j} \frac{\partial \tilde{T}'_p}{\partial x_j} \rangle_p
 \end{aligned} \tag{B.2}$$

- transport equation of the mean RUM temperature variance:

$$\begin{aligned}
n_p C_{p,p} \frac{D\delta q_\theta^2}{Dt} &= -\frac{\partial}{\partial x_j} \left[n_p C_{p,p} \langle \delta \Omega_{p,j} \rangle_p + n_p C_{p,p} \langle \tilde{u}_{p,j} \delta \theta \rangle_p \right] \\
&\quad - \frac{n_p C_{p,p}}{\tau_{fp}^{F\theta}} 2\delta q_\theta^2 \\
&\quad - n_p C_{p,p} \delta \mathbb{F}_{p,j} \frac{\partial \bar{T}_p}{\partial x_j} \\
&\quad - n_p C_{p,p} \langle \delta \Theta_{p,j} \frac{\partial \tilde{T}'_p}{\partial x_j} \rangle_p
\end{aligned} \tag{B.3}$$

- transport equation of the mean mesoscopic heat flux:

$$\begin{aligned}
n_p C_{p,p} \frac{D\tilde{\mathbb{F}}_{p,i}}{Dt} &= -\frac{\partial}{\partial x_j} \left[n_p C_{p,p} \langle \tilde{u}_{p,i} \tilde{u}_{p,j} \tilde{T}'_p \rangle_p + \langle \tilde{u}_{p,i} \delta \Theta_{p,j} \rangle_p + \langle \tilde{T}'_p \delta R_{p,ij} \rangle_p \right] \\
&\quad - n_p C_{p,p} \left(\frac{1}{\tau_{fp}^F} + \frac{1}{\tau_{fp}^{F\theta}} \right) \tilde{\mathbb{F}}_{p,i} + n_p C_{p,p} \left[\frac{1}{\tau_{fp}^F} \langle v'_{f,i} \tilde{T}'_p \rangle_p + \frac{1}{\tau_{fp}^{F\theta}} \langle \tilde{u}_{p,i} T'_f \rangle_p \right] \\
&\quad - n_p C_{p,p} \tilde{\mathbb{R}}_{p,ij} \frac{\partial \bar{T}_p}{\partial x_j} - n_p C_{p,p} \tilde{\mathbb{F}}_{p,j} \frac{\partial \bar{V}_{p,i}}{\partial x_j} \\
&\quad + n_p C_{p,p} \langle \delta R_{p,ij} \frac{\partial \tilde{T}'_p}{\partial x_j} \rangle_p + n_p C_{p,p} \langle \delta \Theta_{p,j} \frac{\partial \tilde{u}'_{p,i}}{\partial x_j} \rangle_p
\end{aligned} \tag{B.4}$$

- transport equation of the mean RUM heat flux:

$$\begin{aligned}
n_p C_{p,p} \frac{D\delta \mathbb{F}_{p,i}}{Dt} &= -\frac{\partial}{\partial x_j} \left[n_p C_{p,p} \langle \delta \Delta_{p,ij} \rangle_p + n_p C_{p,p} \langle \tilde{u}_{p,j} \delta \Theta_{p,i} \rangle_p \right] \\
&\quad - n_p C_{p,p} \left(\frac{1}{\tau_{fp}^F} + \frac{1}{\tau_{fp}^{F\theta}} \right) \delta \mathbb{F}_{p,i} \\
&\quad - n_p C_{p,p} \delta \mathbb{R}_{p,ij} \frac{\partial \bar{T}_p}{\partial x_j} - n_p C_{p,p} \delta \mathbb{F}_{p,j} \frac{\partial \bar{V}_{p,i}}{\partial x_j} \\
&\quad - n_p C_{p,p} \langle \delta R_{p,ij} \frac{\partial \tilde{T}'_p}{\partial x_j} \rangle_p - n_p C_{p,p} \langle \delta \Theta_{p,j} \frac{\partial \tilde{u}'_{p,i}}{\partial x_j} \rangle_p
\end{aligned} \tag{B.5}$$

Appendix C

Additional results

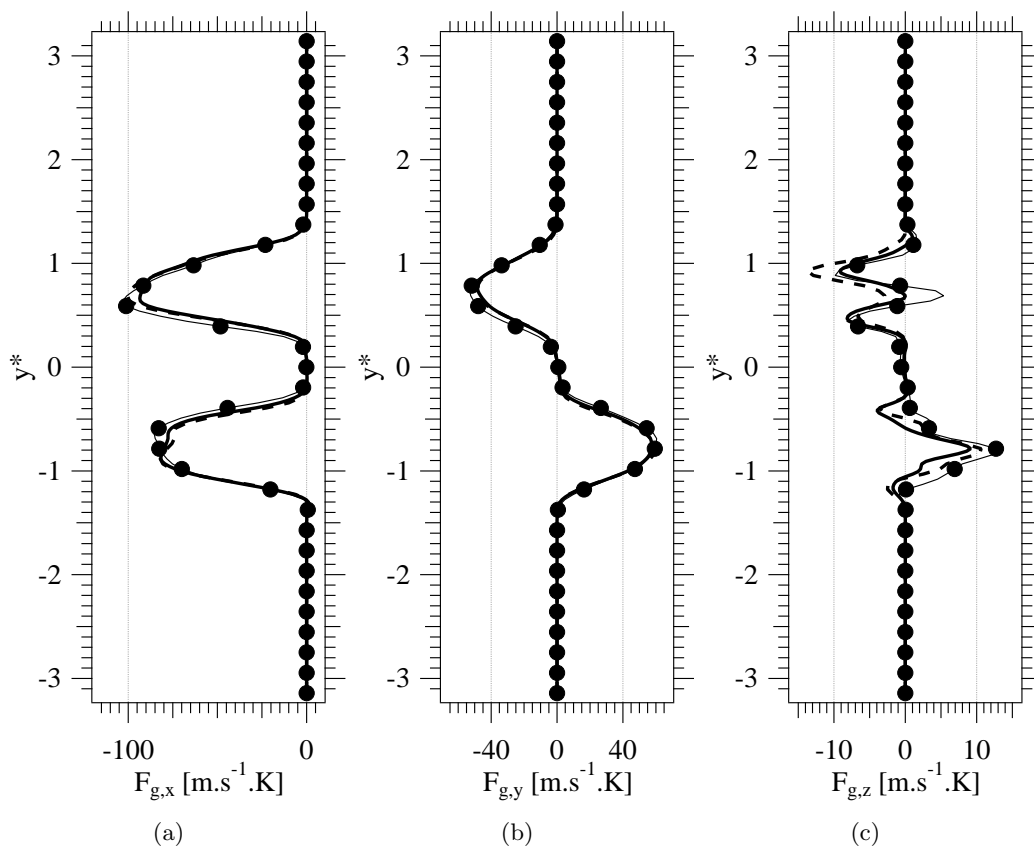


Figure C.1: Streamwise (left), spanwise (center) and cross-stream (right) heat fluxes of the carrier phase at $t^* = 40$. Simulations carried out with AVBP (fine mesh M3H (—) and coarse mesh M2H (----)) are compared with NTMIX (---●---).

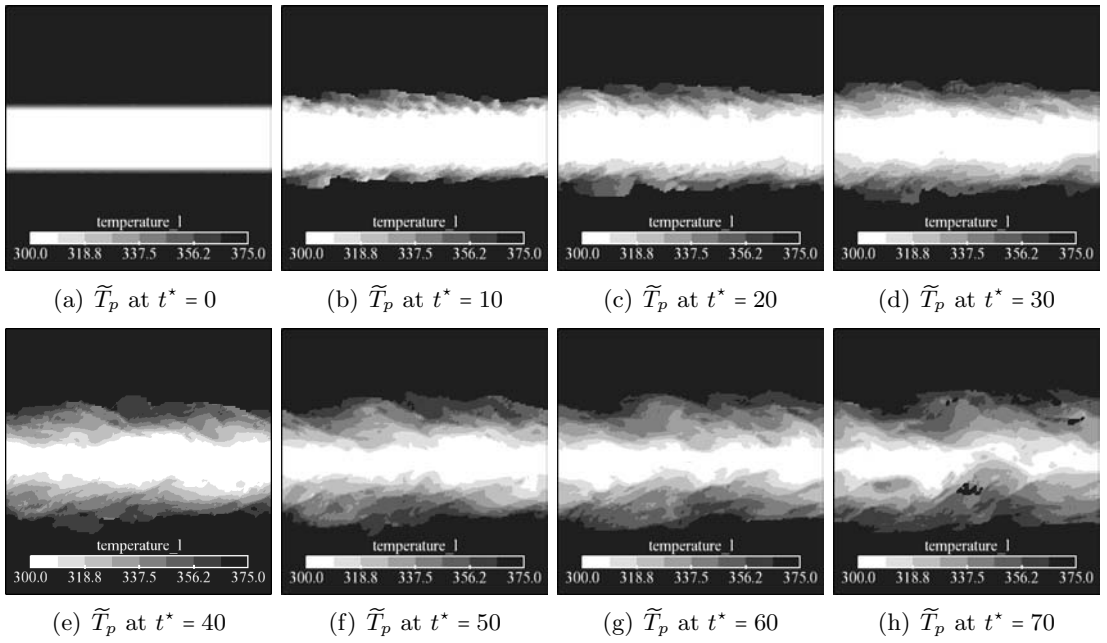


Figure C.2: Time evolution of particle temperature of the Lagrangian simulation. Cut at $Z = 0$.

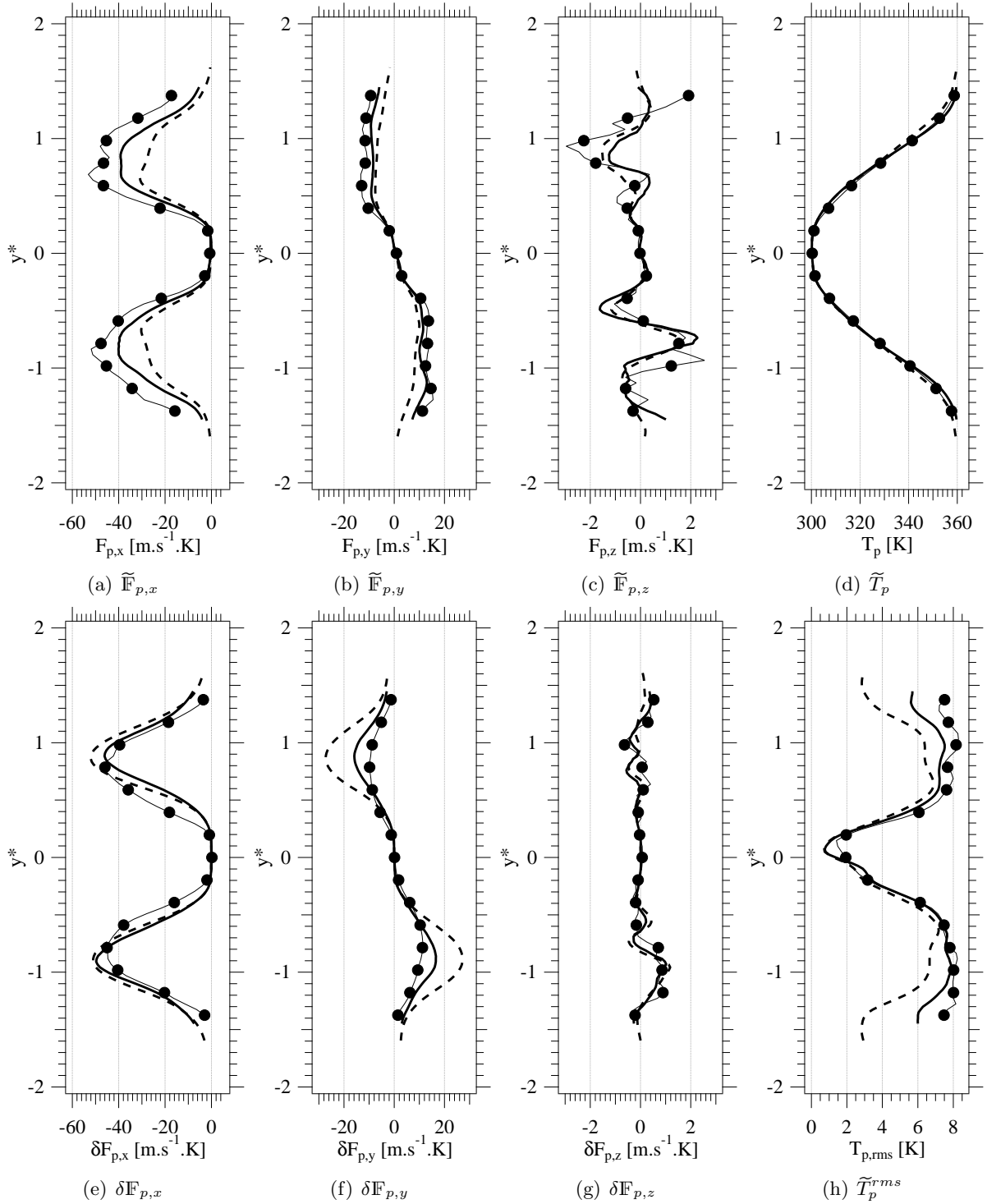
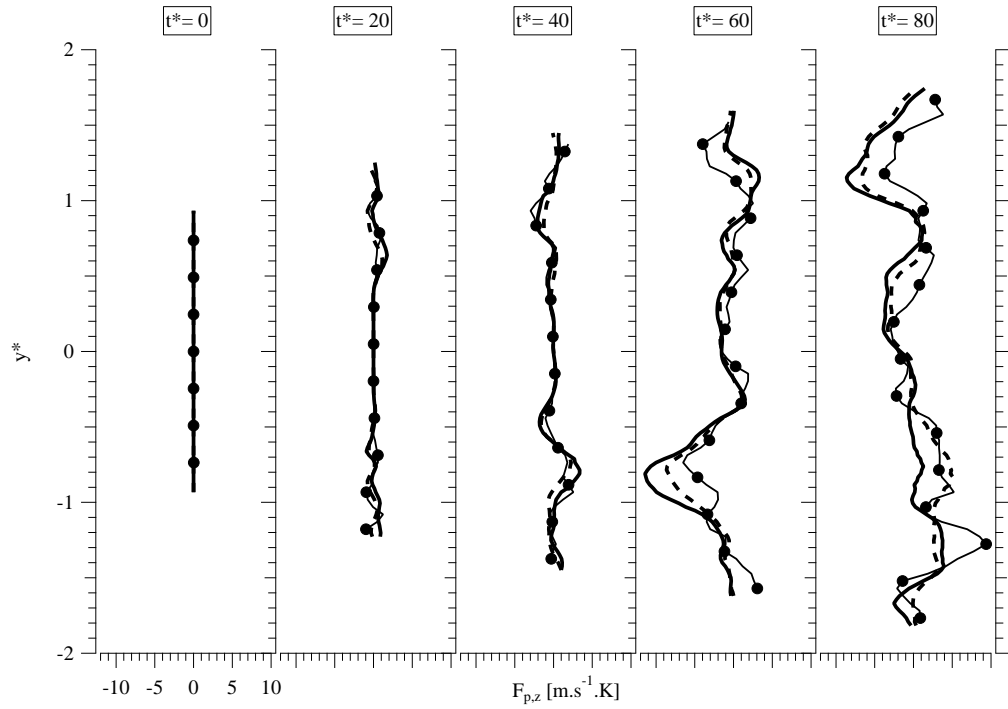
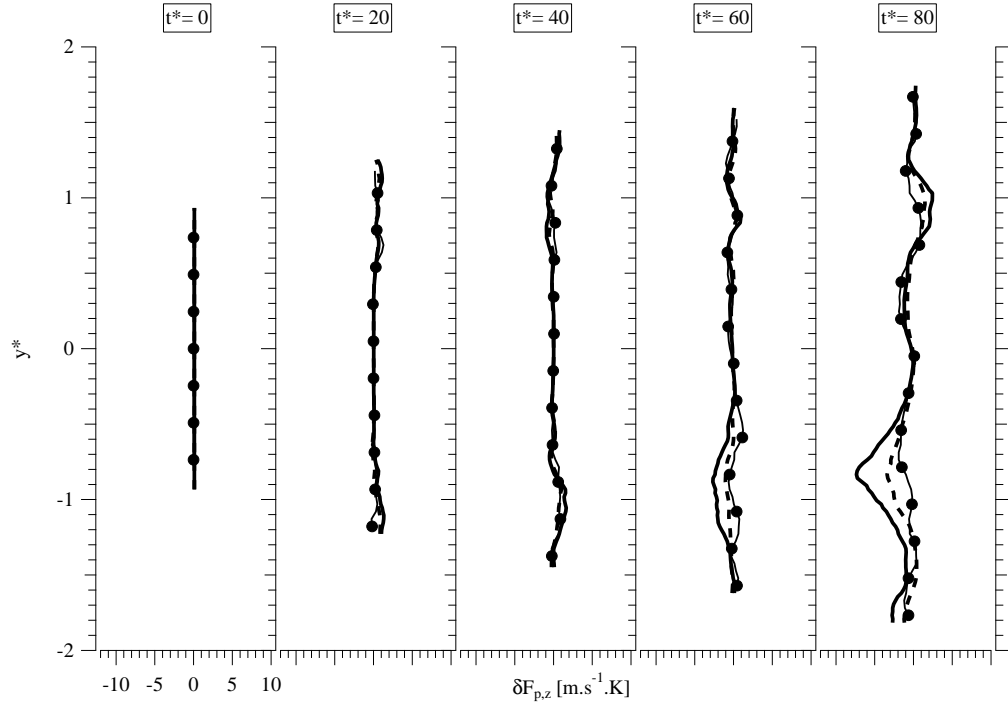


Figure C.3: Influence of the RUM model on the thermal variables of the dispersed phase at $t^* = 40$ when the RUM-HF are turned on. Eulerian simulations performed with AXISY-C (—) and VISCO (----) RUM models are compared with the Lagrangian reference (—●—).



(a)



(b)

Figure C.4: Influence of the RUM HF model on the particle cross-stream heat flux statistics with the AXISY-C model. (Top) mesoscopic $\tilde{F}_{p,z}$ and (Bottom) RUM $\delta F_{p,z}$. Eulerian simulations without (—) and with (---) RUM HF are compared with the Lagrangian reference (—●—).

Bibliography

- [1] R. Abgrall. Toward the ultimate conservative scheme: following the quest. *Journal of Computational Physics*, 167(2):277–315, 2001.
- [2] R. Abgrall, A. Larat, and M. Ricchiuto. Construction of very high order residual distribution schemes for steady inviscid flow problems on hybrid unstructured meshes. *Journal of Computational Physics*, 230(11):4103 – 4136, 2011. Special issue High Order Methods for CFD Problems.
- [3] R. Abgrall, A. Larat, M. Ricchiuto, and C. Tav. A simple construction of very high order non-oscillatory compact schemes on unstructured meshes. *Computers & Fluids*, 38(7):1314 – 1323, 2009. Special Issue Dedicated to Professor Alain Lerat on the Occasion of his 60th Birthday.
- [4] B. Abramzon and C. Elata. Unsteady heat transfer from a single sphere in stokes flow. *International journal of heat and mass transfer*, 27(5):687 – 695, 1984.
- [5] S. K. Aggarwal. Relationship between stokes number and intrinsic frequencies in particle-laden flows. *AIAA Journal*, 32(6):1322–1325, 1994.
- [6] J. D. Anderson. *Modern Compressible Flow*. McGraw-Hill, New York, 1990.
- [7] S. V. Apte, M. Gorokhovski, and P. Moin. Large-eddy simulation of atomizing spray with stochastic modeling of secondary breakup. *International Journal of Multiphase Flow*, 29:1503–1522, 2003.
- [8] S. Balachandar. A scaling analysis for point-particle approaches to turbulent multiphase flows. *International Journal of Multiphase Flow*, 35(9):801 – 810, 2009. Special Issue: Point-Particle Model for Disperse Turbulent Flows.
- [9] S. Balachandar and J. K. Eaton. Turbulent dispersed multiphase flow. *Annual Review of Fluid Mechanics*, 42:111–133, 2010.
- [10] A. Berlemont, M.-S. Grancher, and G. Gouesbet. On the Lagrangian simulation of turbulence influence on droplet evaporation. *International journal of heat and mass transfer*, 34:2805–2812, 1991.
- [11] M. Boileau, G. Staffelbach, B. Cuenot, T. Poinsot, and C. Bérat. LES of an ignition sequence in a gas turbine engine. *Combustion and Flame*, 154(1-2):2–22, 2008.

-
- [12] M. Boivin, O. Simonin, and K. D. Squires. Direct numerical simulation of turbulence modulation by particles in isotropic turbulence. *Journal of Fluid Mechanics*, 375:235–263, 1998.
- [13] F. Bouchut, S. Jin, and X. Li. Numerical approximations of pressureless and isothermal gas dynamics. *SIAM Journal on Numerical Analysis*, 46(1):135–158, 2003.
- [14] H. Boughanem and A. Trouvé. Validation du code de simulation directe NTMIX3D pour le calcul des écoulements turbulents réactifs. Technical Report 42907, Institut Français du Pétrole, 1996.
- [15] CERFACS. *AVBP Handbook* - http://cerfacs.fr/~avbp/AVBP_V5.X/HANDBOOK. CERFACS, 2009.
- [16] C. Chalons, RO Fox, and M. Massot. A multi-gaussian quadrature method of moments for gas-particle flows in a les framework. In *Proceedings of the Summer Program*, pages 347–358, Center for Turbulence Research, NASA AMES, Stanford University, USA, 2010.
- [17] S. Chapman and T. G. Cowling. *The Mathematical Theory of Non-Uniform Gases*. Cambridge University Press, cambridge mathematical library edition, 1939 (digital reprint 1999).
- [18] P. Chassaing. *Turbulence en mécanique des fluides, analyse du phénomène en vue de sa modélisation à l’usage de l’ingénieur*. Cépaduès-éditions, Toulouse, France, 2000.
- [19] H. H. Chiu, H. Y. Kim, and E. J. Croke. Internal group combustion of liquid droplets. In *19th Symp. (Int.) on Combustion*, pages 971–980. The Combustion Institute, Pittsburgh, 1982.
- [20] O. Colin. *Simulations aux grandes échelles de la combustion turbulente prémélangée dans les statoréacteurs*. Phd thesis, INP Toulouse, 2000.
- [21] O. Colin. A finite element operator for diffusion terms in avbp. Technical report, Institut Français du Pétrole, 2003.
- [22] O. Colin and M. Rudgyard. Development of high-order taylor-galerkin schemes for unsteady calculations. *Journal of Computational Physics*, 162(2):338–371, 2000.
- [23] A. Couzinet. *Approche PDF jointe fluide-particule pour la modélisation des écoulements diphasiques anisothermes*. PhD thesis, Institut National Polytechnique de Toulouse, France - Dynamique des Fluides, 2008.
- [24] Anthony Couzinet, Benoit Bédard, and Olivier Simonin. Numerical study and Lagrangian modelling of turbulent heat transport. *Flow, Turbulence and Combustion*, 80:37–46, 2008. 10.1007/s10494-007-9081-7.
- [25] J. Crank and P. Nicolson. A practical method for numerical evaluation of solutions of partial differential equations of the heat-conduction type. *Advances in Computational Mathematics*, 6:207–226, 1996. 10.1007/BF02127704.

- [26] P. I. Crumpton, J. A. Mackenzie, and K. W. Morton. Cell vertex algorithms for the compressible navier-stokes equations. *Journal of Computational Physics*, 109:1–15, 1993.
- [27] S. De Chaisemartin. *Modèles Eulériens et Simulation Numérique de la dispersion turbulente de brouillards qui s'évaporent*. PhD thesis, Ecole Centrale de Paris, Chatenay-Malabry, France, 2009.
- [28] S. de Chaisemartin, L. Frret, D. Kah, F. Laurent, R.O. Fox, J. Reveillon, and M. Massot. Eulerian models for turbulent spray combustion with polydispersity and droplet crossing. *Comptes Rendus Mcanique*, 337(6-7):438 – 448, 2009. Combustion for aerospace propulsion.
- [29] O. Desjardins, V. Moureau, and H. Pitsch. An accurate conservative level set/ghost fluid method for simulating turbulent atomization. *Journal of Computational Physics*, 227:8395–8416, 2008.
- [30] J. Dombard, B. Leveugle, L. Selle, J. Reveillon, T. Poinso, and Y. D'angelo. Modeling heat transfer in dilute two-phase flows using the mesoscopic Eulerian formalism. *submitted to the International journal of heat and mass transfer*, 2011.
- [31] J. Donea. Taylor-galerkin method for convective transport problems. *International Journal for Numerical Methods in Fluids*, 20(1):101–119, 1984.
- [32] O. A. Druzhinin. On the two-way interaction in two-dimensional particle-laden flows - the accumulation of particles and flow modification. *Journal of Fluid Mechanics*, 297:49–76, 1995.
- [33] O. A. Druzhinin and S. Elghobashi. Direct numerical simulations of bubble-laden turbulent flows using the two-fluid formulation. *Physics of Fluids*, 10(3):685–697, 1998.
- [34] S. Elghobashi. On predicting particle-laden turbulent flows. *Applied Scientific Research*, 52:309–329, 1994. 10.1007/BF00936835.
- [35] S. Elghobashi and G. Truesdell. On the two-way interaction between homogeneous turbulence and dispersed solid particles. *Physics of Fluids*, 5(7):1790–1801, 1993.
- [36] S. Elghobashi and G. C. Truesdell. Direct simulation of particle dispersion in a decaying isotropic turbulence. *Journal of Fluid Mechanics*, 242:655–700, 1992.
- [37] J. Ferry and E. Balachandar. A fast Eulerian method for disperse two-phase flow. *International Journal of Multiphase Flow*, 27:1199–1226, 2001.
- [38] J. Ferry and E. Balachandar. Equilibrium Eulerian approach for predicting the thermal field of a dispersion of small particles. *International journal of heat and mass transfer*, 48:681–689, 2005.
- [39] J. Ferry, E. Balachandar, and S. Rani. A locally implicit improvement of the equilibrium Eulerian method. *International Journal of Multiphase Flow*, 29:869–891, 2003.
- [40] P. Février. *Etude numérique des effets de concentration préférentielle et de corrélation spatiale entre vitesses de particules solides en turbulence homogène isotrope stationnaire*. PhD thesis, INP Toulouse, 2000.

-
- [41] P. Février, O. Simonin, and K. Squires. Partitioning of particle velocities in gas-solid turbulent flows into a continuous field and a spatially uncorrelated random distribution: Theoretical formalism and numerical study. *Journal of Fluid Mechanics*, 533:1–46, 2005.
- [42] M. García. *Développement et validation du formalisme Euler-Lagrange dans un solveur parallèle et non-structuré pour la simulation aux grandes échelles*. Phd thesis, INP Toulouse, 2009.
- [43] R. Gatignol. The Faxén formulae for a rigid particle in an unsteady non-uniform stokes flow. *Journal de Mécanique Théorique et Appliquée*, 1(2):143–160, 1983.
- [44] M.A. Gorokhovski and M. Herrmann. Modelling primary atomization. *Annual Review of Fluid Mechanics*, 40:343–366, 2008.
- [45] V. Granet, O. Vermorel, T. Leonard, L. Gicquel, , and T. Poinso. Comparison of nonreflecting outlet boundary conditions for compressible solvers on unstructured grids. *American Institute of Aeronautics and Astronautics Journal*, 48(10):2348–2364, 2010.
- [46] J. B. Greenberg, I. Silverman, and Y. Tambour. On the origin of spray sectional conservation equations. *Combustion and Flame*, 93:90–96, 1993.
- [47] D. Gueyffier, J. Li, A. Nadim, R. Scardovelli, and S. Zaleski. Volume-of-fluid interface tracking with smoothed surface stress methods for three-dimensional flows. *Journal of Computational Physics*, 152(2):423 – 456, 1999.
- [48] D. C. Haworth and S. B. Pope. A generalized Langevin model for turbulent flows. *Physics of Fluids*, 2:738–744, 1986.
- [49] M. Herrmann. A balanced force refined level set grid method for two-phase flows on unstructured flow solver grids. *Journal of Computational Physics*, 227(4):2674 – 2706, 2008.
- [50] M. Herrmann. A parallel Eulerian interface tracking/Lagrangian point particle multi-scale coupling procedure. *Journal of Computational Physics*, 229(3):745 – 759, 2010.
- [51] P. Fede and O. Simonin. Effect of particle-particle collisions on the spatial distribution of inertial particles suspended in homogeneous isotropic turbulent flows. In Michel Deville, Thien-Hiep Lê, and Pierre Sagaut, editors, *Turbulence and Interactions*, volume 110 of *Notes on Numerical Fluid Mechanics and Multidisciplinary Design*, pages 119–125. Springer Berlin / Heidelberg, 2010.
- [52] J. O. Hinze. *Turbulence*. McGraw-Hill, New-York, 1975.
- [53] C. Hirsch. *Numerical Computation of Internal and External Flows*. John Wiley, New York, 1988.
- [54] C. Hirsch. *Numerical Computation of Internal and External Flows*, volume 2. John Wiley & Sons, New York, 1990.
- [55] K. Hishida, K. Takemoto, and M. Maeda. Turbulent characteristics of gas-solids two-phase confined jet. *Japanese Journal of Multiphase Flow*, 1(1):56–69, 1987.

- [56] L. Howarth and T. Karman. On the statistical theory of isotropic turbulence. In *Proc. of the Roy. Soc. Göttingen Nachrichte*, volume A164(917), pages 192–215, 1938.
- [57] F. A. Jaber. Temperature fluctuations in particle-laden homogeneous turbulent flows. *International journal of heat and mass transfer*, 41(24):4081 – 4093, 1998.
- [58] F. A. Jaber and F. Mashayek. Temperature decay in two-phase turbulent flows. *International journal of heat and mass transfer*, 43(6):993 – 1005, 2000.
- [59] F. Jaegle. *LES of two-phase flow in aero-engines*. PhD thesis, Université de Toulouse - Ecole doctorale MEGeP, CERFACS - CFD Team, Toulouse, December 2009.
- [60] A. Jameson, W. Schmidt, and E. Turkel. Numerical solution of the Euler equations by finite volume methods using Runge-Kutta time stepping schemes. In AIAA paper 81-1259, editor, *14th Fluid and Plasma Dynamic Conference*, Palo Alto, 1981.
- [61] D. Kah. *Prise en compte des aspects polydispersés pour la modélisation d'un jet de carburant dans les moteurs à combustion interne*. PhD thesis, Ecole Centrale de Paris, 2010.
- [62] Damien Kah, Frédérique Laurent, Lucie Fréret, Stéphane de Chaisemartin, Rodney Fox, Julien Reveillon, and Marc Massot. Eulerian quadrature-based moment models for dilute polydisperse evaporating sprays. *Flow, Turbulence and Combustion*, 85:649–676, 2010. 10.1007/s10494-010-9286-z.
- [63] A. Kaufmann. *Vers la simulation des grandes échelles en formulation Euler/Euler des écoulements réactifs diphasiques*. Phd thesis, INP Toulouse, 2004.
- [64] A. Kaufmann and M. Moreau. A spectral projection method for analysis of autocorrelation functions and projection errors in discrete particle simulation. *International Journal for Numerical Methods in Fluids*, 58(7):709–725, 2008.
- [65] A. Kaufmann, M. Moreau, O. Simonin, and J. Hélie. Comparison between Lagrangian and mesoscopic Eulerian modelling approaches for inertial particles suspended in decaying isotropic turbulence. *Journal of Computational Physics*, 227(13):6448–6472, 2008.
- [66] K.T. Kim, J.G. Lee, B.D. Quay, and D.a. Santavicca. Response of partially premixed flames to acoustic velocity and equivalence ratio perturbations. *Combustion and Flame*, 157(9):1731–1744, September 2010.
- [67] R.H. Kraichnan. Diffusion by a random velocity field. *Physics of Fluids*, 13:22–31, 1970.
- [68] K. K. Kuo. *Principles of combustion*. John Wiley & Sons, Inc., Hoboken, New Jersey, 2nd edition, 2005.
- [69] N. Lamarque. *Schémas numériques et conditions limites pour la simulation aux grandes échelles de la combustion diphasique dans les foyers d'hélicoptère*. PhD thesis, Institut National Polytechnique de Toulouse, France - Dynamique des Fluides, 2007.
- [70] F. Laurent and M. Massot. Multi-fluid modelling of laminar polydisperse sprayflames: origin, assumptions and comparison of sectional and sampling methods. *Combustion Theory and Modelling*, 5:537–572, 2001.

-
- [71] F. Laurent, M. Massot, and P. Villedieu. Eulerian multi-fluid modeling for the numerical simulation of coalescence in polydisperse dense liquid sprays. *Journal of Computational Physics*, 194(2):505–543, 2004.
- [72] P. D. Lax and B. Wendroff. Systems of conservation laws. *Communications on Pure and Applied Mathematics*, 13:217–237, 1960.
- [73] P. D. Lax and B. Wendroff. Difference schemes for hyperbolic equations with high order of accuracy. *Communications on Pure and Applied Mathematics*, 17:381–398, 1964.
- [74] NS Lewis. Powering the planet. *MRS bulletin*, 103(43):15729–35, October 2007.
- [75] Tim Lieuwen and Ben Zinn. The role of equivalence ratio oscillations in driving combustion instabilities in low NOx gas turbines. *Proceedings of the Combustion Institute*, 27(2):1809–1816, 1998.
- [76] Daniele L. Marchisio, R. Dennis Vigil, and Rodney O. Fox. Quadrature method of moments for aggregation-breakage processes. *Journal of Colloid and Interface Science*, 258(2):322–334, 2003.
- [77] L. Martinez. *Simulation aux Grandes Échelles de l’Injection de carburant liquide dans les moteurs à combustion interne*. PhD thesis, Université de Toulouse - Ecole doctorale MEGeP, Institut Français du Pétrole, Paris, September 2009.
- [78] E. Masi. *Theoretical and numerical study of the modeling of unsteady non-isothermal particle-laden turbulent flows by an Eulerian-Eulerian approach*. Phd thesis, INP Toulouse, 2010.
- [79] E. Masi, E. Riber, P. Sierra, O. Simonin, and L.Y.M Gicquel. Modeling the random uncorrelated velocity stress tensor for unsteady particles Eulerian simulation in turbulent flows. In *Proc. 7th International Conference on Multiphase Flow*, Tampa, USA, 2010. ICFM-2010.
- [80] E. Masi, O. Simonin, and B. Bédard. The mesoscopic Eulerian approach for evaporating droplets interacting with turbulent flows. *Flow, Turbulence and Combustion*, pages 1–21, 2010-11-06.
- [81] M. Maxey and J. Riley. Equation of motion for a small rigid sphere in a nonuniform flow. *Physics of Fluids*, 26(4), 1983.
- [82] M. R. Maxey. The gravitational settling of aerosol particles in homogeneous turbulence and random flow fields. *Journal of Fluid Mechanics*, 174:441–465, 1987.
- [83] M. Moreau. *Modélisation numérique directe et des grandes échelles des écoulements turbulents gaz-particules dans le formalisme eulérien mésoscopique*. Phd thesis, INP Toulouse, 2006.
- [84] M. Moreau, P. Fede, O. Simonin, and P. Villedieu. Stochastic Lagrangian turbulence modelling and Monte Carlo simulation of collisions in gas-solid homogeneous turbulent flows. In *5th International Conference on Multiphase Flow*. ICMF, 2004.

- [85] K. W. Morton and M. F. Paisley. A finite volume scheme with shock fitting for the steady Euler equations. *Journal of Computational Physics*, 80:168–203, 1989.
- [86] V. Moureau. *Simulation aux grandes échelles de l'aérodynamique interne des moteurs à piston*. Phd thesis, Ecole Centrale Paris, 2004.
- [87] V. Moureau, G. Lartigue, Y. Sommerer, C. Angelberger, O. Colin, and T. Poinso. Numerical methods for unsteady compressible multi-component reacting flows on fixed and moving grids. *Journal of Computational Physics*, 202(2):710–736, 2005.
- [88] H. Murat Altay, Raymond L. Speth, Duane E. Hudgins, and Ahmed F. Ghoniem. The impact of equivalence ratio oscillations on combustion dynamics in a backward-facing step combustor. *Combustion and Flame*, 156(11):2106–2116, November 2009.
- [89] R.-H. Ni. A multiple grid scheme for solving the Euler equations. *AIAA Journal*, 20(11):1565–1571, 1982.
- [90] P. J. O'Rourke. *Collective drop effects on vaporizing liquid sprays*. Phd thesis, Princeton University, 1981.
- [91] S. Pascaud. *Vers la simulation aux grandes échelles des écoulements turbulents diphasiques réactifs: application aux foyers aéronautiques*. Phd thesis, INP Toulouse, 2006.
- [92] T. Passot and A. Pouquet. Numerical simulation of compressible homogeneous flows in the turbulent regime. *Journal of Fluid Mechanics*, 181:441–466, 1987.
- [93] T. Poinso and S. Lele. Boundary conditions for direct simulations of compressible viscous flows. *Journal of Computational Physics*, 101(1):104–129, 1992.
- [94] T. Poinso and D. Veynante. *Theoretical and Numerical Combustion*. R.T. Edwards, 2nd edition, 2005.
- [95] S. B. Pope. *Turbulent flows*. Cambridge University Press, 2000.
- [96] S. Rani and E. Balachandar. Evaluation of the equilibrium Eulerian approach for the evolution of particle concentration in isotropic turbulence. *International Journal of Multiphase Flow*, 29:1793–1816, 2003.
- [97] W. E. Ranz and W. R. Marshall. Evaporation from drops. *Chem. Eng. Prog.*, 48(4):173, 1952.
- [98] M. W. Reeks. On a kinetic equation for the transport of particles in turbulent flows. *Physics of Fluids*, 3(3), 1991.
- [99] Yuriko Renardy and Michael Renardy. Prost: A parabolic reconstruction of surface tension for the volume-of-fluid method. *Journal of Computational Physics*, 183(2):400 – 421, 2002.
- [100] J. Réveillon and F.-X. Demoulin. Effects of the preferential segregation of droplets on evaporation and turbulent mixing. *Journal of Fluid Mechanics*, 583:273–302, 2007.

-
- [101] J. Reveillon, C. Pera, and Z. Bouali. Examples of the potential of dns for the understanding of reactive multiphase flows. *International Journal of Spray and Combustion Dynamics*, 3:65–94, 2011.
- [102] J. Réveillon and L. Vervisch. Analysis of weakly turbulent diluted-spray flames and spray combustion regimes. *Journal of Fluid Mechanics*, 537:317–347, 2005.
- [103] E. Riber. *Développement de la méthode de simulation aux grandes échelles pour les écoulements diphasiques turbulents*. Phd thesis, INP Toulouse, 2007.
- [104] E. Riber, M. Moreau, O. Simonin, and B. Cuenot. Towards large eddy simulation of non-homogeneous particle laden turbulent gas flows using Euler-Euler approach. In *11th Workshop on Two-Phase Flow Predictions*, Merseburg, Germany, 2005.
- [105] E. Riber, V. Moureau, M. García., T. Poinsot, and O. Simonin. Evaluation of numerical strategies for LES of two-phase reacting flows. *Journal of Computational Physics*, 228:539–564, 2009.
- [106] J. J. Riley and G. S. Paterson. Diffusion experiments with numerically integrated isotropic turbulence. *Physics of Fluids*, 17:292–297, 1974.
- [107] P. L. Roe. Error estimates for cell-vertex solutions of the compressible Euler equations. Technical Report ICASE Report No.87-6, NASA Langley Research Center, 1987.
- [108] A. Roux. *Simulation aux grandes échelles d’un statoréacteur*. PhD thesis, Université de Toulouse - Ecole doctorale MEGeP, CERFACS - CFD Team, Toulouse, July 2009.
- [109] A. Roux, S. Reichstadt, N. Bertier, L. Y. M. Gicquel, F. Vuillot, and T. Poinsot. Comparison of numerical methods and combustion models for les of a ramjet. *Comptes rendus de l’Académie des sciencesMécanique*, 337(6-7):352–361, 2009.
- [110] M. Rudgyard. Multidimensional wave decompositions for the Euler equations. In Von Karman Institute for Fluid Dynamics, editor, *Lectures Series 1993-04*, volume 1993-04. Von Karman Institute for Fluid Dynamics, 1993.
- [111] M. A. Rudgyard. *Cell Vertex methods for compressible gas flows*. Phd thesis, Oxford University Computing Laboratory, 1990.
- [112] M. Sanjosé. *Evaluation de la méthode Euler-Euler pour la simulation aux grandes échelles des chambres à carburant liquide*. PhD thesis, Institut National Polytechnique de Toulouse, France - Dynamique des Fluides, 2009.
- [113] Y. Sato, E. Deutsch, and O. Simonin. Direct numerical simulations of heat transfer by solid particles suspended in homogeneous isotropic turbulence. *International journal of heat and mass transfer*, 19(2):187–192, 1998.
- [114] R. Sawyer. Science based policy for addressing energy and environmental problems. *Proceedings of the Combustion Institute*, 32(1):45–56, 2009.
- [115] L. Schiller and A. Nauman. A drag coefficient correlation. *VDI Zeitung*, 77:318–320, 1935.

- [116] L. Selle, G. Lartigue, T. Poinsot, R. Koch, K.-U. Schildmacher, W. Krebs, B. Prade, P. Kaufmann, and D. Veynante. Compressible large-eddy simulation of turbulent combustion in complex geometry on unstructured meshes. *Combustion and Flame*, 137(4):489–505, 2004.
- [117] J.-M. Senoner. *Développement de méthodes numériques pour la simulation aux grandes échelles de la combustion diphasique*. PhD thesis, Institut National Polytechnique de Toulouse, France - Dynamique des Fluides, 2010.
- [118] J.M. Senoner, M. Sanjosé, T. Lederlin, F. Jaegle, M. García, E. Riber, B. Cuenot, L. Gicquel, H. Pitsch, and T. Poinsot. Evaluation of numerical strategies for two-phase reacting flows. *Comptes rendus de l'Académie des sciences Mécanique*, 337(6-7):528–538, 2009.
- [119] B. Shotorban, F. Mashayek, and R. V. R. Pandya. Temperature statistics in particle-laden turbulent homogeneous shear flow. *International Journal of Multiphase Flow*, 29(8):1333 – 1353, 2003.
- [120] P. Sierra. *Modeling the dispersion and evaporation of sprays in aeronautical combustion chambers*. Phd thesis, INP Toulouse, 2011, in preparation.
- [121] O. Simonin. Combustion and turbulence in two phase flows. Lecture Series 1996-02, Von Karman Institute fo Fluid Dynamics, 1996.
- [122] O. Simonin. Statistical and continuum modelling of turbulent reactive particulate flows. Part 1: Theoretical derivation of dispersed Eulerian modelling from probability density function kinetic equation. Lecture Series 2000-06, Von Karman Institute fo Fluid Dynamics, 2000.
- [123] O. Simonin, P. Fevrier, and J. Lavieville. On the spatial distribution of heavy particle velocities in turbulent flow: from continuous field to particulate chaos. *Journal of Turbulence*, 3, 2002.
- [124] O. Simonin, L. Zaichik, V. Alipchenkov, and P. Février. Connection between two statistical approaches for the modelling of particle velocity and concentration distributions in turbulent flow: The mesoscopic Eulerian formalism and the two-point probability density function method. *Physics of Fluids*, 18(12):125107, 2006.
- [125] W. A. Sirignano. Fuel droplet vaporisation and spray combustion theory. *Progress in Energy and Combustion Science*, 9:291–322, 1983.
- [126] A. Smirnov, S. Shi, and I. Celik. Random flow generation technique for large eddy simulations and particle-dynamics modeling. *Trans. ASME. Journal of Fluids Engineering*, 123:359–371, 2001.
- [127] W. H. Snyder and J. L. Lumley. Some measurements of particle velocity autocorrelation functions in a turbulent flow. *Journal of Fluid Mechanics*, 48(1):41–71, 1971.
- [128] M. Sommerfeld and H. H. Qiu. Experimental studies of spray evaporation in turbulent flow. *International Journal of Heat and Fluid Flow*, 19:10–22, 1998.

-
- [129] K. D. Squires and J. Eaton. Measurements of particle dispersion obtained from direct numerical simulations of isotropic turbulence. *Journal of Fluid Mechanics*, 226:1–35, 1991.
- [130] K. D. Squires and J. K. Eaton. Particle response and turbulence modification in isotropic turbulence. *Physics of Fluids A*, 2(7):1191–1203, 1990.
- [131] K. D. Squires and J. K. Eaton. Lagrangian and Eulerian statistics obtained from direct numerical simulations of homogeneous turbulence. *Physics of Fluids A*, 3(1):130–143, 1991.
- [132] K. D. Squires and J. K. Eaton. Preferential concentration of particles by turbulence. *Physics of Fluids*, 3(5):1169–1178, 1991.
- [133] S. M. Stringer and K. W. Morton. Artificial viscosity for the cell vertex method. Technical report, Oxford University Computing Laboratory, 1996.
- [134] R. Struijs. *A multi-dimensional upwind discretization method for the Euler equations on unstructured grids*. Phd thesis, Technical University of Delft, 1994.
- [135] S. Sundaram and L. R. Collins. Collision statistics in an isotropic particle-laden turbulent suspension. part 1. direct numerical simulations. *Journal of Fluid Mechanics*, 335:75–109, 1997.
- [136] M. Sussman, P. Smereka, and S. Osher. A level set approach for computing solutions to incompressible two-phase flow. *Journal of Computational Physics*, 114(1):146 – 159, 1994.
- [137] R. Swanson and R. Radespiel. Cell centered and cell vertex multigrid schemes for the navier-stokes equations. *AIAA Journal*, 29(5):697–703, 1982.
- [138] C.-M. Tchen. *Mean Value and Correlation Problems connected with the Motion of Small Particles suspended in a turbulent fluid*. Phd thesis, Technical University of Delft, Netherlands, 1947.
- [139] Core Writing team, R.K Pachauri, and A. Resinger. Climate Change 2007: Synthesis report. Contribution of Working Groups I, II and III to the fourth Assessment Report of the Intergovernmental Panel on Climate Change. Technical report, IPCC, Geneva, Switzerland, 2007.
- [140] Gaurav Tomar, Daniel Fuster, Stphane Zaleski, and Stphane Popinet. Multiscale simulations of primary atomization. *Computers & Fluids*, 39(10):1864 – 1874, 2010.
- [141] G. Tryggvason, B. Bunner, A. Esmaeeli, D. Juric, N. Al-Rawahi, W. Tauber, J. Han, S. Nas, and Y. J. Jan. A front-tracking method for the computations of multiphase flow. *Journal of Computational Physics*, 169(2):708 – 759, 2001.
- [142] O. Vermorel. *Étude numérique et modélisation de la turbulence dans un écoulement de nappe chargée en particules*. Phd thesis, INP Toulouse, 2003.
- [143] O. Vermorel, B. Bédard, O. Simonin, and T. Poinsot. Numerical study and modelling of turbulence modulation in a particle laden slab flow. *Journal of Turbulence*, 4, 025, 2003.

- [144] M. R. Vetrano, S. Gauthier, J. van Beeck, P. Boulet, and J.-M. Buchlin. Characterization of a non-isothermal water spray by global rainbow thermometry. *Experiments in Fluids*, 40:15–22, 2006.
- [145] A. Vié. *Simulation aux grandes échelles d'écoulements diphasique turbulent à phase liquide dispersée*. PhD thesis, Institut National Polytechnique de Toulouse, France - Dynamique des Fluides, 2010.
- [146] T. von Kármán. Progress in the statistical theory of turbulence. In *Proc. Natl. Acad. Sci. USA*, 34 (11): 530:539, 1948.
- [147] J. von Neumann and R. D. Richtmeyer. A method for the numerical calculation of hydrodynamic shocks. *Journal of the Applied Physics*, 21:231, 1950.
- [148] L.-P. Wang and M. R. Maxey. Settling velocity and concentration distribution of heavy particles in homogeneous isotropic turbulence. *Journal of Fluid Mechanics*, 256:27–68, 1993.
- [149] L. P. Wang, A. S. Wexler, and Y. Zhou. Statistical mechanical description and modelling of turbulent collision of inertial particles. *Journal of Fluid Mechanics*, 415:117–153, 2000.
- [150] R. F. Warming and B. J. Hyett. The modified equation approach to the stability and accuracy analysis of finite-difference methods. *Journal of Computational Physics*, 14(2):159 – 179, 1974.
- [151] S. Wetchagarun and J. J. Riley. Dispersion and temperature statistics of inertial particles in isotropic turbulence. *Physics of Fluids*, 22(6), 1991.
- [152] F. A. Williams. Spray combustion and atomization. *Physics of Fluids*, 1:541–546, 1958.
- [153] F. A. Williams. *Combustion Theory*. Benjamin Cummings, Menlo Park, CA, 1985.
- [154] A. A. Wray. Minimal storage time advanced schemes for spectral methods. *Journal of Computational Physics*, 1990.
- [155] L.P. Yarin and G. Hetsroni. Turbulence intensity in dilute two-phase flows—2 temperature fluctuations in particle-laden dilute flows. *International Journal of Multiphase Flow*, 20(1):17 – 25, 1994.